UNIVERSIDAD COMPLUTENSE DE MADRID

FACULTAD DE CIENCIAS FÍSICAS
DEPARTAMENTO DE FÍSICA DE LA TIERRA, ASTRONOMÍA Y ASTROFÍSICA I

TESIS DOCTORAL

Analysis and physical interpretation of ionosferic plasma irregularities effect on positioning

Análisis e interpretación física del efecto de las irregularidades de plasma ionosférico en el posicionamiento

MEMORIA PARA OPTAR AL GRADO DE DOCTOR

PRESENTADA POR

Izarra Rodríguez Bilbao

DIRECTORES

Gracia Rodríguez Caderot
Miguel Herraiz Sarachaga

Madrid, 2017

Universidad Complutense de Madrid
Departamento de Física de la Tierra, Astronomía y Astrofísica I
(Geofísica y Meteorología), Facultad de Ciencias Físicas

ANALYSIS AND PHYSICAL INTERPRETATION OF IONOSPHERIC PLASMA IRREGULARITIES EFFECT ON POSITIONING

ANÁLISIS E INTERPRETACIÓN FÍSICA DEL EFECTO DE LAS IRREGULARIDADES DE PLASMA IONOSFÉRICO EN EL POSICIONAMIENTO

A thesis submitted in partial fulfillment of the requirements for the degree of Doctor of Philosophy in Physics by /Memoria para optar al grado de Doctor en Física por:

Izarra Rodríguez Bilbao

Advisors /Directores:

Dr. Gracia Rodríguez Caderot **Dr. Miguel Herraiz Sarachaga**

Supervised by /Supervisado por:

Prof. Sandro M. Radicella (ICTP)

Madrid, 2016

ANALYSIS AND PHYSICAL INTERPRETATION OF IONOSPHERIC PLASMA IRREGULARITIES EFFECT ON POSITIONING

ANÁLISIS E INTERPRETACIÓN FÍSICA DEL EFECTO DE LAS IRREGULARIDADES DE PLASMA IONOSFÉRICO EN EL POSICIONAMIENTO

Izarra Rodríguez Bilbao

Departamento de Física de la Tierra, Astronomía y Astrofísica I
(Geofísica y Meteorología)
Facultad de Ciencias Físicas
Universidad Complutense de Madrid

Tesis Doctoral

This work has been funded by the Predoctoral Research Fellowship "*Beca de formación y perfeccionamiento de personal investigador (PREDOC)*" from the Basque Government.

Two scientific stays at the ICTP from January to March 2012 and in June 2015, were supported by the EGONLABUR fellowship from the Basque Government.

Other stays and conferences attendance were partially supported by the "Group of Ionospheric studies and GNSS Techniques" of the Universidad Complutense de Madrid.

This study was carried out also in the framework of the projects PR/12/AYU/190 and AYA2013-47735-P funded by Fundación Mapfre and the Spanish Ministry of Economy and Competitiveness respectively.

Resumen

La ionosfera constituye una de las mayores fuentes de error en el posicionamiento GNSS (Global Navigation Satellite System) no sólo debido al hecho de que la refracción ionosférica puede introducir errores de algunos metros en las medidas de distancia satélite-receptor, sino también a la frecuente aparición de irregularidades en la densidad de plasma que dan lugar a degradaciones de las señales electromagnéticas que las atraviesan. El efecto de las irregularidades ionosféricas sobre las señales GNSS se puede cuantificar por medio de la estimación del TEC (*Total Electron Content*) a partir de observaciones de señales en doble frecuencia. En latitudes medias se espera que los valores de TEC varíen de una forma suave en los periodos tranquilos mientras que la presencia de irregularidades importantes está relacionada con tormentas magnéticas y otros fenómenos significativos de la Meteorología Espacial. En cambio, las características físicas de la ionosfera a bajas latitudes magnéticas inducen, entre otros fenómenos, la aparición de un tipo peculiar de irregularidades conocidas como burbujas de plasma ecuatorial (EPBs) que se caracterizan por disminuciones bruscas del TEC. La diferencia en la física de la ionosfera para bajas y medias latitudes marca una de las pautas fundamentales de este trabajo en el que se utiliza el parámetro ROT (*Rate Of change of TEC*) para evaluar las variaciones del contenido electrónico con el tiempo.

En el caso del posicionamiento realizado mediante receptores de doble frecuencia, el error introducido por la ionosfera puede ser eliminado en primera aproximación mediante la corrección conocida como "combinación libre de ionosfera". Sin embargo, se ha observado la presencia de errores significativos en la altura obtenida mediante el Posicionamiento Puntual de Precisión (PPP) bajo condiciones de fuerte variación del ROT.

Teniendo en cuenta lo expuesto anteriormente, esta Tesis Doctoral ha perseguido dos objetivos principales:

Primero: analizar de manera general el efecto de las variaciones fuertes de ROT en el posicionamiento. Para ello se ha prestado especial atención a la existencia de EPBs en bajas latitudes y a las características de la actividad magnética y solar existentes en latitudes medias durante el tiempo de análisis.

Segundo: explicar la aparición de estos errores y las características de los fenómenos físicos implicados. Para ello se ha investigado el efecto de fluctuaciones aleatorias del ROT sobre el PPP con objeto de hallar las causas del deterioro en la precisión del posicionamiento en cada época aun cuando la solución utilizada se consideraba libre de los efectos de la ionosfera.

En este trabajo se proponen diferentes procedimientos para tratar la detección de distintos tipos de irregularidades atendiendo a las características observadas en el ROT.

En cuanto a la baja latitud, se han seleccionado 6 estaciones que cubren diferentes longitudes y se ha definido un valor umbral común para separar los períodos ionosféricos tranquilos de los activos. La aparición de valores de ROT que superan este valor umbral depende de la hora local, la temporada del año, la longitud geográfica de la estación, la actividad geomagnética, y la actividad solar. Además, se ha observado una variabilidad día a día.

Se ha observado un aumento en los fallos de los receptores GNSS, y en última instancia una disminución en la precisión PPP en modo cinemático, para los mismos períodos en los que se observa la presencia de irregularidades asociadas a bajas latitudes. Los resultados que se muestran en este trabajo presentan diferencias que dependen en gran medida del tipo de receptor. Así mismo, se aprecia una mejora en la precisión obtenida con los datos de los años más recientes que es atribuida a la calidad de los productos precisos proporcionados por el IGS (*International GNSS Service*). Se ha visto que la repetitividad se deteriora por la pérdida de señal, la dilución de precisión y la re-estimación de ambigüedades, debido a las deficiencias de los filtros del software de PPP para hacer frente a la información en los observables que se caracterizan por estar afectados por un gran ROT. También se aprecia que el deterioro de la solución final diaria en modo cinemático puede ser superior a un orden de magnitud con respecto a la solución esperada.

Los resultados también muestran que un número crítico de satélites no es tan decisivo en la precisión del PPP cinemático, a menos que la distribución de los satélites en el cielo no sea lo suficiente buena o que las ambigüedades estén pobremente establecidas. Se ha observado que la incorporación de la constelación GLONASS al procesado PPP produce una mejora de los resultados en ambos períodos de alto y bajo ROT. Además, una frecuencia de muestreo de los datos mayor también puede disminuir el deterioro de PPP inducido por la reestimación de ambigüedades.

Con respecto a las estaciones de latitudes medias, después de analizar más de 10 años de datos, se ha observado que las estructuras irregulares predominantes son TIDs (perturbaciones ionosféricas itinerantes), que se producen durante el día principalmente en el primer y último trimestre de cada año, y durante la noche de mayo a agosto. No se han observado errores grandes asociados a las irregularidades que se generan en las latitudes medias.

También se han detectado irregularidades asociadas a la Meteorología Espacial. Se ha propuesto un nuevo procedimiento de detección para los SITECs (aumentos repentino del TEC debido a la respuesta ionosférica de fulguraciones

solares) que se producen tanto en bajas como en medias latitudes. En esta línea, se analiza un caso estudio en relación con el evento del 28 de octubre de 2003. Con respecto a este suceso, se ha observado un efecto combinado de la interferencia inducida por la emisión solar de ondas de radio y el efecto del SITEC sobre la degradación de la precisión producida en el PPP cinemático en varias estaciones del hemisferio iluminado cuando se analizan los datos con una tasa de muestreo de 30 s.

En su conjunto, los trabajos realizados en esta Tesis contribuyen notablemente a la comprensión de los efectos ionosféricos sobre la precisión del PPP llevada a cabo en modo cinemático, y a los procesos físicos que los generan.

Abstract

The ionosphere is one of the largest sources of error in the GNSS (Global Navigation Satellite System) positioning not only because the ionospheric refraction can induce errors of several meters in the satellite-receiver signals ranges but also due to the frequent occurrence of plasma density irregularities that lead to signal degradation when crosses them. The effect of the ionospheric irregularities on GNSS signals can be quantified by estimating the TEC (Total Electron Content) from dual frequency GNSS observations. At mid-latitudes it is expected that TEC values vary smoothly in the quiet periods whereas large electron density irregularities occurrence will be related to magnetic storms and other Space Weather phenomena. On the other hand, the physical characteristics of the ionosphere at low magnetic latitudes induce, among other phenomena, the appearance of a peculiar kind of irregularities known as equatorial plasma bubbles (EPBs) which are characterized by TEC depletions. The difference in the physics of the ionosphere at low-latitudes and mid-latitudes marks one of the fundamental guidelines of this Doctoral Thesis and the ROT (Rate of change of TEC) parameter is introduced to evaluate the changes in the electron content over time.

In the case of positioning performed using dual-frequency receivers, the error introduced by the ionosphere can, in first approximation, be eliminated by the correction known as "ionospheric-free combination" (iono-free). However, significant errors in the height estimated by Precise Point Positioning (PPP) has been observed in the presence of strong variation in the ROT.

Based on that, this Doctoral Thesis has two main objectives:

First: to analyze the effect of the strong variations of ROT in positioning. For this purpose, in low latitudes special attention has been paid to the existence of EPBs and in mid-latitudes to the current solar and magnetic activity characteristics.

Second: to explain the occurrence of these errors and the characteristics of the physical phenomena involved. For this purpose, we have investigated the effect of random fluctuations of ROT on kinematic PPP to find out the causes of accuracy deterioration in the position estimated at each epoch (every 30 seconds), although the solution was considered to be free of the effects of the ionosphere.

In this work, different procedures to deal with the detection of distinct kinds of irregularities according to the characteristics observed in their ROT have been proposed. The shortcomings with regards to the ROT calculated only with carrier phases and the use of a mapping function for geometric effect reductions, are also explained.

Regarding low-latitude stations, 6 stations covering different longitudes have been selected and a common threshold value has been defined to separate quiet from disturbed ionospheric periods. The occurrence of ROT values exceeding a proposed threshold value presents local-time, seasonal/longitudinal, geomagnetic and solar activity dependencies, although a day to day variability has been also observed. Additionally, irregularities occurring after dawn have been also identified but the reason for their occurrence is presently unknown.

The presence of low-latitudes irregularities may cause receiver tracking performance troubles and in last instance, a decrease in kinematic PPP accuracy for the same periods. The results shown in this work present differences that largely depend on the receiver type. An accuracy improvement is observed in the most recent years which is attributed to the quality of the precise products provided by the IGS (International GNSS Service). Solution repeatability deteriorates due to signal loss, dilution of precision and ambiguities re-estimation due to the shortcomings of the PPP software filters to deal with the observable information characterized by a large ROT. It is also observed that the daily final solution deterioration in kinematic mode PPP may exceed one order of magnitude.

Results also show that a critical number of satellites is not as decisive as expected in kinematic PPP performance unless the distribution in the sky is no good enough, or the ambiguities are poorly stablished. Adding GLONASS produces an improvement of the results in comparison to using only GPS, in both periods of high and low ROT. Besides, a higher sampling rate in the data may also diminish the deterioration of PPP induced by ambiguities reset. However, the precise satellite and clock products interpolation needed to deal with this sampling deteriorates position accuracy.

Regarding mid-latitude stations, the predominant trends identified are wavelike patterns characterizing TIDs (Travelling Ionospheric Disturbances). After analyzing more than 10 years of data from mid-latitude stations, it has been observed that these structures occur both in daytime and nighttime hours of low to high solar activity periods. Daytime structures occur mostly in the first and last trimester of each year, from sunrise to sunset, and nighttime events from May to August from sunset to sunrise. No large errors that may be attributed to the irregularities occurring at mid-latitudes have been observed.

Space Weather related irregularities occurring at both low- and mid-latitudes almost simultaneously have been also detected. A novel procedure has been proposed for the detection of SITECs (sudden increases in TEC) and a case study regarding the October 28th, 2003 event of these characteristics is analyzed. In this particular case, a combined effect of solar radio burst (SRB) induced interference and the SITEC influence is observed. Results show that accuracy degradation may happen in kinematic PPP in several stations of the sunlit hemisphere when 30 s

sampling rate data are analyzed. The observed errors in the position are the result of the difficulties that cycle slip (CS) detection strategies have to deal with the observables that have been affected by the SITEC.

In this way, this manuscript contributes to the understanding of the ionospheric effects causing errors in kinematic PPP and the physical processes that generate them.

Acknowledgments

During the last five years of work I have received different kinds of support from several people and institutions that helped me to achieve the completion of my studies.

First, I would like to thank Dr. Miguel Herraiz Sarachaga and Dr. Gracia Rodríguez Caderot for providing me the opportunity to pursue my graduate studies with this topic. These years have been one of the most enriching periods of my life and this has happened thanks to your continuous support, for encouraging me to participate in a so wide variety of projects that has given me the opportunity to work in multidisciplinary assignments, and also for the freedom you have given me to take decisions based on my own intuition for which I am very grateful.

I would also like to acknowledge Professor Sandro M. Radicella for his role as a supervisor of this work. Thank you for your endless help and patient guidance.

I would like to express my gratitude to Prof. Dr. Hab. Inż. Andrzej Krankowski, for his hospitality and advices during my visit to the University of Warmia and Mazury in Olsztyn, Poland.

Thank you Dr. Beatriz Moreno Monge for generously giving me access to the MAP3 positioning software, but also for your help and instructions every time I got lost, especially at the beginning.

I would also like to acknowledge the other different sources of data and software used in the development of this work: The IGS community for providing GNSS data and products; the NRCan for providing the online CSRS-PPP service; the USC Space Science Center for SOHO/SEM EUV data; and Dr. Mauro Messerotti of the Solar Radiophysics and Meteorology of Space Group of the INAF-Astronomical Observatory of Trieste, for solar radio flux data.

Thanks to Dr. Luigi Ciraolo for giving me the advices that made me look beyond. In this sense, I would like to thank also Bruno Nava. They both provided valuable insight during my stays in the ICTP in Trieste. Additionally, I would like to express my gratitude to all the members of the T/ICT4D group of the ICTP for their always warm welcome. Thank you also for co-organizing the multitude of workshops I had the opportunity to attend and for all the resources you invest in training people like me. They all have been very enriching experiences.

To Dr. Sreeja Vadakke Veettil and Dr. Dalja Buresova for their valuables suggestions as members of the external evaluation committee of this thesis. Thanks also to Dr. Claudio Brunini for his willingness to collaborate in this task.

There are many other people I would like to thank for all the support I have received during the last years. I would like to express my special thanks also in my native languages and more.

Primero quisiera agradecer a mis compañer@s de despachos y a los componentes del departamento de Física de la Tierra, Astronomía y Astrofísica I en general la buena acogida y la amabilidad con la que me habéis tratado. Merecen una especial mención aquellos que se han atrevido a subir en mi montaña rusa: Bea S.-C., Diana, Gonzalo, Javi, Jon Ander, María, Mariano, Marina, Marta C., Marta R., Sara y Sergio. El compartir las experiencias con vosotros da un valor añadido a este periodo. Gracias por los consejos y la "terapia". Pero sobre todo gracias por vuestra incondicional disposición siempre a echar una mano en lo que sea.

En este sentido también quisiera agradecer a los miembros del "UAH Space Weather team" Antonio, Consuelo, Elena, Judith y Yolanda su apoyo y el buen ambiente de trabajo que generan, el cual es de lo más motivador. Tampoco me puedo olvidar de los arqueólogos Marisa y Emilio. Trabajar con todos vosotros ha sido como un soplo de aire fresco.

Por otro lado también tengo que agradecer a aquellos que nos facilitan tanto nuestro trabajo. Gracias a Salva y Lucia por facilitarnos muchísimo las cuestiones técnicas y burocráticas y a la colaboración prestada por el departamento FTAA I. El tiempo que nos dais vosotros es tiempo invertido en este trabajo. También me gustaría extender este agradecimiento a Stanka del ICTP, por su labor.

Additionally I would like to thank all the people that made my stays far from home much more pleasant than expected, especially for their endless kindness in and out of work, especially to Anton, Claudia, Ermanno, Katy and Yenca. Ewa, bez Ciebie bym stracił istotę Polsce. Dziękuję. Sandra, grazie per avermi accolto a casa tua come una figlia.

Antes de acabar no me puedo olvidar de la gente más cercana, aquí y allá incluyendo a l@s compañer@s del equipo de Futbol Sala de la facultad, "mi escape", gracias por tan buenos ratos. A todos los que os habéis montado en algún vagón de esta atracción que ha recorrido los últimos años. A mis pipiolas: Ana, Bea S., Cris, Natalí y Vivy sea donde sea volveremos a encontrarnos; Etorreri, Joneri eta Estiri, urte askotarako! A Juan y Luca, todo queda en familia. A Amalia, Araceli, Berto, Carlos, Charlie, Diana, Daniela, Domingo, Edgar, Emilio, Esther, George, Ginevra, Guillermo, Irene, Javi, Jenn, Jenny, Jorge B., Jorgito, José A. C., Laura (pitu), Loren, Marco B., Marco D., Markus, Pablo, Ricardo, Rober, Rodri, Santos, Silvia, Viole, Zule y más. Vuestra compañía durante estos años en una gran diversidad de contextos ha mejorado notablemente la experiencia, siempre es un placer y una alegría teneros cerca. Gracias por acogerme tan bien. Eta eskerrik asko, batez be, kuadriliri (izenik ez da bihar), zenbat gauze bizi izan doguz bidai hau hasi orduko, eta zenbat horrenbeste galdu dodazen bidai hau hasi zanetik. Zeuekaz egotie etxien egotie da. Lan honek eroan dauen denbora, batez be, zeuori kendute dau eta horregaitik, tesis honen zatitxu bat be zeuona da. Asko gutzutie.

Azkanik, etxekueri. Quisiera expresar mi más sincero aprecio y cariño a mi familia quienes, por la educación que me han dado y el apoyo siempre incondicional a todas las decisiones académicas como laborales que he tomado, sin duda, esta tesis les pertenece. A los Rodríguez y a los Bilbao. Eskerrik asko bene-benetan. Maite zaitsutie, os quiero.

Bidean nabil emen eta an. -
Bidean beti: goizean, illuntze, gauan. -
Bidean, matan ta oian, jolas ta arrantzan. -
Gorputza geldi, pakean, ta barrua egaz. -
Ezin geratu. -
Aurrera orduk narama. -
Nai ta naiez bidetan. -
Beti bidean. -
Texiki nintzan antziñan. -
Gaztea ere bai. -
Eldu orain. -
Laburrean zugaitz zimela. -
Bidean. -
Lurrik ez naukan iñoiz aurrean. -
Gorputza lotan. -
Barrena ames bidean. -
(Pedro de Anasagasti, 1980) -

Amari, aitari eta Edurneri

Beti... noiz akabako... noiz akabako... -
eta hasi orduko joan zinelako... -

zeuri
amumari
Goian bego

Izarra -

Table of contents

List of tables

List of figures

Acronyms

AGW	Atmospheric Gravity Wave
AR	Active Region
AS	Anti-Spoofing
AU	Arbitrary Units
C/A	Coarse Acquisition
CEJ	Counter Electrojet
CELIAS	Charge ELement, and Isotope Analysis System
CH	Coronal Hole
CIR	Co-rotating Interaction Region
CMC	Code Minus Carrier
CME	Coronal Mass Ejection
CODE	Center for Orbit Determination
CS	Cycle Slip
CSRS-PPP	Canadian Spatial Reference System-Precise Point Positioning
DCB	Differential Code Bias
DD	Disturbance Dynamo
DGPS	Differential Global Positioning System
DoY	Day of Year
DOP	Dilution Of Precision
EEJ	Equatorial Electrojet
EIA	Equatorial Ionospheric Anomaly
EPB	Equatorial Plasma Bubble
EUV	Extreme Ultra Violet
GF	Geometry-Free
GLONASS	Global'naya Navigatsionnaya Sputnikovaya Sistem
GMF	Global Mapping Function
GNSS	Global Navigation Satellite System
GPS	Global Positioning System

GPT	Global model of Pressure and Temperature
GSWM	Global Scale Wave Model
GW	Gravity Waves
HSA	High Solar Activity
HDOP	Horizontal Dilution Of Precision
IERS	International Earth Rotation Service
IEF	Interplanetary Electric Field
IF	Ionosphere-free
IFB	Inter-Frequency Bias
IGRF	International Geomagnetic Reference Field
IGS	International GNSS Service
IMF	Interplanetary Magnetic Field
IPP	Ionospheric Piercing Point
ISB	Inter-System Bias
ITRF	International Terrestrial Reference Frame
IQR	Inter Quartile Range
LoL	Loss of Lock
LoS	Line-of-sight
LSA	Low Solar Activity
LT	Local Time
LSTID	Large-Scale Travelling Ionospheric Disturbance
MAP3	Multi-frequency Algorithm for PPP
MSTID	Medium-Scale Travelling Ionospheric Disturbance
NL	Narrow-Lane
NRCan	Natural Resources Canada
PCO	Phase Centre Offset
PCV	Phase Centre Variation
PRE	Pre-reversal Enhancement
PRN	Pseudo Random Noise
PPEF	Prompt Penetration Electric Fields
PPP	Precise Point Positioning

PPS	Precise Positioning Service
PZ	Parametry Zemli
RHCP	Right-Hand Circularly polarized
RMS	Root Mean Square
RTI	Rayleigh-Taylor Instability
RINEX	Receiver Independent EXchange format
ROT	Rate of change of Total electron content
SC	Solar Cycle
SAMA	South Atlantic Magnetic Anomaly
SEM	Solar EUV Monitor
SID	Sudden Ionospheric Disturbance
SINEX	Solution Independent Exchange format
SITEC	Sudden Increase in Total Electron Content
SNR	Signal to Noise Ratio
SOHO	Solar and Heliospheric Observatory
SPS	Standard Positioning Service
SRB	Solar Radio Burst
STD	Standard Deviation
SSW	Sudden Stratospheric Warming
SWHA	Summer Winter Hemispheric Asymmetry
SZA	Solar Zenith Angle
TEC	Total Electron Content
TECU	Total Electron Content Unit
TID	Travelling Ionospheric Disturbance
US	United States
USSR	Union of Soviet Socialist Republics
UT	Universal Time
UTC	Coordinate Universal Time
UV	Ultra Violet
VDOP	Vertical Dilution Of Precision
vTEC	Vertica Total Electron Content

WDC	World Data Center
WGS	World Geodetic System
WL	Wide-Lane

Chapter 1.
Introduction

1.1. Thesis Background and Motivation

Ionospheric physics started as a discipline that arose from the desire to understand the origin of the ionized upper atmosphere and its effects on radio wave propagation. From the 90's up to now ionospheric research has greatly benefited from the Global Navigation Satellite System (GNSS), especially, in the last decade with the establishment of large number of GNSS station networks, for purposes other than ionospheric research itself. This gave rise to a wide variety of fields of study some of them related to basic physics research and others dealing with both well-established and possible applications. In fact, the ionosphere under certain conditions, still is a limitation for high accuracy positioning.

In this Thesis we will focus on Precise Point Positioning, or PPP, which is a technique that was designed for precise absolute positioning, based on single receiver un-differenced code and carrier phase GNSS observations [Zumberge et al., 1997]. This technique was proposed as an alternative to the existing differential (relative) positioning (DGPS) techniques, which were the ones providing the accuracies required for land and hydrographic surveying: centimeter-level in kinematic mode and millimeter-level in static.

Contrary to the conventional relative method, PPP does not need a reference station, and simplifies operational complexities, such as, equipment costs and logistics.

Nowadays, PPP can be performed with single or dual frequency observables, in static or kinematic mode and in real time or post-processing providing different levels of accuracy. In all these cases the quality of the PPP solution highly depends on the accuracy of satellite orbits and clock corrections. The International GNSS Service (IGS) provides these data as products with a wide variety of accuracies and latencies [Dow et al., 2009]. The most accurate PPP results are obtained when satellites orbits and clocks precise final products are used, due to both the high accuracy and the higher sampling rate of those products. The problems that may arise from the latency in the acquirement of precise products, especially for real time applications, have been overcome in recent years with the establishment of the IGS Real-time Service [Caissy et al., 2012].

After the application of precise satellites clock and orbit products the ionosphere is the dominant error source. One of the main difference between single-

and dual-frequency PPP is the way ionospheric errors are handled: by including an ionospheric model corrections in single-frequency PPP or by observables linear combination in dual-frequency PPP. Since single-frequency PPP and real time kinematic are not under the scope of this thesis, they will not be discussed in this work and the interested reader is referred to Grinter and Roberts, [2011, 2013]. On the other hand, in the case of study, dual-frequency PPP, the ionosphere-free (IF) observables linear combination removes the first order term in the series expansion of the refractive index of the ionosphere. With the joint use of precise satellite orbits and clocks final products and the modelling of most of the rest of systematic errors affecting the GPS range, centimeter- to decimeter-level accuracy is reached depending on the processing mode used, static or kinematic [Kouba and Heroux, 2001; Bisnath and Gao, 2009].

Although post-processed PPP offers accuracies the most comparable to DGPS, PPP solution still provides slightly less accurate results than the differential positioning [Ebner and Featherstone, 2008; Grinter and Janssen, 2012]. This difference is mainly attributable to the non-integer character of the carrier-phase ambiguities in the standard PPP technique (using IF combination) since the receiver- and satellite- electronic delays are absorbed by the ambiguities and thus the latter ones cannot be considered integers anymore (they are biased). These uncalibrated phase electronic biases originated in receivers and in the satellites, are cancelled in DGPS by double differencing instead. Based on that idea, PPP ambiguities can nowadays be resolved through a differential approach by means of a regional permanent receivers' network analysis. Several works have confirmed that resolving the integer cycle ambiguity in the carrier-phase data can significantly improve positioning accuracy especially in the East-West direction [Ge et al., 2008] and with short time observations [Collins et al., 2008; Geng et al., 2009]. A better performance can be reached in places where denser networks are available, [Geng et al., 2010] even for stations far from the network [Geng et al., 2009].

Another limitation of PPP is the initialization period, since achieving the centimeter to decimeter position accuracy typically requires tens of minutes for the ambiguity to converge to the "true" value. In normal conditions, solving or determining the ambiguities takes around 30 min and depends on many parameters: method used, quality of observations, user environment and dynamics, satellites geometry, availability of redundant observations or even data sampling rate [Bisnath and Gao, 2009]. Recently, it has been observed that combined GNSS constellations may be used to reduce this convergence time and improve the accuracy [Cai et al., 2015; Li et al., 2015]. However, the key procedure for getting convergence time reduction and centimeter-level PPP in less time is again the ambiguity resolution [Ge et al., 2008; Geng et al., 2009] also in real time applications [Mervart et al., 2008]. Other methods developed to reduce the convergence time (also for near real time applications) include those that introduce

corrections based on (regional or not) receivers network solution [Zhang et al., 2013; Shi et al., 2014].

Due to the conventional initialization times required in PPP prior to achieve the final accuracy, the performance of this positioning technique is extremely vulnerable to cycle slips (CSs) and signal tracking interruptions. This occurs because they lead to biased ambiguity solutions resulting in time periods of tens of minutes to the position to re-converge to the centimeter/decimeter accuracy.

All in all, PPP offers a high accuracy positioning performance and although early PPP applications focused on geodesy and land survey science (static mode applications) [Calais et al., 2006; Ebner and Featherstorm, 2008, Rajner and Liwosz, 2011], there are many kinematic mode applications of this technique both scientific [Rocken et al., 2005] and commercial [Dixon, 2006].

As mentioned, after solving the satellites orbits and clocks related errors, the ionosphere is the source of largest errors. The first-order ionospheric group delay (phase advance) ranges from 1 to 50 m depending on satellite elevation, local time related ionospheric conditions, season and solar cycle, inter alia. Second order term not only depends on the magnitude of the parameters involved such as the electron density or the geomagnetic field and their variabilities, but also on the signal propagation mode (ordinary or extraordinary) with respect to the magnetic field vector [Moore and Morton, 2011]. The remaining errors due to higher order ionospheric terms are in the submillimeter- to several centimeters-level [Petit and Luzum, 2010]. Standard dual-frequency PPP algorithms construct the IF mathematical model above mentioned to correct the 99.99% of the delay produced by the ionosphere. However, although first order effect is mitigated, the second and third-order terms in the refractive index formula and errors due to signal bending including the TEC difference along different paths still remain uncorrected [Hoque and Jakowski, 2008; Kashcheyev et al., 2012; Petrie et al., 2011]. Moore and Morton [2011] show that a mis-interpretation of the propagation mode may lead to errors in the second order ionospheric effects corrections. If millimeter-level accuracy is wanted to achieve, this higher ionospheric effect should be corrected (at least the second order effect) since they may introduce errors with diurnal and seasonal variability [Kedar et al., 2003] that can lead to some mis-interpretations of the positioning results. Nevertheless, this accuracy is still far to reach if ambiguity resolution is not performed.

As long as no ionospheric perturbation occurs, PPP will perform with the accuracies mentioned. However, as noted by Moreno et al., [2011], and more recently by Pi et al., [2013] or Jacobsen and Dähnn [2014], PPP accuracy may be much more strongly degraded under perturbed ionospheric conditions, producing errors that reach several meters.

In this case, position accuracy depends on the receiver ability to deal with the presence of scintillation, which may cause CSs, loss of lock (LoL) or a complete loss of signal tracking [Skone et al., 2001], which affect CS detection algorithms [Banville et al., 2010]. Additionally, signal loss constitutes a serious threat for positioning softwares since it takes some minutes to the re-estimated ambiguities to converge. In this context, a big effort is being accomplished to improve the robustness of GPS receivers to deal with signals affected by scintillation [Aquino et al., 2009]. On the other hand, a more recent publication [Carrano et al., 2013] suggests that diffraction effects that may arise due to signal scintillation may not be cancelled in the IF combination, inducing additional errors.

Considering all the information above, it seemed necessary to start a work in which ionospheric irregularities effect on PPP accuracy is analyzed, to evaluate how severe and pervasive it is and to analyze the errors sources and phenomena involved. Keeping in mind, this goal, in this thesis, a general analysis of the mid- and low-latitudes ionospheric irregularities occurrence and its effect on kinematic PPP is studied.

1.2. Thesis Objectives and contributions

The overall objectives of this Ph.D. study were twofold:

1) To analyze the effects of fast variations of ionospheric Total Electron Content (TEC) on position by means of the rate of change of TEC (ROT) parameter.
2) To identify the cause of the errors and to investigate the characteristics of the physical phenomena involved.

In concrete, special attention has been paid to low- and mid-latitudes, considering in the first region the existence of equatorial plasma bubbles, and in both zones the solar and magnetic activity of the period of analysis. The general analysis of the ionospheric irregularities by means of ROT has permitted to provide an overview of the occurrence of various kinds of irregularities affecting GNSS signals.

On the other hand, regarding positioning, this work analyzes the CSRS-PPP online service's results offered by the Natural Resources of Canada (NRCan) to test the PPP software performance under ionospheric perturbed condition. The kind of irregularities affecting PPP and inducing decimeter-level or larger errors are identified and the reason for PPP accuracy degradation is recognized. Kinematic PPP errors increase; (1) when satellites signal is lost and the number of satellites used in positioning decreases and dilution of precision increases; (2) when ambiguities re-estimation occur in short arcs or after a misdetection.

In literature, ionospheric studies focus on the climatology of the ionospheric irregularities occurrence, while more technical works related to positioning focus on how to solve certain PPP limitations related to the GNSS signal. However, none of them provides an overview of the various kinds of ionospheric irregularities affecting PPP precision, and this is what is presented in this work.

1.3. Thesis Outline

The current manuscript is structured as follows:

Chapter 1 introduces the reader to PPP, and presents the motivation and structure of this Thesis.

Chapter 2 provides an introduction to the ionosphere focusing mainly on the low- and mid-latitude phenomena involved in the irregularities formation and their occurrence variability. It also introduces the ionospheric and ionospheric irregularities effect on GNSS signal propagation.

Chapter 3 gives a brief description of the GPS data and the methodology used to detect ionospheric disturbances and the strategy followed regarding positioning.

Chapter 4 provides the occurrence of the observed irregularities both in low- and mid-latitudes, by means of the rapid fluctuations of TEC.

Chapter 5 summarizes the phenomena observed in PPP in the presence of high ROT, analyzing both receiver tracking and CSRS-PPP performance. In this chapter, GLONASS influence is also evaluated.

Chapter 6 presents a case study related to the errors observed in PPP in presence of the Sudden Increase in the Total Electron Content that occurred on October 28th, 2003.

Results are summarized in Chapter 7 where some research perspectives are proposed.

Chapter 2.
The Earth's Ionosphere and its effects on GNSS signals

The Earth's ionosphere is the layer of the upper atmosphere that contains a significant number of free electrons and ions that lies at the interface between the atmosphere and space. As a whole it is considered an electrically neutral medium and at this altitude, the charged particles are a minority when compared to the number of neutral particles present there (from 10^8 times lower at 100 km of altitude to 100 times at around 1000 km). However, the neutral and charged particles inside this region constitute a partially ionized and magnetized plasma in which occur a variety of electrodynamic phenomena that depend on the atmosphere-ionosphere-magnetosphere system coupling processes resulting in a plasma density variability with altitude, latitude, longitude, time of the day, season, solar activity and geomagnetic activity dependencies.

The interest of the ionospheric structure, dynamics and variability lays especially on its applications in radio communications, being especially important its effects on GNSS signals and its impact on the performance of GNSS based technologies.

In particular, this work concerns about the effects that ionospheric plasma irregularities and ionospheric disturbances have on PPP, since the errors that the regular ionosphere's introduces in this positioning technique is considered corrected in a 99.99%.

This chapter provides an introduction to the ionosphere focusing mainly in the low- and mid- latitude phenomena involved in the irregularities formation and their occurrence variability. Firstly, Section 2.1 introduces the ionospheric structure. Next, Section 2.2 describes briefly the phenomena involved in the occurrence of the irregularities that are observed in this work. Section 2.3 introduces the space weather events of interest for this study. At last Section 2.4 explains the ionospheric and ionospheric irregularities effect on GNSS signal propagation.

For more details about the ionospheric structure and variability the interested reader is referred to Schunk and Nagy [2009], and for electrodynamics and instabilities at different altitudinal and latitudinal regions Kelley [2009] is suggested. Moreover, for a review of the latest progress achieved in the field of the Aeronomy in recent years Abdu et al., [2011] is recommended. Part of the following text has been based on these bibliographic references.

2.1. The ionospheric structure

The terrestrial ionosphere is the result of the dynamic equilibrium that exists between the electron (ion) production by neutral species ionization and loss by ion-electron recombination, while ion-molecule reactions also exist in the whole process.

The ionosphere is mainly formed by the ionization of atmospheric gases such as N_2, O_2 and O by solar radiation emissions in the EUV (17-175 nm) and X-ray (0.1-17 nm) ranges of the spectrum. In addition, energetic particles precipitation presents another source of ionization especially in high-latitudes and in the vicinity of the *South Atlantic Magnetic Anomaly* or SAMA [Abdu et al., 2005]. The photoionization is by far the main production process in the ionosphere, and as a result, the electron density peak occurs during the day, although, during the night the ionosphere does not completely disappear because the recombination time between ions and electrons is comparable to the rate of rotation of the Earth.

Photons of different energies penetrate at different altitudes in the atmosphere so that they interact with diverse atomic and molecular species, whose density varies with height. On the other hand, the recombination rates of those species depend on the type of ion that exists in the plasma at that altitude but also on its interaction with the neutral gas, resulting in a recombination that decreases with height. Despite the fact that different processes dominate in different latitudinal regions, the combination of the ionization and recombination rates creates a horizontally stratified region which is formed by different levels, each of which (except the lower one) is characterized by a local maximum in the ion and electron density (Ne) at certain altitudes. In general, we can distinguish four main regions referred as D, E, F_1 and F_2 (shown in Figure 2.1), although additional layers such as sporadic Es and F_3 [Balan et al., 1997; Paznukhov et al., 2007; Klimenko and Klimenko, 2011; Zhu et al., 2013] may appear.

The D-region is the closest ionospheric layer to the Earth's surface and extends approximately from 50 km to 90 km in height. This region is controlled by chemical processes being molecular ions and neutrals the dominant species at these altitudes. Hard X-rays (0.2-0.8 nm) are the main source of ionization at this altitude and predominantly ionize N_2 and O_2 molecules. In addition, Lyman-α radiation (121.6 nm) or the EUV radiation (102.7-111.8 nm) also ionize several minor constituents that play a crucial role in this region chemistry. In this region, the neutral density and hence, recombination are high, and although cosmic rays produce a residual ionization during the night, practically this layer only appears in daytime. It is worth mentioning that, at high-latitudes, ionization by solar or auroral energetic particles cannot be ignored.

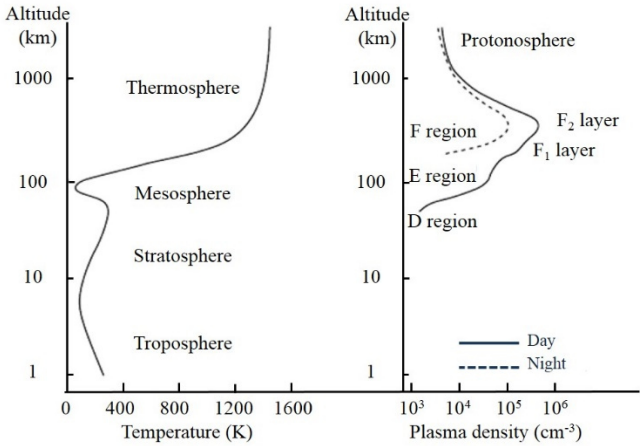

Figure 2.1 Typical profiles of neutral atmospheric temperature and ionospheric plasma density. (Adapted from Kelley, [2009]).

The region in the 90 to 120 km interval is the E-layer (originally called the Heaviside or Kennelly-Heaviside layer). The source of energy responsible for this layer existence comes from X-rays (1-10 nm) and EUV radiation. The peak electron density of this layer is 100 times larger than the D layers' because recombination is not so intense at this height. This region also vanishes during the night although at high-latitudes energetic particles precipitation also ionize this layer, especially at night.

The densest region in the ionosphere is the F-layer, which extends from an altitude of 120 km up to the plasmasphere (which is at around 1000 km). The maximum value in the density of the ionosphere, referred as the peak plasma density, is at around 300 km of altitude and reaches values as high as 10^{12} m^{-3} near noon time. The ionospheric density decreases in the *topside* of the ionosphere (the region that goes from the peak value to the plasmasphere). It is formed mainly due to the ionization of atomic O by EUV radiation but the recombination rate at these altitudes is lower than in D- and E-regions and it doesn't disappear completely at night. This region is usually divided into two sub-regions: F_1 and F_2. The F_1-layer, the lowest one, is dominated by the photoionization process of atomic O to get O^+ and losses by reaction with N_2 and O_2 species. On the other hand, in the F_2-layer region there is a transition in the processes that are important, from chemical to diffusion, and this last one dominates the topside ionosphere.

2.2. The ionospheric variability

2.2.1. The role of the magnetic field

The plasma transport processes in the ionosphere are affected by the Earth's magnetic field that results from the combination of the magnetic fields of internal and external origin. The first ones are the ones originated in the Earth's core, plus the contribution of local fields produced in the Earth's crust, while the later are caused in the ionosphere and magnetosphere as a result of the Earth-Sun interaction.

The main magnetic field (~3-6·10^4 nT at the Earth's surface), represents most of the Earth magnetic field intensity and for altitudes between the Earth's surface and the ionosphere it can be approximated by a tilted geocentric dipole; while, for higher altitudes (distances greater than a few Earth radii), the interaction of the dipolar magnetic field with the solar wind transporting the interplanetary magnetic field (IMF, ~6 nT at 1 AU), which is the source of the magnetosphere, must be considered. The main magnetic field suffers from a long term non periodic variation, called *secular variation*, which result in a displacement of the magnetic poles with respect the geographic ones. Additionally, ionospheric currents cause a diurnal variation that depend on the latitude considered that varies from tens of nT to few hundred in the equator, while alterations in the solar wind composition due to a variety of solar events may result in magnetic field variations of some hours duration (such as, geomagnetic storms) that may reach hundreds of nT.

Geomagnetic storms are global disturbances of the magnetic field caused by the solar wind energy transfer from the interplanetary magnetic field (IMF) to the northward Earth's magnetic field by reconnection in the daytime magnetopause [Gonzalez et al., 1994]. This reconnection occurs when the IMF reaching to the Earth has a component directed to the South. Geomagnetic storms produce a decrease in the horizontal component of the magnetic field (caused mainly by the enhancement of the *ring current*) which is called the *main phase* of the storm and which is followed by a *recovery phase* in which the values return to the ones of quiet times. Based on that the broadly used Disturbance storm-time (Dst) index is defined for geomagnetic storms classification, in which the main phase of the storm is characterized by a large decrease of this parameter. This is the index that will be used in this work to define the days occurring geomagnetic storms. In this interaction process, energy and momentum is also transferred to the high-latitude ionosphere mainly via particle precipitation and electromagnetic energy input that may affect globally the dynamics of the ionosphere which in "normal" conditions is ruled by the thermospheric wind system and the generated electric fields that will be introduced in Section 2.2.2. The global disturbance arising from geomagnetic storms may occur covering a broad range of time scales (from minutes to few days).

The ones related to immediate changes in the IMF cause the so called *prompt penetration of electric fields* (PPEF) which are "short" duration perturbations (few hours) that may affect the low-latitude ionosphere [Nishida et al., 1966] producing plasma drift perturbations, and, in last instance changes in the local ionization density. The long lasting perturbation, the so called *disturbance dynamo* (DD) [Blanc and Richmond, 1980], appears on 1 h delay and is are driven by the enhanced energy deposition into the high-latitude ionosphere, that leads to thermospheric winds pattern variation which also affect the ionospheric plasma transport from mid- to low-latitudes and lead to variations in the ionization density. The PPEFs occur simultaneously at all longitudes, but with different amplitudes, whereas the equatorial DD effects may last up to 30 h after large storm-time energy deposition into the high-latitude ionosphere mostly due to *joule heating*. More effects related to geomagnetic storms will be introduced in sections 2.2.5 and 2.3.2.

In the text we will refer as geomagnetic field to the dipolar modeled field, which help us to figure out the main characteristics of the Earth's magnetic field, although we know that the actual magnetic field is more complex and important differences with the dipolar approximation exist. The no-antipodal nature of the geomagnetic poles and the presence of the SAMA are examples of these discrepancies. This last phenomenon deserves a comment because of its proximity to some of the low-latitude IGS stations that will be used in our work. The SAMA is a low magnetic field region located over Brazil and the South Atlantic Ocean where, due to the asymmetry between the magnetic and rotation axes, the Van Allen radiation belts are the closest to the surface of the Earth. Because of its close relationship with the Earth's magnetic field, the location, shape, and intensity of the SAMA change over the time [Hartmann and Pacca, 2009]. Navigation systems may be affected by SAMA related phenomena as it was the positioning problem associated to the anomalous behavior of DORIS instrument nº2 onboard Jason-1 satellite [Willis et al., 2004; Lemoine and Capdeville, 2006]. However, by the time of finishing this thesis manuscript, no report showing similar effects on GNSS have been found. With respect to the effects that SAMA has on the ionosphere, they are commented in Section 2.2.4.

According to the geomagnetic latitude the ionosphere is traditionally divided into three regions that have different characteristics: low-, mid- and high-latitude. The low-latitude is the region extending from the magnetic equator to around 25º both North and South sides. The main characteristic of this zone is that it is strongly influenced by the electromagnetic forces arising as a result of the horizontal magnetic field over the magnetic equator. On the other hand, high-latitudes correspond to regions where magnetic field is nearly vertical to the Earth's surface, connecting the lower atmosphere to the outer part of the magnetosphere and leading to phenomena that largely depend on the solar wind. It is situated at around 60º magnetic latitude and higher including both auroral ovals and polar caps regions.

The mid-latitude corresponds to the region between low- and high-latitudes. Although it is the "less" variable zone, its boundaries are not static, and geomagnetic perturbations may produce the expansion of low- and high-latitudes ionospheric phenomena influence.

As mentioned above, high-latitudes studies are not under the scope of this work and the processes that affect the ionosphere outside mid- and low-latitudes may be commented but will not be explained in the following sections.

2.2.2. The ionospheric dynamo

The low- and mid- latitude ionosphere is governed by the electric fields, the plasma drift and the currents that are generated by the E- and F-region neutral wind driven dynamos. The morphology of the low-latitude ionosphere is quite different from that at other latitudes because the magnetic field, $\vec{B}$, is nearly parallel to the Earth's surface. As a result it shows some of the most complex phenomena of the upper atmosphere, which is affected by a number of local driving processes that lead to local time, seasonal, longitudinal and day to day variabilities.

The ionosphere is embedded in the thermosphere (Figure 2.1), thus, the interaction between the ionospheric plasma and neutral air taking place at certain altitudes in the upper atmosphere has a strong influence on both constituents producing a wide variety of electrodynamic phenomena. The ions, electrons and neutral species can be considered as three interpenetrating fluids coupled by collisions and self-generated electric and magnetic fields. At lower altitudes the collisional force plays a crucial role while over a certain altitude diffusion becomes important.

The various forces acting on plasma drive electric currents that create the electric fields that modify the plasma dynamics. These are called the *dynamo electric fields*. The energy comes primarily from the kinetic energy of thermospheric winds and from the coupling processes with the magnetospheric plasma. At mid- and low-latitudes these electric fields are generated primarily by the neutral wind field.

The action of this ionospheric (wind) dynamo is frequently separated in E- and F-region dynamos because the neutral wind structure and the electrical, chemical, and transport characteristics differs substantially between these two regions.

The E-region dynamo is driven by the current and electric polarization fields that result from the tidal oscillations of the neutral winds in this region. Due to the high conductivity parallel to the magnetic field, magnetic field lines act as nearly equipotentials resulting in a coupling between hemispheres and between the E- and F-regions. Consequently, the dynamo electric fields that are generated in the E-

region by thermospheric winds are transmitted along the magnetic field lines to F-region altitudes [Risbeth, 1997; Heelis, 2004].

As a result of the ionospheric wind dynamo, there are two important characteristics to consider in low-latitudes since they affect to the plasma distribution and the irregularities occurrence there: the *equatorial electrojet* (EEJ) and the F region $\vec{E} \times \vec{B}$ vertical plasma drift.

The EEJ is a current confined to a narrow latitudinal ($\pm 3^{o}$ N with respect to the magnetic equator) and altitudinal (100-110 km) band, that can reach peak values of 10^{-5} Am^{-2} that in normal condition flows towards East in daytime and towards West in nighttime. Nevertheless, high-latitudes *sudden stratospheric warmings* (SSW) related changes in tidal amplitudes [Sridharan et al., 2009] or the PPEFs from high- to low-latitudes during geomagnetic storms [Kikuchi et al., 2003; Veenadhari et al., 2010] have been reported to produce the reversal of the EEJ, called *counter electrojet* (CEJ).

As mentioned, the wind dynamo electric fields of the E-region are mapped into the F-region via (almost-equipotential) magnetic field lines. The $\vec{E} \times \vec{B}$ plasma drift velocities induced in the equatorial F-region by these electric fields can be clearly differentiated in two components the zonal (East-West) and the vertical (Up-Down), both perpendicular to the magnetic field lines, which except for near sunrise and sunset periods, vary very little with altitude [Fejer et al., 2014]. Fejer et al., [2005] show that over Jicamarca, in the F-region and above, the zonal $\vec{E} \times \vec{B}$ plasma drift is westward during the day, with typical values of 40 ms^{-1}, and eastward during the night, with values that may exceed 100-150 ms^{-1}, depending on solar activity conditions. The authors additionally note that enhanced geomagnetic activity drives perturbations of zonal drifts that depend on season. On the other hand, the F-region vertical $\vec{E} \times \vec{B}$ plasma drift is upward during the day and downward at night. It has a typical magnitude that varies in the range of 10-30 ms^{-1} although suffers from diurnal, seasonal, solar cycle (SC) and longitudinal dependencies [Scherliess and Fejer, 1999]. It can also vary with geomagnetic activity since disturbance electric fields may appear in the equatorial region during geomagnetically perturbed periods as a result of the mentioned PPEFs from high- to low-latitudes [Sastri, 2002; Huang et al., 2007] or of the DD action of storm-generated neutral winds [Blanc and Richmond, 1980; Maruyama et al., 2005]. Fejer et al., [2008] show that (in average) the vertical drift related to the PPEF are mostly upward during the day and downward during the night, at any season, reaching peak values during June solstice. On the other hand these authors show that DD drift has small daytime values, downward near sunset (increasing with solar flux) and has largest magnitude during equinox and smallest during June solstice. Nighttime DD drift is upward, does not change much with solar flux, and peaks near sunrise, especially during December solstice. Evening downward (nighttime

upward) drifts are largest in the East (West) Hemisphere. Additionally, SSW may also perturb equatorial-region drifts, and in this case the effects may last for several days [Fejer et al., 2011].

In addition to the typical diurnal variation of daytime upward and nighttime downward F-region vertical drifts, equatorial latitude ionosphere is also characterized by a brief pre-reversal strengthening of the vertical drift after local sunset, which is thought to be responsible of the occurrence of the equatorial post-sunset plasma irregularities. This phenomenon is caused by the *pre-reversal enhancement* (PRE) of the eastward electric field that occurs in the early evening, just before it reverses to westward. The PRE is generally attributed to the F-region dynamo intensification [Fesen et al., 2000], caused by polarization electric fields that appear due to the combination of increased eastward winds and sharp day night E-region conductivity gradients across the terminator. However, the mechanism is not completely understood yet [see Eccles, 1998; Kelley et al., 2009; Eccles et al., 2015 and the references there in].

The vertical plasma drift has a pronounced effect on the low-latitude ionosphere since it is involved in the processes that generate the equatorial ionization anomaly while the evening vertical drift also plays a fundamental role in the occurrence of equatorial postsunset plasma irregularities [Fejer et al., 1999]. Recently, equatorial plasma irregularities occurrence related to upward drifts (eastward electric field), occurring before sunrise have been also reported [Kelley et al., 2014].

2.2.3. The equatorial ionospheric anomaly

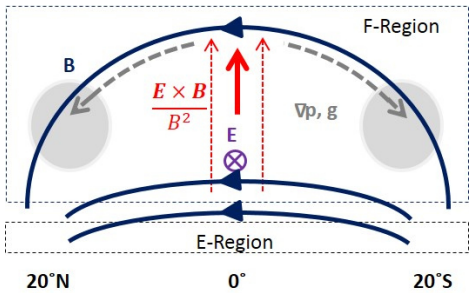

Figure 2.2 Diagram describing the development of the EIA.

In daytime, the plasma that is lifted due to the F-region $\vec{E} \times \vec{B}$ vertical drift to altitudes above 600 km over the magnetic equator diffuses down the magnetic field lines away from the equator due to the action of gravity and pressure gradients. This

combination of electromagnetic drift and diffusion produces a fountain-like pattern of plasma motion called the *equatorial fountain* (see Figure 2.2). Consequently, two ionization peaks develop on both sides of the magnetic equator at around 15º-20º. This feature is termed the *equatorial ionospheric anomaly* (EIA) or the *Appleton anomaly* [Schunk and Nagy, 2009].

The EIA is one of the most important features in the daytime to evening sectors of the Earth's ionosphere and presents a variability that depend on latitude, longitude, season, solar activity and local time [Lin et al., 2007].

It develops soon after sunrise (by ~09:00 LT) and presents a maximum in intensity at around 16:00 LT. Then, it decays towards sunset and at that time resurges often with intensity higher than in daytime due to the PRE induced increase in vertical drift. This effect is more accentuated during high solar activity (HSA). In nighttime its intensity goes down until sunrise. EIA crests density is smaller during low solar activity (LSA) than in HSA periods due to the low background ionization density that results from lower solar radiation intensity. It is worth mentioning that in daytime the solar activity dependence is stronger in the crests regions than in the trough zone due to the influence of the combined fountain effect and the enhanced photoionization which increase in higher solar activity periods. In addition, in post-sunset time the strengthening of the fountain process together with the lack of photoionization leads to an even larger difference in the crests and through densities between different solar activity periods [Liu et al., 2007]. The solar activity dependence is stronger in equinoxes than in solstices, and in December solstice than in June solstice because, the $\vec{E} \times \vec{B}$ vertical drift also shows larger values in the equinoxes and the smallest near the June solstice [Whalen, 2004].

With regards to the local time, it shows remarkably larger dependence after sunset than at noon due to the intensification of the fountain effect. The electron density in the two peaks is asymmetric as a result of a meridional neutral wind that transport the plasma (due to collisions along the magnetic field lines) from the summer hemisphere to the winter hemisphere. This plasma movement results in inter-hemispheric transport of ionization. In nighttime the $\vec{E} \times \vec{B}$ drift is downward, the height of the F-layer at the magnetic equator drops and the ionization peaks move closer to the equator (showing less asymmetry).

Additionally, EIA shows a *wavenumber-4 modulation* in the longitudinal variability that results from lower-atmospheric tidal forcing of the upper atmosphere [Immel et al., 2006; Forbes et al., 2008] probably because it also affects F-region $\vec{E} \times \vec{B}$ plasma drifts [Ren et al., 2009; Fejer et al., 2013]. The reinforcement of the background dynamo winds is concentrated in four peaks around the globe where the (non-migrating) tides are greatest and the dynamo

electric fields are enhanced resulting in the global-scale variation observed in the morphology of the EIA.

The EIA presents the most favorable conditions for the low-latitude F-region nighttime plasma irregularities formation which are introduced in the next section.

2.2.4. Equatorial plasma density irregularities

The low-latitude plasma irregularities characteristics observed depend on the technique used to detect them. For that reason many names have received, spread-F, plumes or total electron content depletions, depending on if they were detected by ionosondes, radar, airglow or GNSS based techniques respectively, being an observed common characteristic the depleted electron density of the structures with respect to the surrounding plasma.

The largest structures usually receive the name of *equatorial plasma bubbles* (EPBs). EPBs are magnetic field aligned westward tilted [Valladares et al., 2004; Kil et al., 2009] electron density depletions with typical dimensions of 100 km in the East-West direction and up to 1200 km in the North-South [Hargreaves, 1992]. These irregularities rise after sunset from beneath the *bottomside* (lowest) F-region along the magnetic field lines to altitudes as high as 1500 km above the magnetic equator [Sahai et al., 1994], and move eastward with drift velocities of the order of 140 m/s [Pimenta et al., 2003; Valladares et al., 2004]. On geomagnetically quite times their occurrence is constrained to nighttime with a maximum in the occurrence in pre-midnight hours, although post-midnight bubbles, which are not a continuation of the ones in the dusk sector, have also been observed [Burke et al., 2009].

The commonly accepted scenario for the formation of EPBs is the non-linear evolution of the generalized Rayleigh-Taylor instability (RTI) which includes: 1) the F-region plasma raising as a consequence of the PRE leading, due to the absence of sunlight, to steep density gradients in the *bottomside* that are unstable to density perturbations that may trigger the instability process; 2) a seeding mechanism that propitiates the commencement of the instabilities; 3) an instability growth process which is thought to be driven by the RTI mechanism [Sultan, 1996; Abdu, 2005].

With some approximations, the (flux-tube integrated) growth rate (γ) of the instability in a linear regime can be expressed by Eq. (2.1) [Sultan, 1996]:

$$\gamma = \frac{\Sigma_P^F}{\Sigma_P^E + \Sigma_P^F}\left(V_P - U_n^P - \frac{g_L}{\nu_{in}^{eff}}\right)\frac{1}{L_n} - R_T \qquad (2.1)$$

Here Σ_P^{EF} are the F- and E-region flux-tube integrated Pedersen conductivities that contribute to the entire Pedersen conductance Σ_P. V_P is the vertically upward component of plasma drift ($\vec{E} \times \vec{B} / B^2$) due to the zonal electric field at the magnetic equator. U_n^P is the vertically upward component of neutral wind velocity perpendicular to $\vec{B}$ (in the meridional plane) and weighted by Σ_P. g_L is the acceleration due to gravity at the magnetic equator on a field line designated by the McIlwain parameter (L) value. ν_{in}^{eff} is the effective flux tube integrated F-region ion-neutral collision frequency weighted by the electron density in the flux-tube. L_n is the scale length of the flux tube integrated plasma density vertical gradient in the F-region measured at the magnetic equator, and R_T, the electron density weighted recombination rate integrated along the flux-tube which may be neglected in the upper F-region but not for applications in the E- and lower F-regions.

For the instability to grow, this γ must be positive, and stay positive long enough for the EPB to grow. If the growth is strong, then the EPBs grow nonlinearly in the vertical direction, crossing the magnetic field lines as they grow. In general, nonlinear instability growth does not occur if the linear growth rate is negative. For typical conditions, the growth rate is low (of the order of 10^{-4} s^{-1}) which implies that some initial disturbance is needed to initialize the process or decreases the time needed to develop a large amplitude disturbance. This seeding mechanism [Singh et al., 1997; Tsunoda, 2006; Abdu et al., 2009], leads to the day to day variability observed in the occurrence of EPBs, in addition to the solar activity, seasonal/longitudinal and local time dependences observed in their climatology.

Depending on the apex height reached above the magnetic equator, bubbles can extend from magnetic equator along the magnetic field lines into the EIA crests. The density gradients in the intersection of the bubbles' walls with the increased background electron density may become unstable and set up secondary instability processes that create condition favorable for the generation of smaller scale plasma density irregularities [Muralikrishna, 2000; Abdu 2005; Muella et al., 2010]. A well-developed bubble structure is associated with an entire spectrum of plasma irregularities that may cause radio signal scintillation and impact transionospheric applications such as the ones based on GNSS [Basu et al., 1978].

The uplift of the F-region is essential for these irregularities generation and evolution [Fejer et al., 1999], and the PRE favors the irregularities formation [Abdu, 2001]. As a result, a clear correlation exists between the maximum PRE and irregularity occurrence periods [Li et al., 2007] with maximums in HSA years [Fejer et al., 1999; Whalen, 2004].

Post-sunset irregularities occurrence depends on season showing a variability which, in turn, varies with longitude (seasonal/longitudinal variability) [Burke et al., 2004; Gentile et al., 2006, 2011; Ren et al., 2009; Magdaleno et al., 2012]. The dependence has been explained by the magnetic field declination control of equatorial F-region dynamo electric field development [Abdu et al., 1981]. RTI is more likely to evolve at longitudes where zonal gradients of Σ_P near the dusk meridian are strongest. The steepest Σ_P^E gradients develop where magnetic flux-tubes closely align with the solar terminator (since both ends of the flux-tubes enter darkness at approximately the same time allowing most $\Sigma_P^E \to 0$ rapidly) [Tsunoda, 1985]. In this sense SAMA will contribute to the observed longitudinal variability in two ways: (1) by introducing a longitudinal variation of the magnetic field declination, and (2) by increasing the conductivity due to the enhanced ionization caused by particle precipitation (both in quiet and disturbed conditions) that result in conductivity longitudinal gradients [Abdu et al., 2005]. Additional longitudinal differences in the EPBs occurrence variability has been also attributed to wavenumber-4 structure of EIA and F-region vertical drifts [Li et al., 2008].

Furthermore, equatorial nighttime plasma irregularities occurrence also depends on magnetic activity [Fejer et al., 1989; Abdu et al., 2003]. The PPEF in the dusk sector may induce the generation of EPBs, also in post-midnight hours [Burke et al. 2009] or near dawn [Kim et al., 2015], whereas a DD effect may suppress early equatorial nighttime irregularities. However, the instability trigger that leads to irregularities development and day-to-day variability is not well established yet.

Contrary to post-sunset irregularities occurrence, which increases with solar activity and maximizes in epochs close to equinoxes, dawn sector depletions have also been observed but most frequently close to solstices in LSA periods. However although the RTI mechanism seem to be responsible of the development of the latter irregularities during quiet times, the seeding mechanism responsible of it is still unclear [Gentile et al., 2011; Yizengaw et al., 2013].

2.2.5. Mid-latitudes ionospheric irregularities' signatures

Mid-latitude ionosphere has been referred in the text as the "less" variable zone of the ionosphere. But this is not totally true since a wide variety of ionospheric structures are observed there even in quite times, and moreover, in perturbed conditions, it may suffer the most remarkable ionospheric perturbations observed in the globe.

The kind of irregularities with the most frequent occurrence are travelling ionospheric disturbances (TIDs) [Hernandez-Pajares et al., 2006]. These irregularities appear as wavelike patterns of plasma density that result from the neutral atmospheric gravity waves (AGW). A review in the topic can be found in Hocke and Schlegel, [1996].

TIDs have wavelengths that range from a few kilometers to more than thousand kilometers and are often classified into *medium-scale travelling ionospheric disturbances* (MSTIDs) and *large-scale travelling ionospheric disturbances* (LSTID) attending to their wavelength, velocity and period.

MSTIDs are characterized by wavelengths of several hundreds of kilometers (although they may reach up to 1000 km), periods between ~10-60 min and propagation velocities of 50-400 m/s [Hernández-Pajáres et al., 2006; Tsugawa et al., 2007a]. The occurrence of these irregularities is independent of geomagnetic activity, snd they may appear both in quiet and geomagnetic perturbed periods. MSTIDs may also occur both in daytime and nighttime. Daytime MSTIDs occur mainly in winter, and propagate equatorward [Hernández-Pajáres et al., 2006]. Tsugawa et al., [2007a] show that over North America, daytime MSTIDs propagate southeastward until mid-afternoon, southwestward in the late afternoon and that they superpose in mid-to late-afternoon. After analyzing a GPS dataset of 10 years over Belgium, Wautelet and Warnant, [2013] show that, MSTIDs occurring in winter-daytime can be considered typical MSTIDs, while the ones that occur in summer nighttime, are "non-classical" MSTIDs, due to their different characteristics and their noisier structure. The latter ones may also appear in winter although less frequently. The same authors have recently presented some results proposing the possible nature of the source of those MSTIDs [Wautelet and Warnant, 2015]. They claim that the irregularities occurring on autumn-winter daytime typical MSTIDs result from the interaction of AGWs with plasma, and they suggest that AGWs may have their main origin in the lower atmosphere rather than in solar terminator, although the later may act as a potential source. On the other hand, considering the irregularities occurring in summer nighttime, these authors clarify that only half of them exhibit the characteristic wave-like pattern of MSTIDs, while the remaining present a noisy pattern superimposed, which they attribute to the presence of small scale irregularities in the F-region (field aligned irregularities) that relate to Es layers.

On the other hand, LSTIDs present a different nature since they are related to geomagnetic disturbed conditions. They are characterized by larger wavelengths (more than 1000 km), periods and propagation velocities than MSTIDs. Analyzing LSTIDs induced by geomagnetic storms over Europe in the 2001-2007 time interval, Borries et al., [2008] found that they were characterized by a mean wavelength of 2000 km, a mean period of 59 min and a mean phase speed of 684 m/s. The differences with respect to the results shown by other authors [Tsugawa

et al., 2004] are attributed to the damping and differences in the geographic/geomagnetic relationship. LSTIDs occur due to joule heating enhancement that cause travelling atmospheric waves that propagate southward as thermospheric temperature enhancements and that are recognized as TIDs when ionospheric sounding techniques are used [Shiokawa et al., 2007]. Additionally, it has been observed that MSTIDs may present mirror images of waves in the conjugate hemispheres, while the LSTIDs occurring in both hemispheres simultaneously are independent among them [Shiokawa et al., 2005]. These results highlight the electrodynamic coupling existing between MSTIDs observed in two hemispheres. The origin of the perturbation is suggested to be a spatially oscillating east-west electric field which produce upward-downward motion of the F layer through $\vec{E} \times \vec{B}$ drift. Nevertheless, the source mechanism has not been totally explained yet.

More ionospheric perturbations depending on solar events are introduced in the following sections.

2.3. Disturbances of solar origin

We will focus now on the disturbances initiated in the Sun that may cause significant changes in the regular behavior of the ionosphere, and impact GNSS based technologies.

The sun has an approximate 22-year cycle (the Hale cycle), within which the polar magnetic fields reverse polarity approximately every 11 years in which the cycle experiences a maximum and a minimum number of sunspots (see Figure 2.3).

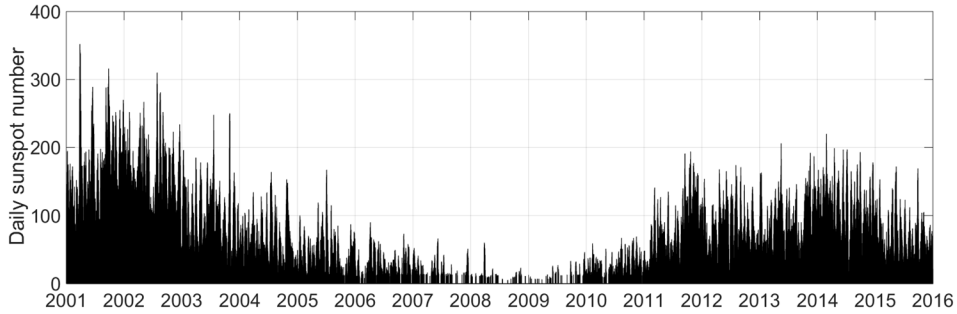

Figure 2.3 Daily value of the solar sunspot number (Rz). Data from omniweb: http://omniweb.gsfc.nasa.gov/

Sunspots are regions of the Sun's photosphere with colder temperature than the surrounding plasma, from which magnetic field lines come up from the Sun's interior. They may appear in groups which are called *Active Regions* (AR) and give rise to different kind of eruptive phenomena such as flares, energetic particles or *coronal mass ejections* (CME), which if Earth-directed, may have severe consequences on the ionosphere and on GNSS positioning.

2.3.1. Solar flares

Solar flares are sudden releases of solar irradiance from localized AR on the Sun that last for tens of minutes. Although the emitted radiation covers a wide spectrum of wavelengths (from radio waves to gamma rays), they are classified following a logarithmic scale according to the order of magnitude of the peak burst intensity measured at the Earth in the X-rays 0.1 to 0.8 nm wavelength band, in B, C, M and X classes (see Table 2.1) since the A class remain for typical background levels. Additionally, a multiplier is used to indicate the level within each class.

Table 2.1 Solar flares classification attending to the measured peak intensity in the 0.1-0.8 nm band.

Solar Flare Class	Peak Intensity (W/m^2)
B	$<10^{-6}$
C	$[10^{-6},10^{-5})$
M	$[10^{-6},10^{-5})$
X	10^{-4}

The greatest number of solar flares occurs during and near solar maximum, and although the frequency in the occurrence of flares diminish with the solar activity decrease, intense flares can occur during solar minimum.

Solar flares are especially effective in creating (short duration dayside) sudden ionospheric disturbances (SIDs) [Mitra, 1974]. Different kinds of radiation emanate from different parts of the flare and are released at different times of the flare process [Schwenn, 2006]. X-ray emissions penetrate to depths of 90-to 110- km altitude, and they are able to produce cascading of the ionization process. However, due to the high densities at these altitudes, recombination time scales are relatively short, approximately of tens of minutes. The EUV/UV radiation emitted by solar flares does not penetrate so much and causes effects that last longer due to the recombination time's scales of hours at hundreds of kilometers of altitude.

The SID relevant for GNSS users is the sudden increase in total electron content (SITEC). Which is produced by the atmospheric extra-ionization due to solar flare radiation emitted in X-ray and Extreme Ultra Violet (EUV). The sudden increase in EUV radiation (assumed to be coincident with the X-ray) during solar flares causes immediate enhancement of ion/electron density in the lower F-region and the E-region rather than around F_2. Since the F-region electron density is the main contributor to the total electron content (TEC), a SITEC is largely produced by the ionospheric F-region extra-ionization due to the EUV radiation emitted during a flare.

A particular characteristic of SITECs is that they are not constricted in latitude and may affect the entire dayside ionosphere. The magnitude of the event depends to a large extent on the flare's location on the sun, the emitted radiation flux and the solar zenith angle (SZA). In particular, the ionospheric TEC increases linearly with the cosine of SZA [Wan et al., 2005; Le et al., 2013] and decreases with increasing distance of the flare from the solar central meridian because the solar atmosphere absorbs the EUV flux [Liu et al., 2006; Qian et al., 2010; Le et al., 2013]. Additionally, SITECs show seasonal-hemispheric asymmetry (summer winter hemispheric asymmetry, SWHA) related to F-region neutral species densities [Tsugawa et al., 2006; 2007b].

On the other hand, during a solar flare the Sun not only releases the mentioned radiation but also intense radio burst including the frequencies that may affect GNSS. Solar Radio Burst (SRB) are radio emissions in frequency ranges between tens of MHz to few GHz, with a broad spectrum of characteristic associated with solar AR, flares or proton emissions among others [White, 2007]. SRBs may affect the signal to noise ratio (SNR) of the received GNSS signals by increasing the background noise inducing CSs and in last instance producing the signal LoL [Chen et al., 2005, Cerruti et al., 2006; Demianov et al., 2012; Sreeja et al., 2013]. For that reason they are a potential serious threat for GNSS based technologies, including precise positioning [Sreeja et al., 2014].

2.3.2. Geomagnetic and ionospheric storms

As mentioned in Section 2.2.1 geomagnetic storms are disturbances of the magnetic field caused by the enhancement of the ring current due to primarily the solar wind energy transfer from the IMF to the Earth's magnetic field by reconnection in the daytime magnetopause [Gonzalez et al., 1994].

The strongest geomagnetic storms occur when the IMF overpass the average IMF value (of the order of 5nT) and it is southwardly directed for a substantial period of time (around few hours) in order to have a strong duskward electric field for the energization of the magnetosphere-ionosphere system. The most intense storms occur in the presence of CMEs, Coronal Holes (CH) or Co-rotating

Interaction Regions (CIR). For a detailed description of the phenomena involved the reader is referred to Gonzalez et al., [2001].

Geomagnetic storms, apart from producing the effects mentioned in previous section, such as, LSTIDs or small scale irregularities, also can cause disturbances in the ionosphere called ionospheric storms, which can be considered to have positive phases when an increase of TEC is originated, or negative phases in the opposite case. A review regarding ionospheric storms can be found on BuonSanto [1999].

Both anomalous TEC increases and decreases can be observed although the magnitude of the event will depend on the strength of the magnetic activity. A frequent characteristic is a decrease in ionization density at higher latitudes and an increase at equatorial latitudes. While in mid-latitudes, the increase in TEC is primarily observed in winter or during periods of weaker magnetic activity, the decreased TEC is predominant during equinox and summer, especially during stronger magnetic storms. This is because of the equatorward winds carrying the composition disturbance zone has larger latitude penetration in summer than in winter. The most probable phenomena suggested to contribute to positive phases of storms in mid –latitudes are related to the phenomena producing an uplifting of the ionosphere. The first one is the equatorward directed wind, which produces ion drag along the magnetic field lines pushing the ionization up the inclined magnetic field lines. The second one is an electric field causing $\vec{E} \times \vec{B}$ drift. Auroral heating related changes in the thermospheric circulation contribute to the occurrence of positive phase of ionospheric storms by the downwelling of the neutral species and the uplifting of the F-layer due to neutral winds. On the other hand, the negative phases are related to changes in the composition of neutral gas. Due to the local time variation of winds and neutral composition changes at mid-latitudes, negative storms are frequent in the morning while positive storms are prone to occur in the afternoon and evening.

Geomagnetic disturbed conditions may also lead to additional phenomena such as the expansion of EIA to larger latitudes [Tsurutani et al., 2004] or the auroral oval to lowers [Basu et al., 2005] with the intrusion of those latitudes related phenomena into mid-latitudes.

Furthermore, plasma gradients such as the ones generated by storm enhanced density may also be present. These been observed to degrade DGPS positioning [Skone and Coster, 2009]. However, due to the no differential character of PPP, this kind of irregularity is not expected to affect PPP unless signal fading or loss occur.

The following section is centered in how the ionosphere affects GNSS signal and how it may impact PPP.

2.4. The ionospheric impact on GNSS signal

The ionized plasma can affect radio wave propagation in various ways modifying characteristics of the wave such as amplitude, phase or polarization. The ionosphere produces a propagation delay (phase advance) of the GNSS signal causing the travel distance or the travel time to be larger than the real one, limiting the accuracy of the satellite based positioning, and originating vulnerability in the reliability.

The nature of the propagation delay can be explained based on the refractive index, which depends on the ionospheric plasma density.

2.4.1. Ionospheric refraction

The refractive index of the ionosphere (a weakly ionized, cold and collisionless magnetized plasma) for GNSS signals carrier phase can be expressed according to the Appleton-Hartree formula [Budden, 1985]:

$$n^2 = 1 - \frac{\omega_P^2}{\omega^2 - \frac{1}{2}\omega^2\omega_{c\perp}^2\left(\omega^2 - \omega_P^2\right)^{-1} \pm \sqrt{\frac{1}{4}\omega^4\omega_{c\perp}^4\left(\omega^2 - \omega_P^2\right)^{-2} + \omega^2\omega_{c\|}^2}} \qquad (2.2)$$

$\omega = 2\pi f$	is the radio-wave angular frequency
f	is the radio wave frequency
$\omega_c = \sqrt{\lvert e\rvert B/m}$	is the electron angular gyro-frequency
$\omega_P = \sqrt{N_e e^2/\varepsilon_0 m}$	is the frequency of the plasma
e	is the electron charge ($-1.602 \times 10^{-19}\ C$)
B	is the magnitude of the geomagnetic field
m	is the electron mass ($9.107\times10^{-31} kg$)
c	is the velocity of light in vacuum
N_e	is the electron density (el/m^3)
ε_0	is the permittivity of free space ($8.854\times10^{-12}\ F/m$)

*International System of Physical Units (SI) is used.

Here $\omega_{c\parallel} = \omega_c \cos\theta$ and $\omega_{c\perp} = \omega_c \sin\theta$ are the gyro-frequencies considering the magnetic field component parallel and perpendicular to the wave direction, and θ is the angle between the geomagnetic field vector and the signal propagation direction.

Due to the effect of the Earth's magnetic field, the ionospheric plasma become anisotropic and lead to a double refraction (represented by ± sign): plus sign for the ordinary wave and minus sign for the extraordinary [Petrie et al., 2011].

Since GPS signal are predominantly right-hand circularly polarized (RHCP) waves that are transmitted in L-band (1-2 GHz), which implies $f >> f_P$ and $f >> f_c$, Eq. (2.2) can be expanded up to f^{-4} to obtain Eq. (2.3). The choice in the sign is made based on the explanations of Moore and Morton [2011], who show that RHCP GPS signals propagates in extraordinary mode when $0^\circ \le \theta < 90^\circ$, and in ordinary mode when $90^\circ < \theta \le 180^\circ$. For a detailed step by step explanation and a discussion about the inconsistencies found in literature regarding the choice of the sign in Eq. (2.2) see Moore and Morton [2011] or Petrie et al., [2011].

$$n_{phase} = 1 - \frac{f_P^2}{2f^2} - \frac{f_P^2 f_g \cos\theta}{2f^3} - \frac{f_P^4}{8f^4} - \frac{f_P^2 f_g^2 \left(1+\cos^2\theta\right)}{4f^4} \tag{2.3}$$

The group refractive index for a dispersive media such as the ionosphere can be determined by the expression $n_{group} = n_{phase} + f\, dn_{phase}/df$. The result is shown in Eq. (2.4).

$$n_{group} = 1 + \frac{f_P^2}{2f^2} + 2\frac{f_P^2 f_g \cos\theta}{2f^3} + 3\frac{f_P^4}{8f^4} + 3\frac{f_P^2 f_g^2 \left(1+\cos^2\theta\right)}{4f^4} \tag{2.4}$$

Ignoring the ray path bending effect (a discussion in this topic can be found in Petrie et al., [2011]), the ionospheric effect on the satellite-receiver range can be estimated by differencing the measured range and the geometric path between the satellite, S, and the receiver, R, and substituting the Eq. (2.3) to obtain Eq. (2.5):

$$I_{phase} = \int_S^R n_{phase} ds - \int_S^R ds = \int_S^R \left(n_{phase} - 1\right) ds = -\frac{r_1}{f^2} - \frac{r_2}{f^3} - \frac{r_3}{f^4} \tag{2.5}$$

where

$$r_1 = 40.309 \int_S^R N_e ds \tag{2.6}$$

$$r_2 = 1.1284 \cdot 10^{12} \int_S^R N_e B \cos\theta ds \tag{2.7}$$

$$r_3 = 812.42 \int_S^R N_e^2 ds + 1.5793 \cdot 10^{22} \int_S^R NeB^2 \left(1 + \cos^2 \theta\right) ds \tag{2.8}$$

The equivalent formula for the group delay (codes) can be obtained in an analogous way to get Eq. (2.9):

$$I_{group} = + \frac{r_1}{f^2} + 2\frac{r_2}{f^3} + 3\frac{r_3}{f^4} \tag{2.9}$$

These 3 terms in Eq. (2.5) and Eq. (2.9) are, from left to right, the first-, second- and third-order ionospheric effects, and produce range errors of the order of tens of meters, millimeters to centimeters and submillimeter to millimeters respectively [Petit and Luzum, 2010]. Notice that the 1st and 3rd order effects produce phase advance and code delay, while the second order depends on θ [Moore and Morton, 2011].

Additionally the ionosphere also produces a ray path bending effect that also depends on signal frequency as f^{-4} [Petrie et al., 2011], resulting not only in an excess of path length also called *geometric bending effect* but also in a difference in the integrated electron content along the ray path (defined as TEC), between frequencies due to the slightly difference in the signal bending at each frequency. This effects produce errors of the order of millimeters to few centimeters (in the case of satellites with lowest elevation angle).

The concepts introduced in these lines are a concern for PPP if highest precision is wanted to achieve because, in the IF combination first-order ionospheric effect disappear, whereas higher-order effects and bending terms still may leave residual errors.

2.4.2. The total electron content

The integral in Eq. (2.6) represents the *total electron content* (TEC) between the satellite and the receiver which is measured in *TECUs* (TEC Units, $1 TECU = 10^{16}\, el/m^2$).

The first order ionospheric effect on GNSS signal is 3 orders of magnitude larger than the higher order effects. Note that the first-order effect in Eq. (2.5) and (2.9) show opposite signs ($I_g = -I_p$), with a phase advance and group delay. Neglecting higher order effects and the TEC discrepancies due to the bending effect at different frequencies, the ionospheric delay can be approximated to the expression in Eq. (2.10).

$$I = \frac{40.3}{f^2} TEC \tag{2.10}$$

From this expression it is established that each *TECU* produces in GPS L1 (1575.42 MHz) an error of 16 cm in the satellite-receiver range.

The dispersive nature of the ionosphere allows dual frequency GNSS observables to be used for TEC estimation, traditionally, by means of the geometry free (GF) combination of observables (see Appendix A), in which the main problem raise in estimating the electronic biases [Sardón and Zarraoa, 1997; Ciraolo et al., 2007].

The TEC, like the electron density, is highly variable in space and time and shows differences with latitude, showing high values at low-latitudes (equatorial region), less at mid-latitudes and smallest values at high-latitudes.

The largest TEC values and TEC gradients present in the ionosphere are observed in the EIA vicinity where more than 200 TECU and gradients of 30 TECU/100km have been registered in periods of HSA, while in mid-latitudes rarely exceed 2 TECU/100km [Wanninger, 1993a; Skone et al., 2002]. The largest TEC values reflect the enhancement of the EIA, with a main peak few hours after noon and a secondary peak which is related to the PRE. TEC suffers from day-night, latitudinal, longitudinal, seasonal, solar cycle and geomagnetic activity related variabilities. The diurnal variation of TEC is controlled by solar radiation, however, the structures such as the EIA is dominated by $\vec{E} \times \vec{B}$ drifts, while neutral winds and neutral composition dominates the latitudinal asymmetry present [Liu et al., 2009]. Additionally, mid- and low-latitude regions TEC (and thus, EIA intensity) presents a wave-4 longitudinal structure [Wan et al., 2008; Wang et al., 2015] that is attributed to non-migrating tides excited in the lower atmosphere [Immel et al., 2006; Hagan et al., 2007].

In addition to the regular variation of TEC, the presence of ionospheric irregularities may lead to electron density gradients that produce fast variations of TEC that may cause GNSS signal scintillation. These irregularities are manifested as large fluctuations and values in the rate of change of TEC (ROT). This parameter can be estimated (whenever no cycle slip occur) practically directly from GNSS

observations by the expression in Eq. (2.11) since overcomes the obstacles related to the electronic bias and ambiguities estimation found in TEC calculus, because they are stable and constant (unless CSs occur) respectively in the periods of time considered in the calculus of ROT.

$$ROT_{literature}(t) = 9.52 \cdot \{[L_1(t+30) - L_2(t+30)] - [L_1(t) - L_2(t)]\} \quad (2.11)$$

This is the reason why ROT and ROT-based additional parameters have been extensively used for ionospheric plasma irregularities detection and occurrence characterization [Wanninger, 1993b; Aarons et al., 1996; Pi et al., 1997; Warnant, 1998; Mendillo et al., 2000; Nishioka et al., 2008]. The popularity of ROT-based parameters arise also from the interest emerged around the need to find a proxy for scintillation indexes due to the large number GNSS receivers from different networks displayed widely all around the world.

2.4.3. Ionospheric scintillation

Scintillation is a problem that concerns this study since it may impact unfavorably satellite-based communications and navigation systems, such as the one under study (GNSS-based systems). When radio signals cross plasma irregularities with scale sizes of the Fresnel length suffer from scattering [Kintner et al., 2007]. The irregularities act as a moving diffraction screen after which radio waves will interference each other adding constructively and destructively with the consequent signal power and phase time variations at the observation point (i.e. rapid amplitude and phase fluctuations).

Scintillation comes from irregularities having scale sizes comparable or smaller than the 1st Fresnel zone. For GNSS signals this means F-region irregularities with scale sizes of few hundreds of meters or less [Kintner et al., 2004].

Amplitude scintillation directly affects the SNR in GNSS receivers, as well as the noise levels in code and phase measurements. If the amplitude scintillation is sufficiently severe, the signal intensity received from a given satellite can drop below the receiver tracking threshold, causing the satellite signal LoL and hence, the need to re-acquire it, leading to reduced accuracy navigation solutions, data loss and CSs. If the desired signal is received at a very high SNR level, only deep fades will cause outages, and only as long as the fade persist longer than the time constant of the tracking loop; while at low SNR, also small fades can cause a disruption in tracking [Kaplan and Hegarty, 2005]. An amplitude scintillation index (S_4) can be derived from the detrended signal intensity (signal power) received in a receiver

from each GNSS satellite [Van Dierendonck et al., 1993] based on which scintillation regimes are usually defined attending to their impact on GPS.

Phase scintillation if sufficiently severe, it may jeopardize phase-lock-loops in GPS receivers resulting in loss of phase lock. A phase scintillation index, (σ_ϕ) is determined by the standard deviation of the detrended carrier phase of GNSS signals averaged in 60 s [Van Dierendonck et al., 1993].

The computation of these scintillation indices are affected by effects such as multipath, receiver noise, biases caused by relative movement between the satellite, moving ionospheric irregularities and receiver movements or GPS satellite oscillator faults [Benton and Mitchel, 2012; 2014].

Both index-magnitude depend on the GNSS carrier frequency; so when fading occurs, the index values will be larger for L2 than for L1 [Kaplan and Hegarty, 2005]. The implications of this dependency is that scintillation would be much more likely to cause outages on GPS signals L2 and L5 than on L1 if the same signal was to be broadcast on all three frequencies at similar received power levels. However, variations in signal design and power levels between the GPS signals at different frequencies make it more difficult to make such a general statement. Additionally, the use of codeless and semicodeless techniques for tracking L2 result in lower SNR values making them more vulnerable to signal loss.

Chapter 3.
Data processing and analysis

This chapter provides a brief description of the data and the procedure performed in the development of this thesis.

Section 3.1 presents the main data in this thesis. Section 3.2 introduces the method used for the ionospheric information retrieval in which the shortcomings regarding the code noise and the ionospheric thin shell model altitude selection are highlighted. Section 3.3 explains the method followed for each kind of irregularities detection. Since it is not the goal of this work to introduce new algorithms or improvements related with the PPP processing strategies, but to make a general analysis of ionospheric irregularities effect on PPP, detailed description of the models, filters or techniques used by any PPP software will be omitted. However, a brief description of the software package used, the online CSRS-PPP service, is also introduced in Section 3.4. This section also describes the strategy followed to show positioning results.

3.1. Data description

In order to investigate the presence of TEC gradients at mid- and low-latitudes, data from the IGS stations were used. The stations used in this work and which are listed in Table 3.1, were selected not only due to the data availability but also attending to their location, to include different longitudes but also latitudes with respect to the equator and the EIA crests. This geographic distribution of the stations is plotted in Figure 3.1. Six stations are located in low latitudes (AREQ, KOUR, NKLG, MALI, NTUS, and GUAM) and two in mid-latitudes (AMC2 and MAD2). The information regarding these IGS sites can be found in Appendix B.

Note in Table 3.1 that except for MAD2, where the years analyzed (from 2005 to 2015) cover approximately an entire solar cycle (SC), from the descending phase of SC23 to the maximum of SC24, the rest of the stations data corresponds to selected years that are representative of different solar activity conditions. In particular, 2001, corresponds to a period of HSA, 2004 and 2011 to moderate solar activity (MSA) while 2008 to LSA. Figure 3.2 depicts the solar radio flux emission at 10.7 cm (the so called F10.7 index) in solar flux units (1sfu=10^{-22} W m^{-2} Hz^{-1}), which is an indicator of solar activity.

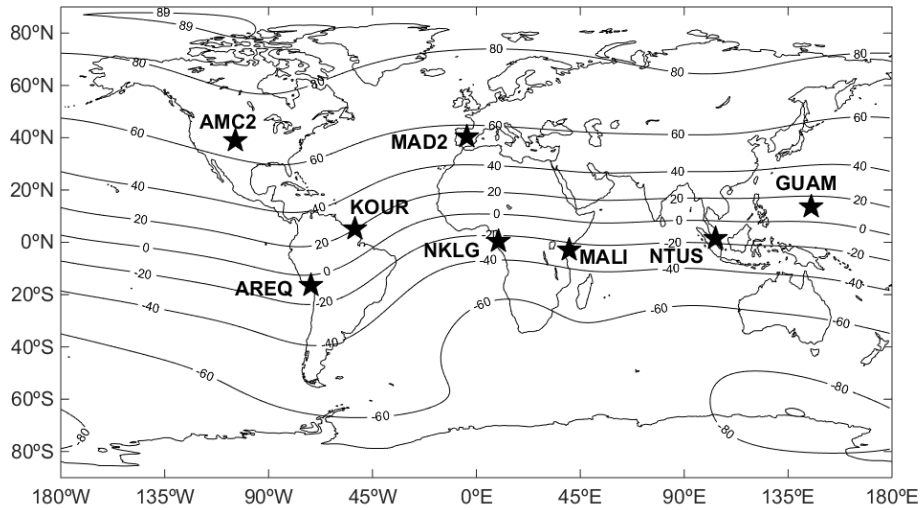

Figure 3.1 Geographic distribution of the selected stations (represented by black stars). Contours represent isoclines of the geomagnetic field calculated using IGRF11 geomagnetic field model updated to epoch 2001.0.

Table 3.1 IGS stations with their geographic coordinates and the geomagnetic coordinates at ground level (IGRF11-2001).

ID	Geographic coord.		Magnetic field		Years under study
	Lat. (º)	Long. (º)	D(ºE)	Iº (º)	
AMC2	38.8	255.5	9.90	66.12	2001, 2004, 2008, 2011
AREQ	-16.57	288.51	-2.2	-7.17	2001, 2004, 2008, 2011
KOUR	5.25	307.10	-17.54	20.13	2001, 2004, 2008, 2011
MAD2	40.43	355.75	-3.10	55.41	2005-2015
NKLG	0.35	9.67	-4.03	-27.45	2001, 2004, 2011
MALI	-3.00	40.19	-1.04	-27.75	2001, 2004, 2008
NTUS	1.35	103.68	0.23	-16.07	2001, 2004, 2008, 2011
GUAM	13.59	144.87	1.51	12.20	2001, 2004, 2008, 2011

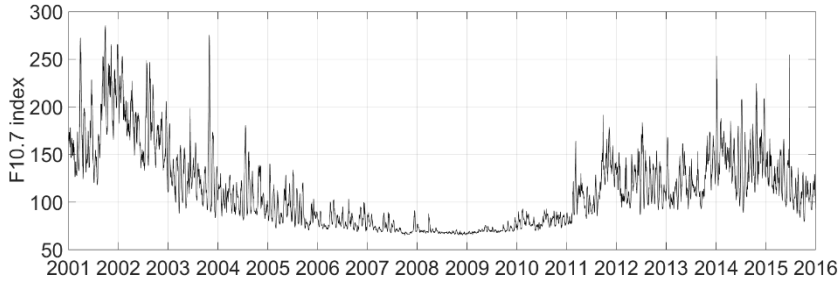

Figure 3.2 Daily F10.7 index in the period 2001-2015. Data from the omniweb: http://omniweb.gsfc.nasa.gov/.

The dataset analyzed in this work are GPS dual frequency code and phase observations at 30 s sampling rate. This sampling rate is the standard for most of the permanent stations, although the number of sites providing data with higher resolution is steadily increasing. The data amount and the computation time for the algorithm (MAP3) used in this work is very long. The computation time for a 1 s solution is at least 30 times longer than for 30 s solution due to the epoch by epoch processing strategy. Therefore, 30 s sampling was chosen for this purpose, even if we know the shortcomings regarding the real applications of data at 30 s sampling for kinematic PPP purposes. However, this is a sampling rate usually used in geodesy and deformation applications, and although they are performed in static, the kinematic PPP accuracy analysis of those data highlights the shortcomings of using those data for other applications. In addition, few case studies corresponding to 1 s sampling were also added to this work to clarify or remark the differences with respect to considering 30 s sampling. Furthermore, NTUS, NKLG and KOUR stations data include GLONASS observation in 2008-2011, 2011 and 2008-2011 respectively, although their products were not available until day of the year (DoY) 226, 2011.

3.2. Methodology: Rate of change of TEC

In this work sTEC is calculated using the relation in Eq. (2.10) for which the ionospheric delay is previously estimated by the technique based on least squares theory approach described in De Lacy et al., [2005] and [2008] which is implemented in the MAP3-1 module algorithms [Moreno et al., 2014].

Dual frequency carrier phase and pseudorange observations of daily RINEX files from each station are preprocessed to detect cycle slips and outliers, and to correct the observables from tropospheric delay (by modelling), satellites and receivers DCBs (obtained by CODE), by phase center offsets and variations, and the phase wind up effects. A detailed step by step description of MAP3 can be found

in Moreno [2012]. The sTEC values are calculated epoch by epoch for all individual satellite tracks with elevation angles over 10º, because this is the cut-off elevation angle used by default in the PPP engine used in this work.

The magnitude of the sTEC depends on the oblique path through the ionosphere, therefore it is larger at lower elevation angles than in the vertical. To diminish the effects related to the satellite elevation angle, the equivalent vertical total electron content or vTEC can be calculated for each ionospheric piercing point (IPP), multiplying the sTEC by an elevation dependent mapping function (see Eq. (3.1)) that can be defined considering an ionospheric thin layer model like the one represented in Figure 3.3.

$$vTEC = sTEC \cdot \cos\left(\arcsin\left(\frac{R_E}{R_E + H_{IPP}}\sin z\right)\right) \tag{3.1}$$

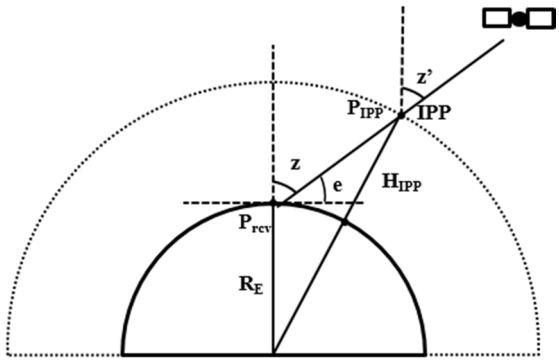

Figure 3.3 Thin layer model of the ionosphere. The ionosphere is represented as a thin shell at height HIPP above the (spherical) earth surface. The IPP is the point where the signal LoS (of a satellite with elevation e and zenith angle z) intersects the thin shell.

Then, ROT is computed by the first time derivative of each vTEC curve (the difference between two consecutive epochs, see Eq. (3.2)):

$$ROT(t) = vTEC(t + t_0) - vTEC(t) \tag{3.2}$$

where t_o is the sampling rate of the data (30 s or 1 s depending on the case).

The ROT obtained with this method differs from the one found in literature, which is usually calculated by the expression in Eq. (2.11), although differences exist between different author's approach when dealing with this parameter since frequent procedures include applying mapping functions to minimize elevation

effects or curves detrending to remove low frequency variations and to isolate the irregularities themselves (fast variation of TEC). As noted by [Nava et al., 2007], the presence of horizontal gradients may lead to errors in the conversion from slant to vertical TEC. Thus ROT may be affected by this conversion errors. Figure 3.4 shows the differences observed when different H_{IPP} are considered: vTEC in the left and ROT in the right. The analysis of the ionospheric thin shell model layer height selection effect on ROT will be developed in Section 3.2.2.

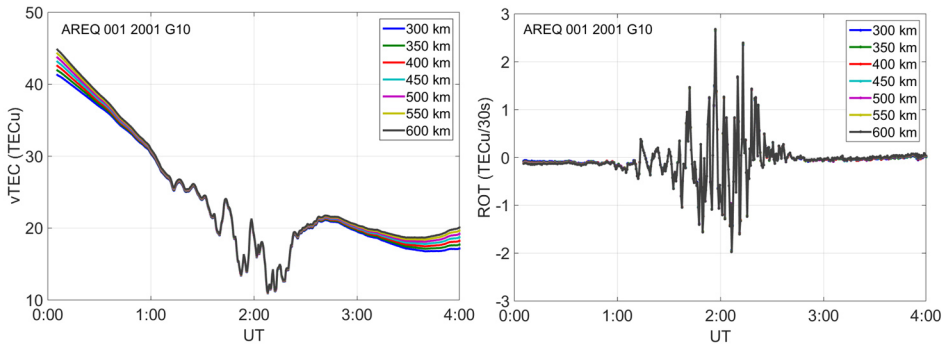

Figure 3.4 Equivalent vTEC (left) and ROT (right) for G10 satellite at AREQ on DoY 001 2001. Each color represents a value of H_{IPP} in the ionospheric thin shell model.

Another difference between the ROT used in this work and the one used in literature is that it is usually estimated in units of TECU/min instead of TECU/30s, which are the units used in this study. This choice is based on the objective of this thesis which is to analyze the irregularities effect on PPP, and positioning results are produced in the same sampling as the dataset.

Furthermore, it is worth noting that additional differences will also exist, especially when low elevation data are considered, due to the fact that no codes (pseudoranges) information are included in the expression of Eq. (2.11), while they are when ionospheric delays are estimated by means of the De Lacy et al., [2005] method. This point will be analyzed in Sections 3.2.1.

The advantage of using a not-detrended ROT relies on the fact that it is sensitive not only to small ionospheric structures related TEC fast variations but also to larger scale changes, and can be used as an indicator of the presence of TEC anomalies such as the ones related to geomagnetic perturbed condition (see Figure 3.5).

Figure 3.5 shows the ROT values in each epoch obtained with satellites above 45º of elevation for AREQ station in the time interval August 4-7, 2011 (DoY 216-219). The trend of ROT dispersion is an indicative of the trace of the first derivative

of the vertical TEC over the station, therefore also shows a quite periodic variation, which depends on local time (LT), geographic location or solar activity among others. The largest spread in ROT observed in DoYs 216, 217 and 219 responds to plasma irregularities present in the LoS between higher elevation satellites and the receiver. In the transition from DoY 217 to 218 2011, another kind of structure is observed with less scattering and larger modulation which exceeds the normal values for that LT. This ROT perturbation reflects the ionospheric TEC response to the geomagnetic storm occurring in August 5th and 6th, 2011.

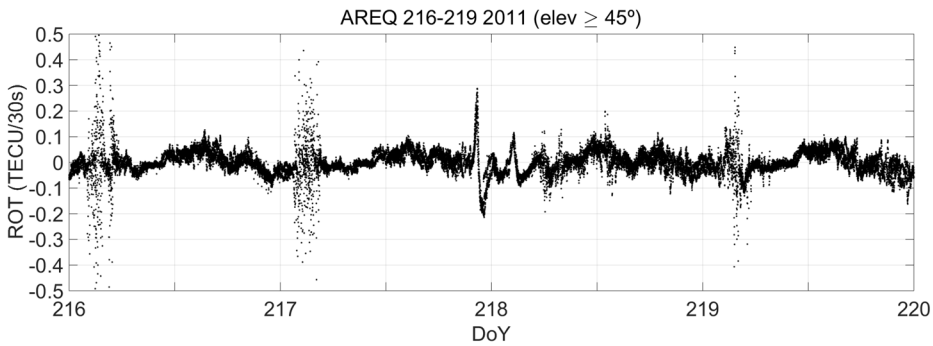

Figure 3.5 ROT values obtained in each epoch by all the satellites in view with elevation above 45º, in AREQ during DoY interval 216-219 2011.

Representing the mean value of the ROT obtained with satellites above 45º at each epoch for a whole year offers an overview of the daily and annual trends of the rate of change of TEC over the station. In Figure 3.6 an example of mean ROT local time and seasonal variation is presented for a low-latitude station (AREQ) in a MSA period (2011). This figure shows not only the diurnal variability of ROT but also the day to day differences. The main characteristics to remark from this concrete picture are: in one hand, the large values reached from dawn to noon around solstices and to afternoon (~15 LT) around equinoxes; the low values reached at dusk and prior to dusk especially in equinoctial months, followed by a high fluctuations activity that goes from sunset to around midnight and later on, the first and last trimesters of the year; and the minimum ROT mean values again from midnight to around 4 LT around equinoctial months. The large nighttime fluctuations in ROT values which are attributed to post sunset ionospheric plasma irregularities are enclosed in time by deeper minimums of mean ROT. This plot of epoch by epoch mean ROT values highlight both diurnal and nighttime trends, and the periods with presence of ionospheric irregularities.

Data from satellites with low elevation angles suffer larger errors in the conversion from sTEC to vTEC. For this reason it is observed that in literature

when referring to ionospheric studies, data corresponding to satellites with elevation angles below 30º are discarded from the analysis. However, in positioning, this information it is valuable and cannot be ignored. Therefore, "low elevation" satellites' data are in general included in this study, although in some cases, to emphasize certain effects, they may have been discarded.

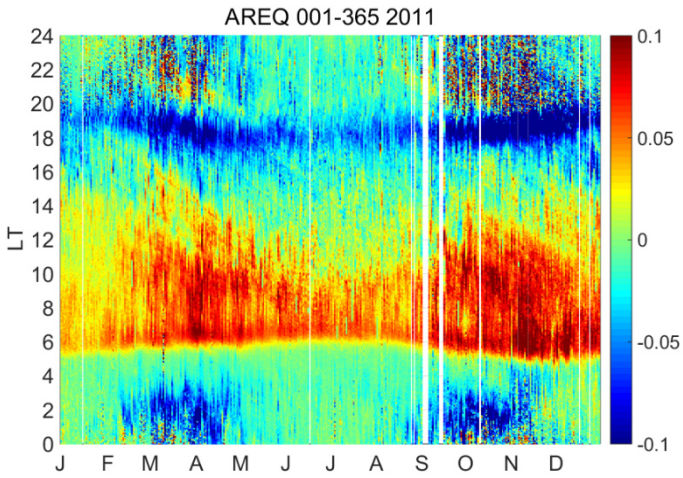

Figure 3.6 Seasonal and local time variation of mean ROT values over AREQ in 2011 considering a satellite's elevation mask of 45º.

3.2.1. The code noise effect on ROT calculus

The first derivative of sTEC calculated by De Lacy et al., [2005] method depends on the noisy code (pseudorange) which, in turn, depends on the receiver, the environment and all the effects that may contribute to noise, while the results of applying Eq. (2.11) do not.

Figure 3.7 shows the monthly accuracy (95%) of the rate of change of sTEC obtained by De Lacy et al., [2005] method with respect to the ROT obtained by the expression in Eq. (2.11). In this figure percentile 95 is shown for the absolute value of the difference in ROT: from top to bottom AREQ, KOUR, NKLG, NTUS and GUAM and from left to right years 2001, 2004, 2008 and 2011 results. Different elevations have been considered in order to discern between different contributions to noise such as multipath. Note that larger differences are present at lower elevation angles, which can be mainly attributed to multipath, and that big differences exist from one year to the other and from one station to the other due to receivers' capabilities when tracking the signal.

AREQ and GUAM show the most homogeneous results, with values that are maintained more or less constant below 0.05 TECU/30s (in 95% of the epochs) for all the years except for the second semester of 2011. It has been checked that coinciding with periods of less accurate results, in December 2011, in GUAM and AREQ the following message appears in log files for dates 2011-09-08, 2011-08-26 and 2011-09-12 respectively (see Appendix B): *"Local Episodic Effects Possibly Affecting Data Quality: Transitioned from .soc to .ash data types. For soc data typed used soc2rnx to do the conversion to RINEX data. For ash data types using teqc directly to do the conversion to RINEX*". Therefore it can be seen that the conversion to RINEX format has been introducing noise to the observables, no matter the elevation of the satellite. In addition to this, in AREQ station the antenna cable was changed (radome removed) on 2011-08-19.

The most inhomogeneous results are observed in KOUR. The lower the elevation angle is, the less the accuracy reached. However, above 30º this difference decreases to 0.03 TECU/30s except for 2001. It is also worth noting that 2004 presents the fewer differences, which might be indicating that the code is not so noisy. However it has been observed that this year the data suffered lot of signal (observables) systematic losses [Rodríguez-Bilbao et al., 2014], that will be shown in Chapter 5. On the other hand, it seems that the low noise present this year makes relevant the peaks observed from October to March in satellites with elevation above 30º. This period of time coincides with the epochs in which high ROT related to ionospheric irregularities is present (see Chapter 4). It has been checked that this increase in the values corresponds only to nighttime contribution, therefore, it can be stated that the discrepancies are probably linked to noise increase due to scintillation effects (or multipath like phenomena related to the signal crossing ionospheric irregularities). The accuracy degradation in ROT hardly reaches 0.015 TECU/30s. On the other hand, 2008 shows strong changes in the accuracy reached for lowest elevation satellites especially in January and after June. The second semester of 2008 was also characterized by an increase in observable loss [see Rodríguez-Bilbao et al., 2014].

NKLG shows almost the same results for 2001 and 2004 and three times better results for elevations above 60º and also in 2011. NKLG shows the noisiest contributions; almost double than the rest of the cases under study.

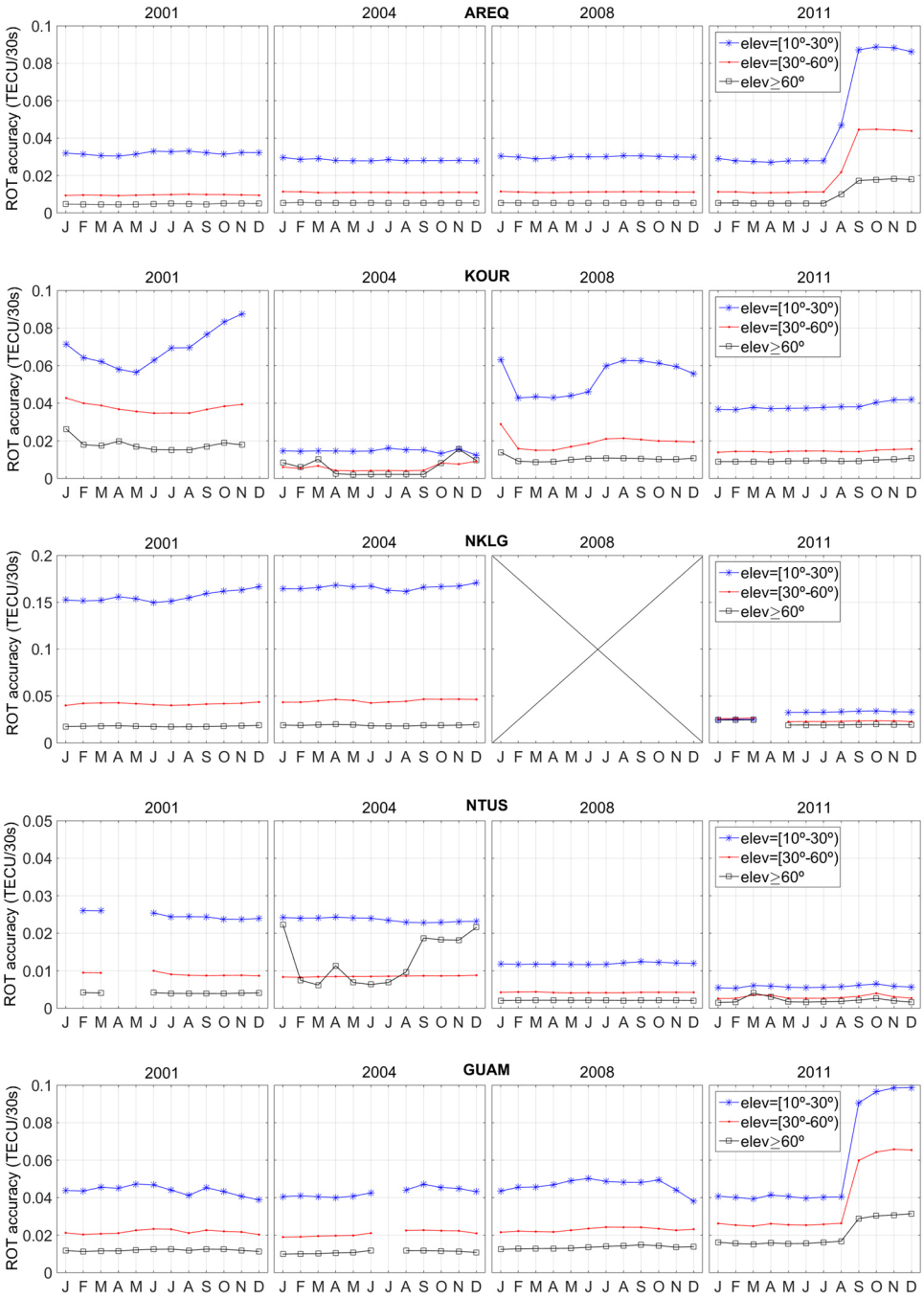

Figure 3.7 Accuracy of ROT: month to month percentile 95 of the deviation of sTEC first derivative with respect the ROT calculated with phases.

On the other hand, NTUS shows the less noisy results of the cases studied. An improvement of the accuracy is observed with years although some strange features appear in 2004 for satellites above 60º which are the result of an increase in the noise of pseudoranges for less than an hour at certain satellites (PRN 16, 19 and 21) passing through the antenna zenith in the North-South direction.

To sum up, except for NKLG in 2001 and 2004 when considering the lowest elevation satellites data, the first time derivative of the sTEC obtained by the De Lacy et al., [2005] method has an accuracy better than 0.1 TECU/30s (95%) with respect to the results obtained only with phases (see Eq. (2.11)). This accuracy increases to 0.05 TECU/30s for satellites with elevations above 30º, except for the second semester of 2011 in AREQ and GUAM, which present problems related to data format conversion.

The elevation dependence of the results denote that the main contribution to the differences observed (i.e. to the pseudoranges noise) is related to the multipath and the site effects. However, the contribution of the ionospheric irregularities related phenomena to the noise is also evident when the accuracy reaches its largest values (below 0.01TECU/30s), as in KOUR for 2004 and NTUS for 2004 and 2011 respectively. Note the peaks around March and November for low elevation satellites.

The differences observed from one year to the other which cannot be attributable to solar activity effects reveal the influence of receiver's contribution to noise.

3.2.2. The impact of the H_{IPP} selection on ROT

As shown in Figure 3.4, the ionospheric thin shell model altitude (H_{IPP}) also contributes to the differences in the estimated vTEC and thus, in ROT.

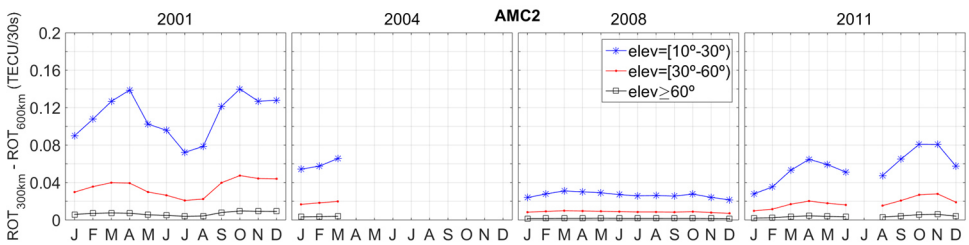

Figure 3.8 Percentile 95 of the difference between the ROT considering a H_{IPP} of 300km and of 600 km for AMC2. From left to right: years 2001, 2004, 2008 and 2011.

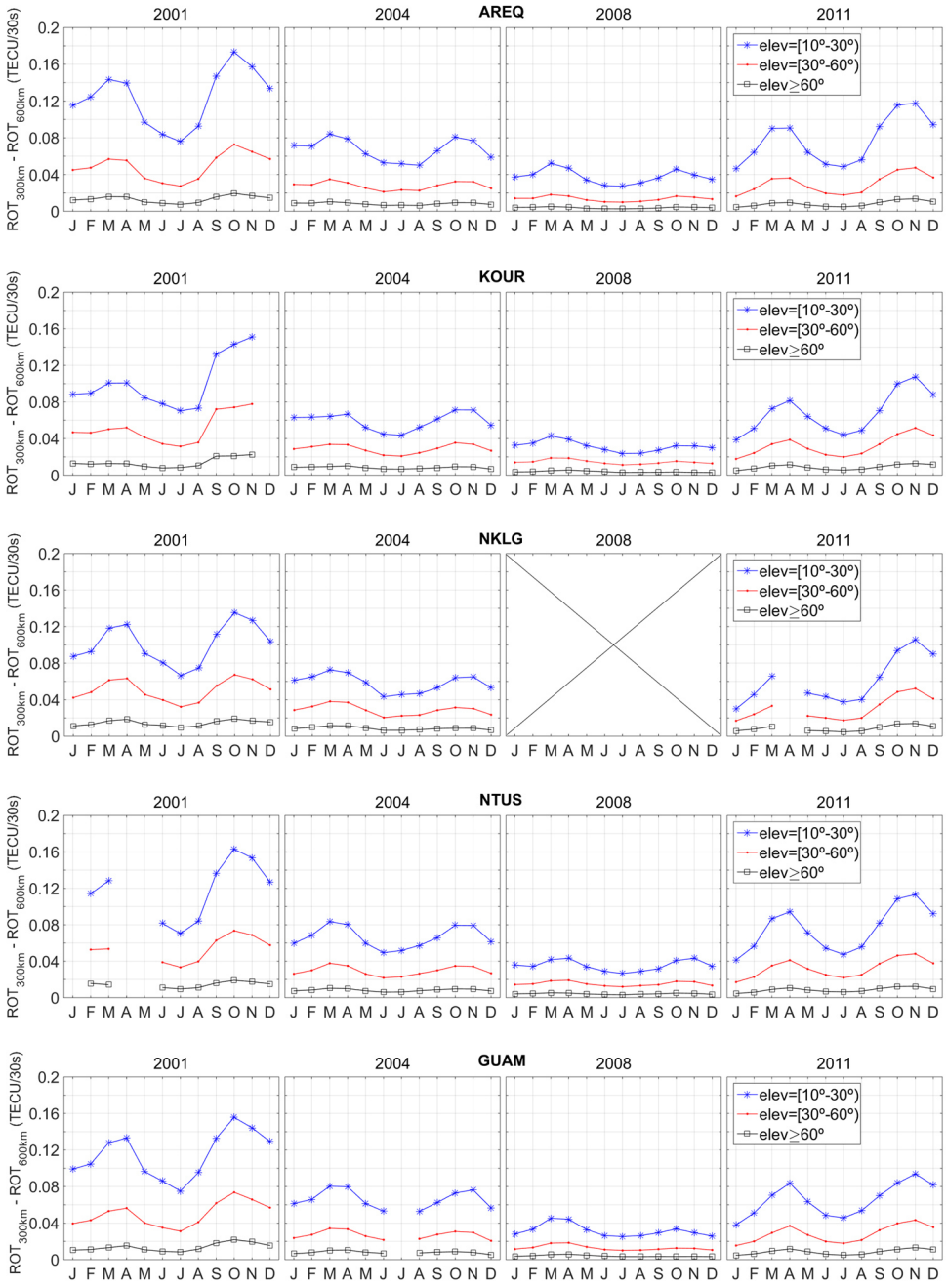

Figure 3.9 The same as Figure 3.8 but for AREQ, KOUR, NKLG, NTUS and GUAM.

In this section the ionospheric thin shell altitude selection effect on ROT is analyzed. The vTEC is obtained at two different altitudes (300 km and 600 km) for AMC2 and the low latitude stations listed in Table 3.1 for the years under study.

The difference in ROT at these two altitudes at each epoch is estimated for each epoch, and again, monthly percentile 95 is calculated and represented in Figure 3.8 for a mid-latitude station and in Figure 3.9 for low-latitudes stations. ROT differences increase with increasing solar activity, being this behavior more prominent in low-latitudes and when low elevation satellites are considered. This difference is maximum in equinoxes and for lowest elevation satellites, due to ray path crossing more ionosphere and probably larger structures (e.g. EIA). Small differences exist between stations in years of LSA and MSA, especially when larger elevation satellites are considered. In these cases ROT differs less than 0.05TECU/30s.

Note that for elevation above 30º, the difference in ROT is at least, half the value obtained with elevations below 30º. Therefore, considering higher elevation satellites would result in a more accurate estimation of ROT. However, to know which the best altitude to consider is, a one by one case study should be done, and this is not the goal of this work. Nevertheless, these tests highlight the situations where the ROT estimated for the analysis introduced in the following lines may be more prone to be less accurate.

Additionally, the variability shown in ROT accuracy confirms one of the reasons why making a general analysis it is not possible to establish a ROT value which is supposed to cause problems in positioning.

3.3. Irregularities detection

The first step in establishing the best procedure for the detection of ionospheric plasma irregularities affecting GNSS signal has been to calculate ROT by the procedure described in the previous section where an altitude of the IPP of 350 km has been considered.

After a previous visual analysis of the ROT shape and characteristics, different approaches depending on the location of the stations, mid- or low-latitudes have been considered. Low-latitude stations are affected by large ROT fluctuations while mid-latitude stations present more wavelike patterns, or faster fluctuations but not as intense as the ones registered in low-latitudes. Additionally sudden ROT increases due to SITECs are observed, no matter the latitude of the station under study. In the following sections the methodology to analyze each kind of irregularities is explained.

3.3.1. Low-latitude irregularities

In order to identify the ionospheric irregularities present in the low-latitude ionosphere, which are characterized by rapid fluctuations of ROT as the one shown in Figure 3.5, a ROT threshold value is established.

As shown in Section 3.2 the noise in ROT depends in one hand on the receiver, and in the other in the ionospheric characteristics and satellites elevation. Therefore, a threshold value could be established for ROT for every station and year. However for a general analysis, it has been decided to set a common threshold value of 0.3 TECU/30s, based on the ROT obtained during 10 days with no presence of irregularities, for every station and year. In addition, a second threshold of 1 TECU/30s is set to highlight the periods with stronger perturbations.

3.3.2. TIDs

Analyzing the ROT obtained from each satellite in mid-latitudes stations, as noted previously by Wautelet and Warnant, [2013] in the present study it is also observed that the most frequent kind of irregularities in this case over MAD2 and AMC2 are, by large, TIDs. These TIDs are characterized by fluctuations in ROT values which appear as amplitude modulated wavelike disturbances that may occur both in daytime and nighttime. In Figure 3.10 a typical example of days with presence of TIDs at daytime (left) and nighttime (right) are shown. They can reach few TECU/30s of amplitude in no-detrended ROT especially when low elevation satellites are considered and Line-of-Sight (LoS) is directed to the South.

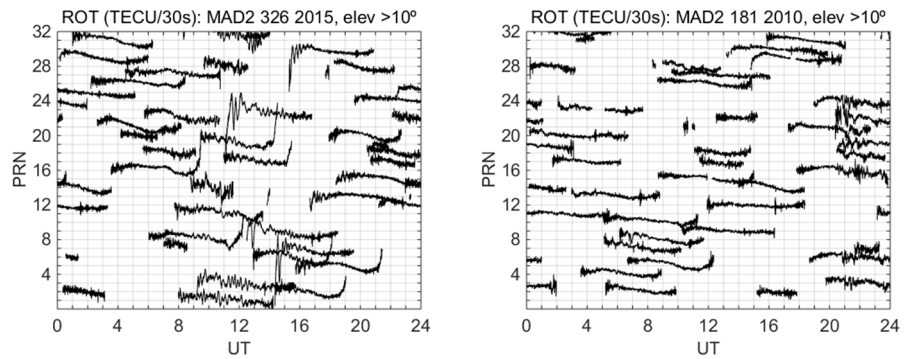

Figure 3.10 No-detrended ROT measured by each GPS satellite in MAD2 station on DoYs 326, 2015 (left) and 181, 2010 (right). Elevation mask: 10º.

However, this kind of irregularities are not a threat for the accuracy reached in dual frequency PPP with the technique used in this work, and therefore, they are discarded from the positioning effect analysis.

3.3.3. SITECs

Another kind of irregularities present in daytime and more frequent in periods of HSA are SITECs. The ROT characterizing a SITEC is a fast increase with the shape of a peak of few minutes of duration that occurs simultaneously in all the satellites whose signal is travelling through the daytime ionosphere. Figure 3.11 displays an example with the presence of a SITEC disturbance in ROT at 8:15 UT.

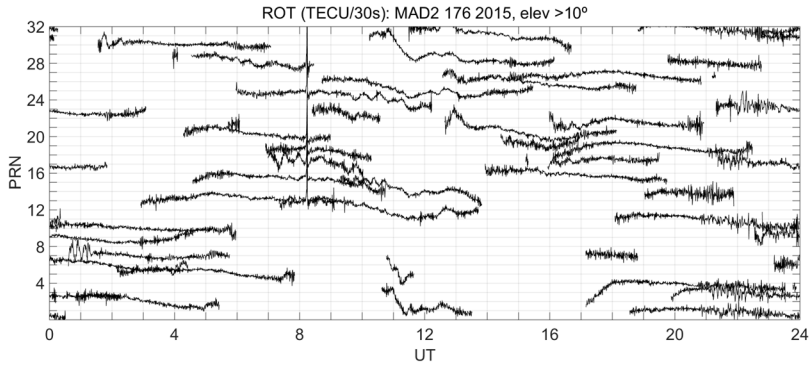

Figure 3.11 No-detrended ROT for all the satellites in view over MAD2 on June 25th, 2015. Elevation mask: 10º. SITEC disturbance at 8:15 UT.

For a certain station, all the satellites signals affected by a SITEC show a simultaneous organized rise in ROT of nearly the same amount, this is especially true for the satellites with highest elevation. When considering at each epoch the measured ROT in all satellites in view, the following properties are observed: (1) a simultaneous growth in the values and (2) less dispersion at those epochs.

Based on that, a parameter has been defined which is calculated by subtracting the standard deviation (STD) of ROT at each epoch to the root mean square (RMS) of ROT. With this procedure the ROT peaks characterizing SITECs (in black in Figure 3.12) can be straightforward visually identified.

To establish an automatic detection, a threshold can be defined statistically by filtering this new parameter by a 30 min moving average (the red curve in Figure 3.12) to calculate the residuals and the standard deviation of those residuals with a sample of one month for instance (2880 data per day). The threshold value (the blue curve in Figure 3.12) can be defined as the values of the parameter exceeding the

result obtained by the moving average filtering (avg) plus 3 times the standard deviation (σ) based on September 2005 data. Note the spikes in Figure 3.12 bottom picture coinciding with the sudden increases of photon flux measured onboard SOHO satellite, that are depicted in top picture of Figure 3.12. However, as in some situations especially in periods of high ROT, the automatic method may not flag the smallest SITEC, visual detection analysis has been also used. The results regarding mid-latitudes will be presented in Chapter 4 and tables can be found on Appendix D.

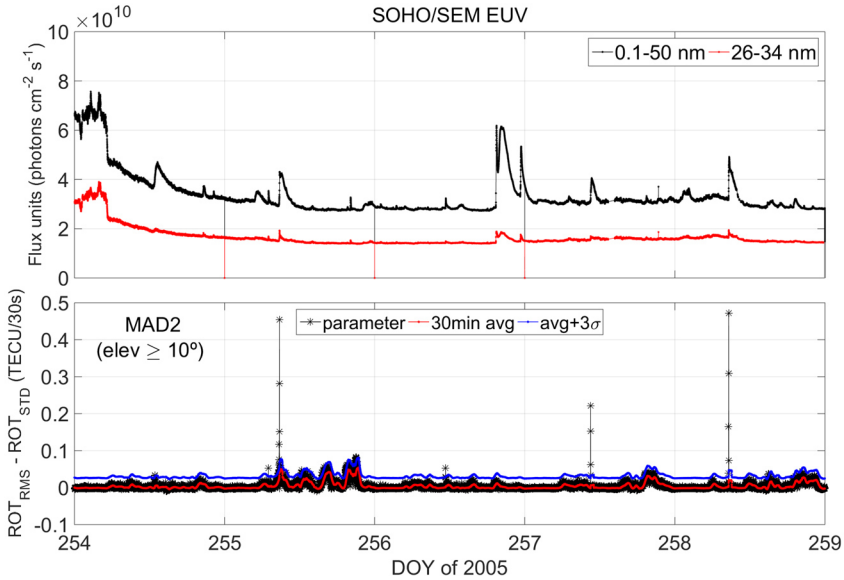

Figure 3.12 SITEC detection in MAD2 for September 2005 DOYs 254 to 258. Top: photon flux measured with SOHO/SEM in the 26–34 nm band pass (red) and in the 0.1–50 nm band pass (black). Data: Courtesy of the USC Space Science Centre for the EUV data of CELIAS/SEM experiment on SOHO spacecraft available at http://www.usc.edu/dept/-space_science/semdatafolder/. Bottom: $ROT_{RMS} - ROT_{STD}$ parameter (black), the 30 min moving average (red) and the threshold value (blue) considering an elevation mask of 10º.

3.4. Positioning strategy: PPP

As stated previously, the first aim of this paper is to assess the performance (accuracy and repeatability) of PPP for dual frequency observations collected at different latitudinal and longitudinal regions that reflect different ionospheric conditions. For this purpose the results given by the CSRS-PPP online service [Mireault et al., 2008] are used.

3.4.1. Overview of online CSRS-PPP service

The CSRS-PPP service is one of the most used PPP online services all around the world. This service is offered by the Natural Resources of Canada (NRCan) and it is available in the website http://webapp.geod.nrcan.gc.ca/geod/tools-outils/ppp.php.

Observation files are uploaded to the service's website and the results are sent back by e-mail with latencies that go from few minutes to some hours, depending on the size of the file. More details about this tool's specifications, its use and the description of output files can be found on NRCan [2004].

In GNSS navigation there are many error sources contributing to the satellite-receiver range, some of which are listed in Table A.2. In DGPS many of these errors cancel out by double-differencing, however due to the zero-difference character of PPP to reach the accuracy level of DGPS, these errors need to be handle properly, either by introducing the corrections or by modelling additional correction terms often cancelled in DGPS.

These error sources include, relativistic effects, phase wind up effect, and tropospheric effect for which accurate physical models are applied. In fact, the error mitigation adopted by CSRS-PPP to account for tropospheric delay correction, include the zenith hydrostatic delay estimation using a Davis, and, as the wet delay is highly variable compared to the dry delay, it is estimated along with position and the receiver clock offset based on initial constrains given by a Hopfield Model [Xu, 2007] which depend on surface meteorological data that are extracted from a Global Model of Pressure and Temperature (GPT) [Boehm et al., 2007]. The conversion to slant tropospheric delay is obtained by applying a Global Mapping Function (GMF) [Boehm et al., 2006]. The satellite clock error is generally modeled while the receiver clock error is one of the unknowns' parameters that need to be solved in PPP. Satellites orbits and clocks bias are corrected by applying IGS precise final products [Dow et al., 2005] (in '.sp3' and '.clk' files), that can be downloaded from ftp://igscb.jpl.nasa.gov/pub/product/) and are interpolated to 30 s. It is worth mentioning that the accuracy of PPP also depends on the sampling of GPS clock corrections [Bock et al., 2009]. The receiver and antenna phase center corrections can be downloaded from the IGS website (ftp://igscb.jpl.nasa.gov/pub/station/-general/). CSRS-PPP uses its own internal files with antenna offsets corrections. Electronic bias in carrier phase observations are not corrected but considered to be absorbed by the initial ambiguities. In code observations, since they cannot be determined in an absolute sense, corrections (monthly differential code bias, DCB) provided by agencies such as the Center for Orbit Determination in Europe (CODE, ftp.unibe.ch/aiub/CODE/) are used. Additionally, when observations from different satellite systems, such as GLONASS, are processed, in addition to the DCBs other corrections need to be considered: inter-frequency bias (IFB) when each satellite

uses its own frequency and inter system bias (ISB) because signals from different satellite system are processed in different parts of the receiver. CSRS-PPP uses P1-C1 and P2 -C2 DCB corrections, and processes GLONASS observations in addition to GPS when products of the additional constellation are available. As will be noted in the results of 2011, NTUS, NKLG and KOUR contains GLONASS observations and CSRS-PPP includes those when satellites products are available: from DoY 226, 2011. For ocean loading, a default NRCan file is used. CSs and ambiguities are set by means of the narrow-lane (NL) and wide-lane (WL) linear combinations (see Appendix A). Finally, the ionospheric effect is cancelled, at first-order, by dual-frequencies observations IF combination (see Appendix A).

The satellites elevation mask considered by default is 10º, and the internal filter may run in either forward or backward modes. The latter reduces the errors associated with the solution convergence. The parameters of the stochastic model used in PPP are summarized in the 'sum' files sent to the e-mail.

CSRS-PPP provides positioning results in two reference frames: the North American Datum 1983 (NAD83) and the International Terrestrial Reference Frame (ITRF) [Petit and Luzum, 2010], being the later, the one chosen for this study.

In static dual frequency, CSRS-PPP has been reported to achieve centimeter-level accuracy while in kinematic, sub-decimeter accuracy is achievable [Mireault et al., 2008].

3.4.2. Positioning accuracy evaluation strategy

To evaluate the kinematic mode PPP daily RINEX files containing 30 s sampling data are sent to the online CSRS-PPP service to be processed in kinematic mode and in ITRF reference system. Exceptionally 1 s sampled data have been processed. It is worth mentioning that the IGS corrections to be applied to the observations, such as clocks and orbits products, need to be interpolated when they are not in the same sampling rate as the measurements, and this interpolation may not be accurate enough for the accuracy expected. In static PPP this *trouble* can be avoided by decimating GPS receiver data in order to coincide with satellite precise products decimation, but this is not reasonable practice in kinematic PPP. Since December 17th, 2006 (GPS week 1406) thanks to the combined effort of different analysis centers, a combined final satellites clock products are available to a sampling of 30 s [Kouba, 2009], but not to 1 s yet. Nevertheless, CSRS-PPP uses 5 min sampled clock products.

The data used in this work correspond to IGS reference stations, therefore they were observed in static mode. For the present study this represents a best scenario than a real dynamic dataset since the precise solutions to compare the results are

known and, additionally, no tracking complications such as the ones related to the varying environment or maneuver conditions are included.

The accuracy achieved in position depends on the number of satellites in view and their distribution in space (satellite geometry). Due to the satellite distribution in the sky, always above the receiver, the vertical positioning is less accurate than the horizontal, because dilution of precision (DOP) in the vertical (VDOP) is larger than in the horizontal (HDOP) [Langley, 1999].

Since the errors observed by default in the vertical component of position are assumed to be larger than in horizontal, unless satellites loss occur, this is also expected to happen in periods of presence of ionospheric irregularities. Therefore, the vertical component is the position coordinate to be analyzed in this work. In particular cases, horizontal coordinate's results may also be shown.

To evaluate the PPP accuracy the altitude error is calculated by differencing the altitude estimated by CSRS-PPP with the station precise coordinate in absolute values, which for the shake of accuracy, should be in the same reference frame. The stations coordinates provided after processing by CSRS-PPP are in IGS05 coordinate reference system until the 17th of April of 2011 (DoY 107). From then on, IGS08 is used.

For the results that will be shown in Chapter 5, the reference coordinates in IGS05 and IGS08 realization are obtained from Bernese coordinate ('.CRD') and velocity ('.VEL') files (which are available at ftp://ftp.unibe.ch/aiub/-BSWUSER50/STA/) for epoch 2000.0 and 2005.0 respectively. Those are listed on Table 3.2 and 3.3 respectively. When precise coordinates of a station were not available on IGS08, coordinates in ITRF2008 were used [Rebischung, 2011].

On the other hand, for the results that will be shown in Chapter 5, the weekly SINEX file is used.

The epoch correction is performed by assuming linear time evolution of stations position. Its values at any epoch, t, are derived by using Eq. (3.4)

$$P(t) = P(t_0) + \dot{P} \cdot (t - t_0) \tag{3.3}$$

where t_0 is the initial epoch P is the position and $\dot{P}$ is the velocity (those values are listed in Table 3.2 and 3.3).

On the other hand, to evaluate PPP solution repeatability (which gives a measure of precision), the first derivative of the estimated altitude is performed to analyze how much it differs in consecutive epochs, and the daily standard deviation (STD) value is estimated. Due to the backward filtering of PPP, repeatability can be a good estimator of precision degradation in presence of irregularities, because the convergence period is not discern.

Additionally, the daily final solution of PPP has been evaluated by comparing daily solution in static and in kinematic way. Note that static solution is estimated in forward processing mode, while, kinematic in backward mode. The final daily solution is obtained from the summary file (‘*.sum’*).

Table 3.2 IGS reference stations coordinates in the IGS05 (ITRF2005 IGS realization) at epoch 2000-01-01 00:00:00. Extracted from IGS05.CRD and IGS05.VEL.

IGS05	X (m)	Y (m)	Z (m)	Vx (m/year)	Vy (m/year)	Vz (m/year)
AREQ	1942826.2369	-5804070.2800	-1796894.2642	-0.0051	-0.0080	-0.0001
KOUR	3839591.4109	-5059567.5595	579956.9738	-0.0034	-0.0026	0.0131
NKLG	6287385.8019	1071574.4250	39132.8053	-0.0051	0.0210	0.0193
MALI	4865366.4384	4110737.4961	-331121.6530	-0.0157	0.0219	0.0159
NTUS	-1508022.7311	6195576.6823	148799.4809	-0.0293	-0.0063	-0.0055
GUAM	-5071312.7759	3568363.5143	1488904.3079	0.0064	0.0078	0.0042
AMC2	-1248596.1255	-4819428.2266	3976506.0200	-0.0145	0.0011	-0.0056
MAD2	4849202.4087	-360329.0606	4114913.1304	-0.0067	0.0188	0.0145

Table 3.3 IGS reference stations coordinates in the IGS08 (ITRF2008 IGS realization) at epoch 2005-01-01 00:00:00. Extracted from IGS08_R.CRD, IGS08_R.VEL, ITRF2008_R.CRD and ITRF2008_R.VEL.

IGS08	X (m)	Y (m)	Z (m)	Vx (m/year)	Vy (m/year)	Vz (m/year)
AREQ*	1942826.1976	-5804070.3145	-1796894.2632	0.0027	-0.0053	0.0075
KOUR*	3839591.3907	-5059567.5622	579957.0472	-0.0056	-0.0013	0.0120
NKLG	6287385.7712	1071574.5264	39132.9045	-0.0032	0.0220	0.0191
MALI	865366.3537	4110737.5992	-331121.5694	-0.0172	0.0200	0.0167
NTUS*	-1508022.8546	6195576.6211	148799.4442	-0.0217	-0.0024	-0.0113
GUAM	-5071312.7371	3568363.5483	1488904.3362	0.0061	0.0074	0.0052
AMC2	-1248596.1924	-4819428.2109	3976505.9974	-0.0146	0.0009	-0.0049
MAD2*	4849202.3710	-360328.9666	4114913.2020	-0.0086	0.0194	0.0130

***** ITRF2008

3.4.3. Coordinates transformation

In some cases, it has been decided to show the PPP performance in the East, North and Height (*e, n, h*) coordinates instead of in Cartesians. To estimate the East, North and Height coordinates offsets (d*e, dn, dh*), the Cartesian coordinates (*x, y, z*) displacement with respect to a reference point (x_r, y_r, z_r) from which reference geodesic (ellipsoidal) coordinates are estimated (see Eq. (3.4) and Eq. (3.5)) are transformed by the expression into Eq. (3.6) to Eq. (3.8) [Drake, 2002].

$$\phi_r = -\arctan\left(\frac{z_r}{\sqrt{x_r^2 + y_r^2}}\right) \tag{3.4}$$

$$\lambda_r = -\arctan\left(\frac{y_r}{x_r}\right) \tag{3.5}$$

$$de = \sin(\lambda_r)(x - x_r) + \cos(\lambda_r)(y - y_r) \tag{3.6}$$

$$dn = -\sin(\phi_r)\cos(\lambda_r)(x - x_r) - \sin(\phi_r)\sin(\lambda_r)(y - y_r) + \cos(\phi_r)(z - z_r) \tag{3.7}$$

$$du = \cos(\phi_r)\cos(\lambda_r)(x - x_r) + \cos(\phi_r)\sin(\lambda_r)(y - y_r) + \sin(\phi_r)(z - z_r) \tag{3.8}$$

Chapter 4.
General analysis of the rapid fluctuations of total electron content

As mentioned in Chapter 2, irregularities are characterized by TEC fluctuations and can be identified by large values in ROT. The first objective of this doctoral work is to broadly analyze the large ROT values occurrence to understand the physical phenomena involve in the manifestation of the irregularities that cause them.

The high ROT occurrence suffer strong latitudinal differences. In low-latitudes (Equatorial region) irregularities mostly develop in the evening hours even during geomagnetically quiet conditions while in mid-latitudes the largest perturbations are related to Space Weather events and geomagnetically disturbed conditions. The following sections show the results obtained in these two latitudinal regions.

Section 4.1 presents the occurrence of irregularities over low-latitudes stations which are characterized by ROT values above the threshold established in the previous chapter. Section 4.2 describes the occurrence of irregularities observed mid-latitudes stations in both quiet and perturbed conditions. Section 4.3 account for SITEC events in mid-latitudes, while Section 4.4 summarizes the discussion regarding the present chapter.

4.1. High ROT occurrence in low-latitudes

In low-latitudes small scale irregularities may develop after a cascade effect from broader plasma bubbles characterized by TEC depletions, and may cause rapid phase fluctuations of the signal.

The aim of the present section is to describe the ionospheric irregularities occurrence by means of ROT. For that purpose following the procedure explained in Section 3.3.1, two threshold values have been established, a lower value of 0.3 TECU/30s and a higher of 1 TECU/30s. Note that ROT values exceeding those thresholds may be caused by different kind of irregularities (such as EPBs or SITECs) independently of their nature.

The estimated ROT for all stations and years is analyzed and to simplify the analysis only maximum ROT values (in absolute value) above the threshold are considered in order to distinguish quiet from disturbed ionospheric periods

(characterized by the presence of plasma irregularities causing the observed TEC fluctuations).

Figure 4.1 shows the low-latitude ionospheric irregularities occurrence by means of ROT for all stations and analyzed years. ROT values above 0.3 TECU/30s are shown in blue and above 1 TECU/30s in red. Blanks in the figures are due to the absence of input data files or discarded bad quality files. In the upper row, year 2001 (HSA) results are shown. ROT values above 1 TECU/30 s are observed after the local sunset (~19:00 LT) at the six stations for some hours duration. ROT values above 0.3 TECU/30s observed at 18:00–19:00 LT during equinoxes reflect the no-detrended nature of ROT and is related to the modulation of ROT curves due to the background TEC and its variation. A clear seasonal–longitudinal variability is observed in ROT. The American stations (AREQ and KOUR), present large ROT occurrence around the equinoctial months, clearly displaced to December solstice. On the other hand, the African stations (NKLG and MALI) present large values of ROT during the whole year. The diagonal lines observed in MALI are due to receiver tracking failures (just before and after the signal loss of some satellite signals). MALI observations are missing from March to April (DoY 065 to 116). Contrary to the American stations analyzed in the present work, the Asian (NTUS and GUAM) stations, show increased values around equinoxes slightly displaced to June solstice. NTUS observations are missing for the first half of the year.

The second upper row presents the results regarding year 2004 (which corresponds to MSA). This year ROT occurrence is reduced with respect to 2001 results, although it reaches the highest values in the same time period from sunset to midnight (19:00–00:00 LT). The strong ROT periods are reduced to the months close to the equinoxes in MALI, NTUS and GUAM. The high ROT extends from September to April in the American stations while in NKLG, still covers almost the whole year. The strongest ROT values are reached in the American and African regions, especially in KOUR, where high ROT occurrence also last longer.

The following row in Figure 4.1 presents the results corresponding to year 2008 (the lowest solar activity year under study). Due to the poor data quality, NKLG observations have been discarded from this work. Note that MALI station also shows a big data gap from September to December. ROT values obtained this year are below 0.3 TECU/30s most of the time in all stations. This year presents the lowest high ROT occurrence of all the years analyzed, as expected for LSA periods. In the American stations large ROT periods are still noticeable, with significant occurrence during 20:00–00:00 LT around the December solstice. In the Asian region, the days with largest ROT are centered on the equinoctial months, exceeding the threshold only for few periods and with a short duration of about 3 h.

Finally, the results for year 2011 are presented in the bottom row. As in 2004, the solar activity in 2011 was moderate and the strong ROT occurrence is similar to 2004, but higher (see Table 4.1). 19:00–00:00 LT is again the period when largest ROT values (above 1 TECU/30 s) are observed.

From these results it is evident that the daily occurrence of high ROT values varies with local time, season, station and solar activity, typically covering longer periods of time during equinoxes than in solstices. And as the solar activity decreases, strong ROT tends to concentrate around equinoxes.

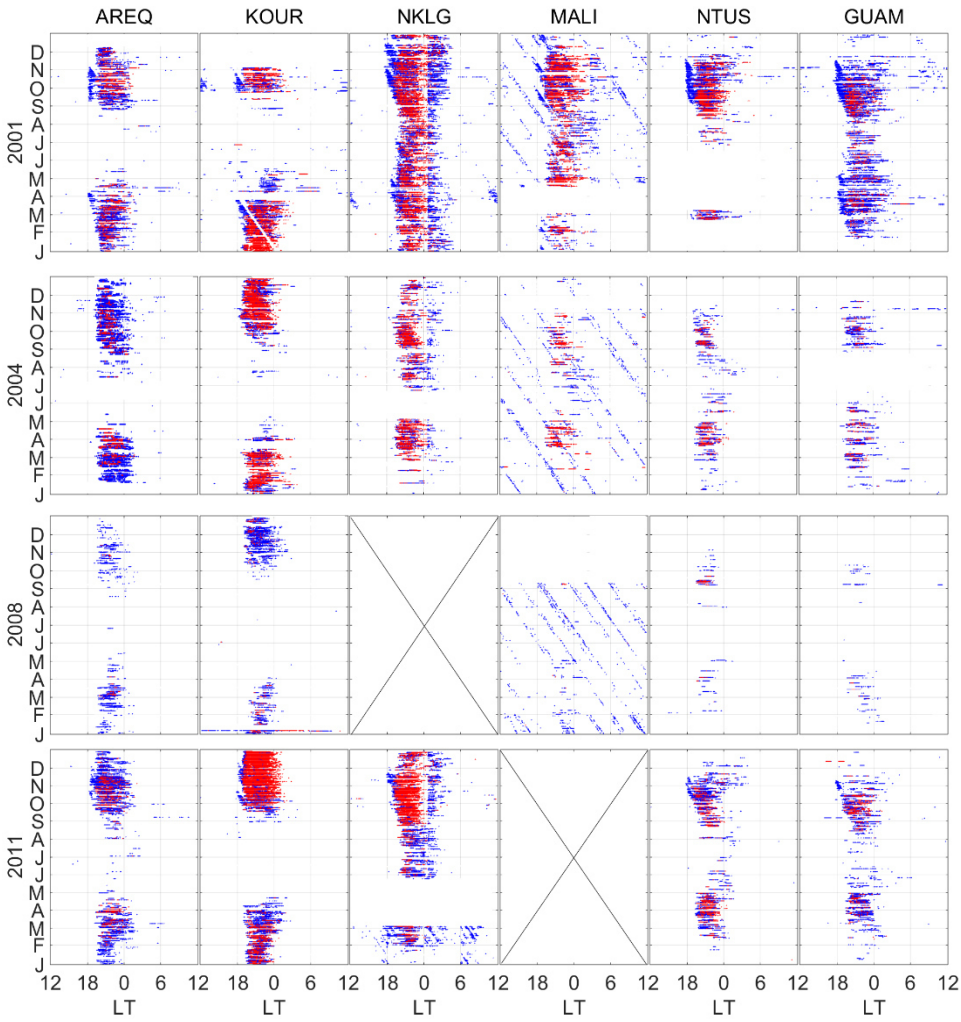

Figure 4.1 Occurrence of high ROT in low-latitudes for each year and station under study. In blue ROT above 0.3 TECU/30s and in red ROT above 1 TECU/30s. From left to right: AREQ, KOUR, NKLG, MALI, NTUS and GUAM stations.

Large ROT values occur mainly from soon after local sunset to midnight, but in some cases, particularly in periods of HSA and around equinoctial months, they may also take place in post-midnight hours. Nevertheless, the largest ROT values barely appear after midnight. The annual behavior of strong ROT occurrence presents a seasonal variability that depends on geographic longitude and solar activity.

Table 4.1 summarizes the percentage of days of each year in which ROT values exceeding the threshold value imposed (0.3 TECU/30 s) are presented. In 2001, American and Asian stations present large ROT values in more than the 60% of the analyzed days, and the African stations around 90% of the days while in 2008 the percentage of active days is reduced to 40%, 10% and 60%, respectively. The drop in the occurrence of the observed large ROT values, especially after midnight and during LSA periods is, in part, due to the lower density of the background ionospheric plasma. Since the method used is very sensitive to the difference that exists between the background ionosphere and the depleted electron density of irregularities, it cannot be stated that plasma irregularities are not there, since the detection depend on the probe, and this method is only sensitive to sharp horizontal gradients. It should be remembered that the ROT calculated in this work, as mentioned in Chapter 3, depends on pseudoranges noise and that the threshold values established could be loose enough not to be able to detect the faintest structures.

Table 4.1 Percentage of days with ROT > 0.3 TECU/30s for the 4 years and 6 stations analyzed.

YYYY/ID	AREQ	KOUR	NKLG	MALI	NTUS	GUAM
2001	60.5	61.9	93.8	86.4	63.3	65.6
2004	72.9	56.5	67.9	72.0	33.6	33.3
2008	37.1	41.7	-	57.2	9.8	9.6
2011	57.8	58.7	88.7	-	42.2	44.2

The day to day variability, has been observed to be affected by magnetic perturbations, in which either irregularities inhibition or induction occur.

Figure 4.2 shows irregularities suppression on the night of March 4th, 2001 over KOUR, coinciding with a geomagnetic storm development which peaks on DoY 064, 2001 at the time the irregularities would be expected to evolve with a minimum Dst value of -73 nT.

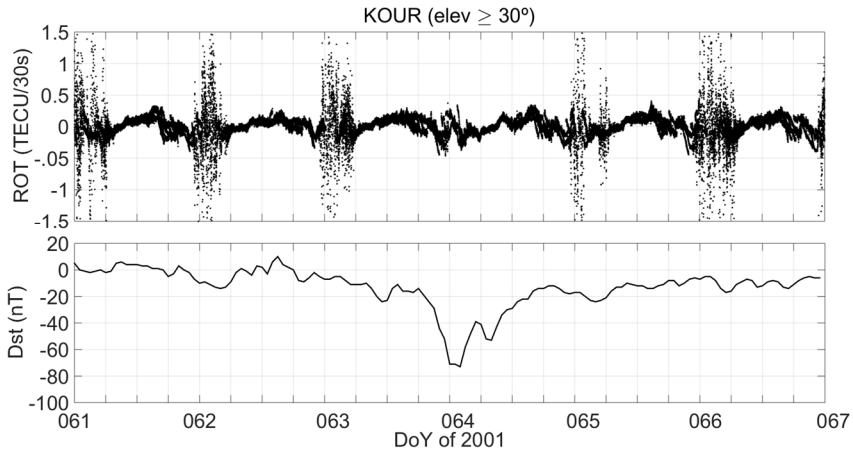

Figure 4.2 Irregularities inhibition from DoY 063 to 064 of 2001 over KOUR (LT=UT-3.527). Top: ROT for all satellites in view above 30º. Bottom: Hourly Dst index values (Data from the omniweb whose source is WDC for Geomagnetism Kyoto: http://wdc.kugi.kyoto-u.ac.jp/dstdir/index.html).

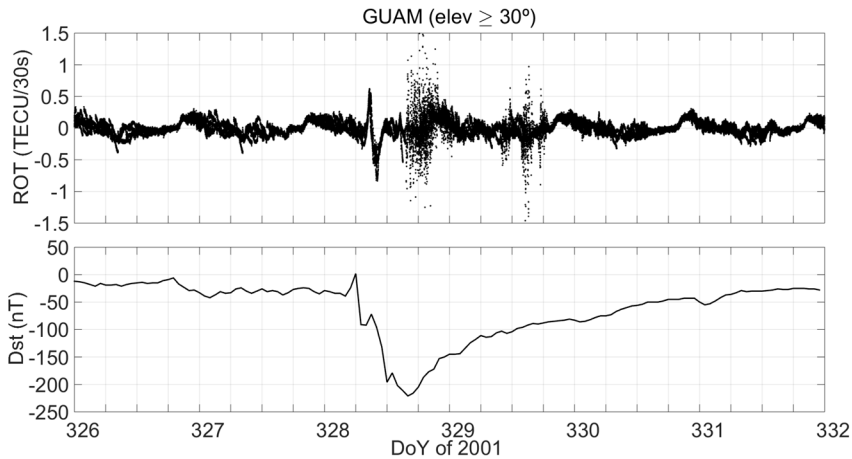

Figure 4.3 Irregularities induction on DoYs 328 and 329 of 2001 over GUAM (LT=UT+9.66). Top: ROT for all satellites in view above 30º. Bottom: Hourly Dst index values (Data from the omniweb whose source is WDC for Geomagnetism Kyoto: http://wdc.kugi.kyoto-u.ac.jp/dstdir/index.html).

On the other hand, Figure 4.3 shows irregularities induction over GUAM on local nights of November 25th (DoY 328) and 26th (DoY 329) of 2001, coinciding with a geomagnetic storm development which peaks on DoY 328, 2001 with a minimum Dst value of -221 nT (in post-midnight hours on November 25th). Note that irregularities evolve in post-midnight hours on November 25th and in post-sunset hours on November 26th.

Dst index is an indicator of the presence of a geomagnetic storm, but does not offer information regarding the source of irregularities induction or suppression (if there is a PPEF effect or a DD effect the one which is altering the electrodynamics of the ionosphere).

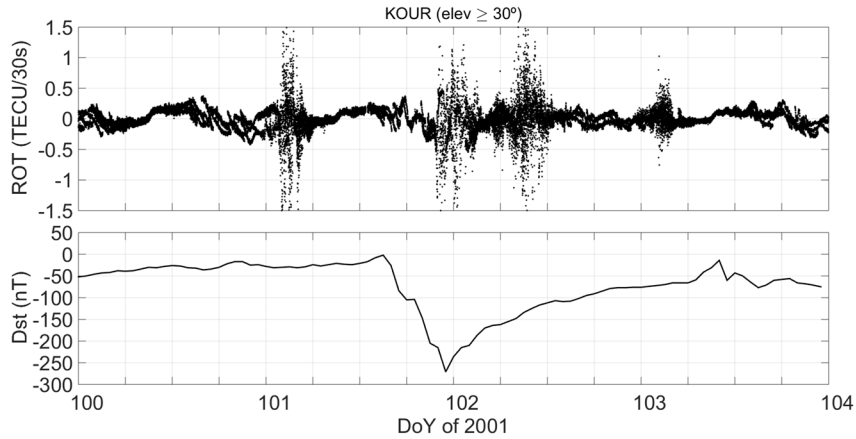

Figure 4.4 Irregularities induction at dawn on DoY 102, 2001 over KOUR. Top: ROT for all satellites in view above 30º. Bottom: Hourly Dst index values (Data from the omniweb whose source is WDC for Geomagnetism Kyoto: http://wdc.kugi.kyoto-u.ac.jp/dstdir/index.html).

Additionally, there are magnetic perturbed days in which irregularities are observed at dawn (or in the vicinity), even if most of the irregularities occurring after midnight, which do not necessarily occur in presence of magnetic perturbations, suppress just prior to sunrise. An example is presented on Figure 4.4 which shows irregularities occurrence to be a little bit anticipated on April 11th, 2001 (DoY 101) and last until almost local midday of April 12th (DoY 102), 2001, coinciding with a geomagnetic storm development which peaks with a minimum Dst value of -271 nT on DoY 101, 2001.

The days reported to present large ROT values at dawn are listed in Table 4.2 (but not the ones that suppress just at that time, at sunrise). The irregularities occurring in post-midnight and that are suppressed at dawn are not listed on that table. It should be pointed out the differences observed in the occurrence of dawn large ROT with location and year. Note that AREQ and GUAM are the stations that present the major occurrence, even if they do not coincide with a remarkable geomagnetic activity. Remember that these are not all the cases that represent the irregularities occurrence at dawn, but also the cases exceeding the mentioned threshold value, which is representative of the varied geomagnetic activity found in that kind of cases.

Table 4.2 DoYs with presence of ROT above 0.3 TECU/30s at dawn. In brackets minimum value reached in Dst (nT) on that day from the WDC for Geomagnetism Kyoto.

YYYY	AREQ	KOUR	NKLG	MALI	NTUS	GUAM
2001	102 (-236)	078 (-105)	---	295 (-177)	229 (-105)	079 (-148)
	108 (-114)	102 (-236)			284 (-70)	118 (-33)
		108 (-114)			328 (-216)	148 (-42)
						149 (-28)
						328 (-216)
2004	025 (-81)	---	---	---	207 (-130)	020 (-38)
	027 (-62)				209 (-170)	022 (-130)
	265 (-19)					042 (-93)
	327 (-35)					
	333 (-50)					
	334 (-34)					
2008	014 (-23)		---	---	---	---
2011	063 (-17)	---	298 (-147)	---	---	096 (-60)
	070 (-83)					148 (-80)
	103 (-45)					
	253 (-75)					
	275 (-32)					
	298 (-147)					

Though there is still lack of knowledge regarding the irregularities occurrence day to day variability and specific sources causing it still remain unidentified, for a better compression of the phenomena involved, a deeper case by case analysis, including multi-instrument observations, is needed. It is not the scope of this work to accomplish that, but to analyze its effect on positioning, which is done in Chapter 5 and a day to day variability analysis is proposed for future works.

4.2. Irregularities occurrence in mid-latitudes

Regarding mid-latitude station analysis, as mentioned in Chapter 3, the more common irregularities present are TIDs, although other kind of irregularities may also appear which include magnetic perturbed conditions related fast fluctuations of ROT and SITECs.

In this section, the ionospheric irregularities observed in AMC2 and MAD2 stations by the procedures explained in Chapter 3 are summarized.

In AMC2 the years analyzed correspond to 2001, 2004, 2008 and 2011, while for MAD2, a longer analysis period has been considered: almost an entire solar cycle from 2005 to 2015. The so long dataset (almost an entire solar sunspot cycle) permits analyzing the occurrence and behavior of mid-latitudes ionospheric irregularities during both geomagnetically quiet and perturbed conditions.

Attending to their characteristics by means of their shape in ROT, four kinds of irregularities are observed: (1) travelling ionospheric disturbances (TIDs), (2) ROT protuberances due to positive ionospheric storms, (3) fast variations in ROT related to small scale irregularities which can be, or not, of geomagnetic perturbed origin and (4) SITECs induced by solar flares. The following subsections present each of these cases.

4.2.1. Regularly occurring irregularities: TIDs

As mentioned, analyzing the ROT obtained from each satellite from daily RINEX files of 11 years of GPS data record, we found that the most frequent kind of irregularities in MAD2 are by large TIDs. The same occurs for AMC2 in 2001, 2004, 2008 and 2011.

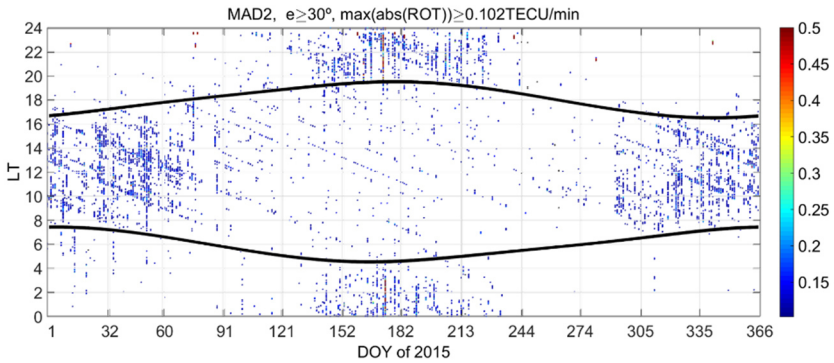

Figure 4.5 Ionospheric irregularities occurrence by means of detrended ROT (in TECU/min units) in MAD2 during 2015. In black, solar terminators.

Figure 4.5 has been obtained by applying three processes; (1) a filtering of ROT values (in TECU/min but still with a 30 s sampling rate) by removal of 15 min running mean to emphasize the modulation of the ROT curves; (2) a smoothing made considering the trend obtained with 2 min average in order to remove fast changes (peaks); and (3) considering the maximum absolute value of this detrended and smoothed new ROT to be larger than a threshold value. This threshold value (0.102 TECU/min in the concrete case of MAD2 2015) is calculated by the expression P75+3IQR, where P75 stands for the percentile 75 and IQR for the inter

quartile range, both calculated with yearly data. In order to remove low elevation effects, satellites below 30º are discarded.

As in the case shown in Figure 4.5, in all the years under study, daytime TIDs have been observed to occur mostly in both the first and the last trimester of each year from sunrise to sunset (~08:00-17:00 LT), also in periods of LSA (see Appendix D). On the other hand, nighttime TIDs occur from May to August from sunset to sunrise (~20:00-04:00 LT).

This kind of fluctuations typically are slowly varying trends, and they may affect PPP only, like the regular ionospheric effect, in terms of higher-order ionospheric effects. As stated by Hoque and Jakowski, [2007] the residual error of the second-order effect of the ionosphere in the IF combination may affect millimeter-level accuracy. However, this effect is unnoticeable when dealing with the actual accuracy expected for the PPP which is of the order of centimeter to decimeter. Therefore, they are not the kind of 'threat', that is under the scope of this work, although fast fluctuations related to these TIDs have been also identified, being in genera more intense in AMC2 than in MAD2. These noisy structures are caused by small scale irregularities whose source is not well understood yet, and they do not cause major problems.

4.2.2. Space Weather related irregularities occurrence

In addition to the regular disturbances the mid-latitude stations studied also show noticeable ionospheric irregularities which depend on Space Weather and leave a characteristic signature in ROT.

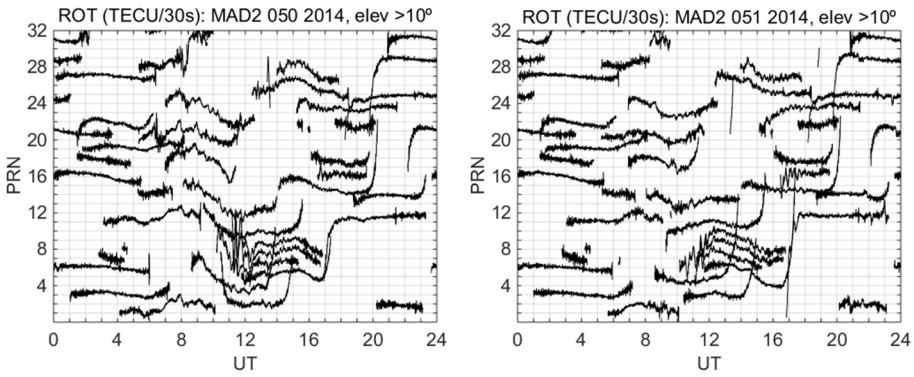

Figure 4.6 Positive ionospheric storms effect on no-detrended ROT of each GPS satellite over MAD2 on DoYs 050 (left) and 051 (right) of 2014.

In particular, daytime positive ionospheric storms exhibit a simultaneous large amplitude modulation in all the group of satellites over a station. Figure 4.6 presents an example of the positive ionospheric storms related to February 19th and 20th, 2014 (DoYs 050 and 051) event [Rodríguez-Bouza et al., 2015]. Note the ROT intensification characterized by wider humps in the 07:00 - 17:00 UT interval on DoY 050 of 2014, and just after 12:00 UT on DoY 051 of 2014.

As with TIDs, this ionospheric electron content variation can be considered to vary "slowly" from the point of view of the trace caused on ROT. From the point of view of its effect on PPP errors magnitude, they may contribute to higher order ionospheric effects, but they are not under the scope of this work.

On the other hand, although no so frequent, strong TEC fluctuations related to geomagnetic disturbed periods are also present (see Figure 4.7), which could be a concern for PPP applications.

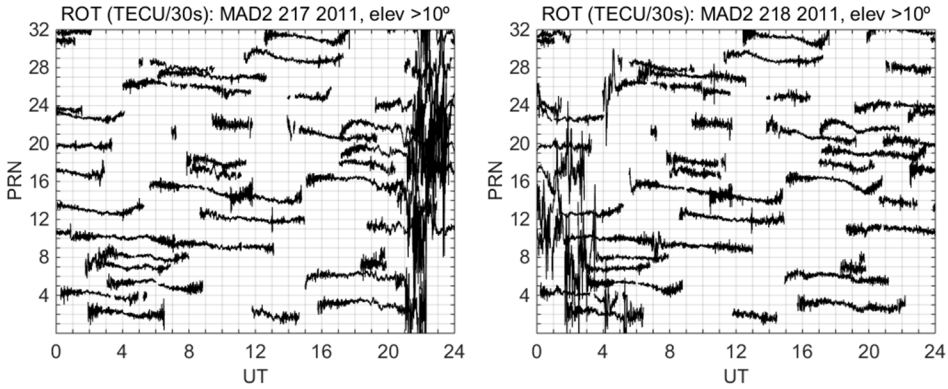

Figure 4.7 Geomagnetic storm induced nighttime irregularities in no-detrended ROT measured by each GPS satellite in MAD2 station from August 5th (DoY 2017, left) to 6th (DoY 218, right) of 2011.

Like in the example shown in Figure 4.7, these irregularities characterized by strong ROT fluctuations have been observed to be particularly severe in geomagnetic nighttime perturbed periods, occurring when the main phase of the geomagnetic storm drops in the interval from sunset to midnight. A list of the observed events in MAD2 and AMC2 is presented in Table 4.3, and figures of ROT and Dst can be found on Appendix D.

It is worth mentioning that, AMC2 is located at higher geomagnetic latitude than MAD2. For that reason during geomagnetic storm periods AMC2 is more prone to be affected by high latitude phenomena, while the later may experience low latitude related singularities. The event of DoY 101, 2001 in AMC2 didn't

happen at local nighttime. Furthermore, DoYs 190 of 2005 and 186 of 2012 also present nighttime irregularities on MAD2. However, these days are not magnetically perturbed, and the possible reason for ionospheric irregularities occurrence is, at present, unknown.

Table 4.3 Dates with presence of fast ROT fluctuations in geomagnetic perturbed periods**.**

AMC2	MAD2
090 2001	021 2005
101 2001*	163-164 2005
301 2001	215-216 2010
310 2001	217-218 2011
328 2001	179-180 2013
298 2011	058-059 2014
	173-174 2015

*not in local nighttime

4.3. SITECs

Another kind of irregularities present in daytime and more frequent in periods of HSA are SITECs. The main characteristic of a SITEC is a fast peak in ROT of few minutes of duration that occurs simultaneously in all the satellites whose signal is travelling by the daytime ionosphere. Figure 3.11 shown in Chapter 3 depict an example of the presence of a SITEC disturbance in ROT at 8:15 UT. The list of SITECs observed in the mid-latitudes stations under study can be found in Appendix D, Tables D.1 and D. 2.

The peak values of mean ROT reached in AMC2 are in the 0.02-0.8 TECU/30s interval, whereas the values in MAD2 are found to be in the 0.04-0.8 TECU/30s range. Smaller intensity SITEC are probably mis-detected, but it is not the scope of this work to develop a procedure for an effective SITEC detection, since the last goal is to analyze its effect on PPP. It is worth mentioning that, the maximum values reached on those SITECs mean ROT, are much smaller than the ones corresponding to the event whose case study will be presented in Chapter 6.

However, due to the large number of SITECs detected it seems a promising technique to exploit and develop for almost real time applications.

4.4. Summary

Regarding low latitude stations AREQ, KOUR, NKLG and MALI present the highest percentage of epochs with ROT > 0.3 TECU/30 s during the period 19:00–01:00 LT, especially in 2001. As the solar activity decreases, strong ROT occurrence tend to reduce towards equinoxes, and tend to last less, with almost no occurrence after local midnight. However, seasonal differences that depend on the longitude of the considered station take place. The results shown in this work follow the pattern noted by other authors where the nighttime irregularities maximum occurrence stands out during high solar activity (Gentile et al., 2006; Nishioka et al., 2008; Magdaleno et al., 2012) and magnetic equinoxes (Burke et al., 2004; Li et al., 2007) even if day to day variability is still observed, whose cause has not been analyzed in the present study since there are contributors to the emergence of irregularities at these longitudes which are out of the scope of this work.

In mid-latitudes, the more common irregularities occurring in both quiet and geomagnetically perturbed periods are TIDs, which follow the occurrence pattern previously described by Wautelet and Warnant, [2013]: daytime TIDs occurring typically in both first and last trimester of each year from and nighttime TIDs occurring from May to August. These TIDs are not a threat for actual PPP accuracy. However, small scale irregularities characterized by fast ROT fluctuations may also appear which can be especially severe in geomagnetic perturbed conditions which have been observed to occur typically at nighttime.

Additionally, SITECs may appear in both low- and mid-latitudes of the sunlit hemisphere, producing fast changes in ROT, which in MAD2 for 2005-2015 interval and AMC2 in 2001, 2004, 2008 and 2011, have been observed to have peak values on the mean ROT that do not reach 1 TECU/30s and to be more frequent in periods of HSA than in LSA.

Slowly varying ROT is not a threat for the actual PPP expected accuracy (centimeter to decimeter-level) since IF combination corrects the ionosphere except higher order effects which are of the order of millimeters. However, fast changes in ROT may be indicate the presence of scintillation which can degrade the GPS signal or catch out the positioning software resulting in accuracy degradation. This irregularities effect on PPP is evaluated in Chapter 5.

Chapter 5.
PPP performance in the presence of large ROT

The second objective of this doctoral work is to analyze the large ROT effects on PPP. In the evolution of this work it has been observed that the irregularities effect on PPP is not a straight forward cause-effect problem, but it looks more like a cascade effect with many contributors that account to the observed errors such as:

(1) signal degradation and scintillation;

(2) problems in the receiver tracking performance with the subsequent observable misinterpretation or, in last instance, signal (observable) loss;

(3) the ability of PPP softwares' to operate with observables that have been affected by (1) and (2), which includes the procedures used to overcome CS, diffraction or higher-order ionospheric effects;

(4) DOP enlargement after signal losses, due to the new satellites constellation geometry.

The aforementioned diffraction or higher order ionospheric effects analysis has not been included to this work because the magnitude of the errors induced are lower than the accuracy of the particular PPP procedure used.

This chapter summarizes the phenomena observed in PPP in the presence of high ROT. Results are based on kinematic mode although some observations with respect to static mode also appear in the end. As in the previous chapter, the intention was to differentiate low- and mid-latitudes; however, no promising results were observed in mid-latitudes and therefore, as in static PPP, no more than few comments are made in the corresponding section. All in all, most results showed in this chapter are referred to low-latitudes stations and kinematic PPP.

In the first section of this chapter (Section 5.1) receivers tracking performance is analyzed by means of signal loss, paying special attention to observable loss in the presence of high ROT. Some remarks regarding the data and results reproducibility are also made. In Section 5.2, kinematic PPP is evaluated in low-latitudes showing accuracy degradation occurrence, and analyzing solution repeatability and ambiguities reset contribution to the errors observed in periods of high ROT. In this part, GLONASS influence is also evaluated and some examples regarding PPP daily final solution are also presented. Section 5.3 shows some case studies regarding DOP, GLONASS and higher sampling rate effect on PPP in

periods of strong ROT. Section 5.4 is used to make some comments regarding mid-latitude results, and Section 5.5 presents a summary of this chapter.

The results of this chapter have been partially published in Rodríguez-Bilbao et al., [2015a].

5.1. Receivers tracking performance

The availability of GPS signals in both frequencies is particularly important not only for ionospheric information retrieval but also for PPP and its applications. For this reason, in this section the GPS receiver tracking performance is analyzed by evaluating the occurrence of observable loss recorded in RINEX files.

5.1.1. Signal Loss

Signal losses for continuous periods of 1.5 min to 15 min, occurring in any of the observables for each station and year under study, are plotted in Figure 5.1. A minimum elevation mask of 20º is imposed to diminish the contribution of losses related to multipath effect. Signal losses from satellites with elevation below 45º (which will be referred in the text as "low elevation satellites") are represented in gray while those corresponding to satellites with elevation above 45º ("high elevation satellites" following this notation) are represented in black. The diagonal lines reflect systematic losses which denote that the signal loss occurs in a concrete satellite constellation geometry which, due to GPS satellites orbital period (11 h 58 min), repeats 4 min earlier every day. The predominating diagonal lines correspond to satellites below 45º (in gray) and may be associated to risings (settings) of satellites, and obstructions present in the LoS.

During 2001, 2004 and 2011 observable loss increases in periods coinciding with high ROT (Figure 4.1), although it is not so evident for AREQ 2001 and NTUS 2004, due to the fewer occurrence of losses even if large ROT was present.

In 2001 a frequent loss of observations occurs especially in NKLG and MALI. From DoY 001 to 064 2001 MALI reflects problems with the receiver performance, and the receiver was replaced later in April (see Appendix D). Note that coinciding with periods of large ROT values, NTUS only loses signals of low-elevation satellites while KOUR, NKLG, MALI and GUAM also lose signals of satellites above 45º. This difference may be related to the magnitude of the gradients present in the local ionosphere or to the receiver sensitivity to those satellite loss.

In 2004 the high ROT situation observed in AREQ, KOUR, NKLG and GUAM produces significant signal losses for satellites above 45º. KOUR station presents tracking problems from June till November and the receiver is replaced on September 30th (see Appendix D).

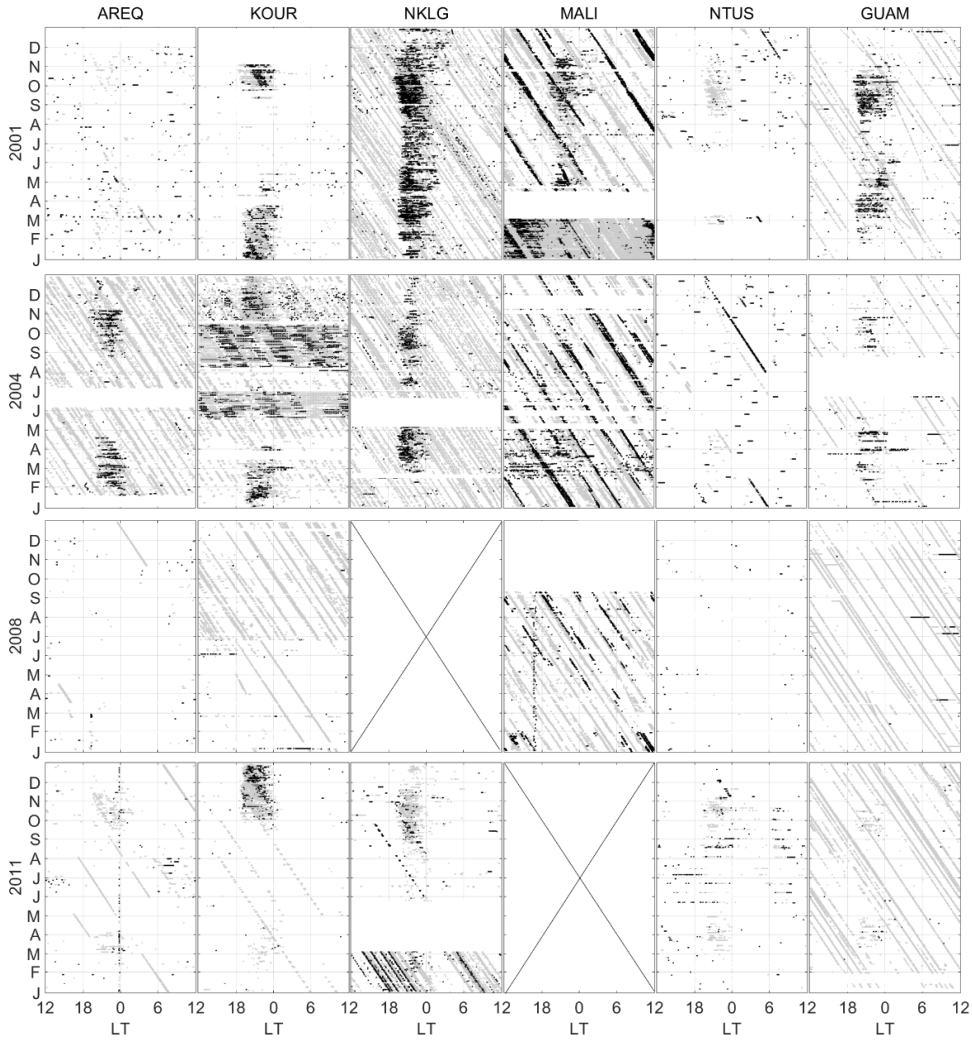

Figure 5.1 Daily occurrence of signal loss for AREQ, KOUR, NKLG, MALI, NTUS and GUAM stations at years 2001 (top), 2004, 2008 and 2011 (bottom). From left to right C1, P1, P2, L1 and L2 observables. In gray, satellites with elevations in the interval 20º- 45º and in black, satellites above 45º.

The signal loss occurring in 2008 cannot be attributed to ROT. During this year, KOUR station receiver is replaced quite often (in January, April, May and June, see Appendix D) and this is manifested in the signal loss behavior represented in Figures 5.1 to 5.4. GUAM receiver is changed in November (see Appendix D) from when it experiences a decrease in the occurrence of signal loss.

Finally, in 2011, despite the large ROT observed in Figure 4.1, the signal loss is not as strong as in 2004, particularly when satellites above 45º are considered.

This can be explained by means of the improvement in the receiver tracking capabilities, especially to overcome the influence of the ionosphere. Nevertheless, numerous signal losses are observed in all stations in periods of strong ROT, especially in KOUR and NKLG in the second half of the year. In January and February, NKLG reflects systematic losses related to a degraded receiver tracking performance.

Comparing Figures 4.1 and 5.1 it is obvious that signal loss occurrence increases in periods of large ROT. Due to the improvement in the receivers' capability to deal with the presence of ionospheric irregularities effects, high elevation satellites signal loss coincident with high ROT periods decrease in 2008 and 2011 with respect to 2001 and 2004. The signal loss peak occurs from 19:00 to midnight, with a maximum around equinoxes, except for KOUR whose peak is displaced to December solstice. It is evident that the lower the solar activity, the fewer the signal losses. A clear exception is NTUS, where in general, no ROT-related signal loss is observed for high elevation satellites, and AREQ, which also shows a particular behavior with no high ROT-related signal loss during 2001.

5.1.2. Observable loss

Although ionospheric conditions were not identical in each station and time, due to geomagnetic coordinates' differences and the irregularities seasonal and SC dependence, the results shown in Section 5.1.1 suggest significant tracking performance differences among receivers during periods of high ROT.

Figure 5.2 independently illustrates the occurrence of missing pseudo range or carrier phase observations for continuous periods of 1.5 min to 15 min, in KOUR station for the 4 years under study. An elevation mask of 10º (the same as in PPP) is applied in this case. Again, signal losses from satellites with elevation below 45º are represented in gray while those corresponding to satellites with elevation above 45º are depicted in black. This station exemplifies a complete case of study since it shows very different tracking performances depending on the receiver installed in each time. Note that post sunset signal losses occur mainly in the 18:00-01:00 LT interval, coinciding with periods of high ROT (see Figure 4.9). However, it is noteworthy, the differences manifested for each receiver in each observable loss. For receiver and antenna information see Appendix D.

In 2001 (see upper row of Figure 5.2), observable losses increase in periods coinciding with high ROT. However, high elevation satellites only lose pseudo ranges (C1, P1, P2), but not carrier phases.

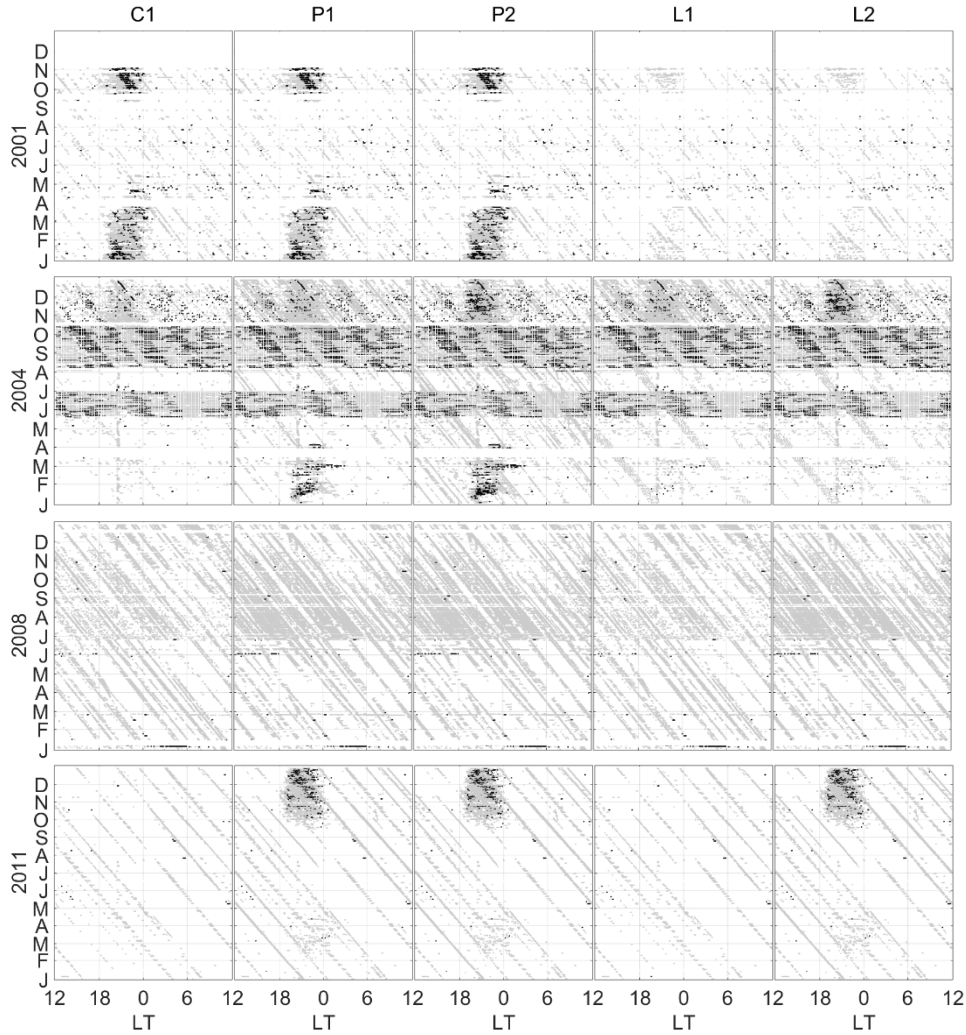

Figure 5.2 Daily occurrence of observable loss in KOUR station for 2001 (top), 2004, 2008 and 2011 (bottom). From left to right C1, P1, P2, L1 and L2 observables. In gray, satellites with elevations in the 10º- 45º interval and in black, satellites above 45º.

On the other hand, in 2004 (see the second row of Figure 5.2), three different behaviors are discerned. The first one, corresponds to the time period from January to mid-October but ignoring end of May-June and August-October periods. In general, L1 and L2 losses are similar, while P2 suffers more losses than P1 and C1, being the later one the observable with less losses. Considering the periods coinciding with high ROT shown in Chapter 4, P1 and P2 are the most affected signals both in low and high elevation satellites. The second behavior corresponds to the time period ignored in the first case where for an unknown reason (unknown because these periods do not coincide with changes in the receivers or the antennas

reported in Appendix D), the receiver suffers an increased amount of signal losses in all observables from several satellites. The receiver has problems to maintain the lock at particular satellites in certain geometry configurations. The third behavior extends from the end of October to the end of 2004. In this period C1, P1 and L1 suffer, a larger amount of losses in low elevation satellites, while L2 and P2 also present high elevation satellites losses in periods coinciding with high ROT.

In 2008 (see third row of Figure 5.2), observables losses increase from June to the end of the year, being L1 and C1 the ones suffering the less amount of losses. High ROT related loss is insignificant this year.

Finally, in 2011 only P1, P2 and L2, observables show increased signal loss in periods coinciding with high ROT, especially in the last trimester of the year.

5.1.3. Good performance vs malfunctioning

After examining Figure 5.1, it can be stated that essentially three sources of signal loss exist: receiver "malfunctioning", signal obstruction (or low elevation multipath effect) and effects of ionospheric origin. Each of them has individual remarkable characteristics.

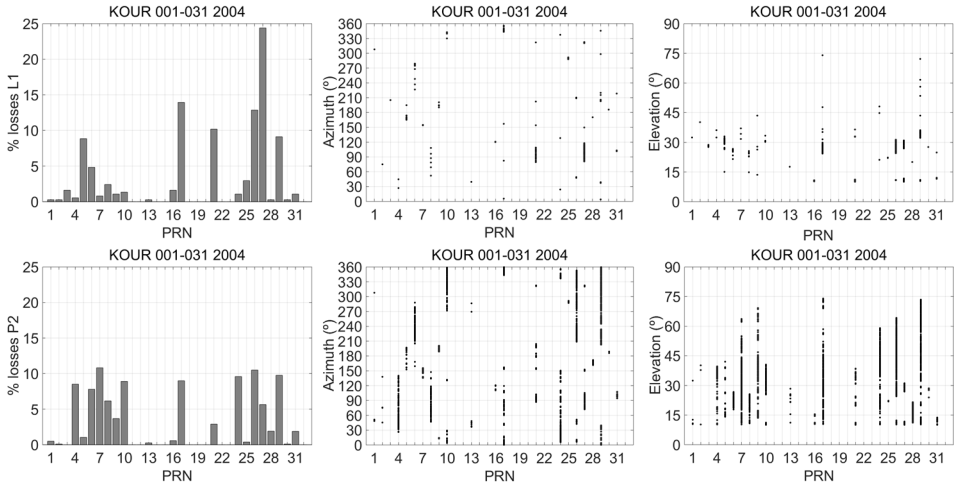

Figure 5.3 L1 observable loss (top) and P2 observable loss (bottom) at KOUR for January 2004. From left to right: PRN vs percentage of losses, PRN vs azimuth and PRN vs elevation.

Figure 5.3 shows L1 (top row) and P2 (bottom row) losses at KOUR in January 2004. In Figure 5.2 it has been pointed out that L1 suffers less losses related to high ROT periods with respect to P2. This difference in losses occurrrence is also observed in Figure 5.3. Since ionospheric irregularities are constricted to a certain local time, only some satellites are affected by them. Note that high elevation satellites losses in P2 only occur in 6 of the GPS satellites (G07, G09, G17, G24, G26 and G29).

On the other hand, Figure 5.4 shows L1 observable losses in a "normal" tracking execution corresponding to April 2004 (left column), and in a receiver "malfunctioning" situation like the one of June 2004 (right column). Losses occurring in satellites with low elevation angles at privileged directions (azimuth) like the ones shown in the left column, suggest signal obstruction and multipath as the main signal loss sources. More isotropic situation like the one shown in the right column pictures is more representative of receiver "malfunctioning".

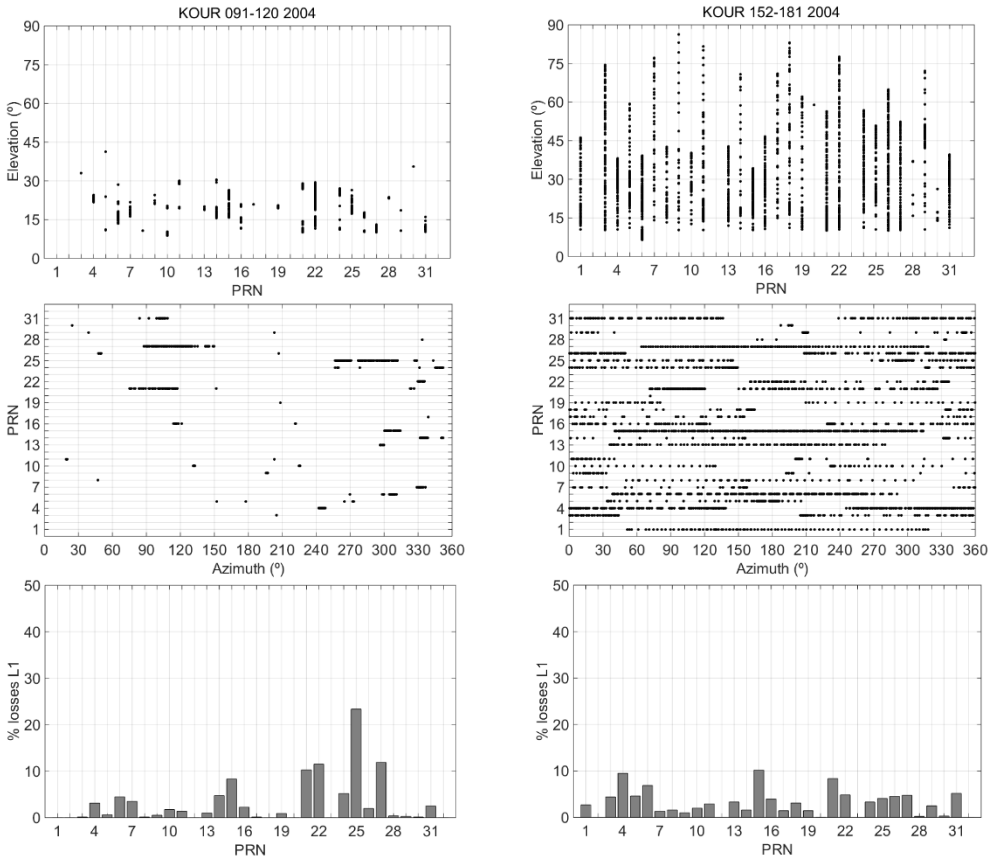

Figure 5.4 L1 observable loss at KOUR in April (left) and June (right) of 2004. From top to bottom: PRN vs elevation, PRN vs azimuth and PRN vs percentage of losses in L1.

5.1.4. Reproducibility checking: receivers performance comparison

Figures 5.1 to 5.4 illustrate not only the receiver tracking performance in "normal" ionospheric unperturbed conditions, but also the way they operate in periods of high ROT, emphasizing the time periods (daily and annual) where signal loss is more prone to occur. Although these represent a clear example of the existing correlation between strong ionospheric gradients characterized by large ROT values and frequent satellite signal losses, as shown in Figure 5.2, it is worth stressing that the receiver characteristics are the ones that under similar conditions lead the occurrence of some observable loss and no others. Under "similar environmental conditions", the different characteristics of the receivers such as the number of satellites tracked, the receiver and antennas characteristics or the introduced noise, will lead to different troubles and results both in ionospheric parameters estimation and in receiver position estimation. To check this statement we present the following case study where the results of three close stations GUAM, GUUG, and CNMR are shown. The characteristics of these stations are summarized in Table 5.1.

Figure 5.5 shows from top to bottom, the root mean square (RMS) of ROT values, the mean value of the number of satellites used in PPP and the standard deviation (STD) of the first derivative of the estimated height for each day. The day interval 060-090 of 2011 is considered for the IGS stations listed in Table 5.1.

Table 5.1 Geographic coordinates and receiver and antenna types of GUAM, GUUG and CNMR stations on DoYs 060-090 of 2011.

STN ID	Geographic Coordinates	Receiver type Number (vers)	Antenna Type (Num.)
GUAM	13.5893ºN, 144.8683ºE 201.9 m	ASHTECH UZ- 12 IR2200722004 (CQ00)	ASH701945B_M (CR519992101)
GUUG	13.4332ºN, 144.8027ºE 134.7 m	TRIMBLE NETR5 4730K06582 (4.19)	ASH701945E_M (CR520022606)
CNMR	15.2297ºN, 145.7431ºE 64.4 m	TRIMBLE NETR5 4730K06594 (4.19)	TRM55971.00 (30518848)

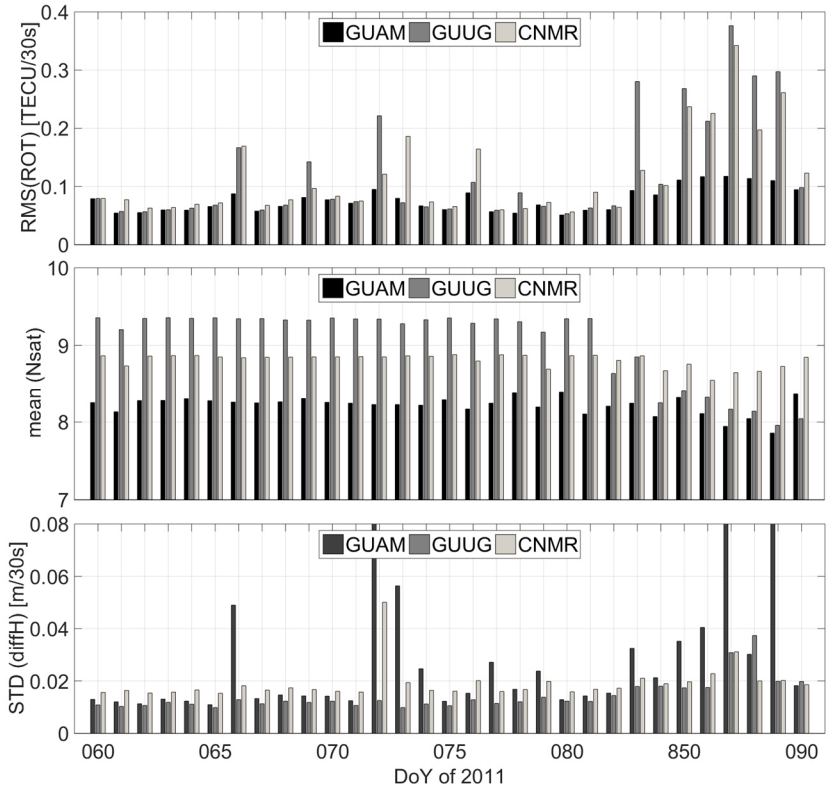

Figure 5.5 Daily values of the root mean square (RMS) of ROT (top row), the mean value of the number of satellites used in PPP (mid-row) and the standard deviation of the first derivative of the estimated height (bottom row) for GUAM, GUUG and CNMR in 060-090 2011 interval.

Note that even if GUAM and GUUG are the each other closest stations, the receiver's characteristics differ. On the other hand, GUUG and CNMR have the same receiver type but they are located further one of each other. All in all, the RMS of ROT suffers small differences from one station to the other except for DoYs that RMS of ROT exceeds 0.1 TECU/30s (top row of Figure 5.5). For these days note that GUUG and CNMR (the ones with the same receiver) show similar performance. On the other hand, when the mean value of the number of satellites is studied (middle row of Figure 5.5), the only resemblance between stations is the shape of the daily performance: a constant value until DoY 081, from which on the number of satellites decreases. The days where RMS of ROT increases notably, especially from DoY 083 to 090 of 2011, the average number of satellites decreases and PPP performance deteriorates. The results are slightly worse for GUAM and it can be attributed, in part, to a decreased number of satellites considered for PPP.

This example shows that an analysis of data and results reproducibility is not a straightforward task with the actual IGS receivers' coverage which in low-latitudes is not so dense and where a variety of receiver types are deployed. However, it evidences that under similar ionospheric conditions, receiver characteristics (including antenna and electronics) mark the differences in the observables (data) and results.

5.2. Kinematic PPP in low-latitudes

To evaluate the kinematic mode PPP results in low latitudes, the same datasets as the ones used in Sections 4.1 and 5.1 for ionospheric parameters estimation and receiver tracking performance analysis are sent to CSRS-PPP, and error in the estimated altitude with respect to the precise epoch are estimated. RINEX files from station NKLG in 2008 were screened out due to abnormal behavior in kinematic processing. The other missing datasets were simply not available or incomplete on the selected days.

The RMS of the altitude errors obtained at all epochs are computed for each year and station under study, and the values are multiplied by 3 in order to acquire a number able to highlight the outliers. Based on the results obtained, common values are set as threshold from which positioning degradation is considered to be significant. The agreed thresholds are 30 cm for 2001 and 2004, and 15 cm for 2008 and 2011. A second threshold of 50 cm is fixed to highlight larger error periods. Two minimum threshold values are set because an improvement of around a half the value of 2001-2004 is achieved in 2008-2011. This improvement with years is largely due to the progress in the IGS products and the larger number of satellites used since no reprocessed product (http://acc.igs.org/reprocess.html) was used for 2001 and 2004, and the GNSS operational constellation has kept growing.

5.2.1. Accuracy degradation

Figure 5.6 shows the temporal distribution of altitude errors for all the stations and years under study. Those with values exceeding the first threshold value (30 cm for 2001 and 2004 and 15 cm for 2008 and 2011 respectively) are plotted in blue, and those above 50 cm in red. The diagonal lines observed in most figures are related to weak satellite configuration geometries caused by a systematic reduction in the number of visible satellites, which may degrade the position accuracy inducing errors that may exceed 50 cm (e.g. MALI and GUAM 2001).

In year 2001 (upper row of Figure 5.6) frequent altitude errors above 30 and 50 cm are identified for all the stations. AREQ and KOUR stations present the highest errors (above 50 cm) during periods of large ROT around the March equinox. A similar result is observed in NKLG from April to December and in

MALI around the September equinox, with altitude errors above 50 cm in periods of strong ROT (see Figure 4.1). The large errors observed in MALI during the first part of the year are due to an incorrect receiver performance. Similarly, significant errors above 50 cm are observed in GUAM during periods of high ROT around equinoxes. The only exception is NTUS, where altitude errors are below 50 cm most of the year.

It should be mentioned that on June 23th of 2001, AREQ station suffered the shock of a strong earthquake which produced the displacement of the site where the monument was set (see Section 5.2.4). Therefore, from that day the reference point considered in this work for that station it is not precise anymore.

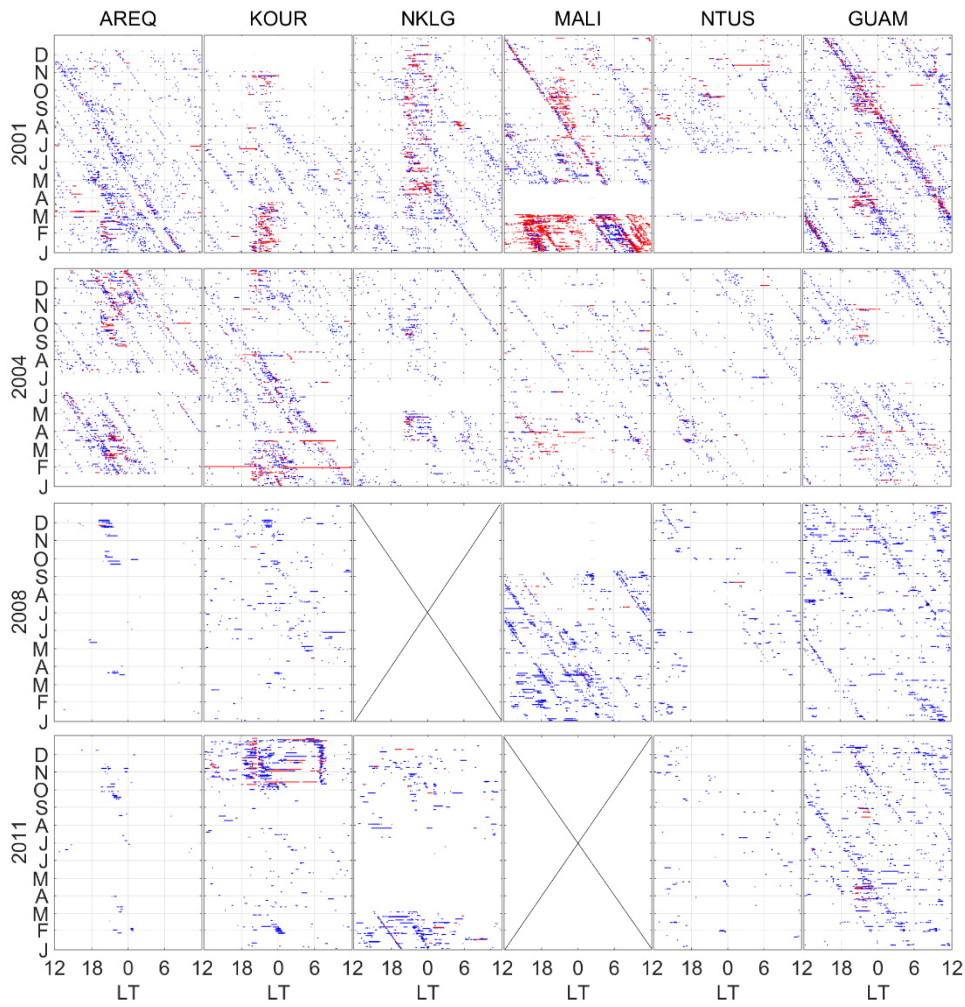

Figure 5.6 Absolute value of altitude error at each epoch. In blue, errors exceeding 30 cm in years 2001 and 2004, and 15 cm in 2008 and 2011. In red, errors above 50 cm.

In year 2008 the altitude error has significantly decreased below 50 cm and even below 15 cm in many cases. This is due to an improvement in the receivers' technology and a reduction in the ionospheric disturbances occurrence. Apart from AREQ and NTUS, frequent altitude errors between 15 cm and 50 cm are observed during the whole year, but in general, they cannot be attributed to have ionospheric origin.

In 2011 results, altitude errors (Figure 5.6 bottom row) remain below 50 cm for most stations except for KOUR and GUAM, that present some high positioning errors during periods of large ROT. The better accuracy observed with respect to previous years is due to many influences such as the increased number of tracked GNSS satellites (including multi-constellation) and improvements in both the IGS products and also in the receivers performance.

5.2.2. Solution repeatability and ambiguities reset

As presented in previous section, in periods of high ROT position solution deteriorates and as depicted in (Figure 5.7 left picture) solution repeatability also may suffer a worsening of centimeter-level. Repeatability is very sensitive to the presence of ionospheric irregularities.

Figures 5.7 and 5.8 show repeatability and ambiguities reset in NKLG for 2011. The worst repeatability occurrence coincides with that of ambiguity reset occurrence (Figure 5.7 right picture). The increase in the number of satellites affected by ambiguities re-estimation (i.e. diagonal lines density in Figure 5.7 right picture) observed from August 2011 is due to the inclusion of GLONASS data. In general, ambiguities reset occur one after the other, except for 18:00-00:00 LT interval of the September to December period, when ambiguities reset may occur (as shown in lighter blue) simultaneously in various satellites in view. The red horizontal lines correspond to punctual day's positioning software's shortcomings. Note in Figure 5.8 that these limitations are present only in figures corresponding to ambiguities reset related to NL and WL combination based filters. From Figure 5.8 it is noteworthy that after signal loss, the main contributor to repeatability worsening is the ambiguity reset. Ambiguities are reestablished after data gaps or CSs detection. The diagonal lines in these pictures represent systematic ambiguities values change which are mainly related to low-elevation effects (e.g. obstructions or satellites rising and setting). As noted in Figure 5.1, signal loss occurrence increased with high ROT in the sunset to midnight period from January to March and from September to December, which may lead to the ambiguities re-estimation after data gaps. On the other hand, even if no signal loss was observed in the rest of the nighttime periods coinciding with high ROT, CSs where flagged and ambiguities reset. Additionally, NL and WL combination based filters flag ambiguities reset especially in periods of high ROT. In this concrete case, NKLG

2011, the filter based on WL combination is more prone to flag ambiguities reset, both systematically and in periods of periods of high ROT, while NL combination based flags appear predominantly from September to December.

Figure 5.8 illustrates not only the presence of cycle slips and the increase of occurrence in periods coinciding with high ROT, but also the positioning software shortcomings to deal with those periods data. This happens because the ambiguities reset are flagged not only by real CS or after gaps, but also due to NL and WL based filters mis-detections too. It is worth mentioning that NL combination based filter is very sensitive to high ROT periods while in general, it flags much less ambiguities resets than WL by systematic causes. Note that the figure corresponding to NL does not show so much diagonal lines.

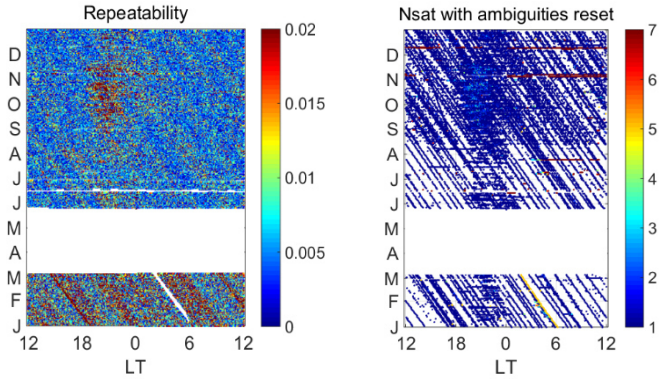

Figure 5.7 Solution repeatability in the vertical component of position in meters (in left), and number of satellites suffering from ambiguity reset (in right) for NKLG 2011.

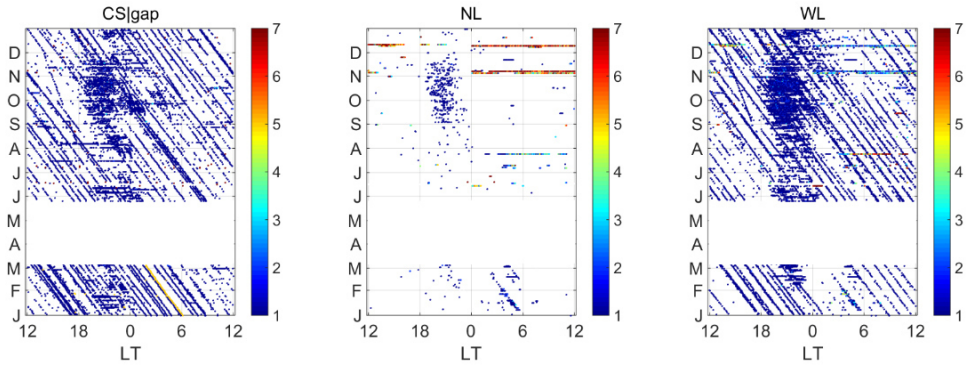

Figure 5.8 Ambiguities reset for NKLG 2011. From left to right: after cycle slips or data gaps, narrow-lane combination based filter and wide-lane combination based filter flags, respectively.

5.2.3. Day to day repeatability

To evaluate PPP solution repeatability the daily STD for the successive difference values of the height component are calculated for each day (see Figure 5.9).

In 2001 and 2004, ignoring the days of larger dispersion which in general corresponds to periods of higher occurrence of large ROT, the daily solution is repeatable in the range of 3-6 cm, although differences exist from one station to the other. It is worth mentioning that in 2001 the repeatability of AREQ and KOUR positions improves steadily from 5 cm, in the early year, to 3 cm at the end of the same year. The reason for this gradual improvement is, at present, unknown. The features observed in previous sections at the beginning of 2001 in MALI is reflected here as decimeter- to meter-level repeatability, which is much higher than the sub-decimeter-level precision, expected. For the days that were characterized by the presence of large ROT values, repeatability values increase from sub-meter-level in AREQ, MALI or GUAM to some meters in KOUR or NKLG. Another characteristic observed in Figure 5.9 is the significant precision improvement from 2001 and 2004 (shown in the left column pictures) to 2008 and 2011 results (shown in the right column pictures). The magnitude of the improvement changes from case to case being AREQ and KOUR the stations that show the largest difference with an improvement of almost an order of magnitude. In most of the cases (even if exceptions exist), the days showing larger dispersion correspond to days with the presence of irregularities (see Figure 4.1). The magnitude of this dispersion varies from centimeter level to some meters.

Table. 5.2 Percentile 75 and 95 of the repeatability (STD of daily epoch by epoch height difference) in meters.

	P_{75}				P_{95}			
	2001	**2004**	**2008**	**2011**	**2001**	**2004**	**2008**	**2011**
AREQ	0.050	0.066	0.010	0.008	0.061	0.129	0.030	0.015
KOUR	0.068	0.057	0.014	0.013	0.755	0.119	0.027	0.051
NKLG	0.070	0.046	---	0.019	0.224	0.056	---	0.035
MALI	0.452*	0.047	0.023	---	1.376*	0.168	0.128	---
NTUS	0.046	0.037	0.011	0.008	0.058	0.041	0.015	0.011
GUAM	0.060	0.048	0.021	0.020	0.207	0.077	0.033	0.049

*when ignoring the results of the first trimester of 2001 in MALI, the result changes to P_{75}=0.107 and P_{95}=1.276

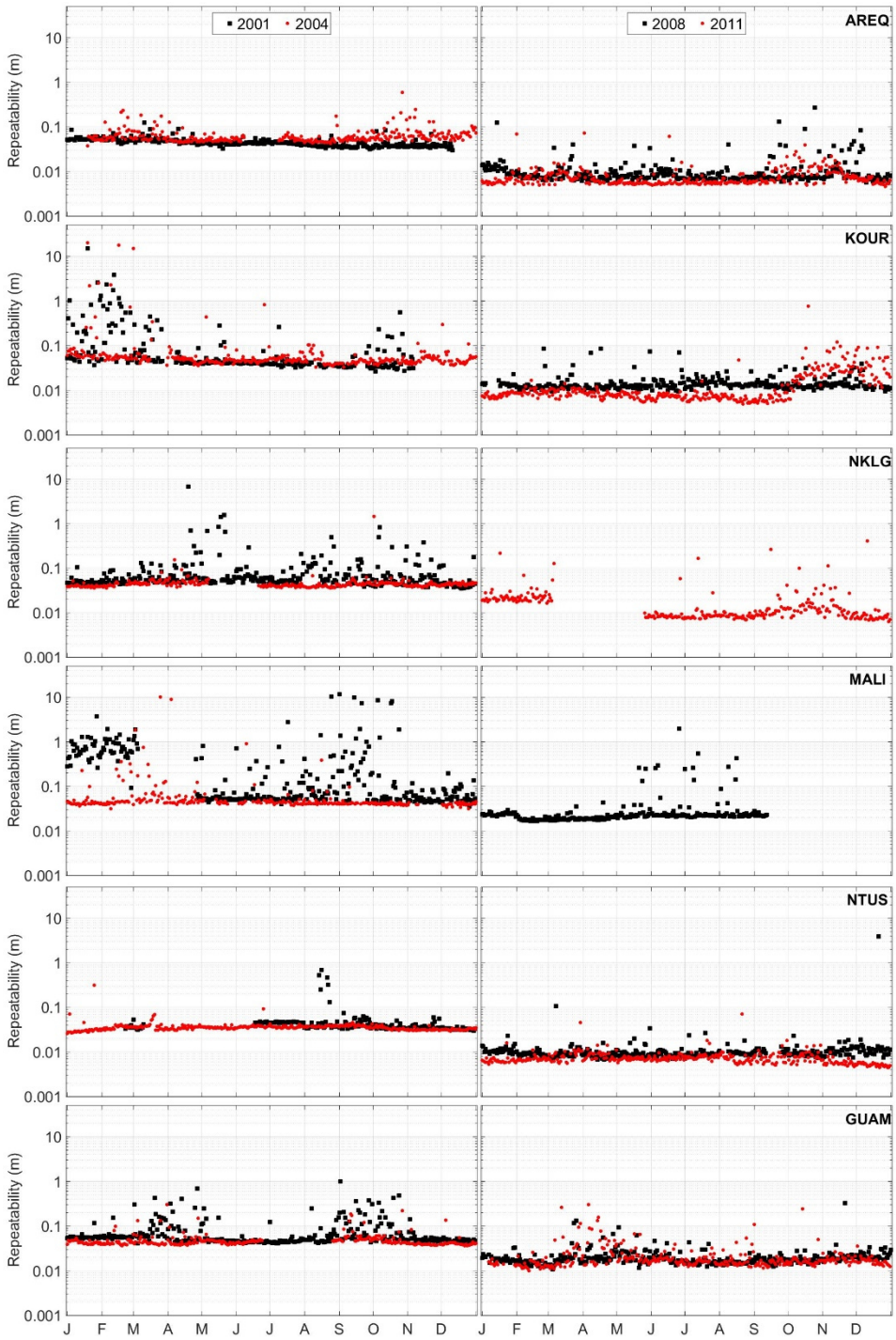

Figure 5.9 Day to day repeatability for each station and year analyzed.

Table 5.2 shows percentiles 75 (P_{75}) and 95 (P_{95}) of the daily repeatability for each station and year under study.

In addition to the cited characteristics in the position day to day repeatability results, GLONASS influence is also noticeable. As previously mentioned GLONASS satellite are included in PPP in August (from DoY 226) 2011. The general effect that multi-constellation has on PPP performance is to slightly improve the accuracy as a result of the higher number of satellites available for positioning. In Figure 5.10 daily repeatability and mean value of the satellites used in PPP divided by 1000 (only to re-scale it) are plotted. This figure reveals that although the repeatability improves in millimeter-level, this is not evident in the presence of ionospheric irregularities where errors enlarge anyway. The improvement of DoYs 226 and 228 with respect to 223 and 225 is shown in Table 5.3.

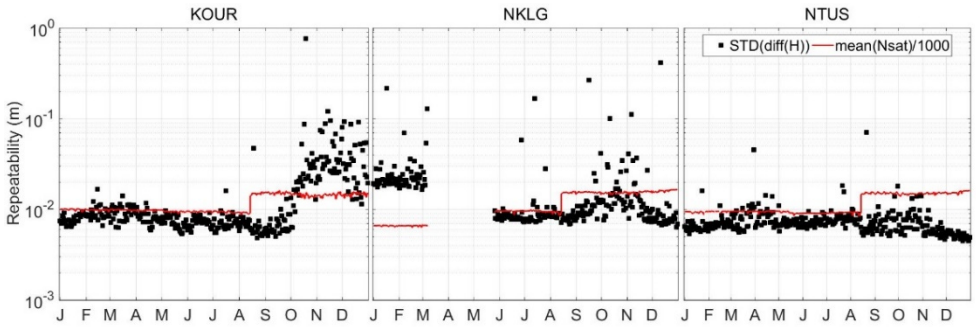

Figure 5.10 Day to day repeatability for KOUR, NKLG and NTUS in 2011.

Table 5.3 Statistics of the repeatability (in meters) for DoYs 223-225 vs 226-228, 2011 intervals.

	223-225 2011				**226-228 2011**			
ID	**mode**	**mean**	**P75**	**P95**	**mode**	**mean**	**P75**	**P95**
AREQ	0.0057	0.0059	0.0060	0.0060	0.0056	0.0057	0.0057	0.0057
KOUR	0.0068	0.0073	0.0077	0.0078	0.0059	0.0060	0.0062	0.0062
NKLG	0.0088	0.0090	0.0090	0.0090	0.0072	0.0080	0.0087	0.0090
MALI	---	---	---	---	---	---	---	---
NTUS	0.0077	0.0079	0.0080	0.0081	0.0056	0.0058	0.0062	0.0064
GUAM	0.0150	0.0182	0.0205	0.0212	0.0138	0.0239	0.0359	0.0429

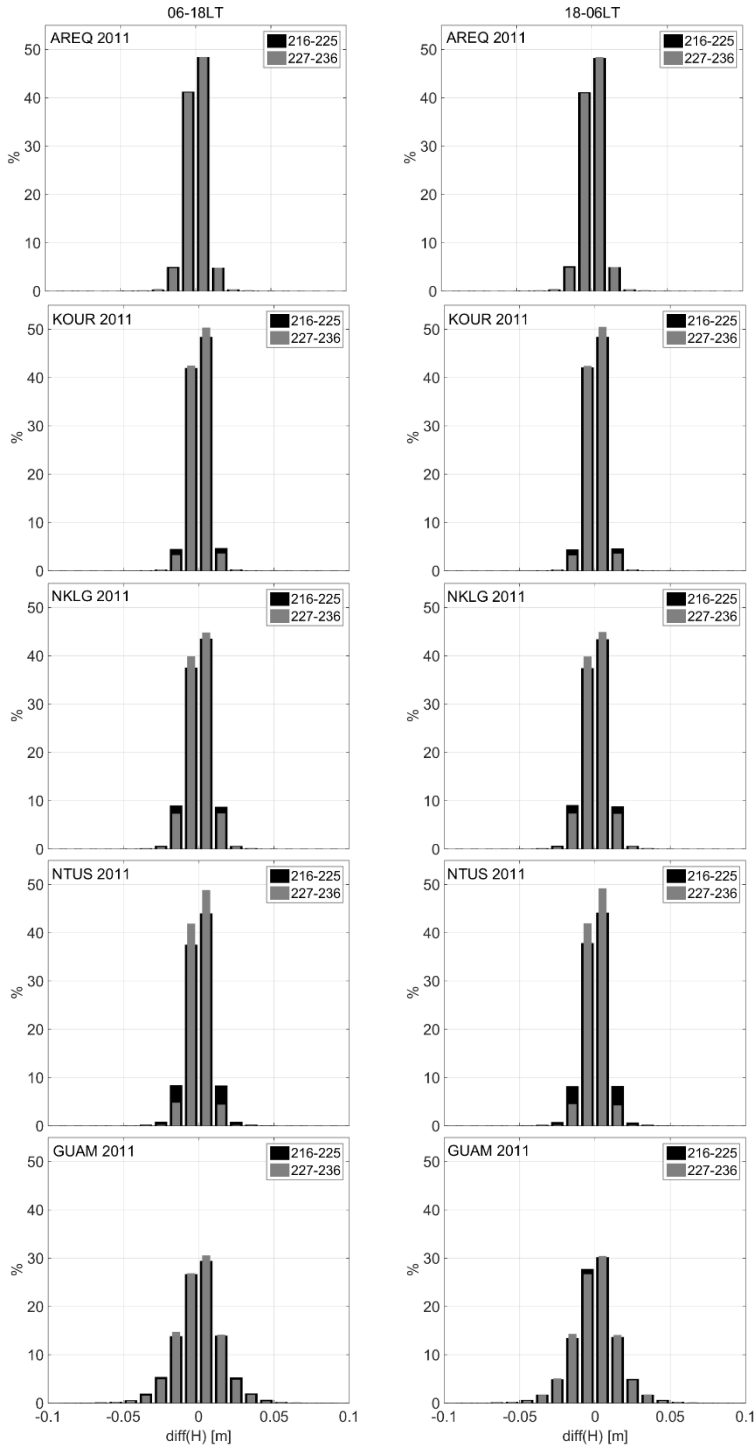

Figure 5.11 PPP precision with only GPS (black) and with GPS+GLONASS (gray).

Figure 5.11 shows the difference in the precision of PPP (the value of the first derivative of the estimated height) between periods where only GPS constellation was considered (216-225 2011, black histogram) and periods where GPS+GLONASS where processed (227-236 2011, gray histogram). The left column shows the histogram for daytime epochs corresponding to 06:00-18:00 LT, while the right column shows the same but for nighttime, 18:00-06:00 LT.

Note the larger improvement present in KOUR, NKLG and NTUS especially from 0.02 m to 0.01 m when GLONASS are also processed, both in daytime and nighttime. It is worth remembering that in this period of time NKLG also registered the nighttime irregularities effect, although no large errors can be attributable to them. To analyze the PPP performance with GLONASS in periods of large ROT, a case study is analyzed in sub-section 5.3.2.

5.2.4. Day to day final solution

One might think that daily PPP solution may mask the effect of ionospheric irregularities. However, it does not have to be that way. In this subsection the daily final solution obtained in kinematic mode is compared with the one obtained in static mode.

The position final solution for each day can be found on the summary file (‘*.sum’*) provided by the CSRS-PPP online service. The estimated daily geocentric Cartesian coordinates are extracted and converted to East, North and Height Coordinates by the expressions shown in Eq. (3.4) to Eq. (3.8) introduced in Chapter 3.

In concrete, Figure 5.12 depict the daily solution of PPP in kinematic mode with respect to the daily solution obtained in static mode for AREQ 120-366, 2008. Note that in any of the coordinates, the reached accuracy is until September, in general, below centimeter-level, from when deteriorates, in the order of millimeters, being the largest offsets of the order of few centimeters. Note that in Figure 4.1, irregularities are observed from September to December 2008.

This example highlight the discrepancies that may be found between the daily solutions obtained by static or kinematic mode. In fact, as shown in the previous section, solution repeatability may be worse on days with presence of large values of ROT, and this may deteriorate the daily final solution (see an example in Figure 5.13).

The time series of daily PPP solution for KOUR in the time interval of DoYs 108-365 2011 is represented in Figure 5.13. Since a reference frame transformation occur from IGS05 to IGS08 on DoY 107 2011 this day coordinate has been considered as a reference point to plot the results. The daily displacements with respect the reference day are in general below 2 cm until October from when noise

increases notably (up to 30 cm) with respect to the previous epochs until December. This example shows that the daily final solution obtained in kinematic mode processing may be deteriorated by tens of centimeters due to the presence of ionospheric irregularities related troubles.

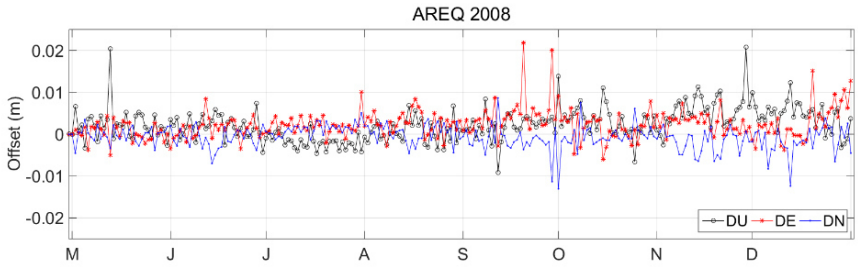

Figure 5.12 Daily horizontal and vertical coordinates offset of kinematic mode PPP with respect to the static mode PPP in AREQ on DoYs 120 to 366 of 2008.

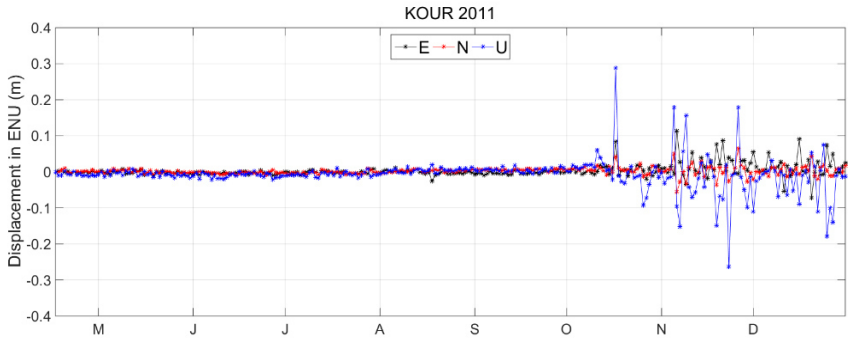

Figure 5.13 Daily displacement of horizontal and vertical coordinates from DoYs 108 to 365 of 2011 with respect to DoY107 of 2011 (IGS08) in KOUR.

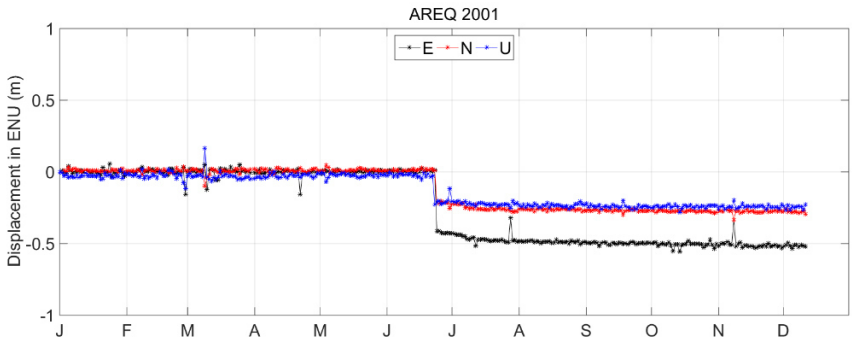

Figure 5.14 Daily displacement of horizontal coordinates from DOY 011 to 365 of 2001 with respect to DoY 011 of 2001 (IGS05 in AREQ).

If this data is used for any application that analyzes temporal series, it should be necessary to be aware that the increase in the standard deviation will be translated in a larger amount of outliers in the processing.

On the other hand, as noted in a case study shown in Figure 5.14, PPP may be very sensible to co-seismic displacements of the monuments where the GNSS stations are placed. In this picture from June 23th (DoY 174), 2001displacements of around 25 cm are observed to the South and down and of 50 cm to the West. The big jump of that day is followed by a faster displacement of the site with respect to the previous days that lasted for a month. These displacements are related to the earthquakes of June 23th and July 7th of 2001 of magnitudes 8.4 and 7.6 respectively, and the post-seismic displacements. The GPS receiver and the data record suffered the effects of the shock, and additionally no precise weekly coordinates (on SINEX) where provided for a time. This effect was not observed in Figure 5.1, due to the noisy epoch by epoch results and the threshold considered to show the errors which may mask other effects, as is this case.

5.3. PPP in periods of high ROT: case studies

This section is dedicated to the explanation of the PPP accuracy degradation that may occur in periods of large ROT. The influence of signal loss, dilution of precision, ambiguities re-estimation, inclusion of additional satellite constellation or contemplation of higher sampling rate effect are introduced by means of case studies.

5.3.1. DOP vs Ambiguities Reset

To demonstrate the first statement, Figures 5.15 to 5.17 show a case study where the influence of satellite loss on DOP and PPP for AREQ 051 2011 is represented.

Figure 5.15 shows the skyplot of the real GPS constellation in the period 10:00-11:00 UT. To create the two situations shown in Figure 5.16, the left picture configuration is obtained by removing satellites G02, G04 and G05 from *RINEX* files; while to get the configuration of the right column G02, G04 and G10 are rejected. Note that after removing those satellites only 5 are present for positioning in the 10:00-11:00 UT interval. This example confirms that a critical number of satellites is not so decisive in PPP performance unless the distribution of satellites in the sky of the receiver is not good enough. On the other hand, the quality of the information of the satellites used to establish the receiver position plays a major role.

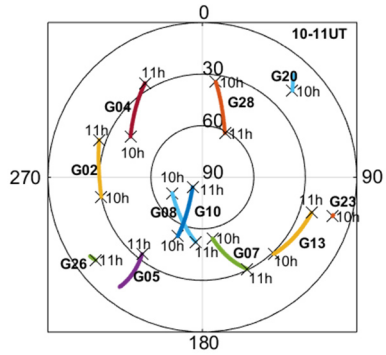

Figure 5.15 Skyplot of AREQ on DoY 051 of 2011 in the 10:00-11:00 UT time interval.

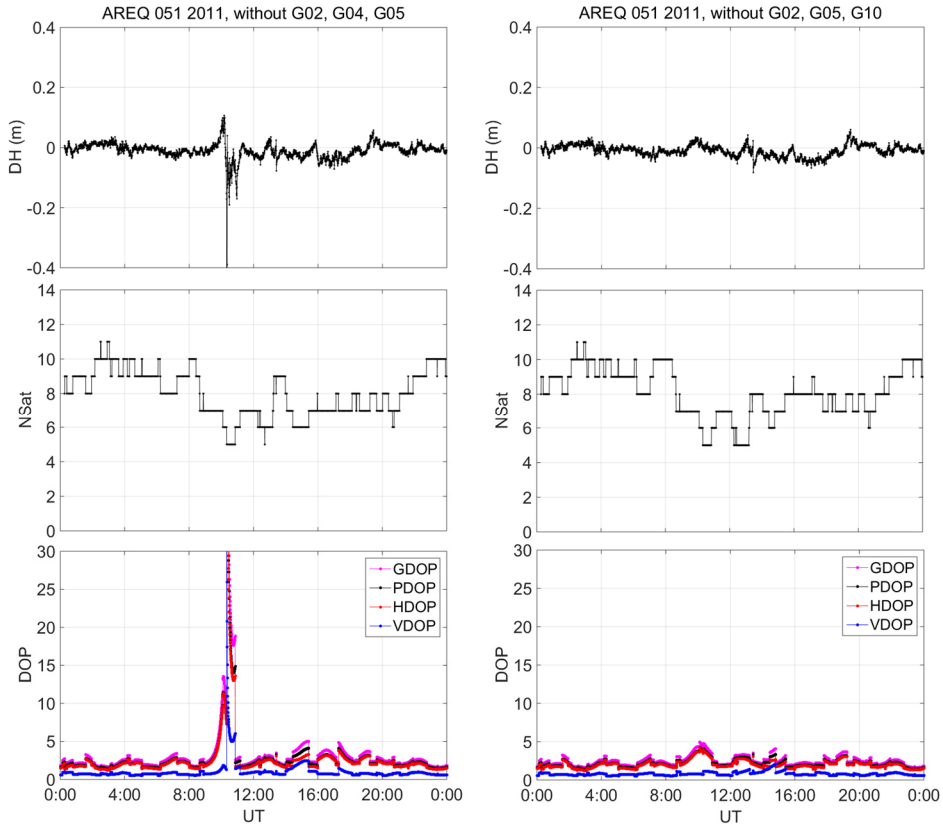

Figure 5.16 Satellites constellation influence on PPP errors. From top to bottom: error in the estimated altitude (IGS05, v 1.05 34613), number of satellites used on PPP, dilution of precision (DOP).

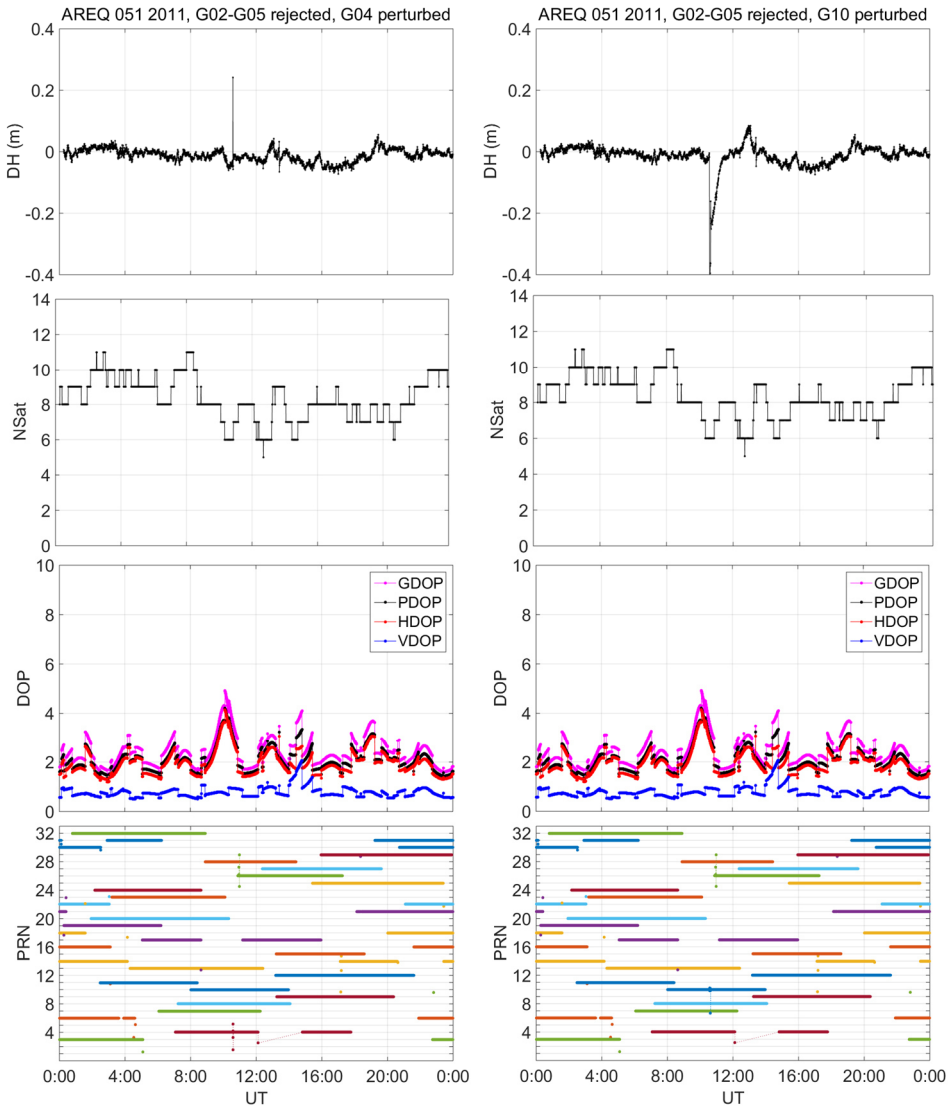

Figure 5.17 PPP performance under a "synthetic" ionospheric perturbation affecting individual satellites in a critic configuration (left column: PRN 4; right column: PRN 10). From top to bottom: error in the estimated altitude (IGS05, v 1.05 34613), number of satellites used on PPP, DOP and first derivative of the ambiguities for each satellite.

Figure 5.17 presents an example like the one in the previous figure. In this case instead of rejecting the data of 3 satellites, two (G02 and G05) are rejected and a SITEC-like ionospheric perturbation has been introduced in the third one (PRN4 in the left column of Figure 5.17 and PRN 10 in the right column).

The pattern of the TEC values introduced in RINEX files observables is based on the SITEC that will be presented in Chapter 6. In concrete: epoch by epoch [0.1 0.14 0.2 0.5 1.2 2.5 3 1.7 2.7 0.8 0.9 0.8 0.7 0.3] TECUs introduction in the 10:33:00-10:39:30 UT interval. It worth's mentioning that this "synthetic" perturbation is removed in the IF combination.

The results in Figure 5.17 show that although the satellite geometry is maintained (appreciate that on the contrary to what it is observed in Figure 5.16 the graphics of the number of satellites (Nsat) and GDOP in the left and in the right columns of Figure 5.17 look alike), the identical perturbation affecting one satellite or another has different consequences. Note that in both cases this "synthetic" perturbation causes ambiguities to be reset (bottom graphics of Figure 5.17). However, as it is observed in the case in which G10 is the perturbed satellite (right column picture) the effect in PPP does not need to be constrained to the exact epochs where new ambiguities are re-established.

Even if a critic satellite constellation of only 5 satellites has been considered, the examples shown in Figure 5.16 and Figure 5.17 confirm that under the presence of ionospheric irregularities it is not a straight forward task to take the right decision between discarding the information and continuing with that, even knowing that in last instance it may affect the PPP performance in the same extent. In the case studies presented, rejecting G04 satellite may produce worse results than maintaining it even if rapid changes in the ambiguities are observed while the opposite occurs with G10. This effect is not so critic when a larger number of satellites are tracked. Therefore, satellite constellation and geometry play a crucial role in PPP performance under different kind of perturbations. For this reason, adding a new constellation may help to avoid or at least to diminish the problem.

5.3.2. GPS vs GPS+GLONASS

To analyze the effect of ambiguities reset and the addition of a new constellation to the PPP, the following case study is introduced: NKLG station on DoY 301 of 2013. Although it does not correspond to one of the days of the complete years studied in previous sections of this works, this date has been chosen because represents a clear example of PPP performance with GPS plus GLONASS.

Figure 5.18 shows the PPP performance with only GPS constellation. In the upper panel of this figure, ROT occurrence for the selected day in the 12:00-24:00 UT interval is presented (only GPS). Each color corresponds to one GPS satellite data. The middle panel shows the error in the estimated altitude (IGb08, v 1.05 34613) while the lower panel represents the number of satellites used in PPP and how many of them suffers from ambiguities re-estimation in each epoch. Figure 5.19 presents the same (except ROT) as previous figure but with GPS+GLONASS.

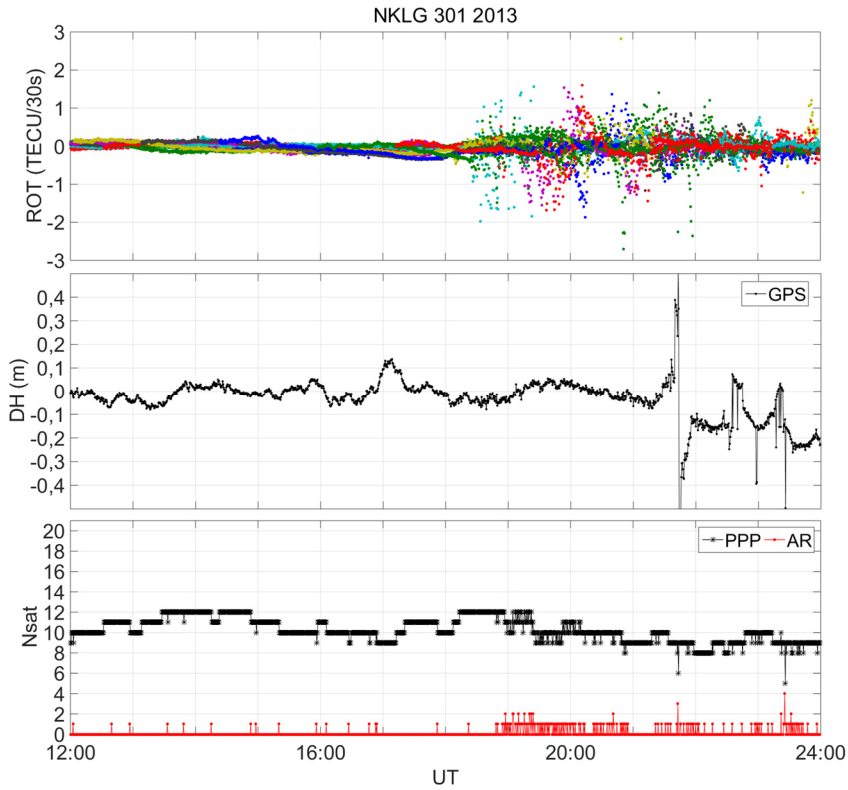

Figure 5.18 PPP performance with GPS in NKLG on DoY 301 of 2013. From top to bottom: ROT (each color represents one satellite), error in the estimated altitude and number of satellites used in PPP (black) and with ambiguities reset (red).

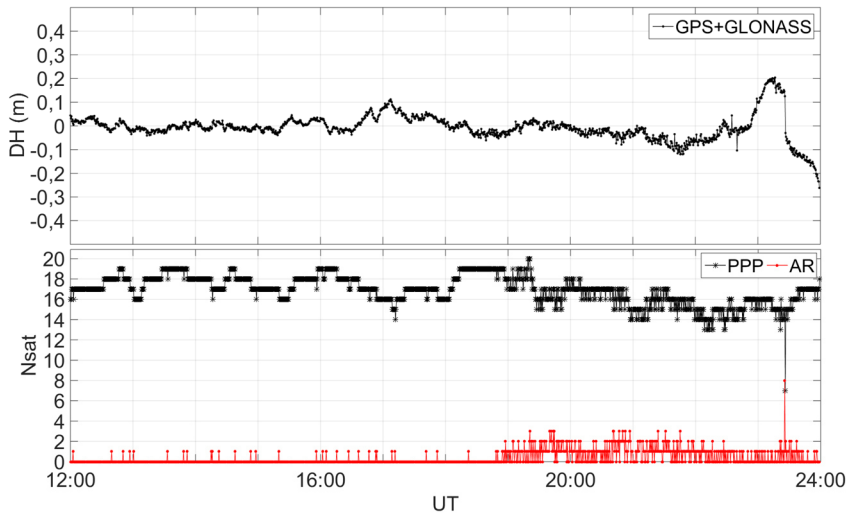

Figure 5.19 Same as lower panel in Figure 5.18 but with GPS+GLONASS.

Analyzing Figure 5.1, it can be noted that ROT starts to fluctuate fast, and in some cases exceeds 1 TECU/30s, from approximately 18:30 UT up to the end of the record (24:00 UT). Some minutes later, the number of satellites available for PPP starts to drop and ambiguities start to be reset. Except for few epochs, in general no more than one satellite ambiguities are re-defined at the same epoch, which doesn't mean that for short arcs the ambiguities could not be erroneously established. However, errors do not increase remarkably until 21:30 UT.

When introducing GLONASS, a clear improvement of the accuracy is observed, especially in the presence of ionospheric irregularities related problems (see Figure 5.19). This improvement is related with the fact that an increase in the satellite constellation implies more signals (in this case seven more satellites) to be processed that are not affected simultaneously by scintillation, loss of lock or, simply, ambiguities reset. In this figure it is observed that from 19:00 to 23:30 UT the number of ambiguities reset and the fluctuations in the number of satellites used in PPP occur more often. However, when compared the occurrence in each epoch with the increase in the number of satellites due to the new constellation, the reason for better PPP accuracy becomes clear.

5.3.3. 30 s vs 1 s sampling rate

Publicly available IGS data normally exhibit sampling intervals of 30 s, whereas kinematic positioning (especially for real-time or near real-time data) require sampling frequencies of 1 Hz or higher.

As explained in previous sections, the computation and storage needs increase with the sampling rate, therefore 30 s was selected for the general analysis and overview. However, it is important to note the shortcomings of this decision and for that reason a case study showing the results of the same receiver and period, comparing 30 s sampling-rate results (see Figure 5.20) with 1 s sampling-rate (see Figure 5.21) is presented. This case corresponds to AREQ 301 2003, which is also analyzed in the following chapter. In this case study, the number of ambiguities reset due to the PPP internal filters (in this case the WL combination) increases in periods of high ROT. In this case, the ambiguities reset coincides, both in epoch and in number of satellites affected, from considering 30 s sampling in Figure 5.20 and considering 1 s in Figure 5.21. Nevertheless, note that in the latter case there are not consecutive resets. However, the error is larger in the results with 1 s sampling rate but this is due to the precise products used which need additional interpolations to work with 1 s sampled data. On the other hand, note that the errors occurring at around 11:00 UT disappear in Figure 5.21. In concrete, this case study is shown in Chapter 6.

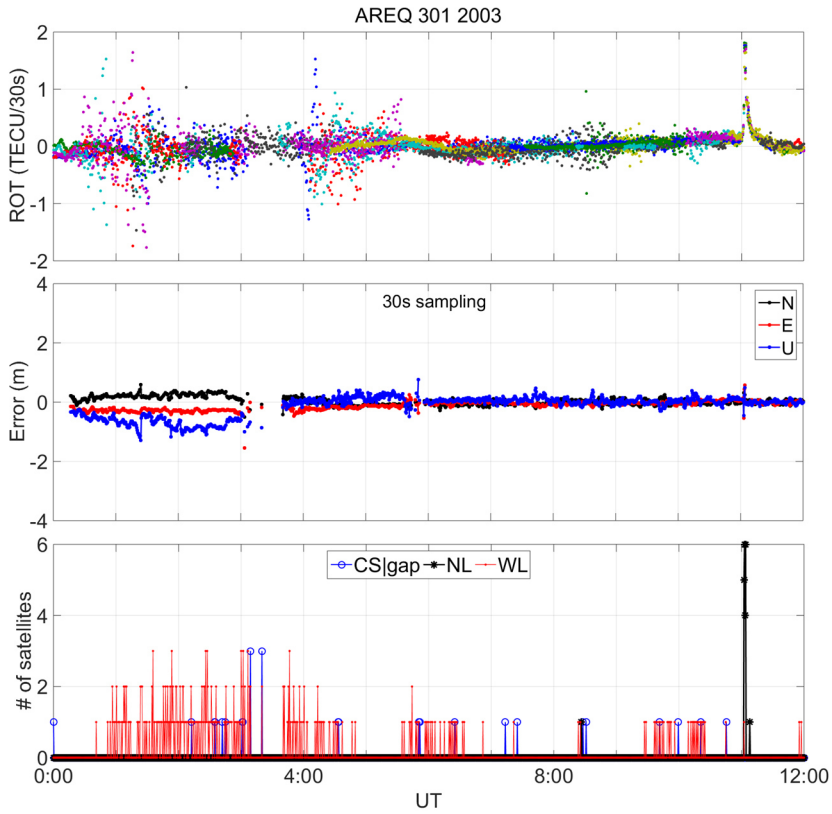

Figure 5.20 Kinematic PPP with 30 s sampling rate: AREQ 301 2003 0:00-12:00 UT.

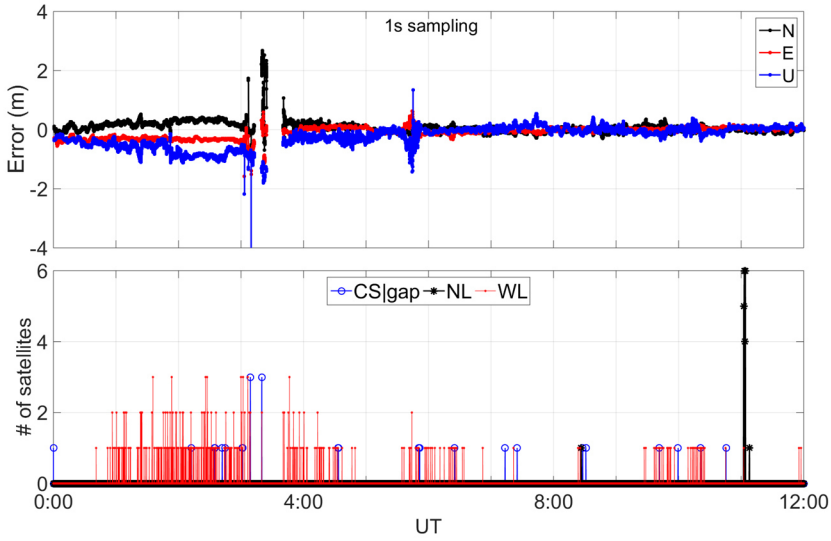

Figure 5.21 Kinematic PPP with 1 s sampling rate: AREQ 301 2003 0:00-12:00 UT.

5.4. PPP in mid latitudes

As shown in Chapter 4, the stations located at mid-latitudes, do not show as large and frequent high ROT values as low-latitudes GNSS stations. Although the irregularities present in mid-latitudes during quiet periods show a seasonal and solar activity dependence, these irregularities are in general innocuous for PPP. On the other hand, the strong ROT that may be present in magnetically perturbed periods such as the ones listed on Table 4.3 or SITECs may produce ambiguities reset specially in low elevation satellites, but in the cases studied, no remarkable position degradation attributable to those events has been observed. An exception is the SITEC of 2003 presented in Chapter 6 which also causes PPP errors in mid-latitudes, although those results are not shown in the present work.

5.5. Summary

In this chapter the impact of low-and mid-latitude ionospheric irregularities on PPP is assessed using data of IGS network. As expected the PPP performance in periods of high ROT is worse in low-latitudes than in mid-latitudes.

The discrepancies in receiver performance are due to manufacturer-depending factors, and this work does not focus on specific aspects of internal receiver algorithms. The objective is instead, to analyze the general impact of irregularities on PPP, and identify the main sources of those errors.

In the first section, an evaluation of the receivers tracking performance at low latitude stations have been performed. These receivers tracking performance has been analyzed in terms of missing observations during periods of high ROT. Note that for satellites suffering signal loss, simultaneous ROT cannot be estimated. While many missing observables are present at lower elevation angles (below 45º), which is due to the multipath and lower SNR, observable losses are also noted above 45º.

Although, results suggest significant performance differences for each receiver during periods of high ROT, it may be argued that ionospheric conditions were not identical in each station located at different geographical and geomagnetic locations. As seen in the reproducibility checking, the main discrepancies under similar ionospheric conditions rely on the receiver characteristics. It must be emphasized that the results are highly receiver-dependent.

A study of long term receiver tracking and PPP performance allows a comprehensive study of seasonal and solar cycle variations.

Peak degradation on PPP accuracy primarily occurs during in periods where large ROT was observed. The low-latitude postsunset irregularities, present in the ionosphere when large ROT values are registered, may significantly degrade the

GNSS transmitted signal, impeding the signal tracking and producing the LoL within the receiver. The sudden loss of observations from a satellite causes the weakening of the satellite configuration geometry, which degrades PPP accuracy and repeatability until the signal is recovered and the ambiguities are estimated with enough accuracy. In general, as it might be expected, the more satellites used in the solution, the smaller the DOP values and hence the solution error. This has been proven with GLONASS data. Additionally, periods of high ROT may also cause ambiguities to be reset by PPP software filters. After DOP, these ambiguities resets are the main contributors to the deterioration of repeatability. Although these filters are expected to have a better performance with higher sampling rate data, in the case studied in the present work this is not observed, since ambiguities are reset anyway even though not continuously as in the case of the lower sampling rate. Furthermore, it has been shown that PPP accuracy is worse than when considering 30 s sampled data, but this is related to the precise products interpolation needed.

PPP accuracy degradation depends strongly on solar activity, location, and receiver performance, and it is enhanced in periods of large ROT with respect to the periods of low ROT. This study allows identifying locations and periods where and when GNSS positioning may be more affected by strong ionospheric variations. The most conflictive periods are from 19:00 LT to midnight around the equinoxes for Asian stations, sifted to December solstices for the studied American stations and almost whole year for African stations. Years of HSA are of special concern for GNSS users.

On the other hand it seems necessary to analyze the role of scintillation in both the ambiguities resets and the severity of ROT.

The results show that the quality of observations are affected not only by obstacles and multipath effects but also by receivers' performance in the presence of ionospheric irregularities. In the example of GUAM, GUUG and CNRM is proved this statement.

Additionally, it has been proven that receivers suffering from equatorial post-sunset irregularities, which may be considered as a recurrent effect, may not be suitable for the generation of quality time series, since they may not be continuous or the information may affect the processing filters that flag outliers that reject data. In this way, the receivers split the continuity in the time series making them useless for applications such as the station velocity estimation, or the changes produced in the land motion just after an earthquake, and they may perturb the calculus of the seasonal dependencies especially in periods of high solar activity.

In the presence of irregularities the arcs considered for PPP or ionospheric analysis may be too short to establish a constant ambiguity value.

On the other hand, the backward filtering helps to avoid errors related to the convergence. A more severe effect would be observed in the errors if only the forward filter was to be used.

The ambiguities may be re-estimated due to mainly two reasons: after a loss of lock and in the presence of CS. However it has been observed that they maybe needlessly reset in periods of high ROT due to the shortcomings of the CS detection filters in the presence of high ROT. Furthermore, if GF filters were supposed to be used in those cases, the PPP degradation should be even more severe.

Chapter 6.
SITEC effect on PPP: a case study

In this chapter the October 28th, 2003 SITEC effects on PPP accuracy is explored. This event is of special interest for GNSS applications for two reasons: the presence of a SRB affecting GNSS frequencies and the almost simultaneous large SITEC produced by the solar flare EUV radiation.

Section 6.1 introduces the source of the SITEC and the SRB events that were followed by the ionospheric response to the flare which is described in Section 6.2. Then, Section 6.3 presents the effect of both phenomena in PPP, including the observed failures on the receiver tracking, the positioning algorithms performance or the results concerning the sampling rate. The chapter concludes with a summary in Section 6.4 where it is stated that both phenomena are source of problems in PPP.

The results of this chapter have been partially published in Rodríguez-Bilbao et al., [2015b].

6.1. Introduction to the event

On October 28th, 2003, a large X-ray flare that was classified as X17.2 (see Table 2.1 for classification), corresponding to the measured power of 1.72 mWm^{-2} blasted at 11:10 UT from solar AR486. The flare was characterized by large X-ray and EUV emissions (see Figure 6.1) from close to the center of the solar disc, which result in one of the largest SITEC of SC23.

This flare was accompanied by a SRB that affected the L-band by radio noise emission. According to the data from the Trieste Solar Radio System (TSRS in Trieste, Italy) (http://radiosun.ts.astro.it/) on October 28th, 2003, the RHCP solar radio flux recorded at 1420 MHz (the closest frequency to GNSS radio frequency registered by this spectrograph) show two main periods of increased noise: 11:00-11:30 UT and 11:37-12:08 UT, being the latter time period also split into two episodes of increased noise (Figure 6.2). Note that the noise in this frequency exceeds 3000 sfu (spectrograph saturation level at this frequency) in the second time interval.

The SNR fades measured on GPS L1 and L2 associated to this SRB were previously reported by Cerruti et al., [2006] while Chen et al., [2005] analyzed receivers' performance by means of the rate of phase LoL in L2. As stated by these authors, the GPS radio signal interference caused by the SRB jeopardized signal

tracking performance, in many receivers of the sunlit hemisphere. According to Chen et al., [2005] the SRB interference was the main cause of GPS signal loss in that time period, while the SITEC played a secondary role.

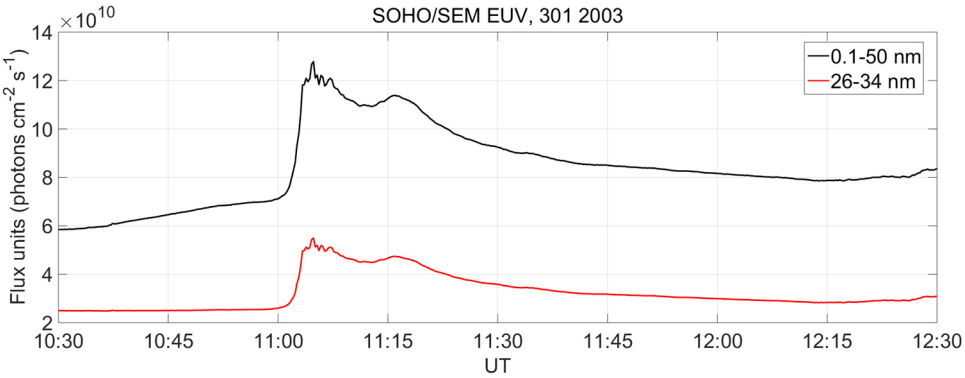

Figure 6.1 Photon flux measured with SOHO /SEM in the 26–34 nm band pass (red) and in the 0.1–50 nm band pass (black) for the 10:30–12:30 UT interval on October 28th, 2003. Data: Courtesy of the USC Space Science Centre for the EUV data of CELIAS/SEM experiment SOHO spacecraft available at http://www.usc.edu/dept/space_science/-semdatafolder/.

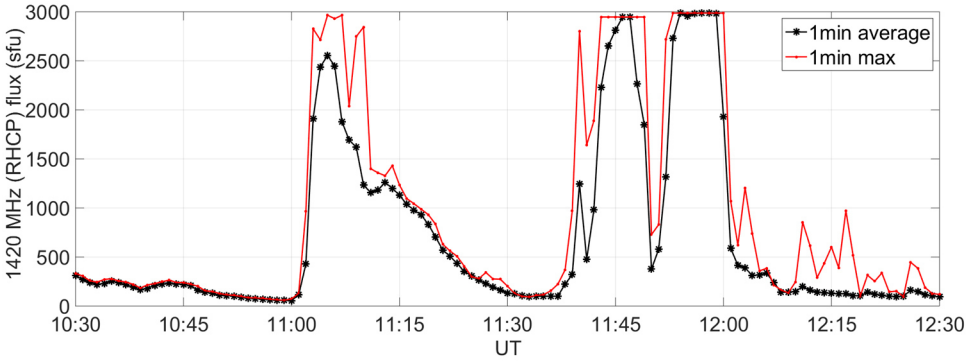

Figure 6.2 Right hand circularly polarized 1420 MHz Solar radiation flux measured in Trieste for October 28th, 2003 in the 10:30-12:30 UT interval. (1 sfu=10^{-22} W m^{-2} Hz^{-1}) Data: Courtesy of M. Messerotti, Solar Radiophysics and Meteorology of Space Group of the INAF-Astronomical Observatory of Trieste.

However, as will be shown in the following sections of this chapter, the SITEC is the main contributor to the PPP accuracy degradation observed in many stations of the sunlit hemisphere. This is not a surprise since previous works studying this SITEC event stated that the TEC increased around 25 TECU in 5 min [Tsurutani et al., 2005] producing one of the largest and fastest SITEC event of SC23 [Liu et al., 2006] that was also registered in dawn and dusk (sunlit) boundary regions [Zhang and Xiao, 2005]. This strong event could produce problems with the reliability of the CS detection filters, especially with the ones based in GF combination.

6.2. Ionospheric response to the solar flare

This rapid TEC enhancement in response to a flare implies large values of ROT to be registered in all satellites whose signals cross the ionosphere of the sunlight hemisphere.

The ROT shown in this chapter has been calculated by the method described in Chapter 3. The information regarding the stations used in this study is summarized in Table 6.1.

Table 6.1 Geographic coordinates and SZA of IGS stations used in this chapter.

ID	Lat (º)	Lon (º)	SZA	Receiver	Tracking mode *
NKLG	0.35	9.67	13	TRIMBLE 4000SSI	Cross correlation
ASC1	-7.95	345.59	25	AOA SNR-8000 ACT	codeless
MALI	-3.00	40.19	31	ASHTECH Z-XII3	codeless
AREQ	-16.47	288.31	78	ASTECH UZ-12	codeless

*from Chen et al., [2005]

Figure 6.3 presents ROT values obtained for all satellites in view in each of the stations of Table 6.1 from 10:30 to 12:30 UT. This event affected the signal of all satellites in the sunlit hemisphere simultaneously with nearly identical effects but with SZA dependence. Not only TEC but ROT peak values depend on SZA and reach maximum values of around 4 TECU/30s over the stations with the lowest SZAs (Figure 6.4). The lower than expected values found in Figure 6.4 in Africa (ZAMB and NKLG) for instance, respond to data gap.

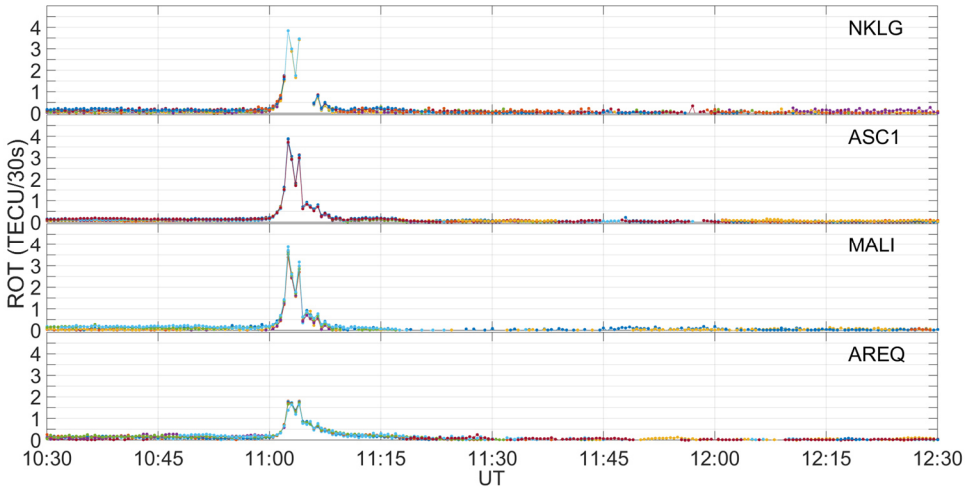

Figure 6.3 ROT values measured in ASC1, VILL and AREQ stations in the period 10:30–12:30 UT on October 28th, 2003. Each color represents a satellite pass. Receivers are ranged according to the SZA from low (top) to high (bottom). Satellites above 10° of elevation are only shown.

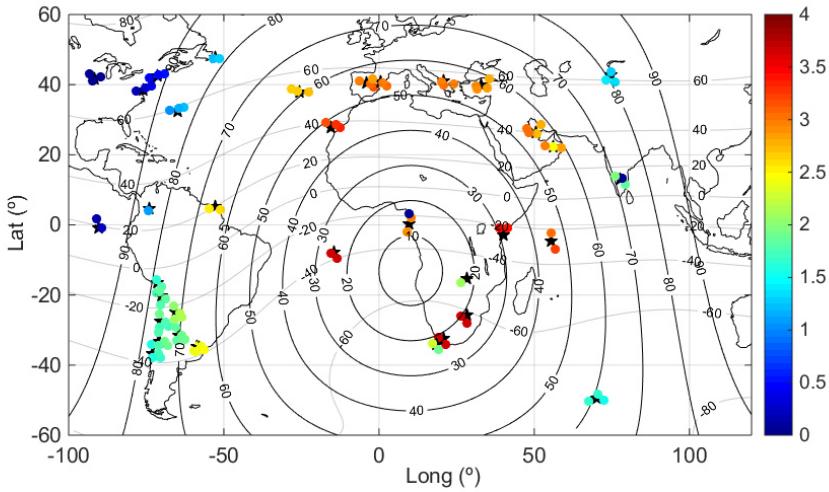

Figure 6.4 Geographical distribution of the IPPs with the ROT values (0 - 4 TECU/30s) registered from 11:03:00 UT to 11:03:30 UT on October 28th, 2003 corresponding to satellites above 45º. Magnetic isoclines (light gray) and SZA (dark gray) are also plotted.

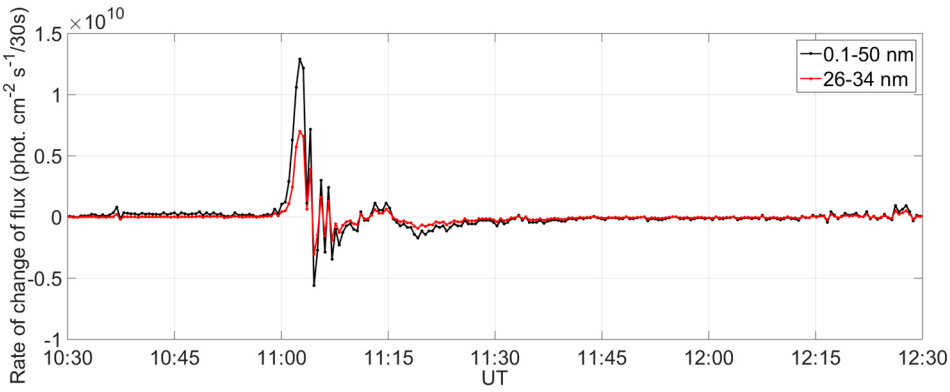

Figure 6.5 30 s rate of change of the photon flux measured with SOHO /SEM in the 26–34 nm band pass (red) and in the 0.1–50 nm band pass (black) for the 10:30–12:30 UT interval on October 28th, 2003.

The large ROT values observed in Figure 6.3 in the 11:00-11:15 UT interval are the ionospheric response to the impulsive increase of the solar radio flux in EUV and X-ray due to the flare. Figure 6.5 presents the 30 s time rate of change of photon flux in EUV and X-rays. Data were obtained by the Solar EUV Monitor (SEM) onboard SOHO (Solar and Heliospheric Observatory) in the 26–34 nm and 0.1–50 nm band passes. Figures 6.4 and 6.5 show that the TEC steps up suddenly every time the flux increases impulsively. The main perturbation, characterized by large positive values of ROT, lasted from 11:01 to 11:10 UT, until the EUV flux radiation started to decrease (Figure 6.1), while the ionospheric "anomalous TEC" lasted for approximately 3 h [Tsurutani et al., 2005]. As will be shown later, the discontinuity observed in NKLG station in the interval coinciding with the SITEC is due to lack of code and phase observables at L2 (1.2 GHz) in many satellites (in some epochs all of them) in the 11:03:00–11:11:30 UT interval.

6.3. Kinematic PPP

6.3.1. Signal fades and signal loss

According to Cerruti et al., [2006] for October 28th, 2003 event, SNR fades were observed both in L1 and L2 corresponding to peak values in solar radio burst. The largest fades in L2 are attributed to the semicodeless cross-correlation technique used to track the L2 signal, while the discrepancies observed in the shape of SNRs on L1 and L2 are attributed to the difference in the antenna gain and the difference in the SRB power spectral densities at the two frequencies.

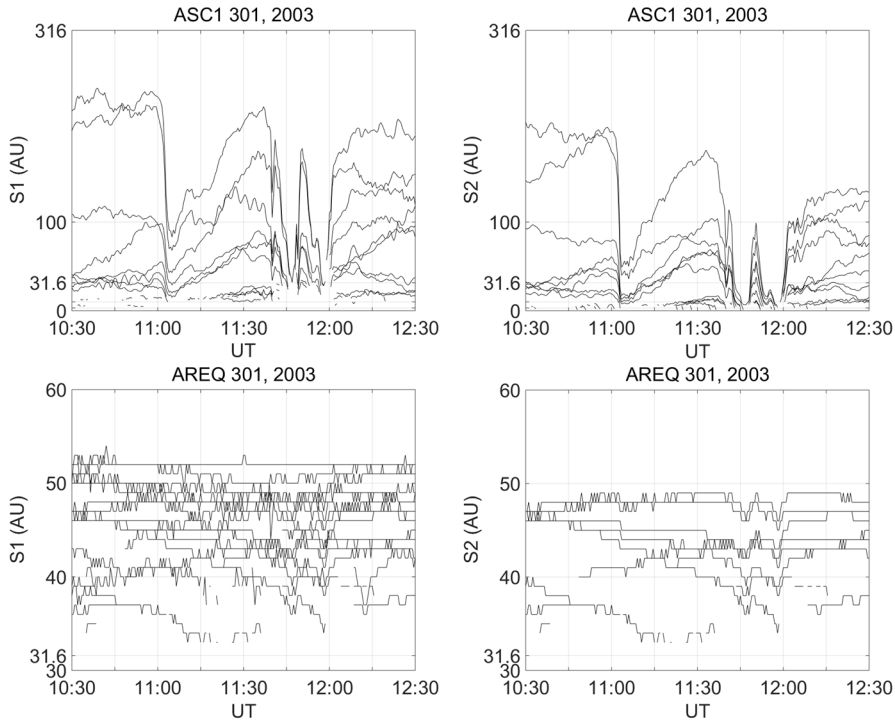

Figure 6.6 SNR in L1 (left) and L2 (right), for ASC1 (top) and AREQ (bottom) on October 28th, 2003 for 10:30-12:30 UT interval.

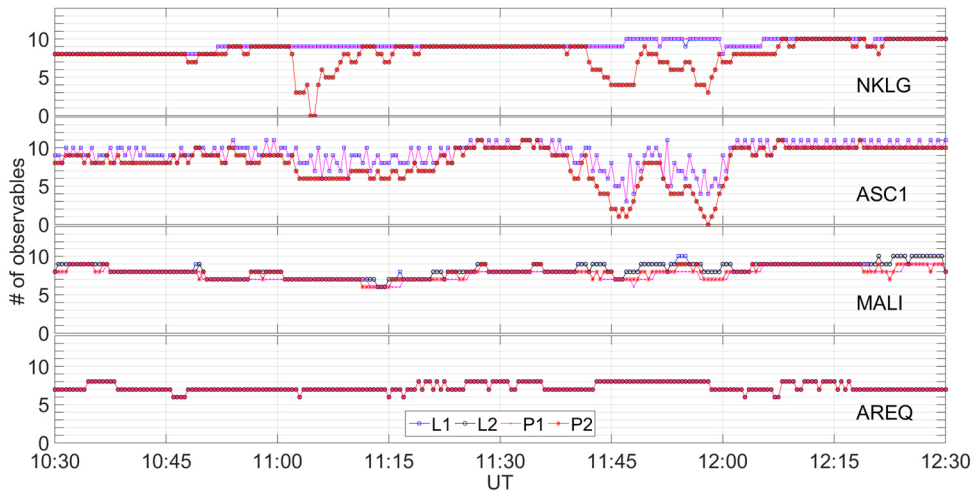

Figure 6.7 Number of GPS observables registered at each epoch by each station during 10:30–12:30 UT interval on October 28th, 2003: carrier phases (L1) and codes (P1) in 1.5 GHz, in blue and magenta respectively; carrier phases (L2) and codes (P2) in 1.2 GHz, in black and red respectively. Only satellites above 10° of elevation are considered.

Attending to the Geodetic Research Laboratory Memorandum of year 2000 accessible at http://gauss.gge.unb.ca/papers.pdf/SNR.memo.pdf [Accessed 01 March 2016], RINEX files (v.2.10, as the ones under study) allow the SNR to be reported as observation types S1 and S2 to represent the original signal strength values given by the receiver for L1 and L2 tracking. However, these observables units are receiver dependent, which means that there is no universal way of reporting SNR. Nevertheless, it has been observed that although magnitude and units cannot be established, these observables work for signal fades detection. Figure 6.6 shows ASC1 and AREQ SNR in arbitrary units (AU). Note that both periods of SRB produce signal fades in ASC1, being the second period more severe, producing more cases which are prone to signal loss, due to the low values reached (below the detection level). On the other hand, in AREQ only the fades corresponding to the second period of the SRB are present, especially in L2. Both stations' S2 are quite below S1, which makes it more susceptible to noise.

Signal loss occurred mainly in the presence of SRB when SNR decreased below the detection level of the receiver. The prominent decrease in SNR, especially in L2, may lead to LoL. This effect depends not only on the kind of receiver but also on its geographic location, since receivers closest to the subsolar point in periods of SRB will be more affected, (see NKLG and ASC1 stations case studies in Figure 6.7).

In the stations studied in this work, signal loss has been observed to be more severe in the second time interval of the SRB influence period, especially for NKLG and ASC1 (see Figure 6.7). Note that in Figure 6.2 the radio noise in the L-band was more intense in the second period of the SRB. However, in Figure 6.7 it is also worth noting that contrary to NKLG, ASC1 also presents tracking problems in 1.5 GHz, while MALI is more sensitive to code noise. AREQ does not present the mentioned tracking problems, although, as shown in Figure 6.6 signal fading is present due to the SRB interference in the second time interval.

6.3.2. PPP performance

In order to investigate the impact of the October 28th, 2003 SITEC on PPP, position solutions are computed by the online CSRS-PPP service (version v. 1.05 34613) introduced in Chapter 3 [Mireault et al., 2008].

We present the influence of the mentioned event on kinematic dual-frequency PPP results and we experiment the shortcomings of the software when dealing with a phenomenon of this magnitude.

There are two main reasons why errors are observed on PPP. The first one is related to signal loss after the SRB caused signal fade, and the second one is due to

the ambiguities reset that results from software shortcomings to deal with SITEC period information.

Figure 6.8 shows the errors on North (N), East (E) and Up (U) components of the estimated PPP position with respect to the reference precise coordinates (IGS05 coordinates from SINEX weakly solution) for the stations under study in the 10:30–12:30 UT interval of October 28th, 2003. The errors observed in this figure in general and except for NKLG and ASC1 in the 11:00-12:00 UT period (due to the solution convergence between gaps), fluctuate around 20 cm. There are two clear periods in which accuracy degradation occurs and decimeter level is exceeded by large. The first one, in the 11:01-11:05 UT interval, corresponds to the first influence period of the SRB and coincides with the epochs when the SITEC related large ROT values where present (see Figure 6.3). The errors are largest in ASC1, with values of some meters, while they barely reach 30 cm in AREQ. Errors are largest in the vertical component followed by the NS direction and the best results are reached in the EW component. Even if PPP errors coincide with epochs of high ROT, and even if a SZA dependence may seem to exist in the sample of stations presented in this chapter, errors magnitude do not show SZA dependence at all. The second period of errors in Figure 6.8 match with the SRB related second time period observables loss shown in Figure 6.7. PPP accuracy degradation in this interval is clearly related to the signal tracking problem.

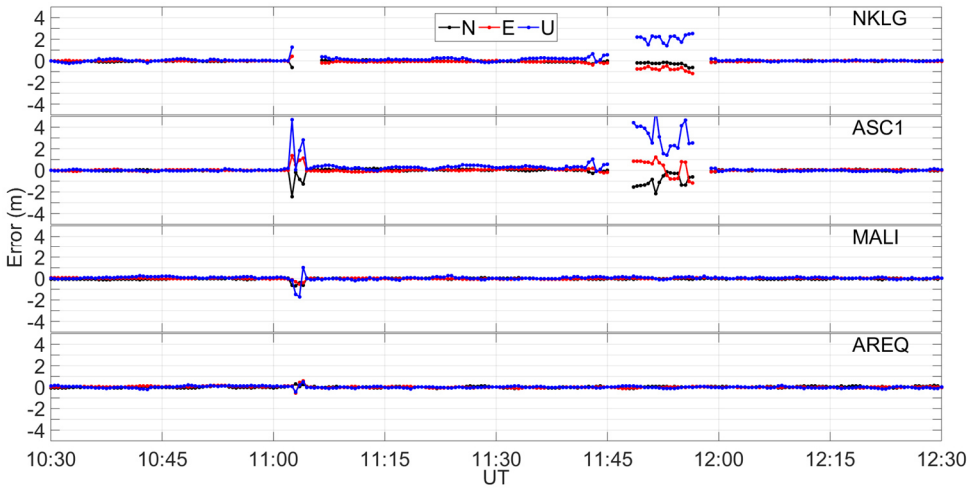

Figure 6.8 Errors produced in the estimation of the North (N), East (E), Up (U) components with respect to precise reference coordinate (IGS05), in 10:30-12:30 UT interval of October 28th, 2003.

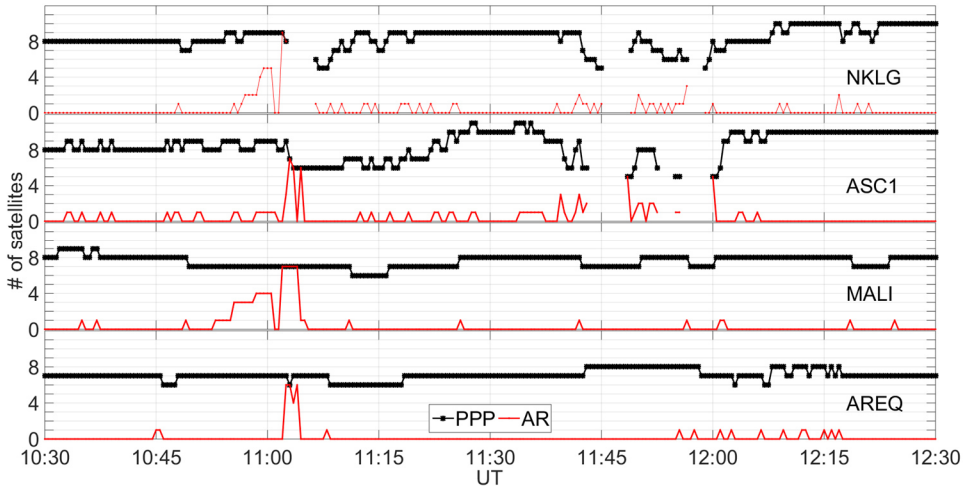

Figure 6.9 Number of satellites used in PPP (black asterisk) and the number of satellites with ambiguities reset (red) at each epoch for each station in the 10:30–12:30 UT interval on October 28th, 2003.

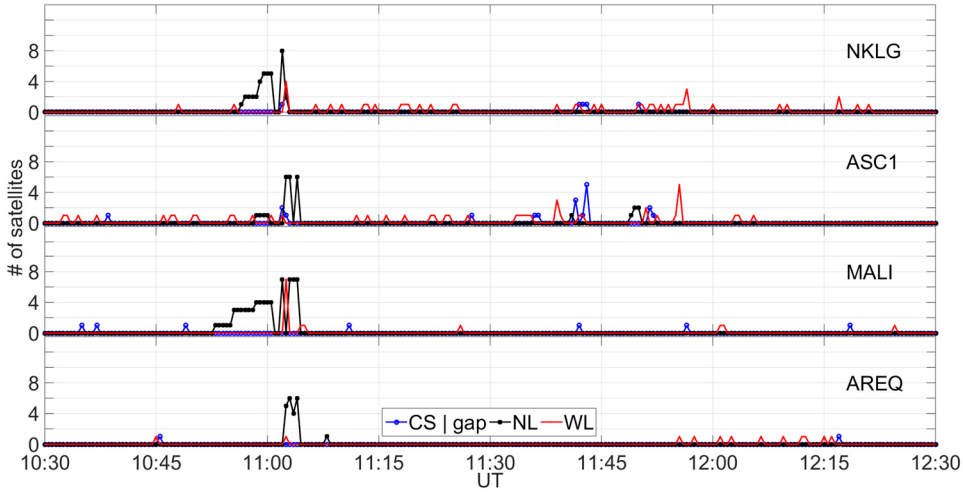

Figure 6.10 Number of satellites suffering ambiguities resets due to CS or gap (blue circle), NL combination (black asterisk), and WL combination (red dot) related problems for each station in the 10:30–12:30 UT interval on October 28th, 2003.

In Figure 6.9 the number of satellites used in PPP are presented with black asterisks. Note that gaps in Figures 6.7 and 6.9 respond to the no-position determination when less than five satellites are available (CSRS-PPP condition). Figure 6.9 also shows the number of satellites that are suffering from ambiguities reset in the PPP processing at each epoch. Note the coincidence of the SITEC

related ROT peak values in Figure 6.4 and the consequence of simultaneous ambiguities reset in Figure 6.9.

As mentioned, since the establishment of the CSRS-PPP online service the output files have suffered many changes. In the latest version used in this work (as of 2015-08-03, V 1.05 34613) *'.res'* files provide a code referring to the reasons why ambiguities were reset. According to that code, Figure 6.10 shows the number of satellites affected in each epoch by CSs or gaps related problems, and NL and WL combination-based filters problems that produced ambiguities resets shown in Figure 6.9. Note that NL combination related problems stand out with respect to the other two (CS/gap or WL). However, the ambiguities reset existing in NKLG, ASC1 and MALI before the SITEC took place seem to be caused by problems with the NL filter performance, although no error increase occur.

These results lead us to assume that the combined effect of the signal to noise ratio decrease due to the SRB and the SITEC related increase in observables noise seems to be the source of problems in the NL combination based filters that produced the mentioned ambiguities reset. It is worth mentioning that the signal fading due to the SRB in the 10:40–12:00 UT period, which is not coincident with the SITEC does not cause any positioning problem, except the ones in NKLG and ASC1 which are attributed to signal loss. On the other hand, we have observed that in AREQ there is no signal fading related to the first period SRB, and, however, errors still occur. Therefore, at least in cases like this, the problems are strictly related to the ionospheric effect on GNSS signal and the PPP software performance problems to deal with the observables information.

To check this statement several observable combinations have been checked and summarized in the following section.

6.3.3. A possible noise induction by the SITEC

As mentioned in Appendix A, the code minus carrier (CMC) observations linear combination can be used to evaluate the measurements noise. The contribution of the ionosphere to the CMC in "quiet" times is a trend which can be removed. In this case, the first derivative of the CMC has been used to evaluate the presence of the SITEC (see Figure 6.11 and Figure 6.12 left panels) and its contribution to noise has been checked by subtracting from CMC linear combination two times the ionospheric contribution, and applying the first derivative of this term in order to remove the ambiguity contribution (which is only valid when no CS occur) (see Figure 6.11 and Figure 6.12 right panels). The result should be the first derivative of multipath, receiver error and noise.

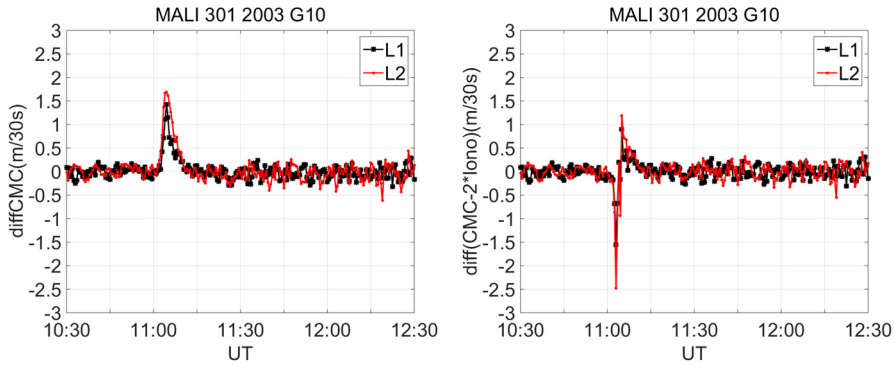

Figure 6.11 First derivative of CMC (left) and the first derivative of CMC after having subtracted the ionospheric contribution in MALI for PRN 10 on October 28th, 2003.

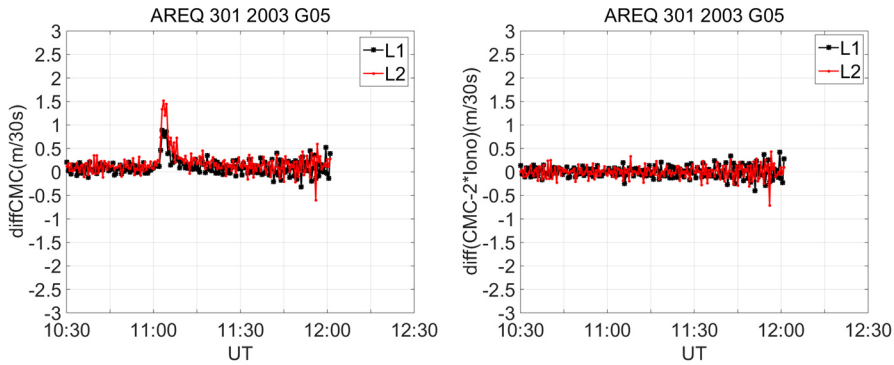

Figure 6.12 First derivative of CMC (left) and the first derivative of CMC after having subtracted the ionospheric contribution in AREQ for PRN 05 on October 28th, 2003.

After testing several stations and satellites observables, two kind of results that depend on the receiver have been obtained: some that show increased noise in the time period of SITEC (such as MALI, MAS1 and VILL) (see an example in Figure 6.11) and others that do not (see an example in Figure 6.12). The receiver showing a behavior as the one displayed in Figure 6.11 is ASHTECH Z-XII3, and it clearly introduces noise to observables, therefore, the rest of the observables linear combination such as NL, WL or MW, will be affected by SITEC induced receiver dependent noise. On the other hand, in cases such as the one in Figure 6.12, where observable noise does not increase, the problem seems to be more clearly related with the PPP processing strategy and ionospheric contribution to the signal. It is worth remembering that other linear combination of observables such as GF, also may present inconveniences in their application when applied to periods of perturbed ionosphere like this.

6.3.4. Higher sampling effect

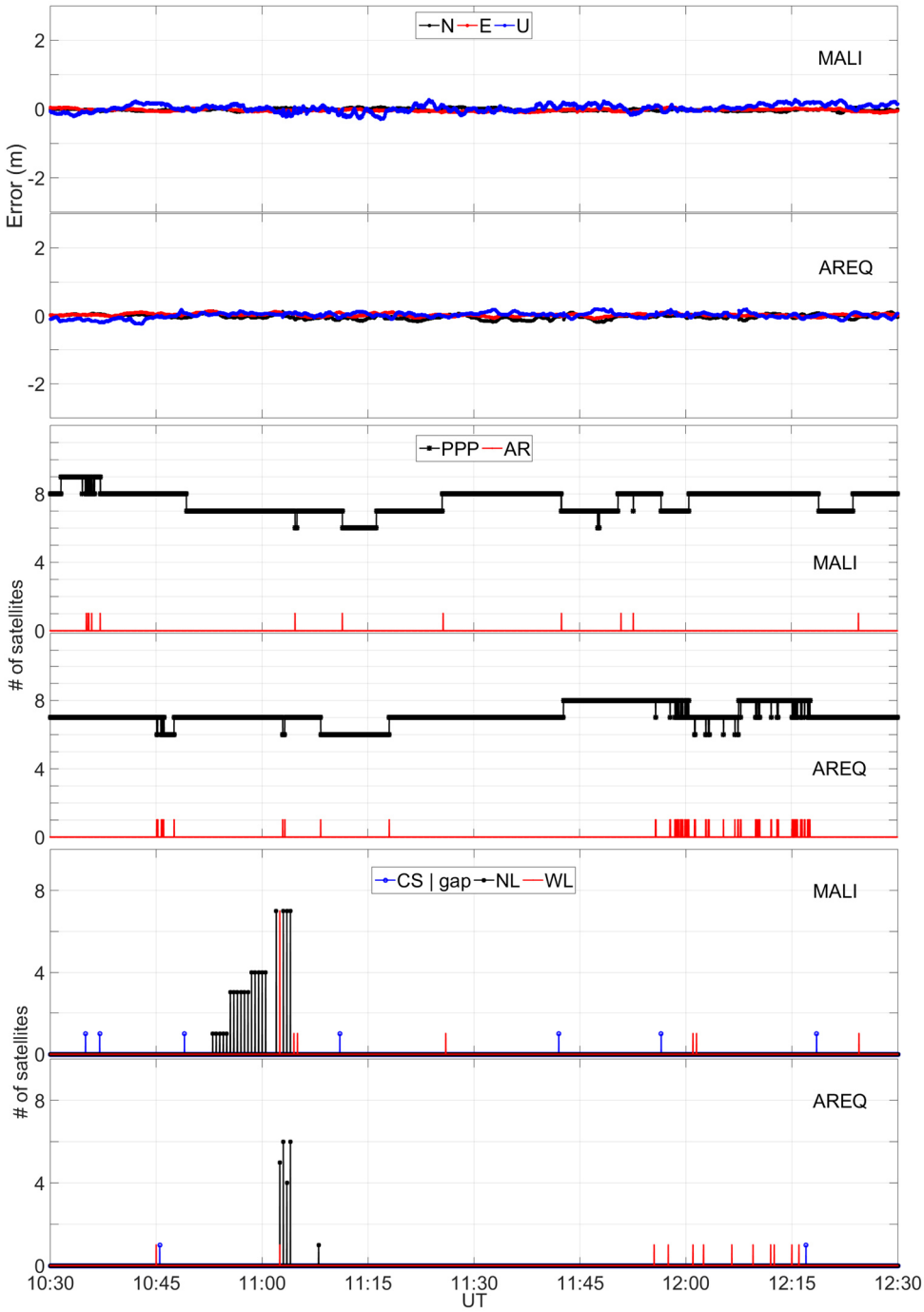

Figure 6.13 From up to down the same as Figure 6.8, Figure 6.9 and Figure 6.10 respectively but with 1 s sampling rate.

Only some of the receivers considered in this chapter offer 1 s sampling rate RINEX files. In this case the same procedure as with 30 s has been carried out with MALI and AREQ station 1 s sampled data (see Figure 6.13). Note that errors existing when considering 30 s, now disappear. Higher sampling rate implies both less problems in data acquisition and CSs detection. It is noteworthy that considering higher rate avoids the SITEC related problems in the CS detection. The problems related to ambiguities reset have disappeared because the NL combination flag are more sparse (1 flag every 30 s).

6.4. Summary

In this chapter we have seen through a case study corresponding to the October 28th 2003 event, that a solar flare can degrade kinematic PPP in two ways, through SRB or SITEC. It has been revealed that in both cases the receiver performance and location play an important role. Only the receivers located in the sunlit hemisphere (including day-night transition zone) suffer their effects but the resulting magnitude of the error does not depend on the SZA.

Deep signal fades have been observed on both the GPS L1 and L2 during the SRB event. They spanned over two main episodes of frequency interference that produced signal loss and consequently errors that result from the lower number of satellites.

In this chapter we have also shown that the encrypted GPS L2 signal is of particular importance since it is much more susceptible to radio frequency interference than L1 due to the signal tracking using codeless/semi-codeless technologies employed by dual-frequency GPS receivers.

On the other hand it has been observed that SITEC may produce large errors in kinematic PPP that are not caused by signal tracking problems related signal loss, but by the simultaneous ambiguities reset induced by the NL combination based filter's problems to deal with the observables that have been affected by the SITEC. The ambiguities are needlessly reset in the epochs where ROT reaches its largest values, which makes the accuracy to drop up to some meters in certain stations. It has also been checked that a higher sampling rate produce a better performance both when tracked and when processed.

Additionally it has been observed that some stations with the same receiver (ASHTECH Z-XII3) also introduce SITEC related noise to the observables.

Chapter 7.
Conclusions and future works

7.1. Summary and conclusions

The analysis carried out during the development of this Ph.D. study has helped to achieve both the general and the specific research objectives established in the introduction of this manuscript. The first goal was set to analyze the effects of fast variations of TEC on positioning by means of ROT, and the second one to identify the cause of the errors and to investigate the characteristics of the physical phenomena involved. These objectives have been applied to low- and mid-latitudes stations and to PPP technique.

Chapter 1 presents an overview of PPP, and introduces the motivation for the study presented in this Ph.D. work. Although PPP is not a novel technique, its maximum potential regarding accuracy and applications is being reached in the latest years with the development of new techniques that solve the main contributors to satellite-receiver range errors. However, it has been observed that there are still some phenomena inducing errors which, up to now, seem to escape the control of the PPP method, and cause errors much larger than the expected accuracy for this technique. In concrete, effects related to ionospheric irregularities.

Chapter 2 introduces the low- and mid-latitudes ionosphere and the processes involved in ionospheric irregularities occurrence. Both, normal ionosphere and irregularities effects on the GNSS signal path are remarked.

Chapter 3 describes the data analysis strategy used in the current work. After introducing the data, the procedure applied to obtain the ROT is commented and its shortcomings concerning the ROT calculated only with carrier phases are explained. Additionally, distinct procedures to deal with the detection of different kind of irregularities according to their characteristics observed in ROT, have been proposed. This chapter has also introduced the CSRS-PPP service and the procedure followed to get stations position.

From the analysis regarding the method used to estimate the ROT it is concluded that:

- The ROT estimates based on sTEC curves and procedures which include pseudoranges are highly dependent on noise and all its contributors are a source of discrepancy with the ROT calculated only with carrier phases.

- The periods which show larger discrepancies probably are time intervals characterized by larger noise and, therefore, may be an indicative of noisier solutions in positioning techniques based on pseudoranges.
- Geometric effect reduction of ROT by a mapping function may induce large errors, especially in low-latitudes and when lower elevation satellites are considered. Results show solar activity and seasonal dependence effects.

Chapter 4 studies the ionospheric irregularities occurrence using the ROT analysis. The no-detrended ROT has been used instead of a filtered one in order to perceive variations with very unlike physical sources. Regarding low-latitude stations data, 6 stations covering different longitudes have been selected and a common threshold value of 0.3 TECU/30s which helps to distinguish between quiet and active ionospheric periods has been defined. The results confirm that this threshold value does not differentiate the kind of irregularities causing the response in TEC.

- As expected, the occurrence of ROT values exceeding 0.3 TECU/30s has been observed to present local-time, seasonal/longitudinal, geomagnetic and solar activity dependencies, although a day to day variability has been also observed.
- Irregularities induction and suppression have been also observed during geomagnetic storms but the causes have not been identified yet.
- Additionally, irregularities occurring after dawn have been also identified but the reason for their occurrence is at present unknown too.

Regarding mid-latitude stations (MAD2 and AMC2), the predominant trends identified are wavelike patterns characterizing TIDs. After having analyzed 11 years of data of MAD2 and 4 in AMC2, these structures have been observed to occur both in daytime and nighttime from low to high solar activity periods. Daytime structures occur mostly in the first and last trimester of each year, from sunrise to sunset, while nighttime structures occur from May to August, from sunset to sunrise.

- This kind of irregularities does not show up the characteristics required for PPP accuracy degradation. However, fast ROT fluctuations related to those nighttime structures have been also observed and, due to the fast change in ROT, they may be considered as a potential threat to PPP if they reach high magnitudes.

Space weather related irregularities have been also identified on no-detrended ROT.

- This parameter is sensitive to positive ionospheric storms and can be useful for their identification.

- Fast and large fluctuations have been observed to occur when the main phase of a storm takes place in postsunset hours. In the case of MAD2, the presence of those irregularities may be related to the expansion of EIA and the displacement of low-latitude phenomena to higher latitudinal area, but a further analysis is needed to confirm this hypothesis.
- SITECs has been detected by a novel promising procedure which is based on the RMS and STD of no-detrended ROT values measured epoch by epoch.

Chapter 5 analyzes the mentioned large ROT effect on kinematic PPP (in particular in CSRS-PPP). First of all, receiver tracking performance has been studied using the GPS observable loss on RINEX files corresponding to low-latitude stations. A general view confirms that a better tracking performance, especially regarding high elevation satellites, is observed in more recent years, 2008 and 2011, compared to 2001 and 2004. This is also observed in periods of high ROT. It has been noted that in years of HSA and MSA, observable loss increases in periods of high ROT, especially from sunset to midnight. Nevertheless, AREQ 2001 and NTUS 2004, where almost no signal loss coinciding to large ROT periods has been observed, are clear exceptions to this behavior. From these observations it is concluded that:

- Although local effects (such as the magnitude of the local ionosphere gradients) may induce the losses, each receiver tracking properties make the signal susceptible for loss.
- Each receiver manifests its own preference to one observable loss or another.
- Regarding results reproducibility, receivers' characteristics mark the differences in the observables, and thus, the discrepancies observed in both the results on ROT and PPP.

In the second place, kinematic PPP accuracy has been analyzed in the vertical coordinate, for 2001, 2004, 2008 and 2011 at 6 low-latitude and one mid-latitude (AMC2) stations. Regarding low-latitudes stations analysis, errors increase in periods coinciding with large ROT, especially in 2001 and 2004, and the observed accuracy degradation may exceed 50 cm. It can be concluded that:

- As expected, peak degradation on PPP accuracy occurs primarily in periods where large ROT is observed.
- An accuracy improvement is observed in the estimated epoch by epoch vertical component in 2008 and 2011 with respect to 2001 and 2004 which is mainly attributed to the upgrade of the IGS products. This improvement is observed more clearly when daily repeatability is analyzed. Then, solutions become two to four times more precise in 2008 and 2011 due to IGS products upgrade. On the other hand, another improvement related to the periods

coinciding with the presence of high ROT can be observed. It also can be due to an upgrade of the receiver's performance under those specific conditions, as shown in signal loss occurrence.

- Solution repeatability worsening has been observed to be caused by an increase in the ambiguities resets that occur as a result of CSs, data gaps, or flags by the NL and WL combinations based filters, being NL based filter the one that causes less systematic resets. The number of ambiguities resets increases in periods coinciding with large ROT and signal loss. Therefore, solution repeatability deteriorates with values that may exceed one order of magnitude. Due to the deterioration of daily repeatability, the daily station position also degrades, especially when kinematic processing mode is performed.
- It has been noted that when each day position solution is plotted, intense site displacements affecting the stations (like the ones produced by an earthquake) may be observed, whereas in the epoch by epoch results they may be masked by the noise. This kind of events does not affect the day to day repeatability of the days after the shock, but influences the reference coordinates which were considered as precise.

Some CS detection filters, like the ones in CSRS-PPP, may flag ambiguities reset, whereas others discard the data corresponding to the epochs in which the CS is detected. Deciding, which is the best procedure is not a trivial task. As it has been noted ambiguity and increased DOP may induce errors when this number falls below a critical value. This effect strongly depends on the satellite which is affected by the ambiguity reset and on the satellite that has been discarded after a CS screening. From this analysis it can be deduced that:

- A critical number of satellites are not so decisive in PPP performance unless the distribution in the sky is no good enough, or the ambiguities are poorly established. An increased constellation may help to reduce this problem.
- As expected, adding GLONASS constellation produce an improvement of the results in periods of high ROT when PPP with only GPS was deteriorated.
- A higher sampling rate in the data, may also diminish the PPP deterioration induced by ambiguities reset. Nevertheless, the problem regarding kinematic PPP with 1 s sampling arises because precise satellite and clock products must be interpolated further, which introduces solution accuracy degradation.

Regarding mid-latitude irregularities effect on PPP it is stated that:

- No big errors attributable to them have been observed in AMC2 2001, 2004, and 2008. The most extreme irregularities observed do not produce significant

errors. However, this is not necessarily extensible to other PPP engines and stations.

Chapter 6 analyzes a case study in which errors have been observed to occur at the same time, independently of the latitude of the GNSS station. Although only the results regarding few low-latitude stations have been shown, they are representative of the general phenomena observed. The case study analyzes the October 28th, 2003 SITEC effect on PPP accuracy. The event under study was characterized by simultaneous SRB and SITEC. Previous works stated that the SNR fades were associated to the SRB, and signal losses in those periods were attributed to this phenomena in which the SITEC played a secondary role. In this chapter it is proven that:

- There are two main reasons for the accuracy degradation observed in kinematic PPP: the signal loss due to the SRB, and the PPP software shortcomings to deal with the observables that have been affected by this SITEC.
- The SITEC is the main contributor to the errors observed in PPP in many stations of the sunlit hemisphere at that time, although SRB contribution to noise cannot be ignored.
- Errors are caused by ambiguities reset induced by this phenomena on the CS detection filters, especially on the NL combination based filter. The scale of those errors does not depend on the magnitude of the ionospheric perturbation at each location.
- The stations with an ASHTECH Z-XII3 receiver, introduce some noise in the observables in the period of SITEC.
- When considering a higher sampling rate (1 s instead of 30 s), the errors related to the SITEC disappear.

It should be noted that large differences may exist between PPP techniques and that some of the results observed cannot be extrapolated to other methods.

All in all, this thesis work contributes to the understanding of the effects causing errors in PPP and the physical processes that generate them, and the role of receivers when dealing with signals affected by ionospheric effects is also highlighted.

The relevance of this study is not constrained to PPP users but is extended to all GNSS community working on aeronomy, positioning or other applications.

Resumen y conclusiones

El análisis llevado a cabo durante el desarrollo de este trabajo de tesis doctoral ha contribuido a alcanzar los objetivos de investigación generales y específicos establecidos en la introducción de este manuscrito. El primer objetivo buscaba analizar de forma general los efectos de las variaciones rápidas de TEC sobre la degradación del posicionamiento, mientras que el segundo consistía en identificar la causa de dichos errores e investigar las características de los fenómenos físicos involucrados. En concreto, estos objetivos se han aplicado al análisis del PPP con datos de estaciones situadas en latitudes bajas y medias.

El Capítulo 1 presenta una visión general del PPP, e introduce la motivación del estudio de la tesis. Este trabajo ha puesto de relieve que aunque el PPP no es una técnica nueva, su potencial máximo en cuanto a la exactitud y sus aplicaciones se están alcanzando en los últimos años con el desarrollo de nuevas técnicas que resuelven las principales causas de error en la distancia satélite-receptor. Sin embargo, el estudio realizado permite confirmar que aún existen algunos fenómenos que inducen errores que, hasta ahora, parecen escapar del control del método de posicionamiento, y causan una notable degradación de la precisión esperada en ésta técnica. En concreto, los errores relacionados con las irregularidades ionosféricas.

El Capítulo 2 recopila una introducción acerca de la ionosfera de medias y bajas latitudes y los procesos que intervienen en la aparición de las irregularidades ionosféricas en dichas latitudes. También se explica el efecto que el medio ionosférico tiene en el recorrido de la señal GNSS y en particular, el papel de las irregularidades de plasma presentes en ella.

En el Capítulo 3, se expone la estrategia seguida en el análisis de datos del presente trabajo. Después de la introducción de los datos, se comenta el procedimiento utilizado para obtener el ROT y se explican sus deficiencias con respecto al ROT calculado únicamente con las fases de las portadoras. Además, este capítulo trata los diferentes procedimientos propuestos para la detección de distintos tipos de irregularidades atendiendo a las propias características observadas en el ROT. En este capítulo también se ha introducido el servicio CSRS-PPP y el procedimiento seguido para obtener la posición de las estaciones.

A partir del análisis del método utilizado para estimar el ROT se concluye que:

- El ROT estimado a partir de las curvas de sTEC que se han obtenido con un procedimiento que incluye pseudo-distancias (los códigos) es muy sensible al ruido, y todos los fenómenos que contribuyen al aumento de éste son una fuente de discrepancia con el ROT calculado solamente con las fases de las portadoras.

- Los períodos observados que muestran una mayor discrepancia, son probablemente los caracterizados por un mayor ruido, y por lo tanto, pueden ser indicadores de una posible solución más ruidosa en las técnicas de posicionamiento basadas en pseudodistancias.

- La reducción del efecto geométrico en el ROT a través de una función de mapeo puede inducir grandes errores en el ROT, especialmente en latitudes bajas y cuando se consideran los satélites de menor elevación. Los efectos dependen tanto de la estación del año como de la actividad solar.

En el Capítulo 4 se ha presentado la aparición de irregularidades ionosféricas en base al análisis del ROT. Se ha utilizado un ROT sin suavizar ni filtrar con el fin de detectar las variaciones debidas a una mayor variedad de fenómenos. En cuanto a los datos de las estaciones de latitudes bajas, se han seleccionado 6 estaciones que cubren diferentes longitudes. Se ha definido un valor de umbral común que ayuda a distinguir los períodos de la ionosfera en calma de los períodos activos, en base al cual se han mostrado los resultados. Este valor umbral no diferencia entre los tipos de irregularidades que causan la respuesta en el TEC, y depende del ruido introducido por el receptor.

- Como cabría esperar, se ha observado la aparición de valores de ROT superiores a 0,3 TECU/30s que dependen de la hora local, la temporada del año, la longitud geográfica a la que se encuentra la estación, la actividad geomagnética y la actividad solar, aunque también se ha observado variabilidad de día a día.

- También se ha observado la inducción e inhibición de irregularidades durante tormentas geomagnéticas, pero el mecanismo que las causas no ha sido identificado aún.

- Además, se han identificado irregularidades que se producen después del amanecer, pero el mecanismo que las genera también es desconocida en la actualidad.

En cuanto a las estaciones de latitudes medias (MAD2 y AMC2), las estructuras predominantes identificadas en el ROT son los patrones en forma de onda que caracterizan a los TID. Tras el análisis de 11 años de datos de MAD2 y 4 en AMC2, se ha observado que estas estructuras se producen tanto de día como de noche y en periodos de baja y alta actividad solar. Las estructuras diurnas se producen sobre todo en el primer y último trimestre de cada año, desde la salida hasta la puesta del sol, mientras que las estructuras nocturnas, entre mayo y agosto.

- Este tipo de irregularidades no muestran las características necesarias para causar una posible degradación de la precisión del PPP. Sin embargo, las fluctuaciones rápidas del ROT relacionadas con las estructuras nocturnas también se caracterizan por variaciones más rápidas del ROT que en función

de su magnitud podrían considerarse como una amenaza potencial para el PPP aunque en este trabajo en concreto no ha sido así.

También se han identificado a través del ROT no filtrado, irregularidades relacionadas con la Meteorología Espacial.

- Este parámetro es sensible a las variaciones debidas a tormentas ionosféricas positivas y sirve para su identificación.
- Se ha observado que cuando la fase principal de una tormenta se produce en la noche local de la estación de medición, pueden aparecer fuertes y rápidas fluctuaciones del ROT. En el caso concreto de MAD2, la presencia de estas irregularidades puede estar relacionada con la expansión de la anomalía ecuatorial y la intrusión de fenómenos de bajas latitudes a mayores latitudes. Sin embargo, para poder afirmarlo con seguridad, es necesario un análisis adicional más exhaustivo.
- Se ha establecido un novedoso procedimiento de detección de SITECs basado en el valor cuadrático medio (RMS) y la desviación estándar (STD) de los valores de ROT en cada época.

En el Capítulo 5 se analiza el efecto del ROT que caracteriza a las irregularidades mencionadas en el PPP cinemático (en particular en la solución del CSRS-PPP). En primer lugar, se ha estudiado el comportamiento de los receptores GPS a partir del estudio de la pérdida de observables de los ficheros RINEX correspondientes a las estaciones de baja latitud. En general, se observa una mejora en los últimos años, 2008 y 2011, con respecto a 2001 y 2004, especialmente en relación con el seguimiento de satélites de alta elevación. Esto se aprecia también en los períodos de mayor ROT. Se ha visto que en los años de alta y media actividad solar, la pérdida de observables aumenta en los períodos de alto ROT, especialmente desde la puesta del sol hasta pasada ligeramente la medianoche, aunque existen excepciones, como por ejemplo AREQ 2001 y NTUS 2004, donde apenas se ha observado un deterioro de la recepción de la señal asociada a los altos valores de ROT. De estas observaciones se concluye que:

- Aunque efectos locales, como la magnitud de los gradientes presentes en la ionosfera, pueden inducir pérdidas de los observables, las características propias de cada receptor condicionan la susceptibilidad a perder la señal.
- Cada receptor provoca la pérdida de un observable u otro.
- En cuanto a los resultados de reproducibilidad, las características de los receptores marcan las diferencias de los observables, y por lo tanto, las discrepancias observadas tanto en los resultados del ROT como del PPP.

En segundo lugar, se ha analizado la precisión del PPP en modo cinemático en la coordenada vertical, para los años 2001, 2004, 2008 y 2011 en una variedad de

estaciones de baja latitud y en AMC2. En cuanto a las bajas latitudes se han observado errores en la posición que aumentan en periodos coincidentes con fuerte ROT que pueden superar los 50 cm, sobre todo en 2001 y 2004. De este análisis se puede concluir que:

- Como se podía esperar, el máximo de la degradación en la precisión del PPP se produce principalmente en los períodos en que se observa un gran ROT.
- Se observa una mejora de la precisión de la componente vertical calculada en cada época para los años 2008 y 2011 con respecto a 2001 y 2004, lo que se atribuye principalmente a la mejora en los productos del IGS. Esta mejora se observa más claramente cuando se analiza la repetitividad diaria, donde la solución es de dos a cuatro veces más precisa en 2008 y 2011 debido a la mejora en dichos productos. Por otro lado, se observa también un progreso en relación con los períodos coincidentes con la presencia de altos valores de ROT que puede estar relacionado con mejoras detectadas en el rendimiento de los receptores bajo ese tipo de condiciones, como se muestra en la manifestación de pérdida de señal.
- Se ha observado un empeoramiento de la repetitividad diaria que es causada por un aumento en la reestimación de ambigüedades que se producen después de saltos de ciclo (CS) o una ausencia de datos, o deberse a los filtros internos del PPP que están basados en las combinaciones NL y WL. Este último produce más reestimaciones de ambigüedad sistemáticas que el primero. El número de ambigüedades restablecidas aumenta en períodos coincidentes con gran pérdida de la señal y fuerte ROT, y por lo tanto, la solución se deteriora con valores que pueden superar un orden de magnitud. Debido al deterioro de la repetitividad diaria, la posición de la estación diaria también se degrada, sobre todo cuando se lleva a cabo el modo de procesamiento cinemático.
- Se ha observado que cuando se representa gráficamente la solución de la posición para cada día, puede verse el desplazamiento intenso de la estación producida por ejemplo, por un terremoto, mientras que en los resultados época a época este efecto puede enmascararse por el ruido de la solución. Este tipo de eventos no afectan a la repetibilidad día a día a partir del día después del terremoto. Sin embargo, las coordenadas de referencia ya no pueden ser considerados como precisas.

Los filtros de detección de CSs de algunos procedimientos PPP, como los de CSRS-PPP, pueden dar lugar a la reestimación de ambigüedades, mientras que otros descartan los datos correspondientes a las épocas en las que se detectan los CSs. Decidir, cual es el mejor procedimiento no es una tarea trivial ya que, como se ha demostrado en este trabajo, bajo una constelación con un número crítico de satélites visibles (ya sea por la localización o por la pérdida de señal), tanto una

ambigüedad mal estimada como el aumento de la dilución de precisión pueden inducir errores. El efecto depende en gran medida del satélite que se ve influenciado por el restablecimiento de la ambigüedad y del que ha sido desechado después de la detección del CS. De este análisis se deduce que:

- Un número crítico de satélites no es tan decisivo en el rendimiento de PPP a menos que la distribución en el cielo no sea lo suficientemente buena, o las ambigüedades estén pobremente establecidas. Un aumento de la constelación puede ayudar a reducir este problema.
- La consideración de los datos de la constelación GLONASS produce una mejora de los resultados de PPP cinemático incluso en períodos caracterizados por un elevado ROT con respecto a los resultados obtenido solo con la constelación GPS.
- Una velocidad de muestreo mayor en los datos, también puede disminuir el deterioro de PPP inducido por la reestimación reiterada de ambigüedades. Sin embargo, el problema con respecto al PPP cinemático con una tasa de muestreo a 1 s reside en que los productos precisos de las orbitas y los relojes de los satélites deben ser interpolados más allá, lo que introduce la degradación de la precisión de la posición.

En cuanto al efecto de las irregularidades de latitudes medias en el PPP:

- En AMC2 para 2001, 2004 y 2008 no se han observado grandes errores atribuibles a la presencia de altos valores de ROT. Las irregularidades más extremas observadas no producen errores significativos, pero, esto no quiere decir que este resultado sea extensible a otras estaciones GNSS y a otros procedimientos de PPP.

Existe un caso en el que se han observado errores de forma simultánea independientemente de la latitud de la estación GNSS. Esta situación se ha analizado en el Capítulo 6, aunque se muestran solamente los resultados relacionados con estaciones de latitudes bajas, ya que se consideran representativos de los fenómenos generales observados. El fenómeno estudiado es el SITEC ocurrido el 28 de octubre de 2003. Dicho evento se caracterizó por la presencia de interferencias debidas a emisiones solares de ondas de radio (SRB) y aumento del TEC (SITEC) simultáneos. Trabajos previos indican que la relación señal ruido disminuyó debido al efecto del SRB y que las pérdidas de señal en esos períodos se atribuyeron a este fenómeno en el que el SITEC desempeñó un papel secundario. En este capítulo se demuestra que:

- Hay dos razones principales para la degradación de la precisión cinemática observada en el PPP: la pérdida de señal debido al SRB y las limitaciones del *software* de PPP para hacer frente a los observables que han sido afectados por este SITEC.

- El SITEC es el principal contribuyente a los errores observados en el PPP en muchas estaciones del hemisferio iluminado en ese momento, si bien, el aporte del SRB al ruido no puede ser ignorada.
- Los errores son causados por el restablecimiento de ambigüedades inducido por la respuesta de los filtros de detección de CS al SITEC, en especial, en el filtro basado en la combinación NL. La escala de los errores no depende de la magnitud de la perturbación ionosférica en cada lugar.
- Las estaciones con un receptor ASHTECH Z-XII3 introducen ruido en los observables en el período de SITEC.
- Cuando se considera una tasa de muestreo más alta, 1 s en lugar de 30 s, los errores relacionados con el SITEC desaparecen.

Debe tenerse en cuenta que pueden existir grandes diferencias entre distintas técnicas de PPP y, que algunos de los resultados observados no se pueden extrapolar a otros procedimientos.

Con todo, este trabajo de tesis contribuye a la comprensión de los efectos ionosféricos que causan errores en el PPP y los procesos físicos que los generan y pone de relieve la importancia del papel que juegan los receptores cuando se trata de señales afectadas por efectos ionosféricos.

La relevancia de este estudio no se limita a los usuarios de PPP sino que se extiende a toda la comunidad GNSS que trabaja en aeronomía, posicionamiento u otras aplicaciones.

7.2. Recommendations and future works

Based on the results obtained in this work, some recommendations arise:

- For future works it is highly recommended to use ROT estimated only with phases.
- The observation campaigns should be carried out taking into account that, depending on the location and the time space considered (low latitudes equinoctial months at local nighttime), the data may be prone to be affected by ionospheric phenomena which may lead to shorter records. Tracking problems or software limitations that can originate errors related with convergence time and ambiguities reset, are the main causes of this adverse effect.
- Since the IGS stations do not provide GNSS signal and scintillation data, detailed description of the units of the RINEX containing SNR information would be appreciated.

This Dissertation provides an overview of the various kind of irregularities affecting the GNSS signal at the latitudes of interest (mid- and low-latitudes); identifies the kind of irregularities affecting PPP; and recognizes the reason for PPP accuracy degradation. However, there are still some questions regarding ionospheric irregularities occurrence, day to day variability, and signal conditions (if affected or not by scintillation, the kind of scintillation and its severity), that still need to be answered. For that reason, future works include:

- The analysis of the day to day variability in the occurrence of large ROT observed in low-latitudes stations.
- A case by case study of the days when MAD2 shows fast and large fluctuations of ROT in presence of a geomagnetic storm effect. The analysis would include interplanetary medium data and magnetometer, digisondes and GNSS observation of stations available in the range of longitudes close to MAD2.
- The improvement of the SITEC detection technique based on RMS and STD of ROT to convert it in a more robust tool for SITEC detection and characterization, and its application to low-latitude station's data.. The developed technique is a promising method for automatization and almost real time applications, because it does not need TEC calibration. A SITEC event that has been considered large by evaluation of the TEC reached, does not necessarily presents a high ROT. Some of the events considered in literature as the most intense, are not characterized by such a sharp and large ROT, and vice versa. Although the ROT does not tell us anything about the recovery of the ionosphere to a "normal" condition, it indicates if the event can be dangerous or not for GNSS applications, due to the data filtering routines. It

should be checked also if it is useful to flag epochs when falsely detected CS occur.

- The analysis of the relationship between X-rays and EUV radiation and the intensity of the ROT that characterizes the SITECs detected in MAD2 for the period 2005-2015.
- The application of different positioning routines to the extreme events listed in the tables of this manuscript to evaluate how damaging they can be and which is the actual possibility of managing their effects.
- The incorporation of scintillation data in the analysis of both PPP routines checking and ionospheric information retrieval, by means of ROT.
- The analysis of SITECs capability to cause GPS signal scintillation to discern if they induce noise in the observables or is the receiver the one which is not able to deal with the ionospheric effect.
- A study of the contribution of ionospheric irregularities to the multipath-noise by comparing records from same and different dual frequency receivers (or antennas) placed at the same site.
- A comparison of the observables linear combinations of receivers tracking L2C with the ones of codeless/semicodeless kind, in presence of ionospheric irregularities, for the evaluation of the receiver's role in the induction of noise on the observables that may generate failures when processed.

Recomendaciones y trabajos futuros

Basándose en los resultados obtenidos en este trabajo, se presentan algunas recomendaciones:

- Para futuras líneas de trabajo es muy recomendable utilizar el ROT estimado solamente con las fases.
- Las campañas de observación deben llevarse a cabo sabiendo que, dependiendo de la ubicación y el espacio de tiempo considerado (como son las noches de meses equinocciales en bajas latitudes), los datos pueden ser afectados por fenómenos ionosféricos capaces de originar el acortamiento de registros. Ello puede ser causado por limitaciones relacionadas con el receptor o con el software de posicionamiento que conduce a errores relacionados con el tiempo de convergencia de la solución o el restablecimiento de ambigüedades.
- Este tipo de trabajos requiere que exista una descripción detallada de los datos GNSS que se proporcionan en los RINEX, como son las unidades de S1 y S2 (SNR). De esta forma a falta de datos de centelleo de la señal se podría conocer la calidad de la señal en circunstancias variadas.

Esta tesis ofrece una visión general de los diferentes tipos de irregularidades que afectan a la señal GNSS en las latitudes de interés (medias y bajas); identifica el tipo de irregularidades que afectan al PPP; y contribuye a reconocer la razón de la degradación de la precisión. Sin embargo todavía hay algunas preguntas que deben ser respondidas respecto a la variabilidad día a día en la manifestación de irregularidades o a la calidad de la señal (si está afectado o no por centelleo, el tipo de centelleo y su gravedad). Por esa razón, los trabajos futuros incluyen:

- Un estudio de la variabilidad día a día en la manifestación del fuerte ROT observado en las estaciones de latitudes bajas utilizando los datos de diversos instrumentos disponibles para la ubicación y el tiempo considerado.
- El análisis de los días en los que MAD2 presenta fuerte ROT en presencia del efecto de tormentas geomagnéticas. Este análisis debe incluir datos del medio interplanetario, magnetómetros, digisondas y la observación de estaciones GNSS disponibles en el rango de longitudes cercanas a dicha estación GNSS.
- La mejora de la técnica de detección de SITECs basada en RMS y STD de ROT para convertirlo en una técnica más robusta para la detección y caracterización de estos fenómenos y su aplicación a las estaciones de baja latitud. Esta técnica parece un método prometedor para su automatización y aplicación en tiempo casi real ya que al basarse en ROT calculado sólo con fase no necesitaría calibración del TEC. Se ha observado que un gran SITEC evaluado por medio del nivel de TEC alcanzado no implica necesariamente un

alto ROT. Algunos de los eventos considerados en la literatura como intensos, no se caracterizan por un fuerte ROT, y viceversa. Aunque este parámetro no informa acerca de la recuperación de la ionosfera a una condición "normal", indica si puede ser peligroso o no para aplicaciones GNSS debido a su efecto sobre las rutinas de procesado de datos. Se debe comprobar también si es útil para señalar si se producen falsas detecciones de CSs.

- El análisis de la relación entre la radiación de rayos X y EUV con la intensidad del ROT que caracteriza los SITECs detectados en MAD2 para el período de 2005 a 2015.
- La evaluación de diferentes rutinas de posicionamiento con los eventos extremos que figuran en las tablas de este manuscrito para valorar su impacto adverso y si es posible gestionar este efecto.
- La consideración de datos de centelleo en el análisis de las dos rutinas; la del PPP y la de obtención del ROT.
- El análisis de los SITECs como posible causa de centelleo de la señal GPS para comprobar si inducen ruido en los observables o es el receptor el que no es capaz de tratar el efecto de la ionosfera.
- Un estudio de la contribución de las irregularidades ionosféricas en el multi-trayecto /ruido comparando los resultados de receptores de doble frecuencia (y /o antenas), iguales o diferentes, situados muy próximos unos a otros.
- Una comparación de las combinaciones de observables de receptores que registran L2C con los receptores de tipo codeless /semicodeless.

References

Aarons, J., M. Mendillo, R. Yantosca and E. Kudeki (1996), GPS phase fluctuation in the equatorial region during the MISETA 1994 campaign, J. Geophys. Res., vol. 101, pp. 26851-26862.

Abdu, M. A., (2001), Outstanding problems in the equatorial ionosphere thermosphere electrodynamics relevant to spread F, J. Atmos. Sol.-Terr. Phy., vol. 63, pp. 869-884.

Abdu, M. A., (2005), Equatorial ionosphere-thermosphere system: electrodynamics and irregularities, Adv. Space Res., vol. 35, pp. 771-787.

Abdu, M. A., J. A. Bittencourt and I. S. Batista (1981), Magnetic declination control of the field development and spread F, J. Geophys. Res., vol. 86, no. A13, pp. 11443-11446.

Abdu, M. A., I. S. Batista, H. Takahashi, J. MacDougall, J. H. Sobral, A.F. Medeiros and N. B. Trivedi (2003), Magnetospheric disturbance induced equatorial plasma bubble development and dynamics: a case study in Brazilian sector, J. Geophys. Res., vol. 108, no. A12.

Abdu, M. A., I. S. Batista, A. J. Carrasco and C. G. M. Brum (2005), South Atlantic magnetic anomaly: a review and a new focus on electrodynamic effects in the equatorial ionosphere, J. Atmos. Sol.-Terr. Phy., vol. 67, pp. 1643-1657.

Abdu, M. A., E. Alam Kherani, I. S. Batista, E. R. de Paula, D. C. Fritts and H. A. Sobral (2009), Gravity wave initiation of equatorial spread F/plasma bubble irregularities based on observational data from the SpreadFEx campaign, Ann. Geophys., vol. 27, pp. 2607-2622.

Abdu, M., D. Pancheva and A. Bhattacharyya Eds. (2011), Aeronomy of the Earth's atmosphere and ionosphere, IAGA Special Sopron Book Series, Springer Netherlands, vol. 2, pp. 480.

Aquino, M., J. F. G. Monico, A. H. Dodson, H. Marques, G. De Franceschi, L. Alfonsi, V. Romano and M. Andreotti (2009), Improving the GNSS positioning stochastic model in the presence of ionospheric scintilaltion, J. Geod., vol. 83, pp. 953-966.

Balan, N., G. J. Bailey, M. A. Abdu, K. I. Oyama, P. G. Richards, J. MacDougall and I. S. Batista (1997), Equatorial plasma fountain and its effects over three locations: evidence for an additional layer, the F3 layer, J. Geophys. Res., vol. 102, no. A2, pp. 2047-2056.

Banville, S., R. B. Langley, S. Saito, and T. Yoshihara (2010), Handling cycle slips in GPS data during ionospheric plasma bubble events, Radio Sci., vol. 45, RS6007.

Basu, S., S. Basu, J. Aarons, J. P. McClure and M. D. Cousins (1978), On the coexistence of kilometer-and meter-scale irregularities in the nighttime equatorial F region, J. Geophys. Res., vol. 83, no. A9, pp. 4219-4226.

Basu, Su., S. Basu, J. J. Makela, R. E. Sheehan, E. MacKenzie, P. Doherty, J. W. Wright, M. J. Keskinen, D. Pallamraju, L. J. Paxton and F. T. Berkey (2005), Two components of ionospheric plasma structuring at midlatitudes observed during the large magnetic storm of October 30, 2003, Geophys. Res. Lett., vol. 32, L12S06.

Blanc, M., and A. D. Ridchmond (1980), The ionospheric disturbance dynamo, J. Geophys. Res., vol. 85, no. A4, pp. 1669-1686.

Blewitt, G., (1990), An automatic editing algorithm for GPS data, Geophys. Res. Lett., vol. 17, no. 3, pp. 199-202.

Benton, C. J., and C. N. Mitchell (2012), GPS satellite oscillator faults mimicking ionospheric phase scintillation, GPS Solut., vol. 16, no. 4, pp. 477-482.

Benton, C. J., and C. N. Mitchell (2014), Further observations of GPS satellite oscillator anomalies mimicking ionospheric phase scintillation, GPS Solut., vol. 18, no. 3, pp. 387-391.

Bisnath, S., and Y. Gao (2009), Precise Point Positioning: A powerful technique with a promising future, GPS World, vol. 20, no. 4, April 2009, pp. 43-50.

Bock, H., R. Dach, A. Jäggi and G. Beutler (2009), High-rate GPS clock corrections from CODE: support of 1 Hz applications, J. Geod., vol. 83, pp. 1083-1094.

Boehm, J., A. Niell, P. Tregoning and H. Schuh (2006), Global Mapping Function (GMF): A new empirical mapping function based on numerical weather model data, Geophys. Res. Lett., vol. 33, L07304.

Boehm, J., R. Heinkelmann and H. Schuh (2006), Short Note: A global model of pressure and temperature for geodetic applications, J. Geod., vol. 81, pp. 679-683.

Borries, C., N. Jakowski and V. Wilken (2009), Storm Induced Large Scale TIDs observed in GPS derived TEC, Ann. Geophys., vol. 27, pp. 1605-1612.

Budden, K. G., (1985), The propagation of radio waves: the theory of radio waves of low power in the ionosphere and magnetosphere, Cambridge University Press, New York.

Buonsanto, M. J., (1999), Ionospheric Storms: A review, Space Science Reviews, vol. 88, pp. 563-601.

Burke, B. J., C. Y. Huang, L. C. Gentile and L. Bauer (2004), Seasonal–longitudinal variability of equatorial plasma bubbles, Ann. Geophys., vol. 22, pp. 3089–3098.

Burke, W. J., O. de La Beaujardière, L. C. Gentile, D. E. Hunton, R. F. Pfaff, P. A. Roddy, Y.-J. Su and G. R. Wilson (2009), C/NOFS observations of plasma density and electric field irregularities at post-midnight local times, Geophys. Res. Lett., vol. 36, L00C09.

Cai, C., Y. Gao, L. Pan and J. Zhu (2015), Precise point positioning with quad-constellations: GPS, Beidou, GLONASS and Galileo, Adv. Space Res., vol. 56, pp. 133-143.

Caissy, M., L. Agrotis, G. Weber, M. Hernandez-Pajares and U. Hugentobler (2012), Coming soon: The international GNSS real-time service, GPS World, June 1, 2012, http://gpsworld.com/gnss-systemaugmentation-assistanceinnovation-coming-soon-13044/. [Accessed 09/09/ 2015].

Calais, E., J. Y. Han, C. DeMets and J. M. Nocquet (2006), Deformation of the North American plate interior from a decade of continuous GPS measurements, J. Geophys. Res., vol. 111, B06402.

Carrano, C. S., K. M. Groves, W. J. McNeil and P. H. Doherty (2013), Direct measurement of the residual in the ionosphere-free linear combination during scintillation, in: Proceedings of the 2013 International Technical Meeting (ITM) of the Institute of Navigation, San Diego, CA, January 28–30, pp. 585-596.

Cerruti, A. P., P. M. Kintner, D. E. Gary, L. J. Lanzerotti, E. R. de Paula and H. B. Vo (2006), Observed solar radio burst effects on GPS/Wide Area Augmentation System carrier-to-noise ratio, Space Weather, vol. 4, S10006.

Chen, Z., Y. Gao and Z. Liu (2005), Evaluation of solar radio bursts' effect on GPS receiver signal tracking within International GPS Service network, Radio Sci., vol. 40, RS3012.

Ciraolo, L., F. Azpilicueta, C. Brunini, A. Meza and S. M. Radicella (2007), Calibration errors on experimental slant total electron content (TEC) determined with GPS, J. Geod., vol. 81, pp. 111–120.

Collins, P., F. Lahaye, P. Héroux and S. Bisnath (2008), Precise point positioning with ambiguity resolution using the Decoupled Clock Model, in: Proceedings of ION GNSS 2008, Savannah, GA, United States, 16-18 September, pp. 1315-1322.

Dach, U., U. Hugentobler, R. Fridez and P. Meindl. Bernese GPS Software Version 5.0, 2007.

De Lacy, M. C., F. Sansó, A. J. Gil and G. Rodríguez-Caderot (2005), A method for the ionospheric delay estimation and interpolation in a local GPS network, Stud. Geophys. Geod., vol. 49, pp. 63–84.

De Lacy, M. C., A. J. Gil, G. Rodríguez-Caderot and B. Moreno (2008), A method to estimate the ionospheric bias by using the new GNSS frequencies: Analysis of its theoretical accuracy in a PPP context, Física de la Tierra, vol. 20, pp. 133–150.

Demyanov, V.V., E. L. Afraimovich and S. Jin (2012), An evaluation of potential solar radio emission power threat on GPS and GLONASS performance, GPS. Solut., vol. 16, pp. 411-424.

Dixon, K. (2006), StarFireTM: A global SBAS for sub-decimetre precise point positioning, in: Proceedings of ION GNSS 2006, Fort Worth, Texas, 26-29 September, pp. 2286-2296.

Dow, J. M., R. E. Neilan and C. Rizos (2009), The International GNSS Service in a changing landscape of Global Navigation Satellite Systems, J. Geod., vol. 83, pp. 191-198.

Drake, S. P., (2002), Converting GPS coordinates to navigation coordinates. Defence, Science and Technology Organisation (DSTO). Electronics and Surveillance Research Laboratory (DSTO-TN-0432). Technical note. http://dspace.dsto.defence.gov.au/dspace/bitstream/-1947/3538/1/DSTO-TN-0432.pdf

Ebner, R., and W. E. Featherstone (2008), How well can online GPS PPP post-processing service be used to establish geodetic survey control networks? Journal of Applied Geodesy, vol. 2, pp. 149-157.

Eccles, J. V., (1998), Modeling investigation of the evening prereversal enhancement of the zonal electric field in the equatorial ionosphere, J. Geophys. Res., vol. 103, no. A11, pp. 26709-26719.

Eccles, J. V., J. P. St. Maurice and R. W. Schunk (2015), Mechanisms underlying the prereversal enhancement of the vertical plasma drift in the low-latitude ionosphere, J. Geophys. Res.-Space Physics, vol. 120, pp. 4950-4970.

Fejer, B. G., E. R. de Paula, I. S. Batista, E. Bonelli and R. F Woodman (1989). Equatorial F region vertical plasma drifts during solar maxima, J. Geophys. Res., vol. 94, no. A9, pp. 12049–12054.

Fejer, B. G., L. Scherliess and E.R. de Paula (1999), Effects of the vertical plasma drift velocity on the generation and evolution of equatorial spread F, J. Geophys. Res., vol. 104, no. A9, pp. 19859–19869.

Fejer, B. G., J. R. Souza, A. S. Santos, and A. E. Costa Pereira (2005), Climatology of F region zonal plasma drifts over Jicamarca, J. Geophys. Res., vol. 110, A12310.

Fejer, B. G., J. W. Jensen and S.-Y. Su (2008), Seasonal and longitudinal dependence of equatorial disturbance vertical plasma drifts, Geophys. Res. Lett., vol. 35, L20106.

Fejer, B. G, B. D. Tracy, M. E. Olson and J. L. Chau (2011), Enhanced lunar semidiurnal equatorial vertical plasma drifts during sudden stratospheric warmings, Geophys. Res. Lett., vol. 38, L21104.

Fejer, B. G., B. D. Tracy and F. Pfaff (2013), Equatorial zonal plasma drifts measured by the C/NOFS satellite during the 2008-2011 solar minimum, J. Geophys. Res., vol. 118, pp. 3891-3897.

Fejer, B. G., D. Hui, J. L. Chau and E. Kudeki (2014), Altitudinal dependence of evening equatorial F region vertical plasma drifts, J. Geophys. Res. Space Physics, vol. 119, pp. 5877–5890.

Fesen, C. G., G. Crowley, R. G. Roble, A. D. Richmond and B. G. Fejer (2000), Simulation of the pre-reversal enhancement in the low latitude vertical ions drifts, Geophys. Res. Lett., vol. 27, no. 13, pp. 1851-1854.

Forbes, J. M., X. Zhang, S. Plo, J. Russell, C. J. Mertens and M. Mlynczak (2008), Tidal variability in the ionospheric dynamo region, J. Geophys. Res., vol. 113, A02310.

Ge, M., G. Gendt, M. Rothacher, C. Shi and J. Liu (2008), Resolution of GPS carrier-phase ambiguities in precise point positioning (PPP) with daily observations, J. Geod., vol. 82, pp. 389–399.

Geng, J., F. N. Teferle, C. Shi, X. Meng, A. H. Dodson and J. Liu (2009), Ambiguity resolution in precise point positioning with hourly data, GPS Solut., vol. 13, pp. 263-270.

Geng, J., X. Meng, A. H. Dodson and F. N. Teferle (2010), Integer ambiguity resolution in precise point positioning: method comparison, J. Geod., vol. 84, pp. 569-581.

Gentile, L. C., W. J. Burke and F. J. Rich (2006), A climatology of equatorial plasma bubbles from DMSP 1989-2004, Radio Sci., vol. 41, RS5S21.

Gentile, L. C., W. J. Burke, P. A. Roddy, J. M. Retter and R. T. Tsunoda (2011), Climatology of plasma density depletions observed by DMSP in dawn sector, J. Geophys. Res., vol. 116, A03321.

Grinter, T., and C. Roberts (2011), Precise Point Positioning: Where are we now? In: Proceedings of IGNSS Symposium 2011, Sydney, Australia, 15-17 November.

Grinter, T., and V. Janssen (2012), Post-processed Precise Point Positioning: A Viable Alternative? In: Proceedings of APAS2012, Wollongong, New South Wales, Australia, 19-21 March.

Grinter, T., and C. Roberts (2013), Real Time Precise Point Positioning: Are we there yet? In: Proceedings of IGNSS Symposium 2013, Sydney, Australia. 16-18 July.

Gonzalez, W. D., J. A. Joselyn, Y. Kamide, H. W. Kroehl, G. Rostoker, B. T. Tsurutani and V. M. Vasyliunas (1994), What is a geomagnetic storm? J. Geophys. Res., vol. 99, no. AS4, pp. 5771-5792.

Gonzalez, W. D., A. L. Clúa de Gonzalez, J. H. A. Sobral, A. Dal Lago and L. E. Vieira (2001), Solar and interplanertary causes of very intense geomagnetic storms, J. Atmos. Sol.-Terr. Phy., vol. 63, pp. 403-412.

Hagan, M. E., A. Maute, R. G. Roble, A. D. Richmond, T. J. Immel and S. L. England (2007), Connections between deep tropical clouds and the Earth's ionosphere, Geophys. Res. Lett., vol. 34, L20109.

Hargreaves, J. K., (1992), The solar-terrestrial environment, An introduction to geospace-the science of the terrestrial upper atmosphere, ionosphere and magnetosphere, Cambridge University Press.

Hartmann, G. A. and I.G. Pacca (2009), Time evolution of the South Atlantic Magnetic Anomaly, Anais da Academia Brasileira de Ciências, vol. 81, no. 2, pp. 243-255.

Heelis, R. A., (2004), Electrodynamics in the low and middle latitude ionosphere: a tutorial, J. Atmos. Sol.-Terr. Phy., vol. 66, pp. 825-838.

Hernández-Pajares, M., J. M. Juan and J. Sanz (2006), Medium-scale traveling ionospheric disturbances affecting GPS measurements: Spatial and temporal analysis, J. Geophys. Res., vol. 111, A07S11.

Hocke, K., and K. Schlegel (1996), A review of atmospheric gravity waves and travelling ionospheric disturbances: 1982-1995, Ann. Geophys., vol. 14, pp. 917-940.

Hoque, M. M., and N. Jakowski (2008), Estimate of higher order ionospheric errors in GNSS positioning, Radio Sci., vol. 43, RS5008.

Huang, C.-S., S. Sazykin, J. L. Chau, N. Maruyama and M. C. Kelley (2007), Penetration electric fields: Efficiency and characteristic time scale, J. Atmos. Sol.-Terr. Phy., vol. 69, pp. 1135-1146.

Immel, T. J., E. Sagawa, S. L. England, S. B. Henderson, M. E. Hagan, S. B. Mende, H. U. Frey, C. M. Swenson and L. J. Paxton (2006), Control of equatorial ionospheric morphology by atmospheric tides, Geophys. Res. Lett., vol. 33, L15108.

Jacobsen, K. S., and M. Dähnn (2014), Statistics of ionospheric disturbances and their correlation with GNSS positioning errors at high latitudes, J. Space Weather Space Clim., vol. 4, A27.

Kaplan, E. D., and C. Hegarty Eds. (2005), Understanding GPS: principles and applications, Second edition, Artech House.

Kashcheyev, A., B. Nava and S. M. Radicella (2012), Estimation of higher-order ionospheric errors in GNSS positioning using a realistic 3-D electron density model, Radio Sci., vol. 47, RS4008.

Kedar, S., G. A. Hajj, B. D. Wilson and M. B. Heflin (2003), The effects of the second order GPS ionospheric correction on receiver position, Geophys. Res. Lett., vol. 30, no. 16, pp. 1829.

Kelley, M. C., (2009), The Earth's ionosphere: plasma physics and electrodynamics, Second Edition, Academic Press, Elsevier, pp. 579.

Kelley, M. C., R. R. Ilma and G. Crowley (2009), On the origin of pre-reversal enhancement of the zonal equatorial electric field, Ann. Geophys., vol.27, pp. 2053-2056.

Kelley, M .C., F. S. Rodrigues, R. F. Pfaff and J. Klenzing (2014), Observations of the generation of eastward equatorial electric fields near dawn, Ann. Geophys., vol. 32, pp. 1169-1175.

Kikuchi, T., K. K. Hashimoto, T.-I. Kitamura, H. Tachihara and B. Fejer (2003), Equatorial counter electrojets during substorms, J. Geophys. Res., vol. 108, no. A11, 1406.

Kil H., R. A. Heelis, L. J. Paxton and S.-J. Oh (2009), Formation of a plasma depletion shell in the equatorial ionosphere, J. Geophys. Res., vol. 114, A11302.

Kim, V. P., K. W. Min and V. V. Hegai (2015), Equatorial plasma depletions observed by the DMSP F13 satellite near dawn during geomagnetic disturbances in a solar minimum, Adv. Space Res., vol. 55, pp. 554-565.

Kintner, P. M., B. M. Ledvina, E. R. de Paula and I. J. Kantor (2004), Size, shape, orientation, speed, and duration of GPS equatorial anomaly scintillations, Radio Sci., vol. 39, RS2002.

Kintner, P. M., B. M. Ledvina and E. R. de Paula (2007), GPS and ionospheric scintillations, Space Weather, vol. 5, S09003.

Klimenko, M. V., and V. V. Klimenko (2011), Numerical simulation of the F2-layer stratification and appearance of the F3 and G layers in the equatorial ionosphere: the morphology of the phenomena, Geomagnetism and Aeronomy, vol. 51, no. 5, pp. 646-655.

Kouba, J., and P. Heroux (2001), Precise point positioning using IGS orbit and clock products, GPS Solut., vol. 5, no. 2, pp. 12-28.

Kouba, J., (2009), A guide to using International GNSS Service (IGS) products, https://igscb.jpl.nasa.gov/components/usage.html. [Accesed 19/11/2015]

Langley, R. B., (1999), Dilution of precision, GPS World, vol. 10, no. 5, May 1999, pp. 52-59.

Le, H., L. Liu, Y. Chen and W. Wan (2013), Statistical analysis of ionospheric responses to solar flares in the solar cycle 23, J. Geophys. Res. Space Physics, vol. 118, pp. 576–582.

Lemoine, J.-M., and H. Capdeville (2006), A corrective model for Jason-1 DORIS Doppler data in relation to the South Atlantic Anomaly, J. Geod., vol. 80, pp. 507-523.

Li, G., B. Ning, L. Liu, Z. Ren, J. Lei and S. Y. Su (2007), The correlation of longitudinal/seasonal variations of evening equatorial pre-reversal drift and of plasma bubbles, Ann. Geophys., vol. 25, pp. 2571–2578.

Li, G., B. Ning, L. Liu, B. Zhao, X. Yue, S.-Y. Su and S. Venkatraman (2008), Correlative study of plasma bubbles, evening equatorial ionization anomaly, and equatorial prereversal ExB drifts at solar maximum, Radio Sci., vol. 43, RS4005.

Li, X., X. Zhang, X. Ren, M. Fritsche, J. Wickert and H. Schuh (2015), Precise positioning with current multi-constellation Global Navigation Satellite Systems: GPS, GLONASS, Galileo and Beidou, Sci. Rep., vol. 5, 8328.

Lin, C. H., J. Y. Liu, T. W. Fang, P. Y. Chang, H. F. Tsai, C. H. Chen and C. C. Hsiao (2007), Motions of the equatorial ionization anomaly crests imaged by FORMOSAT-3/ COSMIC, Geophys. Res. Lett., vol. 34, L19101.

Liu, J. Y., C. H. Lin, Y. I. Chen, Y. C. Lin, T. W. Fang, C. H. Chen, Y. C. Chen and J. J. Hwang (2006), Solar flare signatures of the ionospheric GPS total electron content, J. Geophys. Res., vol. 111, A05308.

Liu, H., C. Stolle, M. Föster and S. Watanabe (2007), Solar activity dependence of the electron density in the equatorial anomaly regions observed by CHAMP, J. Geophys. Res., vol. 112, A11311.

Liu, L., W. Wan, B. Ning and M.-L. Zhang (2009), Climatology of the mean total electron content derived from GPS global ionospheric maps, J. Geophys. Res., vol. 114, A06308.

Magdaleno, S., M. Herraiz and B. A. de la Morena (2012), Characterization of equatorial plasma depletions detected from derived GPS data in South America, J. Atmos. Sol.-Terr. Phy., vol. 74, pp. 136-144.

Maruyama, N., A. D. Richmond, T. J. Fuller-Rowell, M. V. Codrescu, S. Sazykin, F. R. Toffoletto, R. W. Spiro and G. H. Millward (2005) , Geophys. Res. Lett., vol. 32, L17105.

Mendillo, M., L. Bosheng and J. Aarons (2000), The applications of GPS observations to equatorial aeronomy, Radio Sci., vol. 35, no. 3, pp. 885–904.

Mervart, L., Z. Lukes, C. Rocken and T. Iwabuchi (2008), Precise point positioning with ambiguity resolution in real-time, in: Proceedings of ION GNSS2008, Savannah, GA, September 2008, pp. 397–405.

Mireault, Y., P. Tetreault, F. Lahaye, P. Heroux and J. Kouba (2008), Online Precise Point Positioning, GPS World, vol. 19, no. 9, September 2008, pp. 59-64.

Misra, P., and P. Enge (2011), Global positioning system: signals, measurements and performance, Ganga-Jamuna Press, Revised Second Edition.

Mitra, A. P. (1974), Ionospheric effects of solar flares. Astrophysics and Space Science Library, vol. 46, pp. 294.

Moore, R. C., and Y. T. Morton (2011), Magneto-ionic polarization and GPS signal propagation through the ionosphere, Radio Sci., vol. 46, RS1008.

Moreno, M. (2012), Development of algorithms for the GNSS data processing: their application to the modernized GPS and Galileo scenarios. PhD Thesis. Universidad Complutense de Madrid.

Moreno, B., S. Radicella, M. C. de Lacy, M. Herraiz, and G. Rodríguez-Caderot (2011), On the effects of the ionospheric disturbances on precise point positioning at equatorial latitudes, GPS Solut., vol. 15, pp. 381–390.

Moreno, B., G. Rodríguez-Caderot and M. C. de Lacy (2014), Multifrequency algorithms for precise point positioning: MAP3, GPS Solut., vol. 18, no. 3, pp. 355–364.

Muella, M. T. A. H., E. A. Kherani, E. R. de Paula, A. P. Cerruti, P. M. Kitner, I. J. Kantor, C. N. Mitchell, I. S. Batista and M. A. Abdu (2010), Scintillation-producing Fresnel-scale irregularities associated with the regions of steepest TEC gradients adjacent to the equatorial ionization anomaly, J. Geophys. Res., vol. 115, A03301.

Muralikrishna, P., (2000), F-region electron density irregularities during the development of equatorial plasma bubbles, Geofísica Internacional, vol. 39, no. 1, pp. 117-125.

Nava, B., S. M. Radicella, R. Leitinger and P. Coïsson (2007), Use of total electron content data to analyze ionosphere electron density gradients, Adv. Space Res., vol. 39, no. 3, pp. 1292–1297.

Nishida, A., N. Iwasaki and T. Nadata (1966), The origin of fluctuations in the equatorial electrojet: a new type of geomagnetic variation, Ann. Geophys., vol. 22, pp. 478-484.

Nishioka, M., A. Saito and T. Tsugawa (2008), Occurrence characteristics of plasma bubble derived from global ground-based GPS receiver networks, J. Geophys. Res., vol.113, A05301.

NRCan (2004), On-line precise point positioning 'How to use' document, ver. 1.1, Natural Resources Canada.

Paznukhov, V. V., B. W. Reinisch, P. Song, X. Huang, T. W. Bullett and O. Veliz (2007), Formation of an F3 layer in the equatorial ionosphere: A result from strong IMF changes, J. Atmos. Sol.-Terr. Phy., vol. 69, pp. 1292-1304.

Petit, G., and B. Luzum (2010), IERS Conventions: IERS Technical Note No. 36.

Petrie, E. J., M. Hernández-Pajares, P. Spalla, P. Moore and M. A. King (2011), A review of higher order ionospheric refraction effects on dual frequency GPS, Surv. Geophys., vol. 32, pp. 197-253.

Pi, X., A. J. Mannucci, U. J. Lindqwister and C. M. Ho (1997), Monitoring of global ionospheric irregularities using the worldwide GPS network, Geophys. Res. Lett., vol. 24, pp. 2283-2286.

Pi, X., A. J. Manucci, B. Valant-Spaight, Y. Bar-Sever, L. J. Romans, S. Skone, L. Sparks and G.M. Hall (2013), Observations of global and regional ionospheric irregularities and scintillation using GNSS tracking networks, in: Proceedings of ION Pacific PNT Conference, Honolulu, Hawaii, April 22–25, pp. 752-761.

Pimenta, A. A., P. R. Fagundes, Y. Sahai, J. A. Bittencourt and J. R. Abalde (2003), Equatorial F-region depletion drifts: latitudinal and seasonal variations, Ann. Geophys., vol. 21, no. 12, pp. 2315-2322.

Qian, L., A. G. Burns, P. C. Chamberlin and S. C. Solomon (2010), Flare location on the solar disk: Modeling the thermosphere and ionosphere response, J. Geophys. Res., vol. 115, A09311.

Rajner, M., and T. Liwosz (2011), Studies of crustal deformation due to hydrological loading on GPS height estimates, Geodesy and Cartography, vol. 60, no. 2, pp. 135-144.

Rebischung, P., (2011), IGSMAIL-6354: Upcoming switch to IGS08/igs08.atx, International GNSS Service. Available from: http://igscb.jpl.nasa.gov/pipermail/igsmail/2006/005518.html [Accessed 01/04/ 2016]

Ren, Z., W. Wan, L. Liu and J. Xiong (2009), Intra-annual variation of wave number 4 structure of vertical ExB drifts in the equatorial ionosphere seen from ROCSAT-1, J. Geophys. Res., vol. 114, A05308.

Risbeth, H., (1997), The ionospheric E-layer and F-layer dynamos-a tutorial review, J. Atmos. Sol.-Terr. Phy., vol. 59, no. 15, pp. 1873-1880.

Rodríguez- Bilbao I., B. Moreno, G. Rodríguez-Caderot, M. Herraiz and S. M. Radicella (2014), Degradación del posicionamiento de precisión originada por irregularidades de plasma ecuatorial, Física de la Tierra, vol. 26, pp. 89-100.

Rodríguez-Bilbao, I., B. Moreno, G. Rodríguez-Caderot, M. Herraiz and S. M. Radicella (2015a), Evaluation of precise point positioning accuracy under large total electron content variations in equatorial latitudes, Adv. Space Res., vol. 55, no. 2, pp. 605–616.

Rodríguez-Bilbao, I., S. M. Radicella, G. Rodríguez-Caderot and M. Herraiz (2015b), Precise point positioning performance in the presence of the 28 October 2003 sudden increase in total electron content, Space Weather, vol. 13, no. 10, pp. 698-708.

Rodríguez-Bouza, M., I. Rodríguez-Bilbao, C. Cid, J. Palacios, E. Saiz, G. Rodríguez-Caderot, M. Herraiz, Y. Cerrato and A. Guerrero (2015), Effect of solar storms on the geomagnetic field and the ionosphere. Case study: event of 18-24 February 2014. 12th European Space Weather Week. Poster.

Rocken, C., J. Johnson, T. Van Hove and T. Iwabuchi (2005), Atmospheric water vapor and geoid measurements in the open ocean with GPS, Geophys. Res. Lett., vol. 32, L12813.

Sahai, Y., J. Aarons, M. Mendillo, J. Baumgardner, J. Bittencourt and H Takahashi (1994), OI 630 nm imaging observations of equatorial plasma depletions at 16ºS dip latitude, J. Atmos. Terr. Phys., vol. 56, no. 11, pp. 1461-1475.

Sardón, E., and N. Zarraoa (1997), Estimation of total electron content using GPS data: How stable are the differential satellite and receiver instrumental biases? Radio Sci., vol. 32, no. 5, pp. 1899–1910.

Sastri, J. H., (2002), Penetration electric fields at the nightside dip equator associated with the main impulse of the storm sudden commencement of 8 July 1991, J. Geophys. Res., vol. 107, no. A12, pp. 1448.

Scherliess, L. and B. G. Fejer (1999), Radar and satellite global equatorial F region vertical drift model, J. Geophys. Res., vol. 104, no. A4, pp. 6829-6842.

Schunk, R. W., and A. F. Nagy (2009), Ionospheres: Physics, plasma physics, and chemistry, Second Edition, Cambridge Atmospheric and Space Science Series, Cambridge University Press, New York.

Schwenn, R., (2006), Space Weather: the solar perspective, Living Rev. Solar Phys., vol.3, no. 2.

Sreeja, V., M. Aquino and K. de Jong (2013), Impact of the 24 September 2011 solar radio burst on the performance of GNSS receivers, Space Weather, vol. 11, pp. 306–312.

Sreeja, V., M. Aquino, K. de Jong and H. Visser (2014), Effect of the 24 September 2011 solar radio burst on precise point positioning service, Space Weather, vol. 12, pp. 143–147.

Singh, S., F. S. Johnson and R. A. Power (1997), Gravity wave seeding of equatorial plasma bubbles, J. Geophys. Res., vol. 102, no. A4, pp. 7399-7410.

Shi, J., C. Xu, J. Guo and Y. Gao (2014), Local troposphere augmentation for real-time precise point positioning, Earth, Planets and Space, vol. 66:30.

Shiokawa, K., Y. Otsuka, T. Tsugawa, T. Ogawa, A. Saito, K. Ohshima, M. Kubota, T. Maruyama, T. Nakamura, M. Yamamoto, and P. Wilkinson, Geomagnetic conjugate observation of nighttime medium-scale and large-scale travelling ionospheric disturbances: FRONT3 campaign, J. Geophys. Res., vol. 110, no. A05303.

Shiokawa, K., G. Lu, Y. Otsuka, T. Ogawa, M. Yamamoto, N. Nishitani, and N. Sato (2007), Ground observation and AMIE-TIEGCM modelling of a storm-time travelling ionospheric disturbance, J. Geophys. Res., vol. 112, no. A05308.

Skone, S., K. Knudsen and M. de Jong (2001), Limitations in GPS Receiver Tracking Performance under Ionospheric Scintillation Conditions, Physics and Chemistry of the Earth (A), vol. 26, pp. 613-621.

Skone, S., and S. Shrestha (2002), Limitations in GPS positioning accuracies at low latitudes during solar maximum, Geophysical Research Letters, vol. 29, no. 10, 1439.

Skone, S., and A. Coster (2009), Studies of storm-enhanced density impact on DGPS using IGS reference station data, J. Geod., vol. 83, pp. 235-240.

Sridharan, S., S. Sathishkumar and S. gurubaran (2009), Variabilities of mesospheric tides and equatorial electrojet strength during major stratospheric warming events, Ann. Geophys., vol. 27, pp. 4125-4130.

Sultan, P. J., (1996), Linear theory and modelling of the Rayleigh-Taylor instability leading to the occurrence of equatorial spread F, J. Geophys. Res., vol. 101, no. A11311, pp. 26875-26891.

Tsugawa, T., A. Saito and Y. Otsuka (2004), A statistical study of large scale travelling ionospheric disturbances using the GPS network in Japan, J. Geophys. Res., vol. 109, pp. 1–11.

Tsugawa, T., T. Sadakane, J. Sato, Y. Otsuka, T. Ogawa, K. Shiokawa and A. Saito (2006), Summer-winter hemispheric asymmetry of sudden increase in ionospheric total electron content induced by solar flares: A role of O/N2 ratio, J. Geophys. Res., vol. 111, A11316.

Tsugawa, T., Y. Otsuka, A. J. Coster and A. Saito (2007a), Medium-scale traveling ionospheric disturbances detected with dense and wide TEC maps over North America, Geophys. Res. Lett., vol. 34, L22101.

Tsugawa, T., S. R. Zhang, A. J. Coster, Y. Otsuka, J. Sato, A. Saito, Y. Zhang and L. J. Paxton (2007b), Summer-winter hemispheric asymmetry of the sudden increase in

ionospheric total electron content and of the O/N2 ratio: Solar activity dependence, J. Geophys. Res., vol. 112, A08301.

Tsunoda, R. T., (1985), Control of the seasonal and longitudinal occurrence of equatorial scintillations by the longitudinal gradient in the integrated E-region Pedersen conductivity, J. Geophys. Res., vol. 90, no. A1, pp. 447-456.

Tsunoda, R. T., (2006), Day-to-day variability in equatorial spread F: is there some physics missing? Geophys. Res. Lett., vol. 33, L16106.

Tsurutani B., A. Mannucci, B. Iijima, M. A. Abdu, J.H.A. Sobral, W. Gonzalez, F. Guarniri, T. Tsuda, A. Saito, K. Yumoto, B. Fejer, T.J. Fuller-rowell, J. Kozyra, J. C. Foster, A. Coster and V. M. Vasyliunas (2004), Global dayside ionospheric uplift and enhancement associated with interplanetary electric fields, J. Geophys. Res., vol. 109, A08302.

Tsurutani B. T., D. L. Judge, F. L. Guarnieri, P. Gangopadhyay, A. R. Jones, J. Nuttall, G. A. Zambon, L. Didkovsky, A. J. Mannucci, B. Iijima, R. R. Meier, T. J. Immel, T. N. Woods, S. Prasad, L. Floyd, J. Huba, S. C. Solomon, P. Straus and R. Viereck (2005), The October 28, 2003 extreme EUV solar flare and resultant extreme ionospheric effects: Comparison to other Halloween events and the Bastille Day event, Geophys. Res. Lett., vol. 32, LS03S09.

Valladares, C. F., J. Villalobos, R. Sheehan and M. P. Hagan (2004), Latitudinal extension of low-latitude scintillation measured with a network of GPS receivers, Ann. Geophys., vol. 22, no. 9, pp. 3155-3175.

Van Dierendonck, A. J., J. Klobuchar and Q. Hua (1993), Ionospheric Scintillation Monitoring Using Commercial Single Frequency C/A Code Receivers, in: Proceedings of ION GPS-93, Salt Lake City, UT, September 1993, pp. 1333-1342.

Veenadhari, B., S. Alex, T. Kikuchi, A. Shinbori, R. Singh and E. Chandrasekhar (2010), Penetration of magnetospheric electric fields to the equator and their effects on the low-latitude ionosphere during intense geomagnetic storms, J. Geophys. Res., vol. 115, A03305.

Wan, W., L. Liu, H. Yuan, B. Ning and S. Zhang (2005), The GPS measured SITEC caused by the very intense solar flare on July 14, 2000, Adv. Space Res., vol. 36, pp. 2465–2469.

Wan, W., L. Liu, X. Pi, M.-L. Zhang, B. Ning, J. Xiong and F. Ding (2008), Wavenumber-4 patterns of the total electron content over the low latitude ionosphere, Geophys. Res. Lett., vol. 35, L12104.

Wanninger, L., (1993a), Effects of equatorial ionosphere on GPS, GPS World, vol. 4, no. 7, July 1993, pp. 48-54.

Wanninger, L., (1993b), Ionospheric monitoring using IGS data, in: Proceedings of the 1993 IGS Workshop, Astronomical Institute, Univ. of Berne, Berne, Switzerland, pp. 351–360.

Wang, S., S. Huang and H. Fang (2015), Wave-3 and wave-4 patterns in the low- and mid-latitude ionospheric TEC, J. Atmos. Sol.-Terr. Phy., vol. 132, pp. 82-91.

Warnant, R., (1998), Detection of irregularities in the total electron content using GPS measurements:-application to a mid-latitude station, Acta Geodaetica et Geophysica Hungarica, vol. 33, no. 1, pp. 121-128.

Wautelet, G., and R. Warnant (2013), Climatological study of ionospheric irregularities over the European mid-latitude sector with GPS, J. Geod., vol. 88, no. 3, pp. 223-240.

Wautelet, G., and R. Warnant (2015), Origin of high-frequency TEC disturbances observed by GPS over the European mid-latitude region, J. Atmos. Sol.-Terr. Phy., vol. 133, pp. 67-78.

Whalen, J. A., (2004), Linear dependence of the postsunset equatorial anomaly electron density on solar flux and its relation to the maximum prereversal E x B drift velocity through its dependence on solar flux, J. Geophys. Res., vol. 109, A07309.

White, S. M., (2007), Solar radio bursts and Space Weather, Asian Journal of Physics, vol. 16, pp. 189-207.

Willis P., B. Haines, J. P. Berthias, P. Sengenes and J. L. Le Mouel (2004), Behaviour of the DORIS/Jason oscillator over the South Atlantic Anomaly, C. R. Geosci., vol. 336, no. 9, pp. 839–846.

Xu, G., (2007), GPS: theory, algorithms and applications, Springer, Berlin, Germany, pp. 340.

Yizengaw, E., J. Retterer, E. E. Pacheco, P. Roddy, K. Groves, R. Caton and P. Baki (2013), Postmidnight bubbles and scintillations in the quiet-time June solstice, Geophys. Res. Lett., vol. 40, pp. 5592–5597.

Zhang, D. H., and Z. Xiao (2005), Study of ionospheric response to the 4B flare on 28 October 2003 using International GPS Service network data, J. Geophys. Res., vol. 110, A03307.

Zhang, X., Z. Gao, M. Ge, X. Niu, L. Huang, R. Tu and X. Li (2013), On the convergence of Ionospheric Constrained Precise Point Positioning (IC-PPP) based on Undifferential Uncombined Raw GNSS Observations, Sensors, vol. 13, pp. 15708-15725.

Zhu, J., B. Zhao, W. Wan and B. Ning (2013), An investigation of the formation patterns of the ionospheric F3 layer in low and equatorial latitudes, J. Atmos. Sol.-Terr. Phy., vol. 102, pp. 48-58.

Zumberge, J. F., M. B. Heflin, D. C. Jefferson, M. M. Watkins and F. H. Webb (1997), Precise point positioning for the efficient and robust analysis of GPS data from large networks, J. Geophys. Res., vol. 102, no. B3, pp. 5005-5017.

Appendix A.
Overview of GNSS

Global navigation satellite system (GNSS) is the collective name used for satellite navigation systems that provide the user with a three dimensional position solution by passive ranging using radio signals transmitted by orbiting satellites. The bias in the receiver clock at the instant of the measurement affects the travel times calculated for all satellites equally. For that reason, the three coordinates of position together with this bias are the four unknowns to be estimated in positioning, and for that, at least four (or more) satellites are need.

Nowadays three GNSS systems aim to provide global coverage: the U.S. Global Positioning System (GPS), the Russian constellation GLONASS (*Global'naya Navigatsionnaya Sputnikovaya Sistem*) and the European system Galileo, being the GPS the most widely used.

The GPS is formed by 3 segments: space, control, and user segments, which work together to provide an accurate position anytime and anywhere.

The *space segment* is constituted by the satellites. The GPS operates with a nominal constellation of 24 satellites although the current (19/10/2015) constellation consists of 31 operational satellites (ftp://tycho.usno.navy.mil/pub/-gps/gpsb2.txt) orbiting at a radius of 26,600 km, in six orbital planes with a 55º tilt relative to the Earth's equator and a period of 11 h 58 min (approximately half a sidereal day). With an elevation angle mask of 5º, between 5 and 14 satellites are visible at most times, assuming a clear line of sight (LOS). Satellite's visibility is higher in Equatorial and Polar Regions than in mid-latitudes.

The *control segment* is integrated by 12 ground stations that monitor the GPS navigation signals continuously; a Master Control Station which provides command and control functions; and the 4 ground antenna stations from which data and corrections are sent back to satellites. The functions of the control segments include: satellites' orbits monitoring, satellites' health and GPS time maintenance, ephemerids and clocks parameters predictions, satellite navigation message update, and orbit adjustments.

Finally, regarding the *user segment*, only to mention that civil user's capabilities differ from the ones of military use according to which Standard Positioning Service (SPP) or Precise Positioning Service (PPS) respectively is provided.

A.1. GPS satellites' signals

The present GPS satellites transmit continuously using a variety of frequencies in the L band (Table A.1). While the legacy GPS satellites transmit in L1 and L2, the modernization programs carried out in the last decade, and which are still nowadays ongoing, have led to include additional navigation signals on the new generation of satellites to fulfil the ongoing military, civil and commercial needs. However, not all of them are broadcast by all satellites yet. Regarding this work, we will focus on the signals used in the processing, although some remarks with respect to the rest of the signals may appear.

Table A.1 Summary of the GPS navigation signals

Frequency Band	Centre Freq. (MHz)	Signal (service name)	Use
L1	1575.42	C/A	SPS
		P1: P(Y)	PPS
		M	PPS
		L1C	SPS
L2	1227.60	P2: P(Y)	PPS
		L2C	SPS
		M	PPS
L5	1176.45	L5	SPS

*SPS=Standard Positioning Service, PPS=Precise positioning Service

Satellites transmit their information in three signals that modulate the L1 and L2 carrier frequencies: the *Coarse Acquisition* (C/A, or clear access) code on L1, a *Precise* (P or P(Y)) code on both L1 and L2 and a *Navigation* data *Message*. P and C/A codes are *Pseudo Random Noise* (PRN) codes. PRN codes are unique to each satellite and are used to identify each of them by the mutually orthogonality property, which enables the receiver to isolate a single satellite from a cross correlation technique and to process each satellite in view individually.

The C/A code is 1,023 chips long and repeats every millisecond (ms) (i.e., modulates the L1 carrier at 1.023 MHz). This makes it relatively easy to acquire but the correlation properties are poor. Each satellite transmits one of 36 C/A code sequences (originally 31), each of them allocated at a PRN signal number selected to minimize cross correlation.

All GPS satellites broadcast the encrypted precise Y-code, which comprises the publicly known precise (P) code multiplied by an encryption code which acts as an anti-spoofing (AS) measure (active nearly continuously since 1994). This is only available to licensed precise positioning service (PPS) users but can be

switched to broadcast P-code. The notation P(Y) –code is commonly used to refer to the P and Y codes collectively. The P code is a product of two PRN codes one of 15345000 chips and the other, 37 chips longer, giving a total code period of over 38 weeks. Each GPS satellite transmits a different 1-week repeating segment of this code on both the L1 and L2 frequencies (i.e. P (Y) code modulates both L1 and L2 at 10.23 MHz and repeats on a 7 day cycle). Due to the 10 times faster bit rate of P with respect to C/A, it provides more accurate positioning and is less vulnerable to jamming.

Additionally, navigation message containing satellites clocks bias, ephemeris, almanac and health status is superimposed to both C/A and P-codes at a 50 bps (bit per second) with a bit duration of 20 ms. Although it takes 12.5 min for the entire message to be received and the entire message repeats every 12.5 min, the satellites ephemerides and clock parameters repeat each 30 s.

On the other hand, since P(Y)-code is too long it is derived after C/A using the timing information that relates C/A and P(Y) and is broadcast in navigation message.

Although applications such as PPP and GPS-TEC retrieval need dual frequency measurements, only P(Y)-code signal was broadcast on L2 before the GPS modernization. This motivated the development of techniques to obtain Y-code pseudorange and carrier phase measurements in L2 without having full access to this signal (the cryptographic knowledge for full access to this signal). These techniques are referred as either *codeless* or *semicodeless* processing [Kaplan, 2005]. Civilian *semicodeless* tracking receivers, such as the ones in the IGS network, employ signal processing techniques that do not require cryptographic access to the P(Y) code. These techniques will become obsolete when the modernized GPS civil signal become available.

Regarding “new” signals, L2C (civilian signal) broadcast provides a higher signal-to-noise (SNR) ratio than L2, enabling better tracking performance, and improving dual frequency applications. L1C will be more robust than the existing C/A, providing better signal reception. On the other hand, L5 offers better correlation properties than C/A code and is expected to be used for precise and robust applications by L1-L5 combination, but its complete availability is not expected until 2018 [Misra and Enge, 2011].

A.2. GPS ranging and errors

The principle of GPS is based on signals travel time measurement by the alignment of the incoming signal with the receiver generated replica. By this principle, two kinds of measurements are provided.

In one hand, code tracking provides an estimation of the apparent travel time of the signal from a satellite to the receiver. This procedure is usually accomplished with C/A-code by the alignment of the incoming code with a replica generated at the receiver and sliding the replica in time to compute the correlation. After this correlation the receiver can read the satellite clock time to determine when the PRN chip was generated at the satellite and compare it with the time of the reception in the receiver clock. This apparent travel time multiplied by the speed of light in vacuum gives the *pseudorange*.

On the other hand, *carrier phase* tracking provides a much more precise, although ambiguous, measurement of the difference between the receiver generated carrier signal and the carrier received from a satellite at the instant of the measurement.

However, the signal from its emission from the satellite to the receiver may be affected by a variety of effects that may introduce errors to the actual range. For that reason, to estimate the receiver position precisely, it is necessary to infer the true range of the satellite (ρ) by correcting, when possible, the GPS observables from the multiple errors sources (including some listed in Table A.2).

Table A.2 Error sources on GPS.

Receiver related errors	**Satellite related errors**
Clocks	Clock and orbit (ephemeris)
Antennas phase center offset and variation	Satellite orbit
Site displacements	Relativistic effects
Sagnac effect	Satellite antenna PCO
Receiver Noise in Code and Carrier	Phase wind up effect
Transmission related errors	**Other kind of errors**
Troposphere	Cycle slips
Ionosphere	Receiver clock jumps
Interference (Jamming, Spoofing)	Satellite eclipse periods
Code and Carrier Multipath	Satellite problems
Scintillation	Satellite geometry

A.3. GPS observables and linear combinations

The GPS observables stored in the RINEX files that are used in the data processing of this thesis are the measured pseudorange (code) and the carrier phase for each carrier frequency (L1 and L2) which can be written in units of distance (meters) as shown in Eq. (a.1) and Eq. (a.2) respectively. In this expressions, relativistic effects, phase wind up and antenna phase offsets corrections have been excluded for the sake of simplicity.

$$P_i = \rho + c\left(dt_R - dt^S\right) + T + k_{1i} I_1 + c\left(B_{Pi}^S + B_{RPi}\right) + M_{Pi} + \varepsilon_{Pi} \tag{a.1}$$

$$L_i = \rho + c\left(dt_R - dt^S\right) + T - k_{1i} I_1 + L_{i0} + N_i \Lambda_i + c\left(B_{Li}^S + B_{RLi}\right) + M_{Li} + \varepsilon_{Li} \tag{a.2}$$

Where i=1,2 are the subscript that correspond to L1 and L2

P_i	measured pseudorange
L_i	measured carrier phase (converted to distance units)
ρ	satellite-receiver geometric distance
c	vacuum speed of light
dt_R, dt^S	receiver and satellite clock errors
T	tropospheric error
$k_{1i} I_1$	ionospheric delay where $k_{1i} = (f_1/f_i)^2$
L_{i0}	initial carrier phase (converted to distance units)
N_i	carrier phase ambiguity (in cycles)
Λ_i	wave length
$B_{Pi}^S, B_{RPi}, B_{Li}^S, B_{RLi}$	Satellite and receiver instrumental bias for code and phase respectively
M_{Pi}, M_{Li}	Code and phase multipath
$\varepsilon_{Pi}, \varepsilon_{Li}$	Measurements noise of code and phase observations (Un-modeled, modeling and measurement errors)

Combining the measured observables in different frequencies permits solving some problems such as ionospheric effect or taking advantage of the properties of the combination for cycle slip detection [Blewitt, 1990] or ambiguity resolution for instance [Dach et al., 2007]. In the following lines the most broadly used dual frequency (GPS L1 and L2) data combinations along with its advantages and disadvantages are listed.

A.3.1.Ionosphere-free linear combination

$$P_{IF} = \frac{f_1^2 P_1 - f_2^2 P_2}{f_1^2 - f_2^2};\ L_{IF} = \frac{f_1^2 L_1 - f_2^2 L_2}{f_1^2 - f_2^2} \tag{a.3}$$

This is the combination used in dual frequency precise point positioning since ionospheric delay effect is almost completely removed [Misra and Enge, 2011]. However, there are still some disadvantages. The ambiguity of the carrier phase can only be estimated as a float unknown (it is not an integer value anymore). The standard deviation of the measurement is 3 times higher than the basic observation (the observation noise increases depending on the frequencies involved in the combination) and higher order ionospheric effects and bending effects are not removed [Petrie et al., 2011].

A.3.2.Geometry-free linear combination

$$P_{GF} = P_1 - P_2;\ L_{GF} = L_1 - L_2 \tag{a.4}$$

The Geometry–free (GF) linear combination, also called ionospheric combination, removes all the terms that are independent on the frequency. The solution is independent of satellites and receivers clocks, orbits and receiver coordinates. Phase's combination contains ionospheric delay and initial phase ambiguities. It cancels all terms that do not depend on frequency such as geometric range, troposphere and so on, leaving the ionospheric contribution, instrumental bias and wind-up effect among others. It is used for CS detection [Blewitt, 1990].

Carrier phase GF combination removes the geometry and all non-dispersive effects. Provides a low-noise signal (multipath and noise less than 1 cm) and is affected by ionospheric refraction (which varies smoothly in mid-latitudes only under quiet days).

A.3.3.Wide-lane and Narrow-lane linear combination

$$L_{WL} = \frac{f_1 L_1 - f_2 L_2}{f_1 - f_2}; P_{NL} = \frac{f_1 P_1 + f_2 P_2}{f_1 + f_2} \quad \text{(a.5)}$$

The wide-lane (WL) combination is used for cycle-slip CS detection since it provides with an effective long wavelength (86.2 cm), around four times larger than L1 and L2 wavelengths. Its standard deviation is 5.7 times larger than L1 observable. Besides, the standard deviation of the narrow-lane (NL) combination is 0.7 times the L1 observable, and the wavelength (10.6 cm), roughly half the value of L1 and L2.

A.3.4.Melbourne-Wübbena linear combination

$$L_{MW} = L_{WL} - P_{NL} \quad \text{(a.6)}$$

The Melbourne-Wübbena (MW) code and phases combination eliminates ionospheric, tropospheric and geometric effects and it is usually used for CS detection [Blewitt, 1990]. It can be used for WL ambiguities resolution.

MW combination cancels all the non-dispersive effects and the ionospheric refraction. However, it is affected by multipath and its performance is worse than GF combination.

A.3.5.Code minus carrier or Code-carrier divergence

$$CMC_i = P_i - L_i = 2k_{1i} I_1 - N_i \Lambda + \varepsilon_{Pi} + \varepsilon_{Li} \quad \text{(a.7)}$$

In this combination all effects are cancelled except the ionospheric delay which, unless ionospheric perturbations, suffers slow variations; the ambiguity parameter, the multipath and the measurement noise. Multipath and noise are both included in ε parameter where in general can be assumed that $\varepsilon_{Li} << \varepsilon_{Pi}$. This combination can be used for multipath estimation. In fact it is used to approximate the psudorange multipath, ignoring very small contributions of carrier multipath and measurement noise. Since the CMC due to the ionosphere varies slower than the one related to multipath, this combination has been also used to distinguish between potential multipath fades and the amplitude scintillation [Aquino et al., 2009]

A.4. Interoperability with GLONASS

Making use of additional systems to GPS brings a number of benefits to the users; however, it requires interoperability. Multi-GNSS receivers are more complex since operating in more frequencies and correlating a greater number of signals of different types requires more complex hardware and software.

GNSS signals are broadcast in a number of frequency bands within the 1-2 GHz L-band region. The fundamental requirement for the coexistence for different systems is the frequency compatibility; in other words, they must operate without interfering with each other. As presently the Galileo system is not operative yet, our attention is paid to GLONASS.

The Russian GLONASS was developed as a military navigation system by the USSR (Union of Soviet Socialist Republics). The current (19/10/2015) constellation comprises 23 operational satellites (https://www.glonass-iac.ru/en/GLONASS/) that orbit at a radius of 25,600 km with a period of 11h 15 min (so each satellite completes $2^{1/8}$ orbits in one sidereal day). The ground track of each individual satellite repeats every 8 sidereal days. GLONASS was designed independently of GPS and uses different frequencies and geodetic and time references. GPS uses WGS 84 datum based on ITRF (International Terrestrial Reference Frame), while GLONASS uses the "Parametry Zemli 1990" (PZ-90) reference frame which from December 31, 2013 is broadcasting the version PZ.90.11 the closest to the ITRF2000 (https://www.glonass-iac.ru/en/content/-news/?ELEMENT_ID=721). Furthermore, GPS and GLONASS timing are based on, the U.S. and Russian versions of UTC respectively, and since no GLONASS-GPS time conversion data is broadcast by the time of writing this thesis, the difference between U.S. and Russian UTC must be treated as an additional unknown in the navigation solution.

Appendix B.
Stations' information

This appendix summarizes the information of the sites relevant for this work. The information was obtained from the site log provided in the IGS website.

B.1. AREQ

Site Log: areq_20130131.log

Site Information		
Site Name *(ID)*	*City or Town (Country)* *Tectonic plate*	*Date Installed*
Arequipa Laser Station (AREQ)	Arequipa (Peru) South American	1993-01-01T00:00Z

GNSS Receiver Information		
Receiver Type *Serial Number* *Firmware Version*	*Satellite System* *Elevation Cutoff*	*Date Installed* *Date Removed*
AOA SNR-8000 ACT T360U 3.3.32.2	GPS 4º	2000-01-28T00:00Z 2002-08-13T20:45Z
ASHTECH UZ-12 ZR220010203 CJ10 1s soc2rnx	GPS 4º	2002-08-13T20:45Z 2006-02-16T17:00Z
ASHTECH UZ-12 ZR220010401 CQ00	GPS 4º	2006-05-21T00:00Z …

GNSS Antenna Information		
Antenna Type *Serial Number*	*Date Installed* *Date Removed*	*Additional Information*
AOAD/M_T JPLA 294	1994-03-29T00:00Z 2002-03-05T13:00Z	Antenna removed and replaced for local survey 05-MAR-2002; off mount from 13:00-20:45 UT.
AOAD/M_T JPLA 294	2002-03-05T20:45Z 2007-12-04T16:00Z	RF signal split to 2nd receiver running as unofficial ARE2. Antenna temporarily removed for local SLR/DORIS tie survey 2007-05-01T12:41Z replaced same day 22:40Z.
AOAD/M_T JPLA 294	2007-12-04T18:00Z 2011-08-19T11:55Z	New antenna cable installed on 2007-12-04T18:00Z. Antenna is now being powered through a powered signal splitter. A Huber-Shuner lightning protector was added. Antenna setup was not changed.
AOAD/M_T JPLA 294	2011-08-19T11:55Z 2012-02-02T23:39Z	JPLA radome removed.

Date	Local Episodic Effects Possibly Affecting Data Quality
2001-06-23	8.4 earthquake
2001-07-07	7.6 aftershock
2011-08-26	Transition from .soc to .ash data types. For soc data types used soc2rnx to do the conversion to RINEX data. For ash data types using teqc directly to do the conversion to RINEX data.

B.2. AMC2

Site log: amc2_20140915.log

Site Information		
Site Name *(ID)*	*City or Town (Country)* *Tectonic plate*	*Date Installed*
Alternate Master Clock AMC2	Colorado Springs (U.S.) North American	1998-10-15

GNSS Receiver Information		
Receiver Type *Serial Number* *Firmware Version*	*Satellite System* *Elevation Cutoff*	*Date Installed* *Date Removed*
AOA SNR-12 ACT 247-U 3.3.32.4	GPS	2000-07-10T20:50Z 2002-06-21T00:00Z
ASHTECH Z-XII3T RT920013101 IL01-1D04-MCF-12MX	GPS	2002-07-03T17:21Z …

GNSS Antenna Information		
Antenna Type *Serial Number*	*Date Installed* *Date Removed*	*Additional Information*
AOAD/M_T NONE 308	1998-03-24 2002-06-14T16:50Z	In the website
AOAD/M_T NONE KW-5-0001	2002-06-14T16:51Z 2007-10-01T18:00Z	In the website

B.3. KOUR

Site Log: kour_20150827.log

Site Information		
Site Name *(ID)*	*City or Town (Country)* *Tectonic plate*	*Date Installed*
Kourou (KOUR)	Kourou (French Guiana) South American	1992-10-18T00:00Z

GNSS Receiver Information		
Receiver Type *Serial Number* *Firmware Version*	*Satellite System* *Elevation Cutoff*	*Date Installed* *Date Removed*
ASHTECH Z-XII3 LP019995005 NAV CD00,CHN 1D02*21	GPS 0º	2000-03-07T00:00Z 2004-09-30T15:00Z
ASHTECH UZ-12 IR1200240020 CJ00	GPS 0º	2004-09-30T16:00Z 2006-10-12T07:00Z
ASHTECH UZ-12 IR1200240020 CJ00	GPS 0º	2007-06-20T12:30Z 2008-01-06T09:30Z
JPS LEGACY 340-0863 3.1	GPS+GLO 0º	2008-01-15T14:00Z 2008-04-08T13:20Z
JPS LEGACY 340-0863 3.2	GPS+GLO 0º	2008-04-08T13:20Z 2008-05-13T12:45Z
JPS LEGACY 340-0863 3.3	GPS+GLO 0º	2008-05-13T13:00Z 2009-06-25T22:00Z
JPS LEGACY 340-0863 3.4	GPS+GLO 0º	2009-06-26T06:00Z 2012-11-06T00:00Z

GNSS Antenna Information		
Antenna Type *Serial Number*	*Date Installed* *Date Removed*	*Additional Information*
AOAD/M_B NONE 270	1998-01-05T13:30Z 2002-01-30T00:00Z	-
ASH701945C_M NONE CR520014804	2002-01-30T00:00Z 2006-10-12T07:00Z	-
ASH701945C_M NONE CR620023903	2007-06-20T12:30Z 2008-01-06T09:30Z	-
ASH701946.3 NONE CR420033512	2008-01-15T14:00Z 2012-11-06T00:00Z	-

B.4. MAD2

Site log: mad2_20130131.log. Antenna is shared with site MADR.

Site Information		
Site Name *(ID)*	*City or Town (Country)* *Tectonic plate*	*Date Installed*
Madrid Deep Space Tracking Station (MAD2)	Robledo (Spain) Eurasian	1989-01-01

GNSS Receiver Information		
Receiver Type *Serial Number* *Firmware Version*	*Satellite System* *Elevation Cutoff*	*Date Installed* *Date Removed*
ASHTECH Z-XII3T RT920041504 1L01-1D04	GPS 4º	2004-11-29T22:50Z …

GNSS Antenna Information			
Antenna Type *Serial Number*		*Date Installed* *Date Removed*	*Additional Information*
AOAD/M_T 451-U	NONE	2003-11-11T13:30Z ---	-

Date	Local Episodic Effects Possibly Affecting Data Quality
2012-02-03	Transitioned from .soc to .ash data types. For soc data typed used soc2rnx to do the conversion to RINEX data. For ash data types using teqc directly to do the conversion to RINEX.
2012-02-08	Wi-Fi antenna located at Building 300 roof has been disconnected and removed on 2012-02-08T14:30 HS Madrid, Spain time. This is in response to finding the source of Madrid GPS signal multipath.
2012-02-21	Part of the handrail nearest to GPS antenna was removed. This appears to have solved the Madrid GPS multipath degradation problem.

Local Ongoing Conditions Possibly Affecting Computed Position	
Effective Dates	*Cause*
2011-11-01/ 2012-02-07	*Radio Interferences*: Wi-Fi antenna system (2.4GHz) located around 45 degrees north and near enough to produce multipath effects.
2011-02-01/ 2012-02-21	*Multipath Sources*: Safety Metallic Roof Handrail

B.5. MALI

Site Log: ftp://igs.org/pub/station/oldlog/mali_20080915.log
Decommissioned in 2008.

Site Information		
Site Name *(ID)*	*City or Town (Country)* *Tectonic plate*	*Date Installed*
Malindi (MALI)	Malindi (Kenya) African	1995-11-12

GNSS Receiver Information		
Receiver Type *Serial Number* *Firmware Version*	*Satellite System* *Elevation Cutoff*	*Date Installed* *Date Removed*
ROGUE SNR-12 RM 230 3.2.32.9	GPS 0	1999-08-19T16:00Z 2001-04-26T00:00Z
ASHTECH Z-XII3 LP020005006 NAV CD00,CHN 1D02*21	GPS 0	2001-04-26T00:00Z 2008-09-11T15:00Z

GNSS Antenna Information		
Antenna Type *Serial Number*	*Date Installed* *Date Removed*	*Additional Information*
AOAD/M_T 205	1997-10-23T13:37Z 2008-09-11T15:00Z	Station decommissioned. Replaced by MAL2.

B.6. NKLG

Site Log: nklg_20151021.log

Site Information		
Site Name *(ID)*	*City or Town (Country)* *Tectonic plate*	*Date Installed*
N'KOLTANG (NKLG)	Libreville (Gabon) African	2000-02-10T00:00Z

GNSS Receiver Information		
Receiver Type *Serial Number* *Firmware Version*	*Satellite System* *Elevation Cutoff*	*Date Installed* *Date Removed*
TRIMBLE 4000SSI 3919A25765 7.29	GPS -	2000-02-10T00:00Z 2008-01-24T10:00Z
TRIMBLE 4000SSI 3919A25765 7.29	GPS 3º	2008-01-24T10:02Z 2010-05-03T11:30Z
TRIMBLE NETR5 4819K55803 4.17	GPS+GLO 3º	2010-10-26T08:15Z 2011-05-26T12:00Z
TRIMBLE NETR9 5038K70406 4.22	GPS+GLO 3º	2011-05-26T12:30Z 2011-10-13T09:30Z
TRIMBLE NETR9 5038K70406 4.42	GPS+GLO 3º	2011-10-13T09:30Z 2012-06-08T14:00Z

GNSS Antenna Information		
Antenna Type *Serial Number*	*Date Installed* *Date Removed*	*Additional Information*
TRM29659.00 NONE 0220160506	2000-02-10T00:00Z 2010-05-03T11:30Z	-
TRM59800.00 SCIS 4811A48439	2010-05-05T16:00Z 2013-03-29T11:30Z	-

B.7. NTUS

Site Log: ntus_20110125.log

Site Information		
Site Name *(ID)*	*City or Town (Country)* *Tectonic plate*	*Date Installed*
Nanyang Technological University (NTUS)	Singapore (Republic of Singapore) Eurasian	1997-06-26T03:00Z

GNSS Receiver Information		
Receiver Type *Serial Number* *Firmware Version*	*Satellite System* *Elevation Cutoff*	*Date Installed* *Date Removed*
AOA SNR-12 ACT 224 3.3.32.3	GPS 0º	2001-02-22T05:20Z 2001-03-11T00:00Z
AOA SNR-12 ACT 225 3.3.32.3	GPS 0º	2001-06-18T03:40Z 2006-11-03T00:00Z
LEICA GRX1200GGPRO 352729 5.10/3.013	GPS+GLO 0º	2007-06-25T06:00Z 2009-09-03T00:00Z
LEICA GRX1200GGPRO 352729 7.80/3.019	GPS+GLO 0º	2010-05-10T07:04Z 2011-01-25T03:14Z
LEICA GRX1200GGPRO 352729 8.10/3.019	GPS+GLO 0º	2011-01-25T06:28Z …

GNSS Antenna Information			
Antenna Type *Serial Number*		*Date Installed* *Date Removed*	*Additional Information*
AOAD/M_T 222	NONE	1998-06-08T00:00Z 2007-05-16T00:00Z	The antenna is mounted on a pillar with a SOKIA Tribrach. The pillar (approx. 1.50m high) is located on the building of the Survey Laboratory of the School of Civil & Structural Engineering of the Nanyang Technological University at Singapore
LEIAT504GG 200240	NONE	2007-05-16T00:00Z …	The antenna is mounted on a pillar with a LEICA GDF 111-1 Tribrach and rotatable Tribrach adapter. The pillar (approx. 1.50m high) is located on the Laboratory of the School of Civil & Structural Engineering of the Nanyang Technological

B.8. GUAM

Site Log: guam_20150121.log (Existing monument installed on roof of Observatory was chosen due to logistical reasons, and to get the site installed quickly, with the tradeoff being higher than normal multipath)

Site Information		
Site Name *(ID)*	*City or Town (Country)* *Tectonic plate*	*Date Installed*
USGS Guam Observatory (GUAM)	Dededo (Guam) Pacific	1992-01-01T00:00Z

GNSS Receiver Information		
Receiver Type *Serial Number* *Firmware Version*	*Satellite System* *Elevation Cutoff*	*Date Installed* *Date Removed*
ASHTECH Z-XII3 LP019990508 CC00	GPS 4º	2000-04-26T00:00Z 2008-11-20T23:59Z
ASHTECH UZ-12 IR2200722004 CQ00	GPS 4º	2008-11-21T02:16Z 2013-11-20T22:00Z

GNSS Antenna Information		
Antenna Type *Serial Number*	*Date Installed* *Date Removed*	*Additional Information*
AOAD/M_T JPLA 481	1995-01-20T00:00Z 2006-05-17T07:00Z	-
ASH701945B_M JPLA CR519992101	2006-05-22T00:00Z …	-

Date	**Local Episodic Effects Possibly Affecting Data Quality**
2011-09-08	Transitioned from .soc to .ash data types. For soc data typed used soc2rnx to do conversion to RINEX data. For ash data types using teqc directly to do the conversion to RINEX.

Appendix C.
Changes in CSRS-PPP

This appendix summarizes the main changes and events published by CSRS-PPP since the beginning of the processing for this thesis. The public release with the establishment of the GPS Processing Engine Version 1.0 was on 2003-10-14.

2015-10-29

Improved version of the online CSRS-PPP application. This upgrade improves system performance and stability, and changes the solution email format. The former email format is replaced with a more streamlined version. This will not change the CSRS-PPP calculation results.

2014-09-04

Delay for GLONASS PPP processing reduced from 24 hours to 4.5 hours. NRCan GLONASS orbits and clocks needed for CSRS-PPP processing of RINEX files containing GLONASS observations are now available every 3 hours resulting in a processing delay ranging between 1.5 to 4.5 hours.

2014-03-07

CSRS-PPP updated from version V1.05_03812 to V1.05_34613

- realistic GDOP now reported for all processing and observation selections
- added high order ionospheric corrections for GLONASS satellites
- adaptive limits for cycle slip detection and correction now satellite specific
- introduced ground antenna specific GLONASS linear inter-frequency differential code biases
- implemented improved yaw modelling for GPS blocks IIA and IIF

2013-11-29

CSRS-PPP updated to report in sum file both CGVD28 and CGVD2013 orthometric heights if estimated position is in Canada. Currently CGVD28 remains the default but can be changed to CGVD2013 on the CSRS-PPP web page.

2013-11-01

CSRS-PPP updated to report in chronological order estimated positions of the pos and csv files for single frequency (L1) processing.

2013-01-07

Updated GNSS processing software from version 05211 to version 03812.

- use of P2C2 biases for C2 observations processing
- minor bug fixing and updates of some models

2012-10-19

National velocity grid for NAD83(CSRS) coordinates epoch transformation updated from velgsb_v1.0 model to NAD83v6VG model.

2012-02-14

CSRS-PPP now accepts user provided ocean loading correction files (OTL). This complements the CSRS-PPP database of ocean loading corrections currently available for some regions.

NOTE: A global grid of OTL corrections will soon be added to CSRS-PPP. These default corrections, once implemented, will be sufficient for most PPP applications. For applications very near to the coasts, the optional OTL file will offer a means to use more accurate ocean loading corrections if needed.

2011-10-04

CSRS-PPP can now process GLONASS data. NRCan GLONASS products (orbits and clocks) are available starting on day 0 of GNSS week 1649.

GLONASS precise orbits and clock corrections used for PPP processing are available in 24 hour files (0 to 24 hour) 15 hours after the end of the GNSS day. User submitting RINEX observation files prior to that time will first receive a GNSS only solution. The combined GNSS and GLONASS PPP solution will be performed and sent once the required GLONASS products are available.

Appendix D.
Mid-latitude irregularities occurrence: additional material

This appendix is dedicated to the mid-latitudes AMC2 and MAD2 stations complementary tables and figures that are related to the observations presented in Chapter 4. Remember that for MAD2 LT=UT-0.283h, while for AMC2 LT=UT-6.967.

D.1. TIDs occurrence in MAD2

In this subsection mid-latitudes ionospheric irregularities occurrence is highlighted plotting the detrended and smoothed ROT (in TECU/min units) that exceeds a threshold value defined by the expression P_{75}+3IQR, which is based on annual percentile 75 (P_{75}) and interquartile range (IQR) values. Note that the higher the solar activity the larger the threshold value.

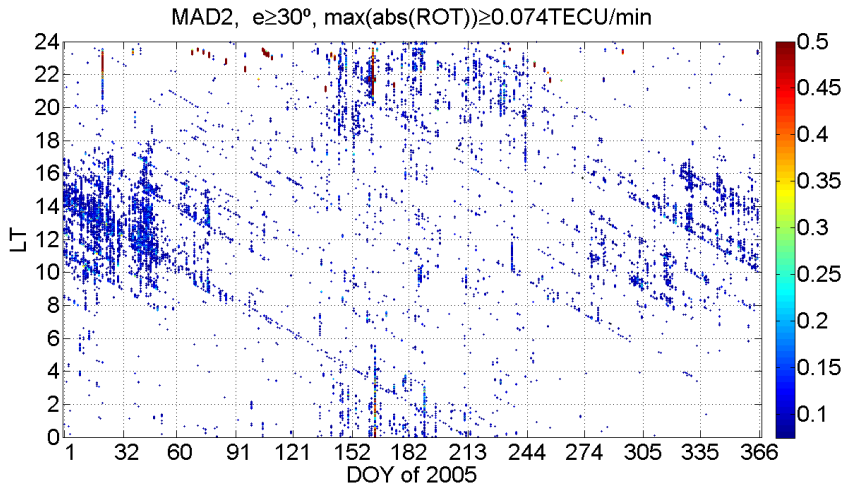

Figure D.1 Ionospheric irregularities occurrence by means of detrended ROT (in TECU/min units) in MAD2 in 2005.

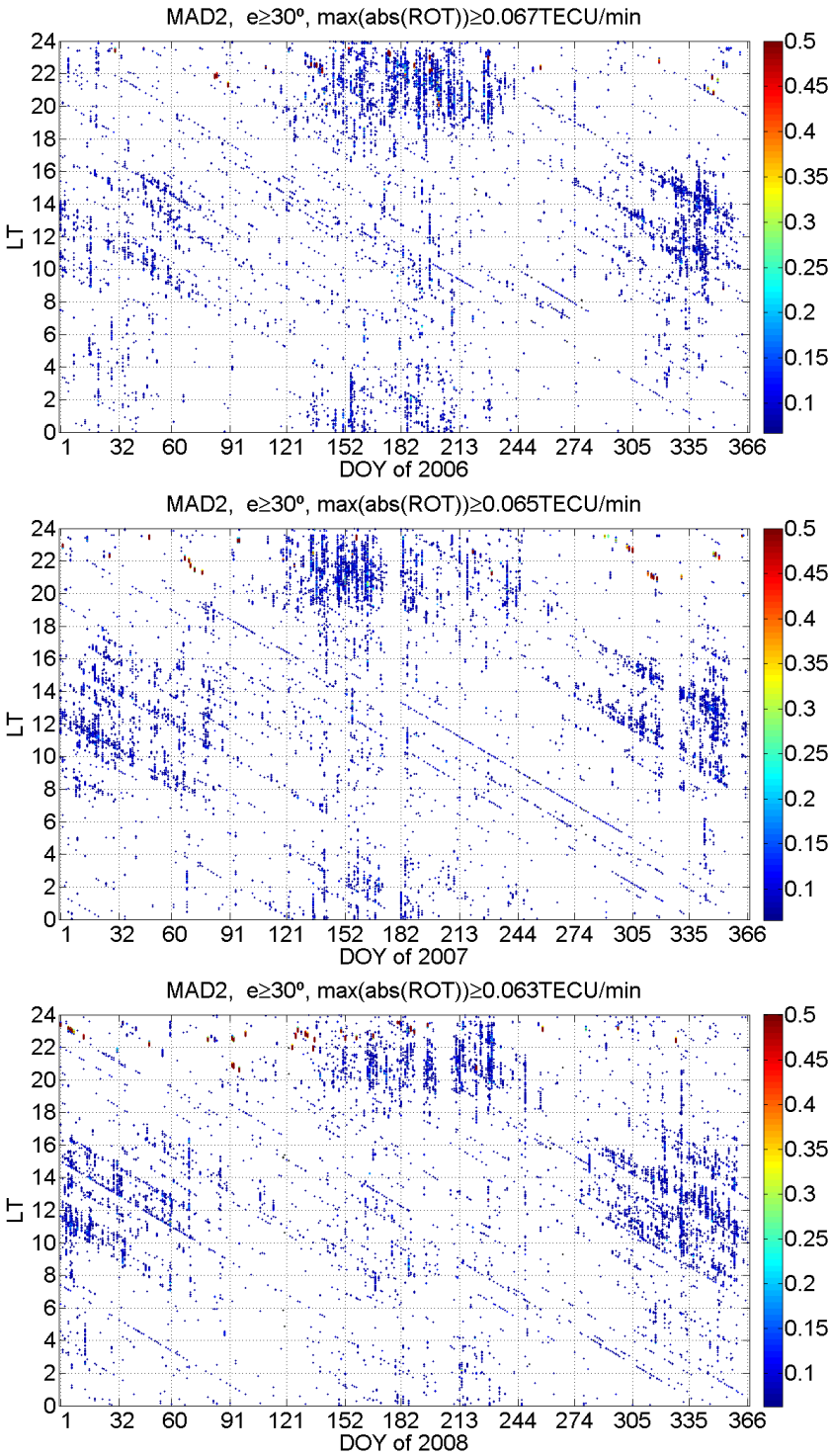

Figure D.2 Same as figure D.1 but for 2006 (top), 2007 and 2008 (bottom), respectively.

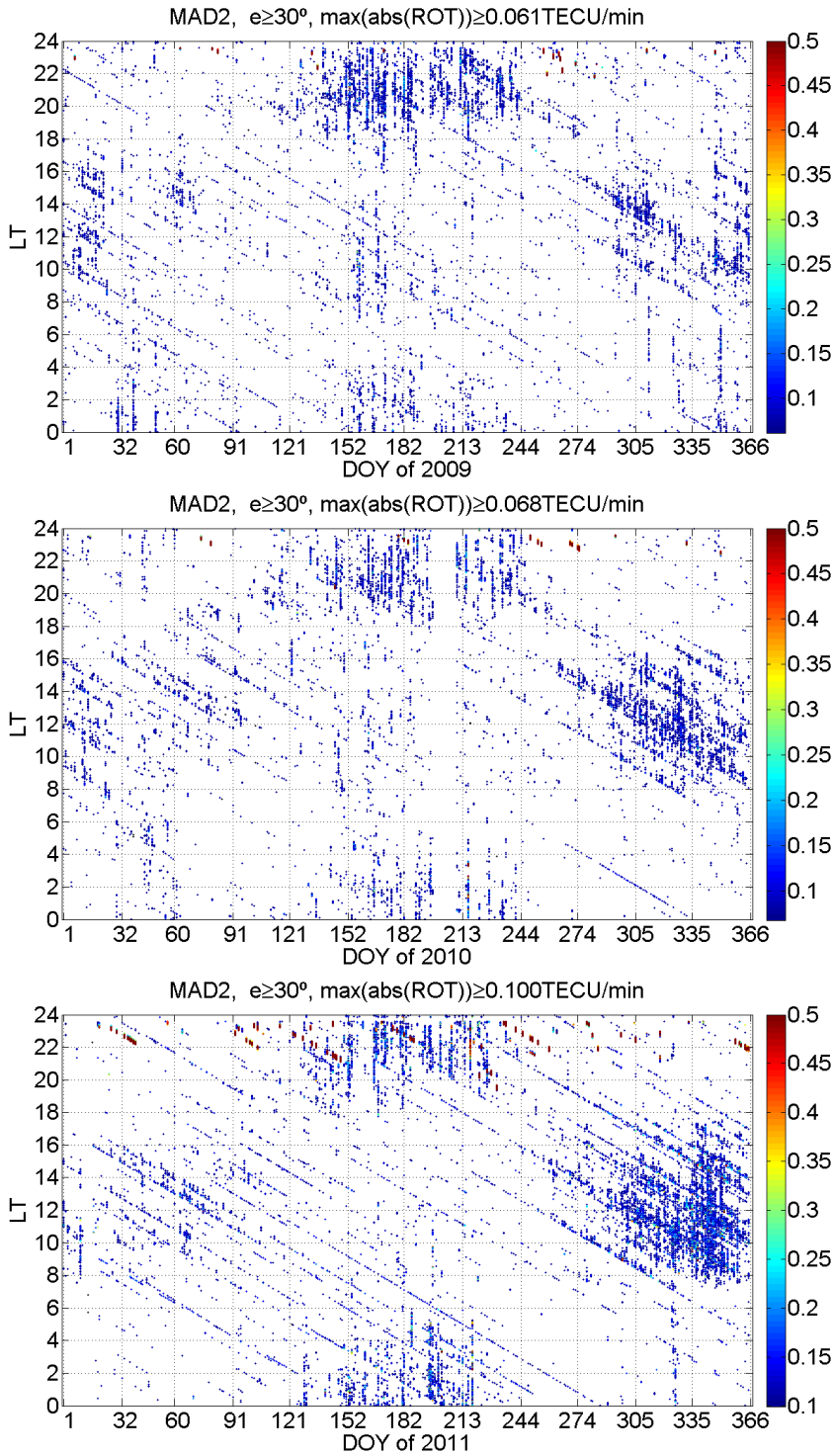

Figure D.3 Same as figure D.1 but for 2009 (top), 2010 and 2011 (bottom), respectively.

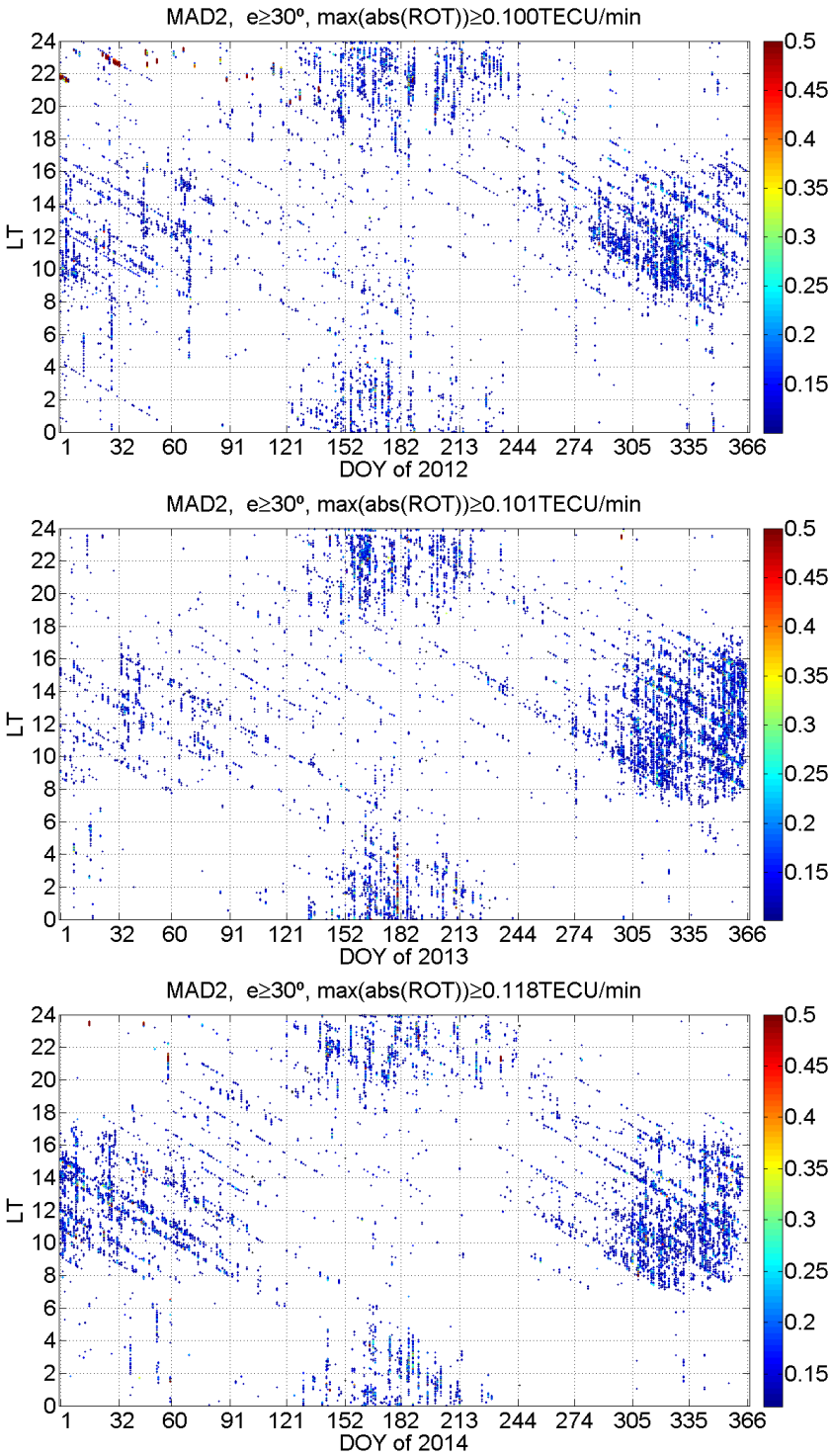

Figure D.4 Same as figure D.1 but for 2012 (top), 2013 and 2014 (bottom), respectively.

D.2. Large ROT in mid-latitudes

This section shows the ROT and Dst index plots corresponding to the events listed in Table 4.3 in Chapter 4. The Dst index data have been downloaded from the *omniweb* whose source is the WDC for geomagnetism, Kyoto. Nevertheless, a time offset is observed between the results shown by one service and the other. This is related to the fact that the hourly Dst index values are calculated by considering the previous hour data and Kyoto website sets the first hour results to 01:00 UT while the *omniweb* assigns it to 00:00 UT.

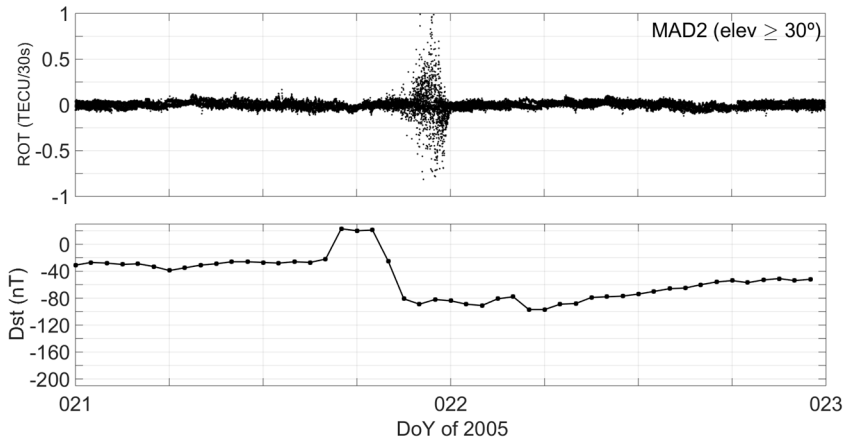

Figure D.5 Fast ROT induction over MAD2 for DoYs 021-022, 2005. Top: no-detrended ROT. Elevation mask: 30º. Bottom: Dst index.

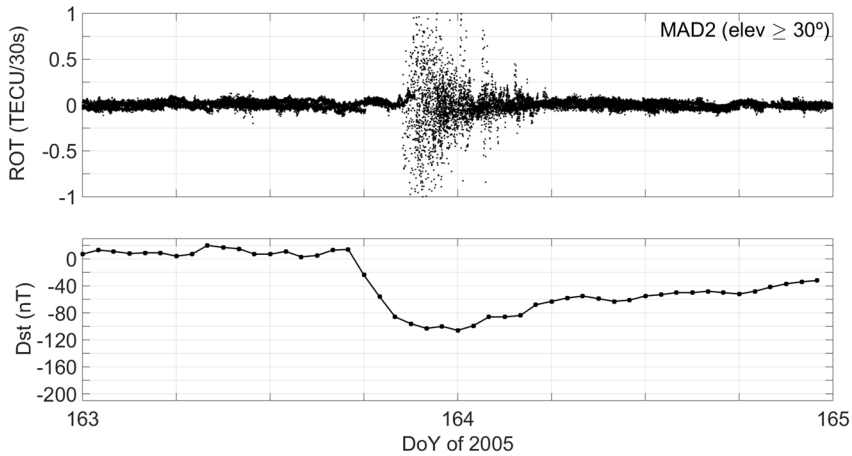

Figure D.6 Same as Figure D.5 but for DoYs 163-164, 2005.

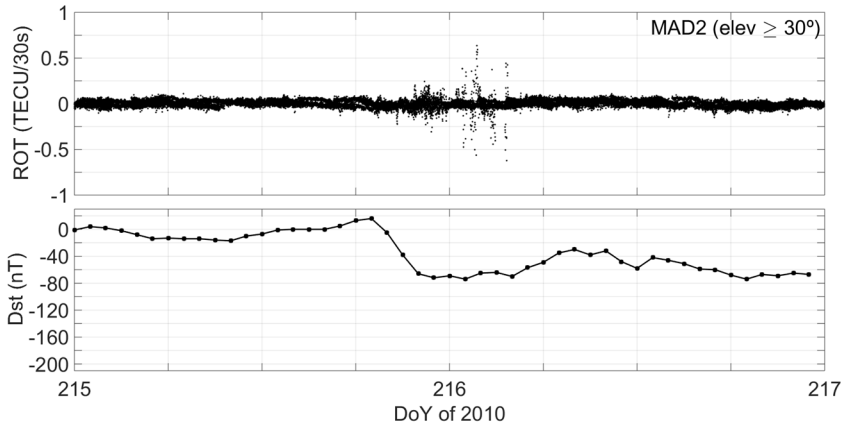

Figure D.7 Same as Figure D.5 but for DoYs 215-216, 2010.

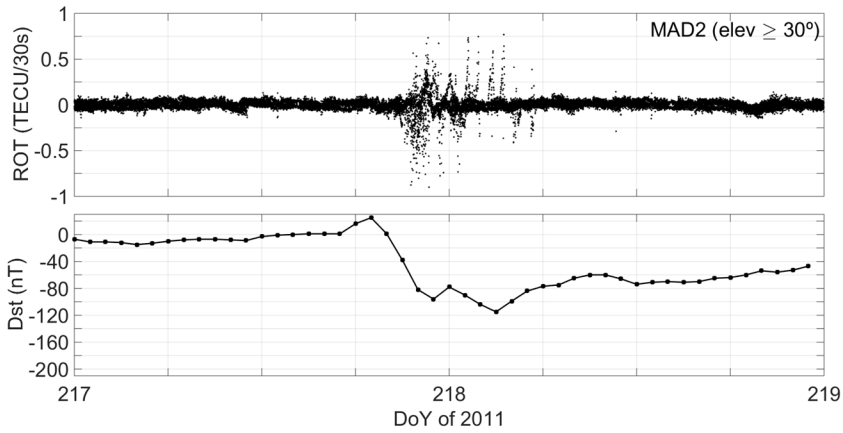

Figure D.8 Same as Figure D.5 but for DoYs 217-218, 2011.

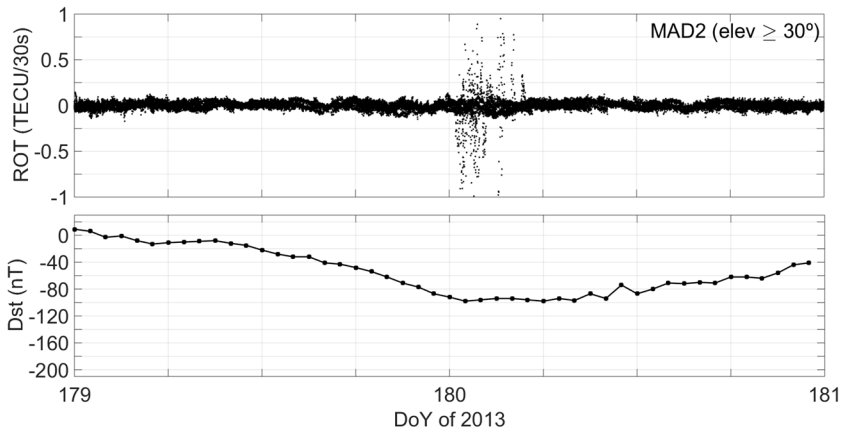

Figure D.9 Same as Figure D.5 but for DoYs 179-180, 2013.

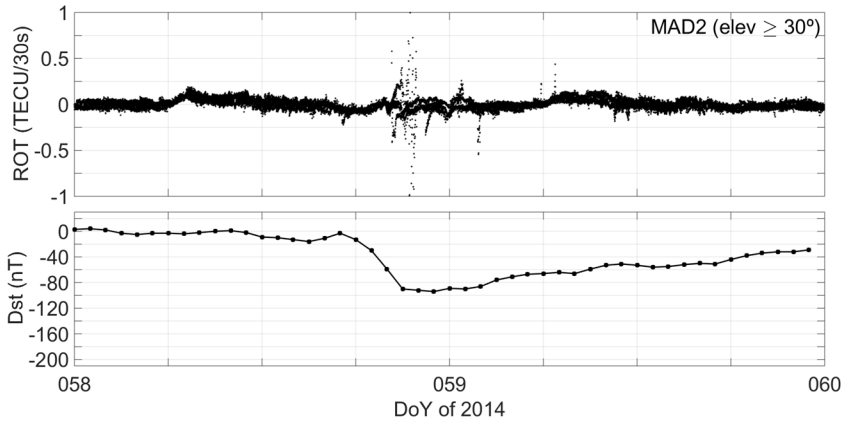

Figure D.10 Same as Figure D.5 but for DoYs 058-059, 2014.

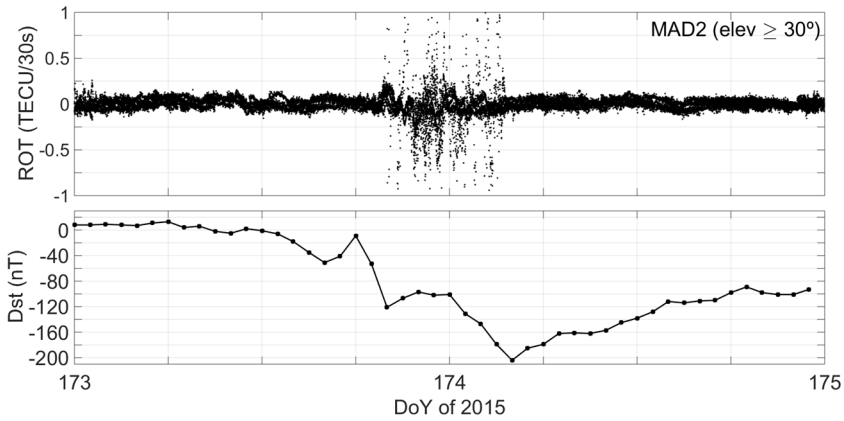

Figure D.11 Same as Figure D.5 but for DoYs 173-174, 2015.

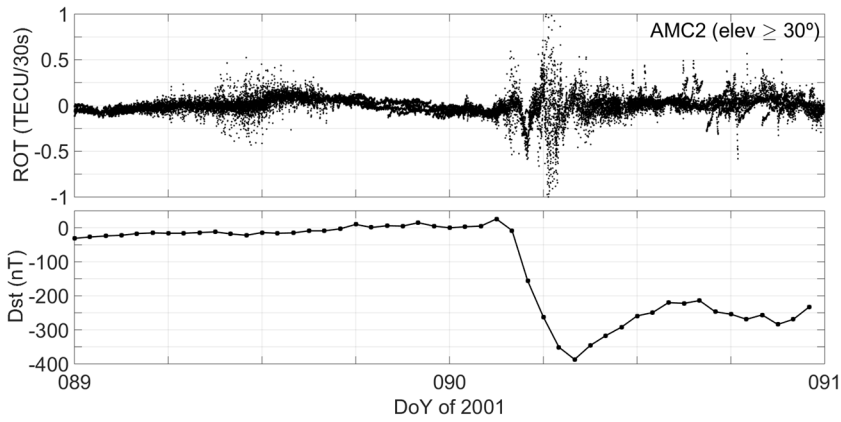

Figure D.12 Same as Figure D.5 but for AMC2 and DoYs 089-090, 2001.

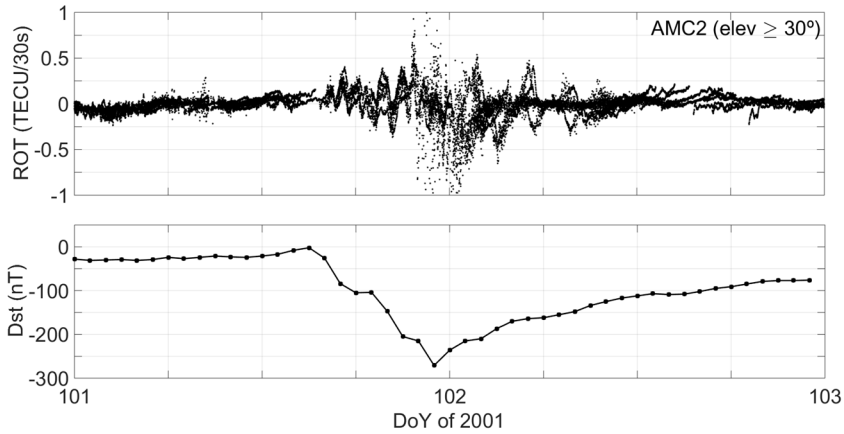

Figure D.13 Same as Figure D.5 but for AMC2 and DoYs 101-102, 2001.

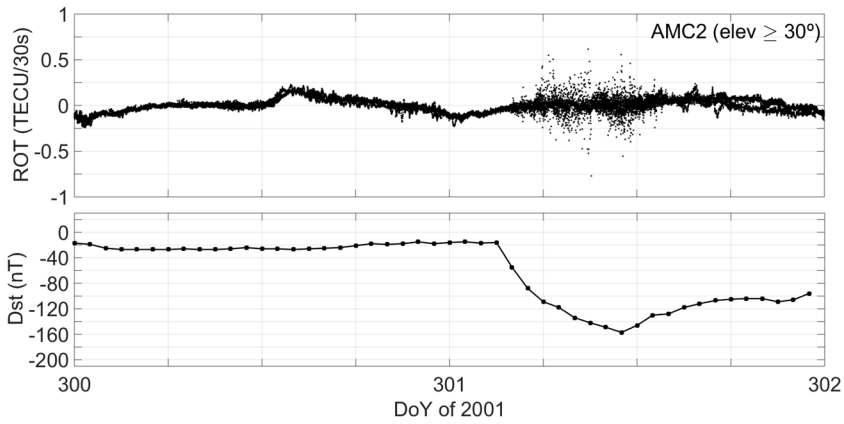

Figure D.14 Same as Figure D.5 but for AMC2 and DoYs 300-301, 2001.

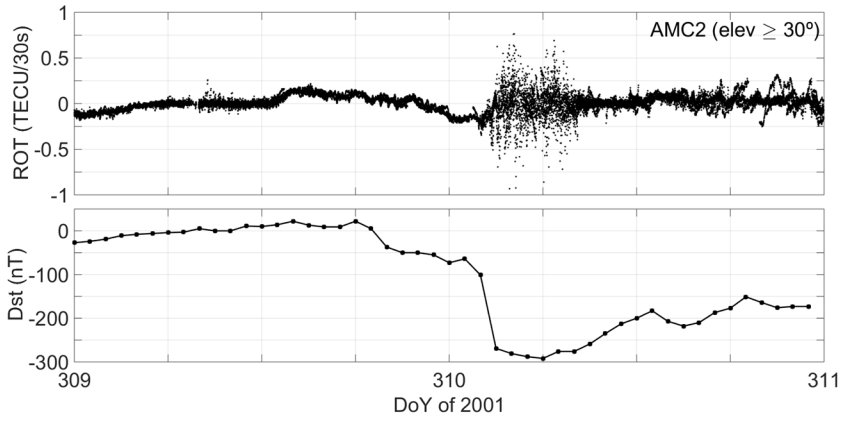

Figure D.15 Same as Figure D.5 but for AMC2 and DoYs 309-310, 2001.

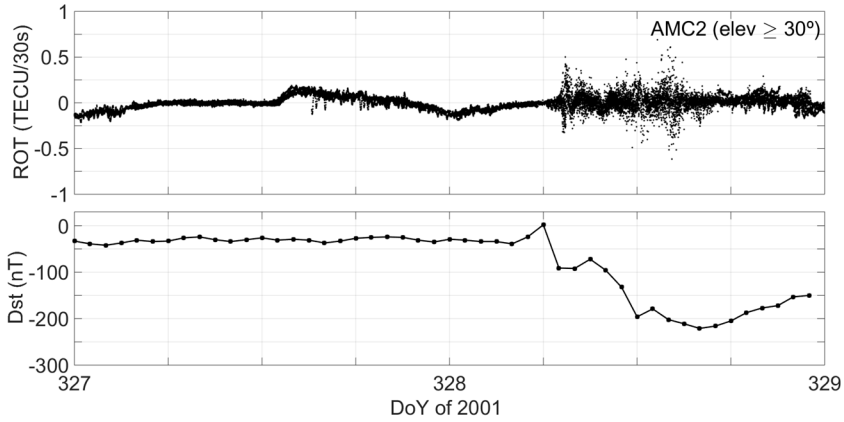

Figure D.16 Same as Figure D.5 but for AMC2 and DoYs 327-328, 2001.

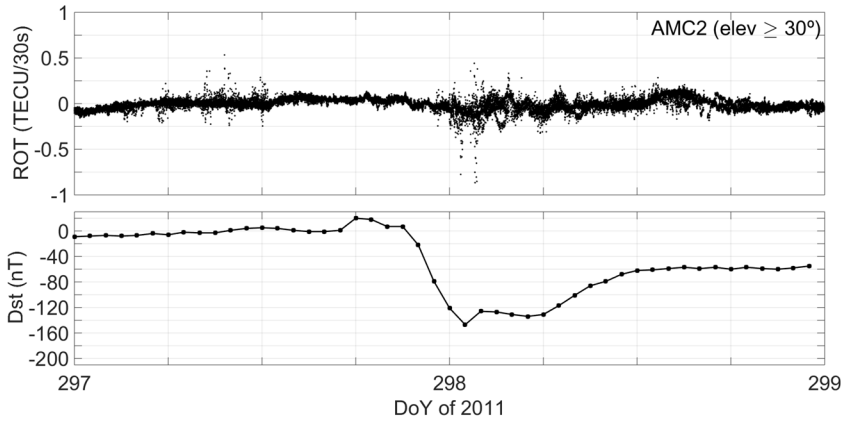

Figure D.17 Same as Figure D.5 but for AMC2 and DoYs 297-298, 2011.

D.3. SITECs in mid-latitudes stations

This appendix provides a list of the SITEC events observed in each station and year of study. The peak value of mean ROT and the time occurring are also listed.

Table D.1 List of SITEC events in AMC2. The peak value of mean ROT in TECU/30s units.

DoY year	Peak ROT	UT	DoY year	Peak ROT	UT
086 2001	0.182	16:29:00	243 2001	0.023	21:24:30
092 2001	0.309	21:47:30	243 2001	0.020	22:41:00
096 2001	0.718	19:14:30	245 2001	0.142	13:46:30
099 2001	0.343	15:25:00	247 2001	0.074	21:55:30
105 2001	0.208	13:47:30	248 2001	0.002	14:28:30
110 2001	0.051	19:53:30	248 2001	0.077	19:06:00
110 2001	0.041	21:32:00	251 2001	0.118	16:44:00
112 2001	0.231	20:41:00	252 2001	0.128	15:15:30
113 2001	0.061	20:21:00	252 2001	0.155	18:40:30
114 2001	0.082	18:10:30	252 2001	0.479	20:43:59
114 2001	0.060	22:21:30	257 2001	0.086	18:42:00
114 2001	0.067	22:22:00	257 2001	0.129	21:45:30
115 2001	0.112	13:44:00	260 2001	0.135	15:48:23
116 2001	0.153	13:10:00	260 2001	0.072	17:11:00
137 2001	0.095	20:44:30	260 2001	0.522	19:39:00
144 2001	0.070	19:35:30	260 2001	0.053	21:05:00
158 2001	0.039	19:09:00	261 2001	0.111	15:37:30
169 2001	0.046	14:55:00	263 2001	0.079	18:15:00
169 2011	0.039	20:03:30	264 2001	0.116	06:39:00
173 2001	0.142	22:18:29	292 2001	0.546	16:22:59
217 2001	0.100	13:20:00	311 2001	0.193	19:33:30
217 2001	0.102	22:20:00	312 2001	0.096	19:03:00
237 2001	0.823	16:31:30	332 2001	0.493	16:34:00
237 2001	0.112	17:32:30	334 2001	0.081	19:59:00
237 2001	0.044	19:53:30	347 2001	0.423	14:25:59

Table D.1 (Continuation)

DoY year	Peak ROT	UT	DoY year	Peak ROT	UT
017 2004	0.325	17:46:00	224 2011	0.156	16:32:30
057 2004	0.056	22:17:59	249 2011	0.420	22:18:30
			250 2011	0.418	22:36:30
074 2008	0.057	17:10:30	251 2011	0.101	15:38:30
			262 2011	0.065	15:38:30
044 2011	0.153	17:34:00	267 2011	0.060	18:03:00
045 2011	0.153	17:25:00	267 2011	0.064	19:11:30
047 2011	0.067	14:23:29	267 2011	0.065	20:34:30
068 2011	0.160	23:21:00	268 2011	0.161	15:31:00
073 2011	0.148	19:51:30	269 2011	0.116	14:41:30
083 2011	0.067	17:05:00	271 2011	0.081	13:27:00
084 2001	0.048	23:14:00	275 2011	0.105	17:22:00
086 2011	0.063	17:01:30	307 2011	0.211	20:21:00
112 2011	0.067	15:51:00	359 2011	0.146	18:14:30
220 2011	0.072	18:03:30			

Table D.2 List of SITEC events in MAD2. The peak value of mean ROT in TECU/30s units.

DoY year	Peak ROT	UT	DoY year	Peak ROT	UT
017 2005	0.201	17:24:30	250 2005	0.107	17:37:00
123 2005	0.062	12:18:00	252 2005	0.235	09:56:30
123 2005	0.066	10:32:00	252 2005	0.066	15:26:00
126 2005	0.078	11:22:30	253 2005	0.107	16:39:00
131 2005	0.067	16:59:30	254 2005	0.048	12:50:00
132 2005	0.059	07:31:00	255 2005	0.525	08:46:30
132 2005	0.074	17:39:00	256 2005	0.076	11:20:30
136 2005	0.105	09:06:30	257 2005	0.270	10:32:30
147 2005	0.092	12:27:30	258 2005	0.520	08:36:00
194 2005	0.123	12:16:30	260 2005	0.071	06:05:00
211 2005	0.121	06:25:30	277 2005	0.064	06:16:00
213 2005	0.107	12:18:00	318 2005	0.091	14:21:00
222 2005	0.067	10:47:30	336 2005	0.256	10:10:59
240 2005	0.078	10:20:00			

Table D.2 (Continuation).

DoY year	Peak ROT	UT	DoY year	Peak ROT	UT
117 2006	0.083	15:47:30	181 2012	0.099	09:19:30
187 2006	0.071	08:20:30	182 2012	0.090	12:51:30
339 2006	0.130	10:28:00	184 2012	0.240	10:47:00
			186 2012	0.123	09:53:00
154 2007	0.140	06:39:30	186 2012	0.080	12:18:30
154 2007	0.077	09:27:00	186 2012	0.809	16:35:60
155 2007	0.083	05:11:30	187 2012	0.288	11:43:30
156 2007	0.055	17:20:00	187 2012	0.055	13:07:00
160 2007	0.047	13:39:30	188 2012	0.076	10:27:30
			190 2012	0.050	12:09:00
039 2010	0.043	12:00:30	190 2012	0.037	16:30:00
039 2010	0.062	13:45:00	211 2012	0.068	06:19:30
043 2010	0.249	11:25:30	212 2012	0.120	14:03:00
017 2011	0.109	10:54:00	013 2013	0.119	08:36:30
049 2011	0.138	10:11:00	175 2013	0.076	11:31:00
066 2011	0.120	09:19:00	297 2013	0.107	10:03:30
083 2011	0.071	12:05:00	297 2013	0.128	10:32:30
221 2011	0.215	08:30:30	298 2013	0.125	07:58:30
251 2011	0.075	15:38:30	298 2013	0.069	14:57:30
252 2011	0.075	12:42:30	310 2013	0.102	13:44:00
267 2011	0.318	09:36:00			
268 2011	0.154	14:25:00	007 2014	0.484	10:11:30
269 2011	0.121	14:41:30	033 2014	0.076	14:04:30
271 2011	0.280	12:29:30	038 2014	0.126	10:28:00
			047 2014	0.168	09:24:00
121 2012	0.070	10:25:00	128 2014	0.128	10:02:30
129 2012	0.081	13:07:19	213 2014	0.299	14:47:00
130 2012	0.065	12:26:00	234 2014	0.065	12:54:00
130 2012	0.162	14:06:30	236 2014	0.123	12:11:30
134 2012	0.077	08:11:00	289 2014	0.157	13:02:30
155 2012	0.198	17:53:30	293 2014	0.200	09:24:00
161 2012	0.064	11:31:00	294 2014	0.268	13:37:30
180 2012	0.080	16:11:00	295 2014	0.398	14:06:30
181 2012	0.060	06:47:00			

Table D.2 (Continuation).

DoY year	Peak ROT	UT	DoY year	Peak ROT	UT
297 2014	0.170	07:42:00	175 2015	0.072	10:49:00
299 2014	0.169	10:49:30	176 2015	0.567	08:14:30
038 2014	0.126	10:28:00	184 2015	0.072	12:50:00
			233 2015	0.062	09:41:30
070 2015	0.119	16:16:30	234 2015	0.141	13:21:30
071 2015	0.084	12:10:30	236 2015	0.138	07:30:30
074 2015	0.092	09:37:30	271 2015	0.212	14:55:30
125 2015	0.052	17:21:00	272 2015	0.105	11:22:00
126 2015	0.100	11:48:00	273 2015	0.085	10:51:30
132 2015	0.089	11:48:30	273 2015	0.068	13:19:30
172 2015	0.128	09:42:00	321 2015	0.547	11:09:30

Glossary

Accuracy. Statistical difference between the estimated (measured) quantity and the true/actual value. Measures the ability to achieve any pre-specified position.

Ambiguity Float value. The ambiguity (integer number of cycles) of the carrier phase plus the remaining uncalibrated hardware satellites and receiver bias.

Ambiguity resolution. The process of determining the integer number of cycles described by the signal carrier. Provides the ability to reach similar levels of accuracy within much shorter observation periods.

Atmospheric Tides. Persistent global scale oscillations in temperature, wind, and density with periods that are harmonics of a solar day.

Co-rotating interaction regions (CIR). Transition zones between fast- and slow-moving solar wind streams.

Coronal Holes (CH). Areas of lower density and temperature with respect to the background Sun's corona, with open magnetic field that begin to form after solar maximum has been reached. These holes grow increasingly larger and can extend from the solar pole area to the solar magnetic equator or even cross it. They are the sources of high-speed solar wind streams which may give rise to recurrent geomagnetic storms.

Coronal Mass Ejections (CME). Huge magnetized plasma structures that are originated in closed magnetic field regions on the Sun and are ejected to the space, not always associated to solar flares. If Earth-directed, they are likely to cause geomagnetic storms. This happens when they are originated close to the solar disc center and carry interplanetary magnetic field (IMF) with southward component.

Convergence time/period. The time required from a cold start to a stable accurate (centimetre/decimetre-level) solution.

Cycle slip. A discontinuity in the carrier phase measurement caused by receiver loss of lock, which is seen as a jump of integer number of wavelengths.

Differential GPS (DGPS) method/relative positioning approach. The position of a station is determined relative to a single or multiple reference stations (in known location within a specific reference frame). By applying carrier-phase double-difference method (between stations and between satellites) the majority of common errors are removed and ambiguities can be fixed resulting in a centimetre-level position accuracy. Common errors decrease with the shorting of the distance between the receiver and the reference/base station. Therefore

the success of the differential method is highly dependent on the length of their baseline. The user will position himself relative to the nearest reference station or several reference stations.

Disturbance Dynamo The mechanism that arise from energy input to the thermosphere during magnetic disturbances that alter the global thermospheric circulation, and consequently modifies the generation of electric fields and currents at mid- and low-latitudes by ionospheric wind dynamo action.

Dst index. It represents the axially symmetric disturbance magnetic field at the dipole equator on the Earth's surface. Major disturbances in Dst are negative, namely decreases in the geomagnetic field. These field decreases are produced mainly by the equatorial current system in the magnetosphere, usually referred to as the ring current. The neutral sheet current flowing across the magnetospheric tail makes a small contribution to the field decreases near the Earth. Positive variations in Dst are mostly caused by the compression of the magnetosphere from solar wind pressure increases. http://wdc.kugi.kyoto-u.ac.jp/dstdir/dst2/onDstindex.html

Flux tube. Magnetized plasma parcel.

Full arc. The period between satellites rising and setting.

Geometric Bending term. The difference between the geometric range (straight line) and the range when signal bending due to the ionospheric refractive index is taken into account (curved line).

The International Geomagnetic Reference Field (IGRF). A worldwide used model representing the Earth's main magnetic field and its secular variation. The latest version IGRF-12 was released on May 2015 and it is accessible in http://www.ngdc.noaa.gov/IAGA/vmod/igrf.html.

Initialization period. The minimum time required for a positioning system to provide a valid solution with a given accuracy.

Interplanetary magnetic field (IMF). The solar magnetic field carried by the solar wind into the interplanetary medium.

Joule Heating. The heating that arises from electric currents (flowing in the ionosphere).

The International Terrestrial Reference Frame (ITRF). It represents the International Terrestrial Reference System (ITRS), which its origin at the mass centre of the whole Earth that takes the oceans and the atmosphere into account. The ITRS is realized by estimates of the coordinates and velocities of a set of observing stations of the International Earth Rotation and Reference System Service (IERS).

Lock time. It indicates how long the receiver has been locked to the carrier phase on the signal.

Loss of lock (LoL). An interruption in the GNSS signal tracking.

Magnetic reconnection. It occurs when a magnetized plasma parcel of one polarity connect with a magnetized plasma parcel of opposite polarity resulting in a change of their topologies. In this process, some energy is taken from the magnetic field and converted to particle kinetic energy.

Magnetically disturbed period periods with $K_p \geq 3^+$ or $a_p \geq 18$. Being K_p and a_p the planetary three hourly geomagnetic activity indexes that are available at http://wdc.kugi.kyoto-u.ac.jp/kp/index.html

Noise. It refers to a quickly varying error that averages out to zero over a short time interval.

Pedersen conductivity. The conductivity which is parallel to the component of the electric field which is perpendicular to the magnetic field.

Phase connected arc. A time series of phase data which has no cycle slip.

Prompt penetration electric fields. Direct penetration of high latitude electric field to lower latitudes.

Reference frame. A reference of coordinates whose purpose is to provide the means to materialize a reference system so that it can be used for the quantitative description of position and motions on the Earth (terrestrial frames) or of celestial bodies including the Earth in space (celestial frames).

Reliability the ability of a positioning system to perform its required functions over a specified time interval. The ability of the positioning system to re-achieve a previously attained position.

RHCP signal. The electric vector of the wave being of constant amplitude and rotating clockwise when viewed from the source of the signal.

Ring current. A magnetic signature of the inner magnetosphere radiation belts which flows westward around the Earth and is mainly due to pressure gradients. Plasma diffusion along the magnetic field lines and plasma injections result in local enhancement of its intensity.

Secular variation. The long term variation of the Earth's magnetic field. It is not constant in time and changes from place to place. It is characterized by a decrease in the strength of the dipole component and a westward drift of the non-dipole field.

Solar terminator Global circle which separates daylight and nighttime zones.

Substorm. A transitory process that starts in the nightside Earth in which a significant amount of energy resulting from the solar wind –magnetosphere interaction is deposited in the auroral ionosphere and magnetosphere.

Sudden Stratospheric Warming. The abrupt increase in the temperature of the polar stratosphere accompanied by a slowing or reversal of the eastward winds in polar vortex.

Scientific contributions

The results of this thesis have been partially disseminated in different conferences and publications (2 peer reviewed). During this period the Ph.D. Candidate has also completed more than three months of short stays, for the fulfillment of the European mention degree. In this period she has also attended different courses and workshops related to her thesis topic.

Publications:

Rodríguez-Bilbao, I., Radicella, S.M., Rodríguez-Caderot, G., Herraiz, M. (2015). Precise point positioning performance in the presence of the 28 October 2003 sudden increase in total electron content. Space Weather, vol. 13, no. 10, pp. 698-708, doi:10.1002/2015SW001201. (IF: 2.149, Q2 (2014))

Rodríguez-Bilbao, I., Moreno, B. Rodríguez-Caderot, G., Herraiz, M., Radicella, S.M. (2015). Evaluation of precise point positioning accuracy under large total electron content variations in equatorial latitudes. Adv. Space Res., vol. 55, pp. 605-616, doi:10.1016/j.asr.2014.11.004. (IF: 1.358, Q3 (2014))

Rodríguez-Bilbao, I., Moreno, B. Rodríguez-Caderot, G., Herraiz, M., Radicella, S.M. (2014). Degradación del posicionamiento de precisión originada por irregularidades de plasma ecuatorial. Física de la Tierra, vol. 26, 89-100, doi:10.5209/FITE.2014.v26.46974.

Rodríguez-Bilbao, I., G. Rodríguez-Caderot, S. M. Radicela, M. Herraiz, L. Ciraolo, B. Moreno y M. C. De Lacy. Análisis de la relación entre las variaciones del contenido de electrones ionosférico (ROT) y el error en el posicionamiento puntual preciso (PPP). 7ª Asamblea Hispano-Portuguesa de Geodesia y Geofísica: Proceedings, Donostia - San Sebastián: ARANZADI, 2012. ISBN 978-84-941323-1-5.

Attended international conferences:

M. Rodríguez-Bouza, **I. Rodríguez-Bilbao**, C. Cid, J. Palacios, E. Saiz, G. Rodríguez-Caderot, M. Herraiz, Y. Cerrato, A. Guerrero. Effect of solar storms on the geomagnetic field and the ionosphere. Case study: event of 18-24 February 2014 (Poster). 12th European Space Weather Week. 23-27 November 2015. Costende, Belgium.

I. Rodríguez-Bilbao, S. M. Radicella, G. Rodríguez-Caderot, M. Herraiz. Precise Point Positioning degradation in the presence of a SITEC (Oral). Triennial URSI Atlantic Radio Science Conference (URSI AT-RASC 2015), 18-22 May 2015, Maspalomas, Gran Canaria, Spain.

M. Rodríguez-Bouza, **I. Rodríguez-Bilbao**, I. Blanco-Cid, M. Herraiz, G. Rodríguez Caderot, B. Moreno-Monge, S. M. Radicella. Effects of two geomagnetic storms on the ionosphere and GNSS positioning in the Iberian

Peninsula (Poster). 2013 Beacon Satellite Symposium, 8-12 July 2013, Bath, United Kingdom.

I. Rodríguez-Bilbao, G. Rodríguez-Caderot, S. M. Radicella, M. Herraiz, L. Ciraolo, B. Moreno, M. C. De Lacy. Análisis de la relación existente entre las variaciones de ROT y el error en el posicionamiento estimado mediante PPP (Oral), 7ª Asamblea Hispano Portuguesa de Geodesia y Geofísica 25-29 de June 2012, Donostia-San Sebastián, Spain.

Short stays in other scientific centers:

Jun 1-30, 2015. Telecommunications/ICT for Development Laboratory (T/ICT4D) at The Abdus Salam International Centre for Theoretical Physics (ICTP) in Trieste, Italy. Supervisor: Prof. Sandro M. Radicella.

Jan 19-Feb 6, 2015. T/ICT4D, ICTP, Trieste, Italy. Supervisor: Prof. Sandro M. Radicella.

Nov 10 -Dec 10, 2014. T/ICT4D, ICTP, Trieste, Italy. Supervisor: Prof. Sandro M. Radicella.

Aug 18-29, 2014. T/ICT4D, ICTP, Trieste, Italy. Supervisor: Prof. Sandro M. Radicella.

Jan 31-Mar 31, 2014. Geodynamics Research Laboratory (GRL/UWM) of the Department of Astronomy and Geodynamics of the University of Warmia and Mazury in Olsztyn, Poland. Supervisor: Dr. Andrzej Krankowski.

Jan 21–Mar 20, 2013. T/ICT4D, ICTP, Trieste, Italy. Supervisor: Prof. Sandro M. Radicella.

Jan 16-27, 2012. T/ICT4D, ICTP, Trieste, Italy. Supervisor: Prof. Sandro M. Radicella.

Attended workshops and courses:

Jul 20-25 2015. 2015 ISR Summer School. Jicamarca (Lima), Peru.

Dic 1-5 2014. The United Nations/ICTP Workshop on the use of Global Navigation Satellite Systems for the scientific applications. ICTP, Trieste, Italy.

May 6-17 2013. Workshop on GNSS Data Application to Low Latitude Ionospheric. ICTP, Trieste, Italy.

Oct 15-17, 2012. Propagation Effects, Channel Models and Related Error Sources on GNSS. ICT COST Action IC0802, Propagation tools and data for integrated Telecommunication, Navigation and Earth Observation systems ESA/ESAC, Madrid, Spain.

Apr 11 -May 1, 2012. Workshop on Science Applications of GNSS in Developing Countries followed by the Seminar on Development and Use of the Ionospheric NeQuick Model, ICTP, Trieste, Italy.